frontiers | Research Topics

Past, present and future of multispacecraft measurements for space physics

Edited by
Joseph E. Borovsky, David Gary Sibeck, David Knudsen, Xochitl Blanco-Cano and Katariina Nykyri

Published in
Frontiers in Astronomy and Space Sciences

ISSN 1664-8714
ISBN 978-2-8325-6144-7
DOI 10.3389/978-2-8325-6144-7

About Frontiers

Frontiers is more than just an open access publisher of scholarly articles: it is a pioneering approach to the world of academia, radically improving the way scholarly research is managed. The grand vision of Frontiers is a world where all people have an equal opportunity to seek, share and generate knowledge. Frontiers provides immediate and permanent online open access to all its publications, but this alone is not enough to realize our grand goals.

Frontiers journal series

The Frontiers journal series is a multi-tier and interdisciplinary set of open-access, online journals, promising a paradigm shift from the current review, selection and dissemination processes in academic publishing. All Frontiers journals are driven by researchers for researchers; therefore, they constitute a service to the scholarly community. At the same time, the *Frontiers journal series* operates on a revolutionary invention, the tiered publishing system, initially addressing specific communities of scholars, and gradually climbing up to broader public understanding, thus serving the interests of the lay society, too.

Dedication to quality

Each Frontiers article is a landmark of the highest quality, thanks to genuinely collaborative interactions between authors and review editors, who include some of the world's best academicians. Research must be certified by peers before entering a stream of knowledge that may eventually reach the public - and shape society; therefore, Frontiers only applies the most rigorous and unbiased reviews. Frontiers revolutionizes research publishing by freely delivering the most outstanding research, evaluated with no bias from both the academic and social point of view. By applying the most advanced information technologies, Frontiers is catapulting scholarly publishing into a new generation.

What are Frontiers Research Topics?

Frontiers Research Topics are very popular trademarks of the *Frontiers journals series*: they are collections of at least ten articles, all centered on a particular subject. With their unique mix of varied contributions from Original Research to Review Articles, Frontiers Research Topics unify the most influential researchers, the latest key findings and historical advances in a hot research area.

Find out more on how to host your own Frontiers Research Topic or contribute to one as an author by contacting the Frontiers editorial office: frontiersin.org/about/contact

Past, present and future of multispacecraft measurements for space physics

Topic editors

Joseph E. Borovsky — Space Science Institute (SSI), United States

David Gary Sibeck — Goddard Space Flight Center, National Aeronautics and Space Administration, United States

David Knudsen — University of Calgary, Canada

Xochitl Blanco-Cano — National Autonomous University of Mexico, Mexico

Katariina Nykyri — Goddard Space Flight Center, National Aeronautics and Space Administration, United States

Citation

Borovsky, J. E., Sibeck, D. G., Knudsen, D., Blanco-Cano, X., Nykyri, K., eds. (2025). *Past, present and future of multispacecraft measurements for space physics*. Lausanne: Frontiers Media SA. doi: 10.3389/978-2-8325-6144-7

Table of contents

frontiers | Frontiers in Astronomy and Space Sciences

TYPE Editorial
PUBLISHED 06 March 2025
DOI 10.3389/fspas.2025.1579994

OPEN ACCESS

EDITED AND REVIEWED BY
Julio Navarro,
University of Victoria, Canada

*CORRESPONDENCE
Katariina Nykyri,
katariina.nykyri@nasa.gov

RECEIVED 19 February 2025
ACCEPTED 21 February 2025
PUBLISHED 06 March 2025

CITATION
Nykyri K, Blanco-Cano X, Knudsen D, Sibeck DG and Borovsky JE (2025) Editorial: Past, present and future of multispacecraft measurements for space physics. *Front. Astron. Space Sci.* 12:1579994. doi: 10.3389/fspas.2025.1579994

Editorial: Past, present and future of multispacecraft measurements for space physics

Katariina Nykyri[1]*, Xochitl Blanco-Cano[2], David Knudsen[3], David Gary Sibeck[1] and Joseph E. Borovsky[4]

[1]Heliophysics Division, NASA Goddard Space Flight Center, Greenbelt, MD, United States, [2]Instituto de Geofísica Unam, National Autonomous University of Mexico México City, Mexico City, Mexico, [3]Department of Physics and Astronomy, University of Calgary Calgary, Calgary, AB, Canada, [4]Center for Space Plasma Physics, Space Science Institute (SSI), Boulder, CO, United States

KEYWORDS

space plasma physics, multi-spacecraft methods, imagers, gradient-based methods, vortex identification, energetic particle detectors, electric field measurements, soft-x ray (SXR) measurements

Editorial on the Research Topic
Past, present and future of multispacecraft measurements for space physics

Measurements of space plasmas have remained challenging as they must cover multiple species, a wide range of flux levels and energies, and time and spatial scales that range over orders of magnitude. Interactions between a wide variety of fundamental physical processes that occur both on both macroscopic and kinetic scales ultimately determine the modes and efficiency of the solar wind-magnetosphere coupling, including magnetic reconnection, particle energization, and ion-neutral interactions, as well as their corresponding ionospheric and ground signatures. During the last 25 years we have transitioned from single and two-point plasma and field measurements to constellation missions, e.g., Cluster, THEMIS and MMS. This has enabled the development of various multi-spacecraft techniques, e.g., using four-point tetrahedron measurement of magnetic field to determine boundary orientations and motion as well as current densities. This Research Topic has invited contributions to discuss the past, present and future of multi-spacecraft measurements as well as a new imaging mission and techniques for space physics. This editorial summarizes the nine articles submitted to this Research Topic: two review articles, three method articles, two original research articles, one opinion paper, and one perspective article.

The curlometer and spatial gradient based methods are comprehensively reviewed by Dunlop et al. These techniques are adaptable to a range of multi-point and multi-scale arrays, originally developed for ESA's Cluster mission, but later adapted for Swarm and MMS. The authors note that "multi-spacecraft estimates of current density and spatial gradients have provided key information on large and small magnetospheric current systems and related transient structures, resolving 3-D currents for a range of conditions in widely different geospace regions. The curlometer technique, in particular, has proved to be reliable and robust. The applicability of the method is limited by certain constraints, particularly those for relatively small structures compared to the spacecraft separation distances." The authors

discuss the further adaptations of these techniques for future constellation missions such as Helioswarm and Plasma Observatory.

A thorough review of solar energetic particle measurements both from historical and current missions, together with the outlook for future missions are given by Reames. The author recommends that "advancing the physics of SEPs may require a return to the closer spacing of the Helios era with coverage mapped by a half-dozen spacecraft to help disentangle the distribution of the SEPs from the underlying structure of the magnetic field and the accelerating shock".

The Kelvin-Helmholtz Instability (KHI), arising from a velocity shear across a plasma boundary, plays a crucial role in plasma, momentum, and energy transfer, e.g., from the shocked solar wind into the planetary magnetospheres and at the boundaries of Coronal Mass Ejections (see, e.g., Nykyri et al. (2021); Nykyri (2024) and references therein). However, a robust vortex detection method by spacecraft has been missing. Here, Kelly et al. develop and validate a novel vortex identification method for ideal MHD, based on existing methods from hydrodynamics. Current techniques, both in hydrodynamics and space plasma physics, are summarized. Then this method is validated against MHD simulations. These techniques have the potential to become useful tools both in simulations and observations, enabling unambiguous detection of events and investigation of the physical effects behind vortex formation.

Tracing plasma, momentum, and energy flow through the geospace systems using *in-situ* data can be difficult due to the limited spatial coverage provided by isolated spacecraft, even when arrayed in formations. Just as in the Earth sciences, imaging missions can play an important role. Here, Murphy et al. review the Solar-Terrestrial Observer for the Response of the Magnetosphere (STORM) mission concept, a global solar wind-magnetosphere imaging mission. They determine how often STORM can observe and image three key science targets: the subsolar magnetopause, ring current, and auroral ovals. STORM's overarching science goal is to study the system science of and flow of energy through the solar wind-magnetosphere system. STORM achieves this by tracking boundary motion and emission intensity variations associated with the Dungey cycle and coupled solar wind-magnetosphere system. While a single spacecraft can readily accomplish these tasks on a case and statistical basis, the authors note that a dual spacecraft STORM mission would significantly enhance science and allow for tomography via stereographic imaging, e.g., Cucho-Padin et al. Such a dual spacecraft mission would however increase both complexity and costs.

Cucho-Padin et al. examined our ability to reconstruct the time-dependent three-dimensional structure of magnetospheric plasmas from observations by wide field-of-view soft X-ray imagers. To calculate emissivities along lines of sight from two imaging spacecraft in various configurations, they employed the OpenGGSM magnetohydrodynamic model for plasma densities and velocities in and near the magnetosphere and assumed a spherically-symmetric exospheric neutral density. This technique could be used in a two-spacecraft STORM mission to reveal three-dimensional dynamical processes in the Earth's magnetosphere.

Akbari et al. present a gradient calculation method for the upcoming, six-spacecraft Geospace Dynamics Constellation (GDC) mission, which will investigate dynamical processes in Earth's upper atmosphere. Achieving this goal will involve resolving and distinguishing spatial and temporal variability of ionospheric and thermospheric structures in a quantitative manner. Specifically, this paper implements the least-squares gradient calculation approach previously developed by J. De Keyser. The authors conclude that: "1) computation of the temporal gradients of neutral and plasma variables, while sensitive to the measurement noise level, are possible with GDC measurements; 2) The spatial gradients of the equatorial ionization anomaly can be reasonably resolved during phase 1 of the mission, while at the later phases the gradients are likely to be underestimated. On the other hand, in the presence of measurement noise, computing the gradients of the neutral temperature would likely be more difficult in the earliest phases of the mission due to the small gradients and large homogeneity lengths involved; 3) Gradients of the neutral wind can be well determined in the earliest phases of the mission even at the highest latitudes where the constellation skews in longitude."

Oberheide et al. discuss how the GDC mission can be used to resolve tidal weather. The GDC mission measures neutral temperatures and winds and thus likely enable significant progress towards resolving the tidal weather of the thermosphere and how it is driven by meteorological processes near the surface and *in situ* forcing in the ionosphere-thermosphere system. The authors demonstrate that GDC can resolve the day-to-day tidal variability (mean, diurnal and semidiurnal, migrating and nonmigrating) at orbit height during the mission. They note that the "mean state of thermosphere can also be recovered on a day-to-day basis throughout mission phases 3 and 4, including the mean meridional circulation".

In an opinion article, Weimer argue that the significance of the small-scale electric fields in the polar ionosphere may be overestimated. This somewhat contradicts earlier studies that highlight the importance of correctly capturing the variability of the electric fields in the models to accurately account for the total amount of Joule heating. The authors conclude that future multi-spacecraft measurements in the polar ionosphere, such as the future GDC mission, will be able to address this issue, "with some limitations due to missing double-probes".

In a perpective article Archer et al. discuss both new and improved observational directions for uncovering magnetopause, magnetospheric, and ionospheric dynamics and how these may aid our understanding of the magnetopause boundary's global importance to the geospace energy budget.

The science goals, methods, and open questions discussed in this Research Topic are well aligned with the Heliophysics Decadal Survey's 2024-2033 vision and strategy NAS (2024). The Decadal survey in Heliophysics "The Next Decade of Discovery in Solar and Space Physics: Exploring and Safeguarding Humanity's Home in Space" was published in December 2024. It sets forth a comprehensive science vision to advance and expand the frontiers of Heliophysics for the next decade. The report provides a prioritized research strategy and recommends both new and existing space missions, ground-based instruments and facilities, as well as modeling and simulation to achieve the identified science goals in the space and solar physics fields.

The extent, to which these can be accomplished in the next decade depends on the funding level of the associated agencies: NASA, NSF and NOAA as well as their international counterparts, and on the state of a healthy and educated workforce.

Author contributions

KN: Writing–original draft, Writing–review and editing. XB-C: Writing–review and editing. DK: Writing–review and editing. DS: Writing–review and editing. JB: Writing–review and editing.

Funding

The author(s) declare that financial support was received for the research, authorship, and/or publication of this article. KN was supported by NASA LWS grant #80NSSC23K0899 and ISFM grants. DS was supported by NASA's LWS and USPI programs.

Conflict of interest

The authors declare that the research was conducted in the absence of any commercial or financial relationships that could be construed as a potential conflict of interest.

The author(s) declared that they were an editorial board member of Frontiers, at the time of submission. This had no impact on the peer review process and the final decision.

Generative AI statement

The author(s) declare that no Generative AI was used in the creation of this manuscript.

Publisher's note

References

NAS (2024). *National academies of sciences: next decade of Discovery in solar and space physics: exploring and safeguarding humanityś Home in space*. Washington, DC: The National Academies Press. doi:10.17226/27938

Nykyri, K. (2024). Giant Kelvin-Helmholtz (KH) waves at the boundary layer of the coronal mass ejections (cmes) responsible for the largest geomagnetic storm in 20 years. *Geophys. Res. Lett.* 51, e2024GL110477. doi:10.1029/2024gl110477

Nykyri, K., Ma, X., Burkholder, B., Rice, R., Johnson, J. R., Kim, E.-K., et al. (2021). Mms observations of the multiscale wave structures and parallel electron heating in the vicinity of the southern exterior cusp. *J. Geophys. Res. Space Phys.* 126, e2019JA027698. doi:10.1029/2019JA027698

frontiers | Frontiers in Astronomy and Space Sciences

TYPE Review
PUBLISHED 31 August 2023
DOI 10.3389/fspas.2023.1254266

OPEN ACCESS

EDITED BY
David Gary Sibeck,
National Aeronautics and Space Administration, United States

REVIEWED BY
Gang Li,
University of Alabama in Huntsville, United States
Nina Dresing,
University of Turku, Finland

*CORRESPONDENCE
Donald V. Reames,
dvreames@gmail.com

RECEIVED 06 July 2023
ACCEPTED 11 August 2023
PUBLISHED 31 August 2023

CITATION
Reames DV (2023), Review and outlook of solar energetic particle measurements on multispacecraft missions.
Front. Astron. Space Sci. 10:1254266.
doi: 10.3389/fspas.2023.1254266

Review and outlook of solar energetic particle measurements on multispacecraft missions

Donald V. Reames*

Institute for Physical Science and Technology, University of Maryland, College Park, MD, United States

The earliest evidence of spatial distributions of solar energetic particles (SEPs) compared events from many different source longitudes on the Sun, but the early *Pioneers* provided the first evidence of the large areas of equal SEP intensities across the magnetically confined "reservoirs" late in the events. More detailed measurements of the importance of self-generated waves and trapping structures around the shock waves that accelerate SEPs were obtained from the *Helios* mission plus IMP 8, especially during the year when the two *Voyager* spacecraft also happened by. The extent of the dozen widest SEP events in a solar cycle, which effectively wrap around the Sun, was revealed by the widely separated STEREO spacecraft with three-point intensities fit to Gaussians. Element abundances of the broadest SEP events favor average coronal element abundances with little evidence of heavy-element-enhanced "impulsive suprathermal" ions that often dominate the seed population of the shocks, even in extremely energetic local events. However, it is hard to define a distribution with two or three points. Advancing the physics of SEPs may require a return to the closer spacing of the *Helios* era with coverage mapped by a half-dozen spacecraft to help disentangle the distribution of the SEPs from the underlying structure of the magnetic field and the accelerating shock.

KEYWORDS

solar energetic particles, shock waves, coronal mass ejections, solar jets, solar system abundances, multispacecraft missions, heliosphere

1 Introduction

The spatial distribution of solar energetic particles (SEPs), and their variation with time, particle species, and energy, is fundamental to an understanding of the physics of particle acceleration and transport in the heliosphere. How much of the variation we see at a single spacecraft is a true time variation and how much is spatial variation being convected past? Is the SEP source itself broadly extended in space or do SEPs somehow diffuse out of a limited source? Does a shock source sample different abundances of seed ions from different places or, for example, does Fe simply scatter less than O, to produce early enhancements and later suppressions in Fe/O? Multispacecraft comparisons can be a key to distinguishing the physical effects dependent upon space and time.

1.1 SEP history and context

Multispacecraft measurements and the perceived need for them generally followed the study of SEPs on or near Earth. The SEP events observed first

(Forbush, 1946) were rare, large, energetic "ground-level enhancements" (GLEs), where GeV protons produce a nuclear cascade through the atmosphere to the ground level that enhances the continuous signal produced similarly by the galactic cosmic rays (GCRs). Since solar flares were found to accompany these early SEP events, flares were considered a possible source. However, the spatial span of these flares, stretching from the east on the Sun to behind the western limb, raised a significant problem: how could the SEPs cross magnetic field lines radiating out from the Sun to find their way to Earth?

Meanwhile, solar radio astronomers, also using ground-based instruments, had identified different sources triggered by energetic solar electrons. Radio emission, excited at the local plasma frequency, depends upon the square root of the local electron density, which decreases with distance from the Sun. Wild et al. (1963) described radio type III bursts where frequencies decreased rapidly, excited by 10–100 keV electrons that streamed out from a source near the Sun. There are also type II bursts where the source moved at the slower speed of a ~1,000 km s^{-1} shock wave. Wild et al. (1963) suggested two types of SEP sources, namely, point sources of mostly electrons near the Sun and fast shock waves that could accelerate energetic protons, like those that produce GLEs. Even though shock acceleration was well-known in other contexts, like the supernova sources of GCRs, Wild et al. (1963) were far ahead of their time in solar physics. After 20 years, the clear 96% association of large SEP events with shocks driven by fast, wide coronal mass ejections (CMEs) was established by Kahler et al. (1984). Yet, 10 years later, Gosling 1993) and Gosling (1994) still needed to point out the error of the "solar flare myth".

Parker (1965) explained particle transport in terms of pitch-angle scattering as SEPs followed magnetic field lines out from the Sun. Diffusion theory is an important tool when there is actually a physical mechanism, like pitch-angle scattering, to produce the random walk. There is also a random walk of the magnetic field footpoints (Jokipii and Parker, 1969; Li and Bian, 2023) prior to events, which can produce an effective random walk perpendicular to the mean magnetic field, but it is independent of SEP-event parameters and is completely inadequate to explain a huge spread of SEPs far from a presumed source longitude near a flare. Other schemes such as the "birdcage" model (Newkirk and Wenzel, 1978) were also invented to spread SEPs from a flare source (see review, Sec 2.3 in Reames, 2021a). Reinhard and Wibberenz (1974) envisioned a mysterious "fast propagation region" extending 60^0 from the flare to spread the SEPs prior to their slower interplanetary journey. Could this region actually match the surface of a shock? After decades of resistance, a flare source has mainly been abandoned for the largest SEP events that are now generally attributed to spatially extensive CME-driven shock waves (Mason et al., 1984; Gosling, 1993; Reames, 1995b; 1999; 2013; 2021b; Zank et al., 2000; 2007; Lee et al., 2012; Desai and Giacalone, 2016), especially for GLEs (Tylka and Dietrich, 2009; Gopalswamy et al., 2012; 2013; Mewaldt et al., 2012; Raukunen et al., 2018). Observations (e.g., Kahler et al., 1984) did replace the "fast propagation region" with the surface of a CME-driven shock wave that actually accelerates the particles, beginning at 2–3 solar radii (Tylka et al., 2003; Cliver et al., 2004; Reames, 2009a; Reames, 2009b) and continuing far out into the heliosphere. We will soon study from STEREO observations (e.g., Figure 5) that shocks easily wrap around the Sun, expanding widely across magnetic field lines where SEPs alone cannot pass.

As the element and isotope abundances in SEPs began to be measured, they would present new evidence for two different physical sources of SEPs. The earliest measurements, during large SEP events with nuclear emulsions on sounding rockets, extended element abundances up to S (Fichtel and Guss, 1961) and then to Fe (Bertsch et al., 1969). Later studies showed that average SEP element abundances in large events were a measure of coronal abundances that differed from photospheric abundances as a simple function of the elements' first ionization potential (FIP; Meyer, 1985; Reames, 1995; Reames, 2014; Reames, 2021a; Reames, 2021b). The FIP dependence of SEPs differs fundamentally from that of the solar wind (Reames, 2018a; Laming et al., 2019), probing the physics of the formation of the corona itself.

However, early measurements in space soon identified a completely new type of event, distinguished by extremely high abundances of ^{3}He in some events, such as $^3He/^4He = 1.52 \pm 0.1$ (e.g., Serlemitsos and Balasubrahmanyan, 1975), vs. a solar value of $\sim 5 \times 10^{-4}$. Production of ^{3}He from ^{3}He by nuclear fragmentation was ruled out by the lack of ^{2}H and Li, Be, and B fragments from C and O, e.g., Be/O and B/O $< 2 \times 10^{-4}$ (McGuire et al., 1979; Cook et al., 1984). The huge enhancements of ^{3}He were produced by new physics, involving a wave–particle resonance (e.g., Fisk, 1978; Temerin and Roth, 1993) with complex spectra (Liu et al., 2004; Liu et al., 2006; Mason, 2007). The ^{3}He-rich events were associated with the beamed non-relativistic electrons (Reames et al., 1985) and their type III radio bursts (Reames and Stone, 1986) studied by Wild et al. (1965). Element abundances of these "impulsive" ^{3}He-rich events were also different from those of the large "gradual" shock-associated events (Mason et al., 1986; Reames, 1988); here, the enhancements increased as a power of the ion mass-to-charge ratio A/Q (Reames et al., 1994), which was especially clear when it became possible to measure elements above Fe with element groups resolved as high as Au and Pb (Reames, 2000; Mason et al., 2004; Reames and Ng, 2004). Average enhancements varied as $(A/Q)^{3.6}$ with the Q value determined at a temperature of ~3 MK (Reames et al., 2014a; Reames et al., 2014b). This power law can be used in a best-fit method to determine source plasma temperatures (Reames, 2016; Reames, 2018b). Impulsive SEP events have been associated with magnetic reconnection (Drake et al., 2009) on open field lines in solar jets (Bučík, 2020), which also eject CMEs that sometimes drive shocks (Kahler et al., 2001; Nitta et al., 2006; Nitta et al., 2015; Wang et al., 2006; Bučík et al., 2018a; Bučík et al., 2018b; Bučík et al., 2021) fast enough to reaccelerate the enhanced ^{3}He and heavy ions along with ambient protons and ions (Reames, 2019; Reames, 2022b). Derived abundances from γ-ray lines suggest that flares involve similar physics (Murphy et al., 1991; Mandzhavidze et al., 1999; Murphy et al., 2016), but those accelerated particles are trapped on loops, losing their energy to γ-rays, electron bremstrahlung, and hot, bright plasma. The opening magnetic reconnections that drive jets also must close neighboring fields to form flares (see, e.g., Figure 4 in Reames, 2021b).

Shock waves can also accelerate residual suprathermal impulsive ions that can pool to provide a seed population (Mason et al., 1999; Tylka et al., 2001; Desai et al., 2003; Tylka et al., 2005; Tylka and Lee, 2006). The combination of two fundamental physical acceleration

mechanisms, magnetic reconnection, and shock acceleration, as well as two distinctive element abundance patterns, led Reames (2020) and Reames (2022b) to suggest four distinguishable SEP event abundance pathways:

SEP1: "Pure" impulsive magnetic reconnection in solar jets with no fast shock.

SEP2: Jets with fast, narrow CMEs driving shocks that reaccelerate SEP1 ions plus ambient coronal plasma. Pre-enhanced SEP1 ions dominate high *Z*, and ambient protons dominate low *Z*.

SEP3: Fast, wide CME-driven shocks accelerate SEP1 residues from active-region pools from many jets, plus ambient plasma. Again, the SEP1 seed ions dominate high *Z*.

SEP4: Fast, wide CME-driven shocks accelerate ions where ambient plasma completely dominates.

Persistent pools of SEP1-residual seed ions available for reacceleration in SEP3 events have now been widely observed and reported (Richardson et al., 1990; Desai et al., 2003; Bučík et al., 2014; Bučík et al., 2015; Chen et al., 2015; Reames, 2022a), and may be fed by numerous impulsive events too small to be distinguished individually.

Large gradual SEP events are frequently accompanied initially by type III bursts. In principle, these impulsive jets could inject a SEP1 seed population. However, any such injection of SEP1 ions seems to be swamped by coronal seed ions in the many large SEP4 events. The extremely abundant type III electrons can be distinguished from shock-accelerated electrons by their proximity to the event source; the latter emerge only in poorly connected events (Cliver and Ling, 2007).

The spatial extent of these features and the underlying physics are of considerable interest. Can we find spatial differences in the seed populations sampled by shocks? Unfortunately, each point on a shock moving radially across Parker spiral fields will have spread particles over 50^0—60^0 by the time it reaches 1 AU (Reames, 2022a). This tends to blur any initial spatial variations in abundances.

2 Near-earth observations

Before we could monitor a single SEP event at multiple locations, we could study multiple events at Earth from different source longitudes on the Sun. Using data from IMP 4, 5, 7, 8, and ISEE 3 over nearly 20 years, Cane et al. (1988) ordered the 20-MeV proton profiles of 235 large SEP events as a function of the solar source longitude. This study gave the typical extent and time profiles of an "average" SEP event, sliced as a function of longitude. Recently, Reames (2023) revisited this study, adding examples that better illustrate the evolving role of the shock source as it propagates outward from the corona. A collection of sample time distributions of protons vs. longitude from this work is shown in Figure 1. Although the SEP events shown in Figure 1 are all different, we expect that slices of a single event at different longitudes could show similar features.

Historically, the intensity peaks at the shock seen on several of the profiles in Figure 1 were called "energetic storm particle" (ESP) events. During their acceleration, particles are trapped near the shock by self-generated Alfvén waves (Bell, 1978a; Bell, 1978b; Lee, 1983; Lee, 2005), creating an autonomous structure that can propagate onto new field lines where earlier accelerated particles may be absent, as shown in Figure 1E (Reames, 2023).

3 Multispacecraft observations

3.1 Pioneer

Some of the early *Pioneer* spacecraft were launched into Earth-like solar orbits, although coverage was only hours per day. When there was no spacecraft near Earth, this led to the awkward comparison of 15-MeV proton data from *Pioneer* 6 and 7 with GeV ground-level neutron monitor measurements at Earth (Bukata et al., 1969). Fortunately, McKibben (1972) was able to include data from IMP 4 near Earth. Although most of these spatial distributions were analyzed in terms of adjustable coefficients in the fashionable perpendicular diffusion, rather than shock acceleration, McKibben also noted that late in SEP events, proton intensities could be identical over large spans of longitude. Later named "reservoirs" by Roelof et al. (1992), these regions involved particles quasi-trapped magnetically behind the shock; as the volume of this magnetic bottle expands, adiabatic deceleration (e.g., Kecskeméty et al., 2009) decreases all intensities, preserving spectral shapes (Reames et al., 1997; Reames, 2013). Extreme SEP scattering, once used to explain this slow decay, is actually found to be negligible in reservoirs since particles from new ^{3}He-rich events travel scatter-free across them (Mason et al., 1989; Reames, 2021a).

3.2 Ulysses

Whenever there was a dependable spacecraft stationed near Earth, like IMP 8, any traveling spacecraft, such as the solar-polar-orbiting *Ulysses*, allowed two-spacecraft comparisons. The reservoir comparisons by Roelof et al. (1992) found uniform intensities behind the shock, extending radially over 2.5 AU from IMP 8 to *Ulysses*. Ulysses observed reservoirs at heliolatitudes up to $>70^0$, N and S (Lario, 2010), and in other electron observations (Daibog et al., 2003).

3.3 Helios, IMP, and *Voyager*

The two *Helios* spacecraft followed neighboring solar orbits from 0.3 to 1.0 AU, beginning in 1974. Beeck et al. (1987) used data from these spacecraft to study the radial and energy dependence of diffusive scattering of protons, while, in a larger study, Lario et al. (2006) fit the peak intensities and the fluence of events to the form $R^{-n}\ exp[-\ k(\phi\ -\ \phi_0)^2]$, where n and k are constants, R is the observer's radius in AU, ϕ is the solar longitude of the observer, and ϕ_0 is the solar longitude of the event centroid. For a Gaussian distribution, $k = (2\sigma^2)^{-1}$. Lario et al. (2006, 2007) also considered the time variation of the point where the observer's field line intercepts the expanding shock source, an important feature of shock acceleration defined by Heras et al. (1995).

Helios provided an excellent opportunity to study spatial distributions of shock-accelerated particles and their reservoirs, especially during 1978 when the *Voyager* spacecraft were nearby

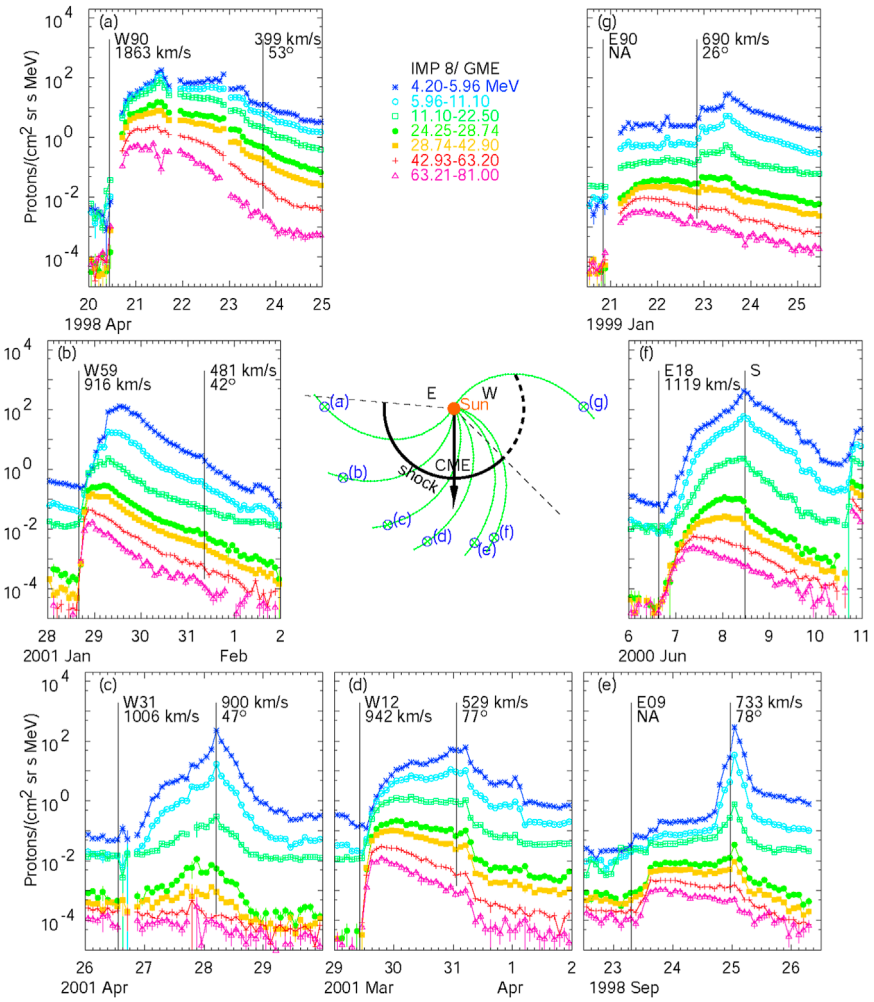

FIGURE 1
IMP 8/GME proton intensities of the listed energies are shown vs. time in each panels **(a–g)** around a central map showing their nominal distribution around a fixed CME-driven shock source. Event onset times in each panel are flagged with the source longitude and the CME speed (when available), and the times of shock passage are noted with the shock speed and θ_{Bn}, the angle between the field *B* and the shock normal (when available). All panels have the same intensity scale. Dashed lines in the central map illustrate that a shock must first encounter any field line at its footpoint on the east flank but may first strike it far from the Sun on the west (Reames, 2023).

(Reames et al., 1996; Reames et al., 1997; Reames et al., 2013; Reames, 2023). An especially interesting event is shown in Figure 2 where the intensities of SEPs at *Voyager 2* (Figures 2A or 2E) do not begin to increase until after the shock passes S1 (Figure 2B), presumably because this is where it first intercepts the field line to *Voyager*. Proton intensities then slowly rise as *Voyager* becomes connected to stronger and stronger regions of the approaching shock until the ESP structure finally arrives at S4 on 6 January. It should be noticed in Figure 2A that the peak intensities near the shock are similar at all four spacecraft. The ESP structure forms as protons streaming away from the shock generate resonate waves of wave number $k \approx B/\mu P$, where *B* is the field strength, *P* is the proton rigidity, and μ is the cosine of its pitch angle (Lee, 1983; Lee, 2005; Ng and Reames, 2008; Reames, 2023). These waves trap particles in ESP structures. As the structure moves out to lower *B*, the resonance shifts so that high energies preferentially leak away early, as also seen in Figure 1E. *Voyager* sees the pure "naked" ESP event with few of the streaming protons that created it. The shock that eventually arrives at *Voyager* generated the intense early streaming protons seen early by *Helios 1* and an intermediate structure as it passed *Helios 2* and IMP 8.

The spacecraft distribution for the event shown in Figure 2 is unique; in this spacecraft sample, the SEPs are produced as the source shock moves radially. The width of this CME is limited, but the spacecraft are positioned to follow the evolution of the event: 1) well-connected *Helios 1* samples its central production near the Sun, 2) *Helios 2* and IMP 8 sample its production near 1 AU, and 3) *Voyager 2* scans its western flank and then samples its central strength as it passes 2 AU. A fortuitous occurrence occurred: NASA did not design *Voyager* as a complement to *Helios*.

Another fortuitous observation with these spacecraft occurred in September 1978 and is shown in Figure 3. In Figure 3A, well-connected IMP 8 shows a fast increase in intensities and a peak near the time of shock passage, while *Helios 1* and *2*, far around the

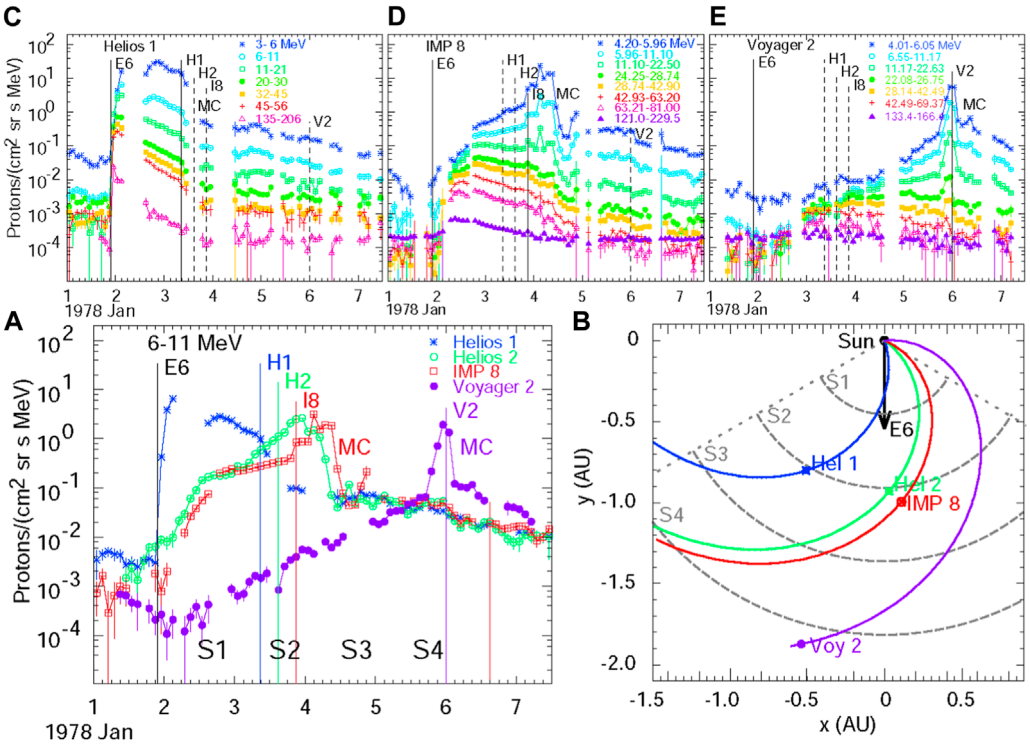

FIGURE 2
In **(A)**, intensities of 6–11-MeV protons are compared for *Helios 1, Helios 2*, IMP 8, and *Voyager 2* during the 1 January 1978 SEP event, while **(B)** shows the spatial configuration of the spacecraft on their initial field lines, and stages in the expansion of the CME-driven shock at S1, S2, etc., are sketched. Intensity–time profiles for a full list of energy intervals are shown for **(C)** *Helios 1*, **(D)** IMP 8, and **(E)** *Voyager 2*. MC is a magnetic cloud from the original CME (Burlaga et al., 1981). The onset time of the event is flagged by E6 and the shock passage at each spacecraft by H1, H2, I8, and V2 (Reames, 2023).

west flank, increase more slowly and then join IMP 8 in a reservoir behind the shock on 25 September. Distant *Voyagers* show a slow SEP increase to a plateau near the time S2, where IMP 8 joins the same intensity once it is no longer constrained by the east flank of the shock. Then, at S3, the *western* flank of the shock strikes field lines that send particles sunward to IMP 8 and outward to *Voyager 2*, and then to *Voyager 1*. This second SEP peak is clearly seen at energies above 40 MeV in Figure 3C and probably even in Figure 3D. A "left" and then a "right" from the same shock are observed; at *Voyager*, the two peaks are comparable in size.

It should be noted that the second peak in the IMP 8 data in Figure 3C shows significant velocity dispersion corresponding to the ~6-AU path inward from the new source (actually a larger delay than in the first peak), while none is seen at Voyager 2 (Figure 3D) near this source. Furthermore, the intensities at IMP 8 and Voyager are quite similar in the second peak; any new injection from the Sun would have produced a huge difference in intensities like that seen in the first peak because of the great difference in radial distances since IMP 8 and the Voyagers seem to be on similar field lines. At the second peak, the shock has filled these field lines, forming a reservoir with similar intensities at IMP and Voyager.

Another parameter that can depend upon solar longitude is the solar particle release (SPR) time derived from velocity dispersion (Tylka et al., 2003; Reames, 2009a; Reames, 2009b). If the first particles of each energy to arrive at the spacecraft have been released at nearly a single time, the SPR time, and have scattered little, their travel time will be $dt = L/v$, where L is the field line length from the source to observer and v is the particle velocity. Plotting the onset times vs. v^{-1} will yield a linear fit with slope L and intercept at the SPR time. Figure 4B shows such a plot from Reames and Lal (2010) for the spacecraft distributed, as shown in Figure 4A, during the GLE of 22 November 1977. The parabolic fit for the height shown in Figure 4D, not from this event, is a fit of 26 GLEs observed from Earth (Reames, 2009b); presumably, it is a first-order correction for weaker, more slowly evolving, shock flanks. Gopalswamy et al. (2013) fit the SPR height for GLEs at Earth directly to the source longitude (uncorrected for foot-point motion). Type II bursts begin near ≈1.3 R_S, but they certainly need not correspond to the same field line longitude or shock physics as the measured SEPs. Non-relativistic electrons that produce type II bursts do not resonate with Alfvén waves like ions and hence are more likely to be accelerated by quasi-perpendicular regions of the shocks.

Thus, *Helios* allowed spatial comparisons of the beginnings of events, their evolution and ESP events at the middle, and their reservoirs at the end (Reames et al., 1997), noted previously.

3.4 STEREO, with *Wind*, ACE, and SOHO

The launch of *Wind* in November 1994 began a new era in SEP coverage from Earth, and it was later joined by SOHO and

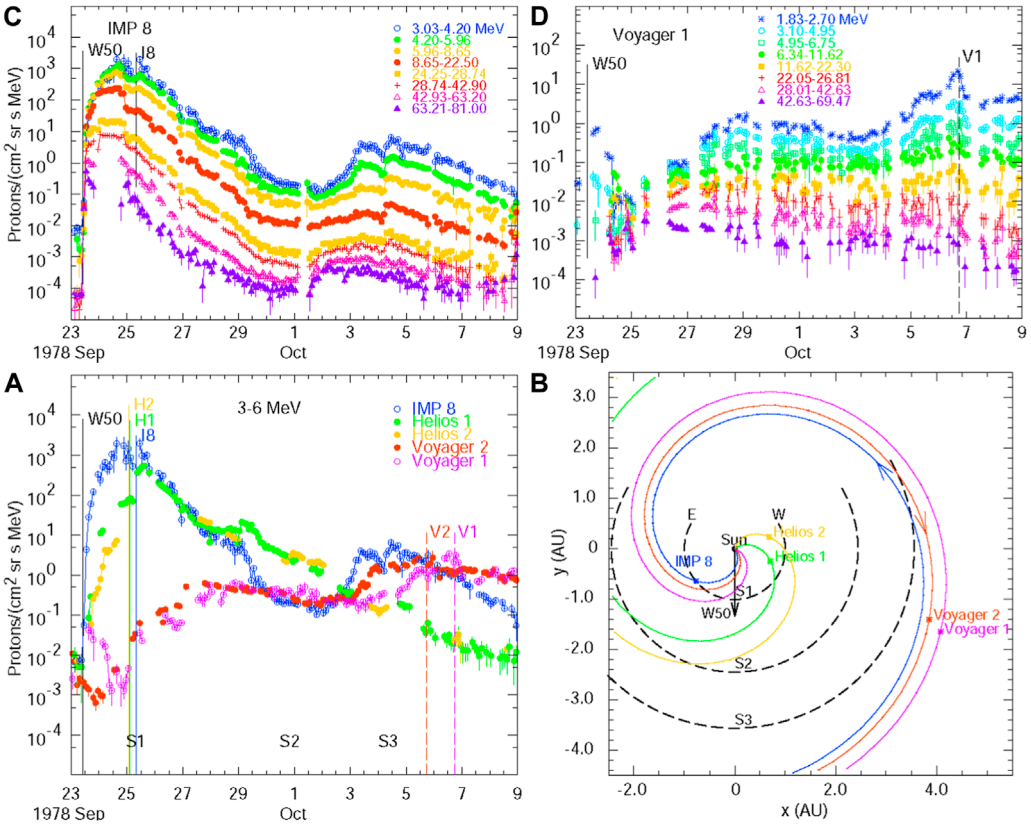

FIGURE 3
In **(A),** intensities of 3–6-MeV protons are compared for IMP 8 (blue), *Helios 1* (green), *Helios 2* (yellow), *Voyager 1* (red), and *Voyager 2* (violet) in the 23 September 1978 SEP event, while **(B)** maps the configuration of the spacecraft on their initial field lines and shows the expansion of a CME-driven shock at S1, S2, and S3. The onset time of the event is flagged as W50, and the shock passage at each spacecraft as H1, H2, I8, V1, and V2. **(B)** Western flank of shock S3 intercepts the blue and red fields, where arrows direct particles accelerated sunward to IMP 8 and then outward to *Voyager 2*, respectively, and later to *Voyager 1*. Intensity–time profiles for a full list of energy intervals are shown for **(C)** IMP 8 and **(D)** *Voyager 1* (Reames, 2023).

ACE, adding different capabilities. This coverage still exists in 2023. STEREO ahead (A) and behind (B) were launched together in late 2006 at the beginning of solar minimum. By September 2012, they had reached the ±120^0 longitude, providing three equally spaced observing points around the Sun and optimal coverage for finding the most extensive SEP events.

With STEREO, it has become even clearer that SEP events can be quite extensive. For >25-MeV proton events, Richardson et al. (2014) found that 17% spanned three spacecraft; 34%, two spacecraft; and 36%, one spacecraft, with 13% unclear. Studying the abundances of H, He, O, and Fe at 0.3, 1, and 10 MeV amu^{-1}, Cohen et al. (2017) found only 10 three-spacecraft events, out of 41.

Most of the studies of particle distributions with STEREO have involved Gaussian fits of the intensity peaks or fluences at three longitudes. Three points determine a parabola, and a Gaussian is a parabola in logarithmic space, so Gaussians tend to fit the data very well. Xie et al. (2019) studied 19–30-MeV protons in 28 events finding $\sigma = 39^0 \pm 6.8^0$. Paassilta et al. (2018) compiled a list of 46 wide-longitude events above 55 MeV, of which seven were suitable, averaging $\sigma = 43.6 \pm 8.3^0$, and for 14 events with E > 80 MeV, de Nolfo et al. (2019) found an average $\sigma \approx 41^0$. Lario et al. (2013) studied the 15–40 and 25–53-MeV proton peak intensities and found $\sigma \approx 45 \pm 2^0$ for both proton energy ranges. Cohen et al. (2017) found average three-spacecraft events centered at $\phi_\theta \approx 22 \pm 4°$ west of the flare site and ≈43° ± 1° wide; they found no dependence of the width on the charge-to-mass ratio Q/A of the elements. This lack of dependence on A/Q seems to argue against lateral diffusive transport. Kahler et al. (2023) fit the data on 20-MeV protons to hourly Gaussians, showing substantial broadening of the distribution with time, especially on the western flank where the shock expanded across new spiral field lines. However, all of these similar widths and parameters only apply to the largest ≈20% of events that span three spacecraft. We have no widths from the one-spacecraft third of the events. For electron events, Klassen et al. (2016) examined events for closely spaced (<72^0) STEREO spacecraft and found they were not well-fit by Gaussians, while Dresing et al. (2018) pointed out that peak intensities used for the Gaussian fits may not represent the real spatio-temporal intensity distribution as the intensity peaks may have been measured at different times.

Some of the space–time coupling in SEP distributions is illustrated by the event shown in Figure 5. Here, the shock itself is seen at each spacecraft, yet the slight onset delay at *Wind* suggests it misses the base of that field line. Both STEREO spacecraft

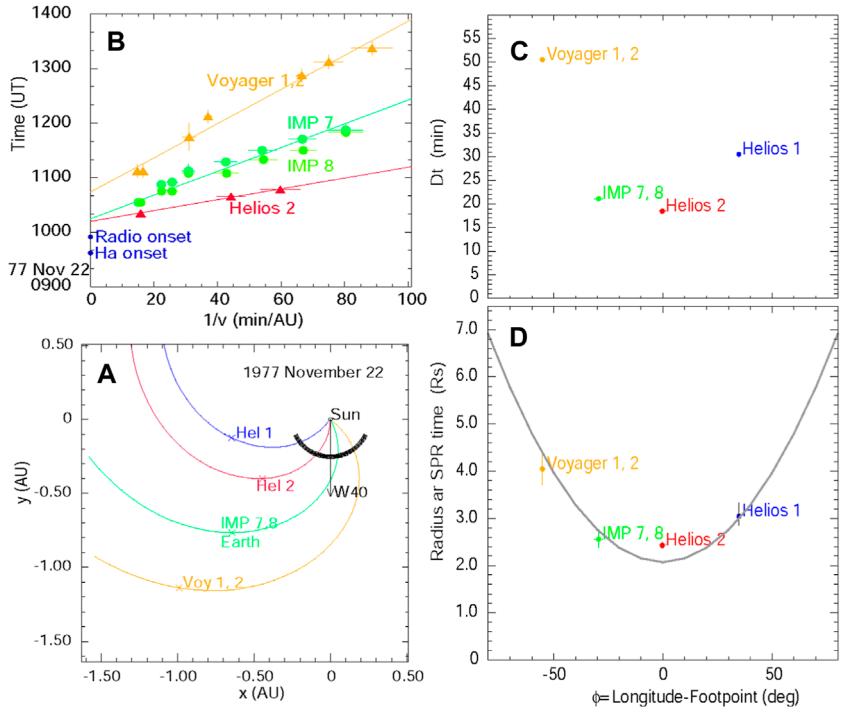

FIGURE 4
(A) Distribution of spacecraft during the 22 November 1977 SEP event at W40; **(B)** plots and least-square fits of the particle onset times vs. v^{-1} at available energies for several spacecraft; **(C)** time delay; **(D)** corresponding shock height of the SPR time vs. solar source longitude minus the footpoint longitude. Data from *Helios 1* are limited (Reames and Lal, 2010). The parabola shown in **(D)**, from Reames (2009b), may just be a first-order correction for the occurrence of the shock on its flanks.

show fast intensity increases, followed by early declines, but the intensity at *Wind* peaks well after the shock passage. How do we distinguish variations in space and time? When does a Gaussian spatial distribution apply? Is the Gaussian formed by the peaks, or by the fluences; is it spatial or also temporal? Even hourly Gaussians miss the true behavior late in an event.

The two pink field lines labeled 1 and 2 in the map shown in Figure 5 will be carried, from their initial positions shown, to the red location of *Wind* by the time the shock reaches 1 or 2 solar radii, respectively, because of solar rotation. Hence, the time profile we see at *Wind* is greatly enhanced behind the shock by SEPs swept in on field lines that were much more centrally located initially. Meanwhile, STEREO A is rapidly acquiring field lines with decreased intensities of SEPs that have rotated from behind the Sun, and STEREO B eventually joins it in a suppressed reservoir region late on 2 March. Can SEP models follow this mixture of space–time variations? Time variations longer than about a day need to accommodate the 13^0 day^{-1} solar rotation. This event evolves over a week.

It should also be noted in Figure 5 that the accelerating shock wave is seen at all three spacecraft, as is often the case. These shock waves are able to wrap around the Sun, crossing field lines that the particles alone cannot cross. Thus, STEREO shows us the way the physics of shock acceleration can easily replace the early confusion of the "birdcage model," "coronal diffusion," and the "fast propagation region"—diffusion from a point source—that once held sway.

3.5 SEP element abundances

Spatial distributions of fluences of element abundances were studied extensively by Cohen et al. (2017) using STEREO and ACE data. The Gaussian distributions of H, He, O, and Fe were found to be similar in 10 three-spacecraft events, suggesting that the widths are independent of rigidity or transport. They found the average three-spacecraft Gaussian distributions to be 43° ± 1° wide, although with significant variations. None of these large three-spacecraft SEP events showed any of the enhancements of heavy elements, e.g., Fe/O, typically found in shock-reaccelerated impulsive suprathermal ions of SEP3 events. An analysis of the A/Q-dependence of the element abundances in a typical large SEP4 event is shown in Figure 6, where power-law fits of flat or suppressed heavy elements extend to include protons (Reames, 2020; Reames, 2022b).

For each time period, the observed abundances of $Z \geq 6$ ions are divided by the corresponding coronal abundances and fit to power-laws. Most SEP4 events show flat fits, i.e., abundances the same as coronal, or declining power laws, as shown in Figure 6. The declining power laws may result from reduced scattering of heavier ions that allows them to leak more easily from the acceleration region SEP3 events have both enhanced protons and power-law heavy-element enhancements that increase with A/Q, reflecting shock acceleration of seed populations of normal ambient coronal ions and impulsive suprathermal ions with their characteristic high-Z enhancement. SEP3 events can be very large. In solar cycle 23, about half of the GLEs were SEP3 events (Reames, 2022a) and half SEP4 events. In

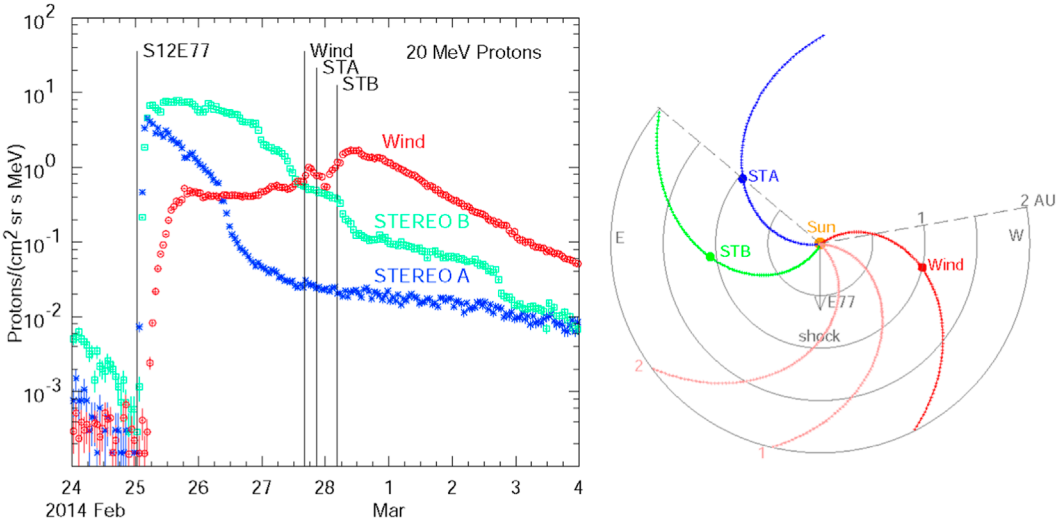

FIGURE 5
Schematic representation of the time variations in ~20-MeV protons in the large three-spacecraft SEP event of 25 February 2014 on the left and the map of spacecraft configuration on the right. Vertical time flags mark the event onset from S12E77 and the shock passage times at each spacecraft. In the map, circles follow expansion of a spherical shock wave, and initial Parker spirals connect the Sun with each spacecraft; these field lines would be distorted as the shock passes. Pink field lines measure solar rotation (see text).

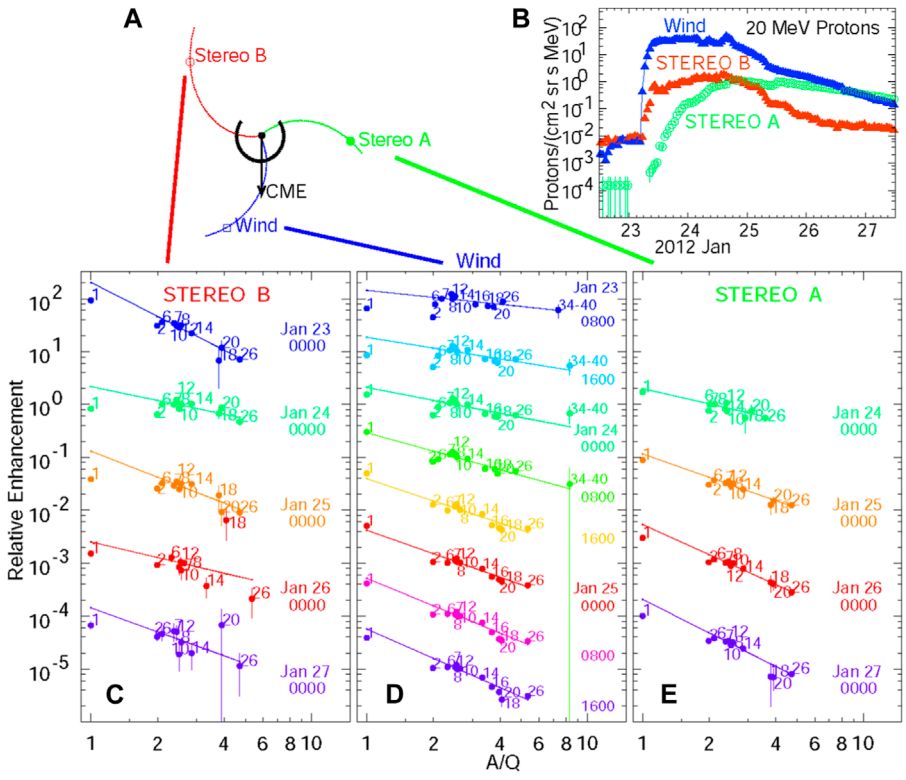

FIGURE 6
(A) Map of the spacecraft distributions during the SEP event of 23 January 2012; **(B)** corresponding intensity–time profiles of 20-MeV protons at each spacecraft. The abundance enhancements, relative to SEP-average (coronal) abundances, for elements noted by *Z*, are shown vs. *A/Q* for the listed time intervals for **(C)** STEREO B, **(D)** *Wind*, and **(E)** STEREO A. Best fit power laws vs. *A/Q* for elements with $Z > 2$ are shown extended down to protons at $A/Q = 1$.

weaker cycle 24, when STEREO was available, we found only one of the two-spacecraft events listed by Cohen et al. (2017) that was an SEP3 event (4 August 2011); this is an SEP3 event at *Wind* (figure 10 in Reames, 2020) and shows similar enhancements at STEREO A, although with poorer statistics. Why are there so few wide SEP3 events? Is it the weak solar cycle or are SEP3 events inherently narrow, perhaps because the primary pools of seed particles are confined?

3.6 Impulsive SEP events

A distinction of impulsive SEP events is that their longitude spread is much more limited than that of gradual events (Reames, 1999), but the width of that distribution depends upon the sensitivity of the instruments observing them and has increased somewhat with time (e.g., Reames et al., 2014a). A significant factor in this width is that variations in the solar wind speed vary with the longitude of the footpoint of the observer's field line, but there is also variation due to the random walk of the footpoints of the field lines (Jokipii and Parker, 1969; Li and Bian, 2023) prior to the event.

A search for ^{3}He-rich events between ISEE 3 and *Helios* (Reames et al., 1991) found several corresponding events. The well-studied event of 17 May 1979 (e.g., Reames et al., 1985) with ^{3}He/^{4}He ≥ 10 was seen with similar ^{3}He enhancement by *Helios 1* near 0.3 AU, as shown in Figure 7 as a sharp spike of very short (~1 h) duration, presumably resulting from reduced scattering. Associated electron trajectories were tracked spatially, using the direction and frequency of the radio type III burst as measured from ISEE 3 (Reames et al., 1991).

The time history for the Kiel Instrument on *Helios 1* in Figure 7 shows composite He; isotope ratios were tabulated separately using pulse-height data. Despite differences in He energies at the two spacecraft, both show the event at 0550 UT with ^{3}He/^{4}He ≈ 10 and that at 1700 UT with ^{3}He/^{4}He ≈ 1.

In the early STEREO era, before the spacecraft were widely separated, Wiedenbeck et al. (2013) found electrons and ions ±20^0 ahead and behind Earth, during an event that occurred during a solar quiet time. The ions showed strong intensity gradients. The event was associated with a weak CME. Moreover, Klassen et al. (2015) studied an electron beam event early in the STEREO mission.

The discovery of fast CMEs associated with impulsive SEP events (Kahler et al., 2001) suggested that impulsive SEPs could be spread laterally when nearly radial shocks in these SEP2 events distributed particles across spiral field lines. Particles from SEP1 jets without fast shocks would be expected to follow any open field lines from the jet, presumably less widely distributed. Suggestions of greater spreads for SEP2 impulsive events with shocks, based upon current understanding, have not been explored, particularly because the available spacecraft are too widely separated.

Opportunities for multiple measurements of impulsive SEP events are rare. Perhaps the best opportunity is for measurements of the radial variation in SEP scattering between *Parker Solar Probe* (PSP) or *Solar Orbiter* and spacecraft near Earth. Are the time profiles of SEPs at PSP near the Sun similar to those of X-ray profiles of the event? To what extent are the jets that release SEPs part of more-extensive flaring systems? Magnetic reconnection that opens some field lines must also close others (e.g., see Figure 4 in Reames, 2021b), but reconnecting closed field lines with other closed lines would allow no escape.

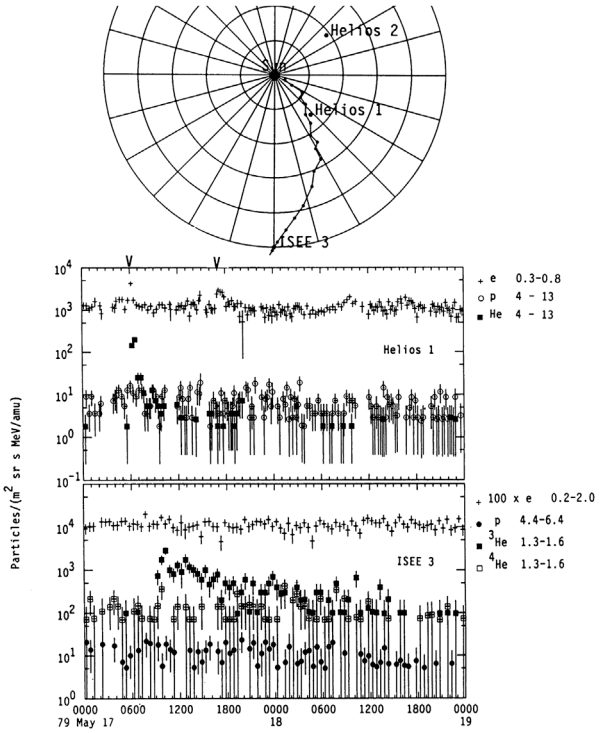

FIGURE 7
Extremely ^{3}He-rich event of 17 May 1979 is shown by the track of its radio type III burst in the upper panel, and time histories of electrons and ions are indicated at *Helios 1* and ISEE 3 in the following panels. Indicated energies are in MeV for electrons and protons, and MeV amu^{-1} for He. Arrows above the central panel mark two times the event sources (Reames et al., 1991).

4 Discussion

STEREO has given us an improved sense of the widths of some of the most extensive SEP events, but are the SEP distributions really characterized by nice smooth Gaussians? Are the SPR times or heights really parabolic? During the *Helios* era, when the *Voyagers* happened by, a few events showed us greater complexity (e.g., Figures 2, 3). Such events allow us to explore the underlying physics. STEREO also allows 3D modeling of the CME and its shock (e.g., Rouillard et al., 2011; Rouillard et al., 2012; Kouloumvakos et al., 2019; Zhang et al., 2023), but this is only beginning to be extended to a 3D modeling of the SEP distribution this shock produces. Correlations between SEP peaks and shock properties at the base of the observer's field line (e.g., Koulomvakos et al., 2019) may have reached their limits. SEP peak intensities and times are controlled, and often limited, by transport and are not determined by any single point on the evolving shock; transport and shock contributions both vary with time in complex ways. No single parameter represents an entire SEP event very well.

Kahler's (1982) "big flare syndrome," while expressed for a specific case, should be a general warning that correlations do

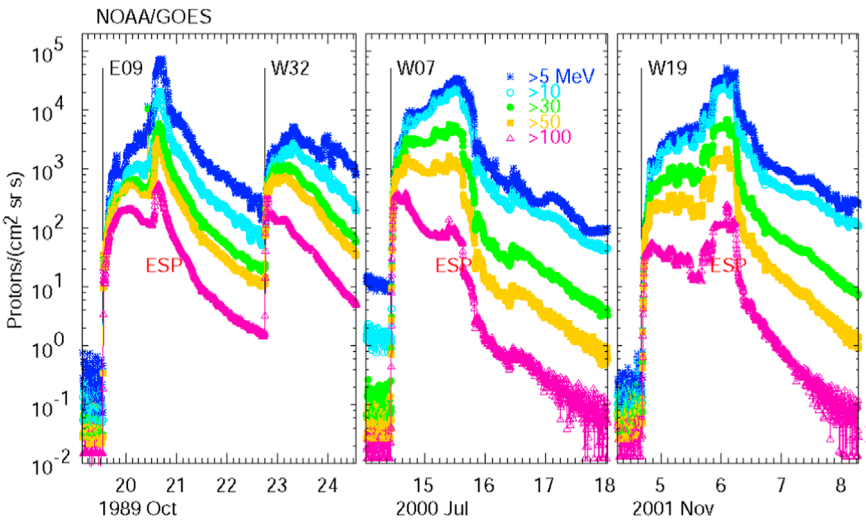

FIGURE 8
High-energy proton intensities during historic large SEP events near the central meridian can be enhanced and extended in time by their ESP events, even at energies >100 MeV (a significant radiation hazard). Early intensities are bounded by the "streaming limit," but the ESP peak is not. All of these events are GLEs, which often occur near the central meridian, allowing the ESP to surface.

not imply causality. Increasingly energetic magnetic reconnection events at the Sun can spawn bigger flares, faster CMEs, and larger SEP events. They are all correlated, yet Hα flares do not *cause* CMEs, or GLEs; ultimately, they are all consequences of magnetic reconnection. Later, Kahler (1992) asked "how did we form such a fundamentally incorrect view of the effects of flares after so much observational and theoretical work?" We need a clearer resolution of the underlying physics that does connect a cause and its effects.

Gopalswamy et al. (2013) sought to understand possible differences between the GLE of 17 May 2012 and six other large SEP events with similar CME speeds that were not GLEs. This event had a smaller flare (M5.1) than any of the others. A large effect was produced by the small latitudinal distance of the shock-nose from the ecliptic, i.e., the GLE was better connected to Earth. The GeV protons in this GLE were all produced within ~8 min. This suggests that a highly localized region of production might occur soon after shock formation (Ng and Reames, 2008) and may differ from the global properties of the CME, discounting correlations. Incidentally, the 17 May 2012 event was the only GLE included in the study by Cohen et al. (2017), and it had very few heavy ions to be studied at three spacecraft; it was not one of the 10 three-spacecraft SEP events.

It has also been observed that GLEs are more likely when shocks pass through solar streamers where the higher densities and lower Alfvén speeds produce higher Alfvénic Mach numbers (Liu et al., 2023) and regions of higher θ_{Bn} (e.g., Kong et al., 2017; 2019) that can enhance acceleration.

Intensities of GeV protons only exceed GCRs for short periods and are too weak to be a practical radiation hazard. However, ~100-MeV protons are much more numerous and persistent and hence a significant hazard to astronauts outside the Earth's magnetic fields. When an event is near central meridian, intensities of high-energy SEPs can be extended and increased by the ESP event when the nose of the shock passes over us. Some historical examples are shown in Figure 8. For western sources, we see the greatest effect of the shock nose early, but the shock then weakens toward our longitude and weakens in strength out to 1 AU. The early SEP intensities at 1 AU are constrained by wave growth, which can establish the "streaming limit" early (Reames and Ng, 1998; Ng et al., 1999; Ng et al., 2003; Reames and Ng, 2010; Ng et al., 2012; Reames and Ng, 2014), while ESP intensities are unbounded. Thus, the spatial distribution of SEP intensities at the shock, i.e., the ESP event, is of both fundamental and practical importance. The SEP events of October 1989 shown in Figure 8 are the basis of SEP "storm shelter" radiation-shielding requirements for astronauts in missions beyond a low Earth orbit (Townsend et al., 2018).

The ESP structure is formed very early in an event when protons streaming away from the shock amplify resonant Alfvén waves (Melrose, 1980; Stix, 1992). Waves trap ions of a given rigidity, scattering them back and forth across the shock so they gain velocity on each transit, subsequently amplifying waves of lower k (longer wavelength) which trap ions of higher P, etc., creating the ESP structure of energetic ions trapped around the shock (Lee, 1983; Lee, 2005). At the streaming limit, higher SEP intensities simply grow more waves, trapping more ions back near the shock. In gradual SEP events, the ESP structure always exists. When the shock is near the Sun, the ESP is initially hidden among the same SEPs that form it as they stream away. The shock we see at 1 AU was much stronger when it began near the Sun. The shock and the ESP event can explain *all* of the SEPs in the gradual event, early and late. It is a key to the physics of SEP acceleration in these events, whether it emerges at your particular longitude or not. The basic ESP structure will only be exposed at some longitudes in some events.

When the flank of a shock crosses to new field lines, where the early emission is absent, the "naked" ESP event emerges, as seen at *Voyager* in Figure 2E or at IMP 8 in Figure 1E. The ESP structure persists as the shock moves outward, but the CME speed decreases, and decreasing B shifts the resonance so the highest energy ions preferentially begin to leak away. Earlier peaks of ~30–100-MeV

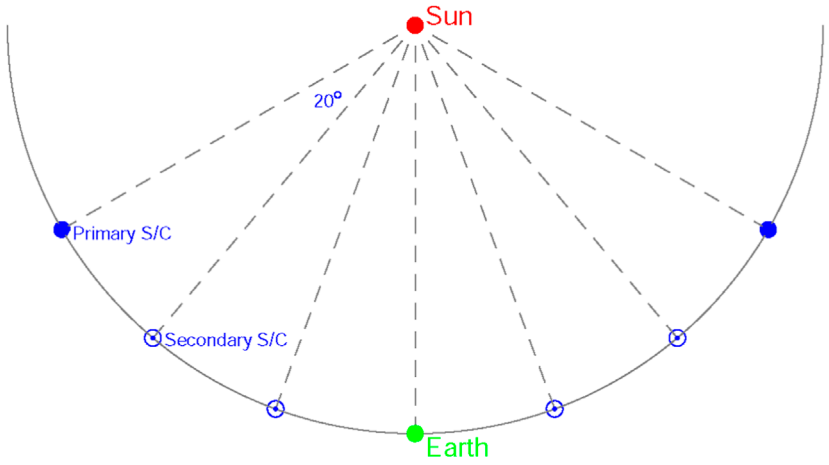

FIGURE 9
A possible multispacecraft configuration of the future might include two primary spacecraft, similar to STEREO, and four small spacecraft measuring SEPs, plasma, and fields, to study *in situ* spatial distributions of SEPs, interplanetary CMEs, and shock waves. The spacecraft would maintain their positions relative to Earth for years, spanning at least one solar maximum.

protons are seen along with the naked ESP events in these figures because they leaked out *after* the ESP events have crossed to the new field lines.

Generally, the time of the peak intensity is a contest: the initial intensities are bounded at the streaming limit, while the ESP peak is unbounded, yet the highest energies in the ESP begin to leak away as the shock slows and moves out to lower *B*. Understanding the high-energy particle acceleration of SEPs is about understanding shock acceleration, wave trapping, and the formation, spatial extent, and persistence of ESP events. The large events shown in Figure 8 are relatively rare, and we tend to assume that the same physics can be studied at lower energies. However, the physics changes for those energies where resonant waves dominate—a function of space and time. Following this, few general questions do arise:

1) Comparing Figures 1C, E, how important is θ_{Bn} in maintaining the ESP event?
2) The increasing intensity ramp at *Voyager* in Figure 2A involves SEPs leaked from the approaching ESP event. Does it show strengthening of the shock with longitude toward the east or mainly increasing proximity?
3) Are the SEP3 events with enhanced heavy ions limited in longitude? Surely, seed-particle populations in an event can change with longitude; where are the events that change from SEP3 to SEP4? Why are STEREO three-spacecraft events all SEP4 events? Half of GLEs are SEP3s.
4) How does the longitude extent of the SEPs compare with that of the shock itself? How does each vary with time?
5) Are GLEs or other high-energy events more limited in longitude? Would they be one- or two-spacecraft events for STEREO? Are broader shocks weaker or less efficient?

We should expect that shocks can accelerate whatever seed population or populations they encounter, wherever they go. We cannot exclude mixtures; we can only distinguish which one dominates at high *Z* and thus label an event SEP3 or SEP4.

We are constantly hampered by the correlated mixture of space and time. The footpoint of a field line from Earth lies 50–60^0 to our west. As our connection point on the shock scans to the east, this shock also weakens with time. How much is the change with longitude; how much is the change with time? The only resolution is to measure spatial variations with a scale substantially less than 50^0. By the time the shock arrives at 1 AU, it has mixed SEPs from ≈50^0 of solar longitude; in longer time intervals, solar rotation causes greater mixing.

5 What is needed next?

SEP evolution in space and time is complicated. STEREO spacecraft separation from Earth of ~120^0 was much too coarse to resolve the SEP-shock evolution we happened to observe in a *Helios*-IMP-*Voyager* period. What kind of observations would help? Multiple points with a better spatial resolution would help. Consider two primary spacecraft, equipped as STEREO was, with coronagraphs and *in situ* instruments, which are fixed in Earth's solar orbit at ±60^0 from Earth, as shown in Figure 9. On each side, between each primary spacecraft and Earth are two much smaller spin-stabilized spacecraft (similar to *Wind*), 20^0 apart, each capable of measuring SEPs, magnetic fields, and solar-wind plasma to map SEP events, shocks, and interplanetary CME structures. This configuration presumes that capabilities similar to a primary spacecraft are preexisting near Earth.

The ≈20^0 spacing would provide at least two measurements between the longitude of a spacecraft and that of its typical solar magnetic footpoint. It would allow meaningful coverage of many spatially small- and moderate-sized events with sampling of variations along the shock for the larger-sized events. "Smaller" SEPs do *not* mean weaker. Of course, it would be better to have more complete coverage, but the configuration in Figure 9 represents a major improvement in spatial resolution, and reasonable (33%)

coverage, at a modest increase in cost and complexity over the dual-spacecraft STEREO mission. A spacing of $\leq 20^0$ seems essential and provides a reasonable tradeoff between spacing and coverage. This would provide a map of the shock strength, direction of propagation, and θ_{Bn} at up to seven points at 1 AU that could be compared with the coronagraph mapping near the Sun and could give seven SEP/ESP profiles with differing onset times and intensities. What does the shock front really look like? Is the nose of the shock a hot spot that could produce a localized GLE; for what longitudes does the peak intensity arrive with the shock?

Are the highest energies in SEP events limited to short time periods and small spatial intervals as Gopalswamy et al. (2013) conclude? If so, what physics defines those intervals, and why do they differ from the apparent STEREO finding of similarly broad Gaussians for most energy bands? Up to some energy, we would expect high SEP intensities to generate enough waves to extend the spatial trapping and the duration of an event (e.g., Figure 8), although not at the absolute peak energy where there are yet few resonant waves. These peaks could be highly localized in well-connected regions that become poorly correlated with the average properties of the CME. Moreover, in some events, particle trapping is increased by the presence of multiple shock waves, as in the 14 July 2000 "Bastille Day" GLE (Lepping et al., 2001). To what extent can the SEP energy profile and the peak energy be predicted from an early coronagraph map of the shock strength? We would have an extra day to predict the strength of the ESP event.

Author contributions

DR: conceptualization, writing-original manuscript, and writing-review and editing.

Acknowledgments

The author thanks Ed Cliver for helpful discussions.

Conflict of interest

The author declares that the research was conducted in the absence of any commercial or financial relationships that could be construed as a potential conflict of interest.

Publisher's note

All claims expressed in this article are solely those of the authors and do not necessarily represent those of their affiliated organizations, or those of the publisher, the editors, and the reviewers. Any product that may be evaluated in this article, or claim that may be made by its manufacturer, is not guaranteed or endorsed by the publisher.

References

Beeck, J., Mason, G. M., Hamilton, D. C., Wibberenz, G., Kunow, H., Hovestadt, D., et al. (1987). A multispacecraft study of the injection and transport of solar energetic particles. *Astrophys. J.* 322, 1052. doi:10.1086/165800

Bell, A. R. (1978a). The acceleration of cosmic rays in shock fronts. I. *Mon. Not. Roy. Astron. Soc.* 182, 147–156. doi:10.1093/mnras/182.2.147

Bell, A. R. (1978b). The acceleration of cosmic rays in shock fronts. II. *Mon. Not. Roy. Astron. Soc.* 182, 443–455. doi:10.1093/mnras/182.3.443

Bertsch, D. L., Fichtel, C. E., and Reames, D. V. (1969). Relative abundance of iron-group nuclei in solar cosmic rays. *Astrophys. J. Lett.* 157, L53. doi:10.1086/180383

Bučík, R. (2020). ^{3}He-rich solar energetic particles: solar sources. *Space Sci. Rev.* 216, 24. doi:10.1007/s11214-020-00650-5

Bučík, R., Innes, D. E., Chen, N. H., Mason, G. M., Gómez-Herrero, R., and Wiedenbeck, M. E. (2015). Long-lived energetic particle source regions on the Sun. *J. Phys. Conf. Ser.* 642, 012002. doi:10.1088/1742-6596/642/1/012002

Bučík, R., Innes, D. E., Mall, U., Korth, A., Mason, G. M., and Gómez-Herrero, R. (2014). Multi-spacecraft observations of recurrent ^{3}He-rich solar energetic particles. *Astrophys. J.* 786, 71. doi:10.1088/0004-637X/786/1/71

Bučík, R., Innes, D. E., Mason, G. M., Wiedenbeck, M. E., Gómez-Herrero, R., and Nitta, N. V. (2018a). ^{3}He-rich solar energetic particles in helical jets on the Sun. *Astrophys. J.* 852, 76. doi:10.3847/1538-4357/aa9d8f

Bučík, R., Mulay, S. M., Mason, G. M., Nitta, N. V., Desai, M. I., and Dayeh, M. A. (2021). Temperature in solar sources of ^{3}He-rich solar energetic particles and relation to ion abundances. *Astrophys. J.* 908, 243. doi:10.3847/1538-4357/abd62d

Bučík, R., Wiedenbeck, M. E., Mason, G. M., Gómez-Herrero, R., Nitta, N. V., and Wang, L. (2018b). ^{3}He-rich solar energetic particles from sunspot jets. *Astrophys. J. Lett.* 869, L21. doi:10.3847/2041-8213/aaf37f

Bukata, R. P., GronstalPalmeira, P. T. R. A. R., McCracken, K. G., and Rao, U. R. (1969). Neutron monitor and Pioneer 6 and 7 studies of the January 28, 1967 solar flare event. *Sol. Phys.* 10, 198–211. doi:10.1007/BF00146170

Burlaga, L., Sittler, E., Mariani, F., and Schwenn, R. (1981). Magnetic loop behind an interplanetary shock: voyager, helios, and IMP 8 observations. *J. Geophys. Res.* 86, 6673. doi:10.1029/JA086iA08p06673

Cane, H. V., Reames, D. V., and von Rosenvinge, T. T. (1988). The role of interplanetary shocks in the longitude distribution of solar energetic particles. *J. Geophys. Res.* 93, 9555. doi:10.1029/JA093iA09p09555

Chen, N. H., Bučík, R., Innes, D. E., and Mason, G. M. (2015). Case studies of multi-day ^{3}He-rich solar energetic particle periods. *Astron. Astrophys.* 580, 16. doi:10.1051/0004-6361/201525618

Cliver, E. W., Kahler, S. W., and Reames, D. V. (2004). Coronal shocks and solar energetic proton events. *Astrophys. J.* 605, 902–910. doi:10.1086/382651

Cliver, E. W., and Ling, A. G. (2007). Electrons and protons in solar energetic particle events. *Astrophys. J.* 658, 1349–1356. doi:10.1086/511737

Cohen, C. M. S., Mason, G. M., and Mewaldt, R. A. (2017). Characteristics of solar energetic ions as a function of longitude. *Astrophys. J.* 843, 132. doi:10.3847/1538-4357/aa7513

Cook, W. R., Stone, E. C., and Vogt, R. E. (1984). Elemental composition of solar energetic particles. *Astrophys. J.* 279, 827. doi:10.1086/161953

Daibog, E. I., Stolpovskii, V. G., and Kahler, S. W. (2003). Invariance of charged particle time profiles at late stages of SCR events from the data of multisatellite observations. *Cosm. Res.* 41, 128.

de Nolfo, G. A., Bruno, A., Ryan, J. M., Dalla, S., Giacalone, J., Richardson, I. G., et al. (2019). Comparing long-duration gamma-ray flares and high-energy solar energetic particles. *Astrophys. J.* 879 (90), 90. doi:10.3847/1538-4357/ab258f

Desai, M. I., and Giacalone, J. (2016). Large gradual solar energetic particle events. *Living Rev. Sol. Phys.* 13, 3. doi:10.1007/s41116-016-0002-5

Desai, M. I., Mason, G. M., Dwyer, J. R., Mazur, J. E., Gold, R. E., Krimigis, S. M., et al. (2003). Evidence for a suprathermal seed population of heavy ions accelerated by interplanetary shocks near 1 AU. *Astrophys. J.* 588, 1149–1162. doi:10.1086/374310

Drake, J. F., Cassak, P. A., Shay, M. A., Swisdak, M., and Quataert, E. (2009). A magnetic reconnection mechanism for ion acceleration and abundance enhancements in impulsive flares. *Astrophys. J. Lett.* 700, L16–L20. doi:10.1088/0004-637X/700/1/L16

Dresing, N., Gómez-Herrero, R., Heber, B., Klassen, A., Temmer, M., and Veronig, A. (2018). Long-lasting injection of solar energetic electrons into the heliosphere. *Astron. Astrophys.* 613, A21. doi:10.1051/0004-6361/201731573

Fichtel, C. E., and Guss, D. E. (1961). Heavy nuclei in solar cosmic rays. *Phys. Rev. Lett.* 6, 495–497. doi:10.1103/PhysRevLett.6.495

Fisk, L. A. (1978). He-3-rich flares - a possible explanation. *Astrophys. J.* 224, 1048. doi:10.1086/156456

Forbush, S. E. (1946). Three unusual cosmic ray increases possibly due to charged particles from the Sun. *Phys. Rev.* 70, 771–772. doi:10.1103/physrev.70.771

Gopalswamy, N., Xie, H., Akiyama, S., Yashiro, S., Usoskin, I. G., and Davila, J. M. (2013). The first ground level enhancement event of solar cycle 24: direct observation of shock formation and particle release heights. *Astrophys. J. Lett.* 765, L30. doi:10.1088/2041-8205/765/2/L30

Gopalswamy, N., Xie, H., Yashiro, S., Akiyama, S., Mäkelä, P., and Usoskin, I. G. (2012). Properties of Ground level enhancement events and the associated solar eruptions during solar cycle 23. *Space Sci. Rev.* 171, 23–60. doi:10.1007/s11214-012-9890-4

Gosling, J. T. (1994). Correction to "The solar flare myth". *J. Geophys. Res.* 99, 4259. doi:10.1029/94JA00015

Gosling, J. T. (1993). The solar flare myth. *J. Geophys. Res.* 98, 18937–18949. doi:10.1029/93JA01896

Heras, A. M., Sanahuja, B., Lario, D., Smith, Z. K., Detman, T., and Dryer, M. (1995). Three low-energy particle events: modeling the influence of the parent interplanetary shock. *Astrophys. J.* 445, 497. doi:10.1086/175714

Jokipii, J. R., and Parker, E. N. (1969). Stochastic aspects of magnetic lines of force with application to cosmic ray propagation. *Astrophys. J.* 155, 777. doi:10.1086/149909

Kahler, S. W., Ling, A. G., and Reames, D. V. (2023). Spatial evolution of 20-MeV solar energetic proton events. *Astrophys. J.* 942, 68. doi:10.3847/1538-4357/aca7c0

Kahler, S. W., Reames, D. V., and Sheeley, N. R., Jr. (2001). Coronal mass ejections associated with impulsive solar energetic particle events. *Astrophys. J.* 562, 558–565. doi:10.1086/323847

Kahler, S. W., Sheeley, N. R., Jr., Howard, R. A., Koomen, M. J., Michels, D. J., McGuire, R. E., et al. (1984). Associations between coronal mass ejections and solar energetic proton events. *J. Geophys. Res.* 89, 9683. doi:10.1029/JA089iA11p09683

Kahler, S. W. (1992). Solar flares and coronal mass ejections. *Ann. Rev. Astron. Astrophys.* 30, 113–141. doi:10.1146/annurev.aa.30.090192.000553

Kahler, S. W. (1982). The role of the big flare syndrome in correlations of solar energetic proton fluxes and associated microwave burst parameters. *J. Geophys. Res.* 87, 3439. doi:10.1029/JA087iA05p03439

Kecskeméty, K., Daibog, E. I., Logachev, Y. I., and Kóta, J. (2009). The decay phase of solar energetic particle events. *J. Geophys. Res. A* 114, 6102. doi:10.1029/2008JA013730

Klassen, A., Dresing, N., Gómez-Herrero, R., and Heber, B. (2015). First simultaneous observations of a near-relativistic electron spike event by both STEREO spacecraft. *Astron. Astrophys.* 580, A115. doi:10.1051/0004-6361/201525700

Klassen, A., Dresing, N., Gómez-Herrero, R., Heber, B., and Müller-Mellin, R. (2016). Unexpected spatial intensity distributions and onset timing of solar electron events observed by closely spaced STEREO spacecraft. *Astron. Astrophys.* 593, A31. doi:10.1051/0004-6361/201628734

Kong, X., Guo, F., Chen, Y., and Giacalone, J. (2019). The acceleration of energetic particles at coronal shocks and emergence of a double power-law feature in particle energy spectra. *Astrophys. J.* 883, 49. doi:10.3847/1538-4357/ab3848

Kong, X., Guo, F., Giacalone, J., Li, H., and Chen, Y. (2017). The acceleration of high-energy protons at coronal shocks: the effect of large-scale streamer-like magnetic field structures. *Astrophys. J.* 851, 38. doi:10.3847/1538-4357/aa97d7

Kouloumvakos, A., Rouillard, A. P., Wu, Y., Vainio, R., Vourlidas, A., Plotnikov, I., et al. (2019). Connecting the properties of coronal shock waves with those of solar energetic particles. *Astrophys. J.* 876, 80. doi:10.3847/1538-4357/ab15d7

Laming, J. M., Vourlidas, A., Korendyke, C., Chua, D., Cranmer, S. R., Ko, Y. K., et al. (2019). Element abundances: A new diagnostic for the solar wind. *Astrophys. J.* 879, 124. doi:10.3847/1538-4357/ab23f1

Lario, D., Aran, A., Agueda, N., and Sanahuja, B. (2007). Radial dependence of proton peak intensities and fluences in SEP events: influence of the energetic particle transport parameters. *AdSpR* 40, 289–294. doi:10.1016/j.asr.2007.01.057

Lario, D., Aran, A., Gómez-Herrero, R., Dresing, N., Heber, B., Ho, G. C., et al. (2013). Longitudinal and radial dependence of solar energetic particle peak intensities: STEREO, ACE, SOHO, GOES, and MESSENGER observations. *Astrophys. J.* 767, 41. doi:10.1088/0004-637X/767/1/41

Lario, D., Kallenrode, M.-B., Decker, R. B., Roelof, E. C., Krimigis, S. M., Aran, A., et al. (2006). Radial and longitudinal dependence of solar 4-13 MeV and 27-37 MeV proton peak intensities and fluences: helios and IMP 8 observations. *Astrophys. J.* 653, 1531–1544. doi:10.1086/508982

Lario, D., Maksimovic, M., Issautier, K., Meyer-Vernet, N., Moncuquet, M., and Pantellini, F. (2010). Heliospheric energetic particle reservoirs: ulysses and ACE 175-315 keV electron observations. *Proc. 12th Sol. Wind Conf. AIP Conf. Proc.* 1216, 625. doi:10.1063/1.3395944

Lee, M. A. (2005). Coupled hydromagnetic wave excitation and ion acceleration at an evolving coronal/interplanetary shock. *Astrophys. J. Suppl.* 158, 38–67. doi:10.1086/428753

Lee, M. A. (1983). Coupled hydromagnetic wave excitation and ion acceleration at interplanetary traveling shocks. *J. Geophys. Res.* 88, 6109. doi:10.1029/JA088iA08p06109

Lee, M. A., Mewaldt, R. A., and Giacalone, J. (2012). Shock acceleration of ions in the heliosphere. *Space Sci. Rev.* 173, 247–281. doi:10.1007/s11214-012-9932-y

Lepping, R. P., Berdichevsky, D. B., Burlaga, L. F., Lazarus, A. J., Kasper, J., Desch, M. D., et al. (2001). The bastille day magnetic clouds and upstream shocks: near earth interplanetary observations. *Sol. Phys.* 204, 285–303. doi:10.1023/A:1014264327855

Li, G., and Bian, N. H. (2023). Lagrangian stochastic model for the motions of magnetic footpoints on the solar wind source surface and the path lengths of boundary-driven interplanetary magnetic field lines. *Astrophys. J.* 945, 150. doi:10.3847/1538-4357/acbd43

Liu, S., Petrosian, V., and Mason, G. M. (2004). Stochastic acceleration of ^{3}He and ^{4}He in solar flares by parallel-propagating plasma waves. *Astrophys. J. Lett.* 613, L81–L84. doi:10.1086/425070

Liu, S., Petrosian, V., and Mason, G. M. (2006). Stochastic acceleration of ^{3}He and ^{4}He in solar flares by parallel-propagating plasma waves: general results. *Astrophys. J.* 636, 462–474. doi:10.1086/497883

Liu, W., Kong, X., Guo, F., Zhao, L., Feng, S., Yu, F., et al. (2023). Effects of coronal magnetic field configuration on particle acceleration and release during the ground level enhancement events in solar cycle 24. Available at: https://arxiv.org/abs/2307.12191.

Mandzhavidze, N., Ramaty, R., and Kozlovsky, B. (1999). Determination of the abundances of subcoronal ^{4}He and of solar flare-accelerated ^{3}He and ^{4}He from gamma-ray spectroscopy. *Astrophys. J.* 518, 918–925. doi:10.1086/307321

Mason, G. M. (2007). ^{3}He-rich solar energetic particle events. *Space Sci. Rev.* 130, 231–242. doi:10.1007/s11214-007-9156-8

Mason, G. M., Gloeckler, G., and Hovestadt, D. (1984). Temporal variations of nucleonic abundances in solar flare energetic particle events. II - evidence for large-scale shock acceleration. *Astrophys. J.* 280, 902. doi:10.1086/162066

Mason, G. M., Mazur, J. E., Dwyer, J. R., Jokippi, J. R., Gold, R. E., and Krimigis, S. M. (2004). Abundances of heavy and ultraheavy ions in ^{3}He-rich solar flares. *Astrophys. J.* 606, 555–564. doi:10.1086/382864

Mason, G. M., Mazur, J. E., and Dwyer, J. R. (1999). [TSUP]3[/TSUP]H[CLC]e[/CLC] Enhancements in Large Solar Energetic Particle Events. *Astrophys. J. Lett.* 525, L133–L136. doi:10.1086/312349

Mason, G. M., Ng, C. K., Klecker, B., and Green, G. (1989). Impulsive acceleration and scatter-free transport of about 1 MeV per nucleon ions in ^{3}He-rich solar particle events. *Astrophys. J.* 339, 529. doi:10.1086/167315

Mason, G. M., Reames, D. V., Klecker, B., Hovestadt, D., and von Rosenvinge, T. T. (1986). The heavy-ion compositional signature in He-3-rich solar particle events. *Astrophys. J.* 303, 849. doi:10.1086/164133

McGuire, R. E., von Rosenvinge, T. T., and McDonald, F. B. (1979). A survey of solar cosmic ray composition. *Proc. 16th Int. Cosm. Ray Conf.* 5, 61.

McKibben, R. B. (1972). Azimuthal propagation of low-energy solar-flare protons as observed from spacecraft very widely separated in solar azimuth. *J. Geophys. Res.* 77, 3957–3984. doi:10.1029/JA077i022p03957

Melrose, D. B. (1980). *Plasma astrophysics*. New York: Gordon & Breach.

Mewaldt, R. A., Looper, M. D., Cohen, C. M. S., Haggerty, D. K., Labrador, A. W., Leske, R. A., et al. (2012). Energy spectra, composition, and other properties of ground-level events during solar cycle 23. *Space Sci. Rev.* 171, 97–120. doi:10.1007/s11214-012-9884-2

Meyer, J. P. (1985). The baseline composition of solar energetic particles. *Astrophys. J. Suppl.* 57, 151. doi:10.1086/191000

Murphy, R. J., Kozlovsky, B., and Share, G. H. (2016). Evidence for enhanced ^{3}He in flare-accelerated particles based on new calculations of the gamma-ray line spectrum. *Astrophys. J.* 833, 196. doi:10.3847/1538-4357/833/2/196

Murphy, R. J., Ramaty, R., Kozlovsky, B., and Reames, D. V. (1991). Solar abundances from gamma-ray spectroscopy: comparisons with energetic particle, photospheric, and coronal abundances. *Astrophys. J.* 371, 793. doi:10.1086/169944

Newkirk, G., Jr., and Wenzel, D. G. (1978). Rigidity-independent propagation of cosmic rays in the solar corona. *J. Geophys. Res.* 83, 2009. doi:10.1029/JA083iA05p02009

Ng, C. K., Reames, D. V., and Tylka, A. J. (1999). Effect of proton-amplified waves on the evolution of solar energetic particle composition in gradual events. *Geophys. Res. Lett.* 26, 2145–2148. doi:10.1029/1999GL900459

Ng, C. K., and Reames, D. V. (2008). Shock acceleration of solar energetic protons: the first 10 minutes. *Astrophys. J. Lett.* 686, L123–L126. doi:10.1086/592996

Ng, C. K., Reames, D. V., and Tylka, A. J. (2003). Modeling shock-accelerated solar energetic particles coupled to interplanetary Alfvén waves. *Astrophys. J.* 591, 461–485. doi:10.1086/375293

Ng, C. K., Reames, D. V., and Tylka, A. J. (2012). Solar energetic particles: shock acceleration and transport through self-amplified waves. *AIP Conf. Proc.* 1436, 212. doi:10.1063/1.4723610

Nitta, N. V., Mason, G. M., Wang, L., Cohen, C. M. S., and Wiedenbeck, M. E. (2015). Solar sources of ^{3}He-rich solar energetic particle events in Solar Cycle 24. *Astrophys. J.* 806, 235. doi:10.1088/0004-637X/806/2/235

Nitta, N. V., Reames, D. V., DeRosa, M. L., Yashiro, S., and Gopalswamy, N. (2006). Solar sources of impulsive solar energetic particle events and their magnetic field connection to the earth. *Astrophys. J.* 650, 438–450. doi:10.1086/507442

Paassilta, M., Papaioannou, A., Dresing, N., Vainio, R., Valtonen, E., and Heber, B. (2018). Catalogue of > 55 MeV wide-longitude solar proton events observed by SOHO, ACE, and the STEREOs at ≈ 1 AU during 2009 – 2016. *Sol. Phys.* 293, 70. doi:10.1007/s11207-018-1284-7

Parker, E. N. (1965). The passage of energetic charged particles through interplanetary space. *Space Sci.* 13, 9–49. doi:10.1016/0032-0633(65)90131-5

Raukunen, O., Vainio, R., Tylka, A. J., Dietrich, W. F., Jiggens, P., Heynderickx, D., et al. (2018). Two solar proton fluence models based on ground level enhancement observations. *J. Spa. Wea. Spa. Clim.* 8, A04. doi:10.1051/swsc/2017031

Reames, D. V. (2000). Abundances of trans-iron elements in solar energetic particle events. *Astrophys. J. Lett.* 540, L111–L114. doi:10.1086/312886

Reames, D. V. (2018b). Abundances, ionization states, temperatures, and FIP in solar energetic particles. *Space Sci. Rev.* 214, 61. doi:10.1007/s11214-018-0495-4

Reames, D. V., Barbier, L. M., and Ng, C. K. (1996). The spatial distribution of particles accelerated by coronal mass ejection-driven shocks. *Astrophys. J.* 466, 473. doi:10.1086/177525

Reames, D. V. (1988). Bimodal abundances in the energetic particles of solar and interplanetary origin. *J. Lett.* 330, L71. doi:10.1086/185207

Reames, D. V., Cliver, E. W., and Kahler, S. W. (2014a). Abundance enhancements in impulsive solar energetic-particle events with associated coronal mass ejections. *Sol. Phys.* 289, 3817–3841. doi:10.1007/s11207-014-0547-1

Reames, D. V., Cliver, E. W., and Kahler, S. W. (2014b). Variations in abundance enhancements in impulsive solar energetic-particle events and related CMEs and flares. *Sol. Phys.* 289, 4675–4689. doi:10.1007/s11207-014-0589-4

Reames, D. V. (1995a). Coronal Abundances determined from energetic particles. *Adv. Space Res.* 15 (7), 41–51. doi:10.1016/0273-1177(94)00018-v

Reames, D. V. (2014). Element abundances in solar energetic particles and the solar corona. *Sol. Phys.* 289, 977–993. doi:10.1007/s11207-013-0350-4

Reames, D. V. (2022a). Energy spectra vs. element abundances in solar energetic particles and the roles of magnetic reconnection and shock acceleration. *Sol. Phys.* 297, 32. doi:10.1007/s11207-022-01961-2

Reames, D. V. (2020). Four distinct pathways to the element abundances in solar energetic particles. *Space Sci. Rev.* 216, 20. doi:10.1007/s11214-020-0643-5

Reames, D. V. (2023). How do shock waves define the space-time structure of gradual solar energetic-particle events? *Space Sci. Rev.* 219, 14. doi:10.1007/s11214-023-00959-x

Reames, D. V. (2019). Hydrogen and the abundances of elements in impulsive solar energetic-particle events. *Sol. Phys.* 294, 37. doi:10.1007/s11207-019-1427-5

Reames, D. V., Kahler, S. W., and Ng, C. K. (1997). Spatial and temporal invariance in the spectra of energetic particles in gradual solar events. *Astrophys. J.* 491, 414–420. doi:10.1086/304939

Reames, D. V., Kallenrode, M.-B., and Stone, R. G. (1991). Multi-spacecraft observations of solar ^{3}He-rich events. *Astrophys. J.* 380, 287. doi:10.1086/170585

Reames, D. V., and Lal, N. (2010). A multi-spacecraft view of solar-energetic-particle onsets in the 1977 November 22 event. *Astrophys. J.* 723, 550–554. doi:10.1088/0004-637X/723/1/550

Reames, D. V., Meyer, J. P., and von Rosenvinge, T. T. (1994). Energetic-particle abundances in impulsive solar flare events. *Astrophys. J. Suppl.* 90, 649. doi:10.1086/191887

Reames, D. V., and Ng, C. K. (2004). Heavy-element abundances in solar energetic particle events. *Astrophys. J.* 610, 510–522. doi:10.1086/421518

Reames, D. V., and Ng, C. K. (1998). Streaming-limited intensities of solar energetic particles. *Astrophys. J.* 504, 1002–1005. doi:10.1086/306124

Reames, D. V., and Ng, C. K. (2010). Streaming-limited intensities of solar energetic particles on the intensity plateau. *Astrophys. J.* 723, 1286–1293. doi:10.1088/0004-637X/723/2/1286

Reames, D. V., and Ng, C. K. (2014). The streaming limit of solar energetic-particle intensities. *Living a Star Workshop Extreme Space Weather Events*. Available at: https://arxiv.org/abs/1412.2279.

Reames, D. V., Ng, C. K., and Tylka, A. J. (2013). Spatial distribution of solar energetic particles in the inner heliosphere. *Sol. Phys.* 285, 233–250. doi:10.1007/s11207-012-0038-1

Reames, D. V. (1999). Particle acceleration at the Sun and in the heliosphere. *Space Sci. Rev.* 90, 413–491. doi:10.1023/A:1005105831781

Reames, D. V. (2021b). Sixty years of element abundance measurements in solar energetic particles. *Space Sci. Rev.* 217, 72. doi:10.1007/s11214-021-00845-4

Reames, D. V. (2021a). "Solar energetic particles," in *Lec. Notes phys. 978* (Cham, Switzerland: Springer Nature). open access. doi:10.1007/978-3-030-66402-2

Reames, D. V. (1995b). Solar energetic particles: A paradigm shift. *Revs. Geophys. Suppl.* 33, 585. doi:10.1029/95RG00188

Reames, D. V. (2022b). Solar energetic particles: spatial extent and implications of the H and He abundances. *Space Sci. Rev.* 218, 48. doi:10.1007/s11214-022-00917-z

Reames, D. V. (2009b). Solar energetic-particle release times in historic ground-level events. *Astrophys. J.* 706, 844–850. doi:10.1088/0004-637X/706/1/844

Reames, D. V. (2009a). Solar release times of energetic particles in ground-level events. *Astrophys. J.* 693, 812–821. doi:10.1088/0004-637X/693/1/812

Reames, D. V., and Stone, R. G. (1986). The identification of solar ^{3}He-rich events and the study of particle acceleration at the sun. *Astrophys. J.* 308, 902. doi:10.1086/164560

Reames, D. V. (2016). Temperature of the source plasma in gradual solar energetic particle events. *Sol. Phys.* 291, 911–930. doi:10.1007/s11207-016-0854-9

Reames, D. V. (2018a). The "FIP effect" and the origins of solar energetic particles and of the solar wind. *Sol. Phys.* 293, 47. doi:10.1007/s11207-018-1267-8

Reames, D. V. (2013). The two sources of solar energetic particles. *Space Sci. Rev.* 175, 53–92. doi:10.1007/s11214-013-9958-9

Reames, D. V., von Rosenvinge, T. T., and Lin, R. P. (1985). Solar ^{3}He-rich events and nonrelativistic electron events - a new association. *Astrophys. J.* 292, 716. doi:10.1086/163203

Reinhard, R., and Wibberenz, G. (1974). Propagation of flare protons in the solar atmosphere. *Sol. Phys.* 36, 473–494. doi:10.1007/BF00151216

Richardson, I. G., Reames, D. V., Wenzel, K. P., and Rodriguez-Pacheco, J. (1990). Quiet-time properties of low-energy (less than 10 MeV per nucleon) interplanetary ions during solar maximum and solar minimum. *Astrophys. J. Lett.* 363, L9. doi:10.1086/185853

Richardson, I. G., von Rosenvinge, T. T., Cane, H. V., Christian, E. R., Cohen, C. M. S., Labrador, A. W., et al. (2014). 25 MeV proton events observed by the high energy telescopes on the stereo a and b spacecraft and/or at Earth during the first ~ seven years of the STEREO mission, *Sol. Phys.* 289 3059–3107. doi:10.1007/s11207-014-0524-8

Roelof, E. C., Gold, R. E., Simnett, G. M., Tappin, S. J., Armstrong, T. P., and Lanzerotti, L. J. (1992). Low-energy solar electrons and ions observed at ULYSSES February-April, 1991 - the inner heliosphere as a particle reservoir. *Geophys. Res. Lett.* 19, 1243–1246. doi:10.1029/92GL01312

Rouillard, A. C., Odstrčil, D., Sheeley, N. R., Jr., Tylka, A. J., Vourlidas, A., Mason, G., et al. (2011). Interpreting the properties of solar energetic particle events by using combined imaging and modeling of interplanetary shocks. *Astrophys. J.* 735, 7. doi:10.1088/0004-637X/735/1/7

Rouillard, A., Sheeley, N. R., Jr., Tylka, A., Vourlidas, A., Ng, C. K., Rakowski, C., et al. (2012). The longitudinal properties of a solar energetic particle event investigated using modern solar imaging. *Astrophys. J.* 752, 44. doi:10.1088/0004-637X/752/1/44

Serlemitsos, A. T., and Balasubrahmanyan, V. K. (1975). Solar particle events with anomalously large relative abundance of ^{3}He. *Astrophys. J.* 198, 195. doi:10.1086/153592

Stix, T. H. (1992). *Waves in plasmas*. New York: AIP.

Temerin, M., and Roth, I. (1992). The production of ^{3}He and heavy ion enrichment in ^{3}He-rich flares by electromagnetic hydrogen cyclotron waves. *Astrophys. J. Lett.* 391, L105. doi:10.1086/186408

Townsend, L. W., Adams, J. H., Blattnig, S. R., Clowdsley, M. S., Fry, D. J., Jun, I., et al. (2018). Solar particle event storm shelter requirements for missions beyond low Earth orbit. *Life Sci. Space Res.* 17, 32–39. doi:10.1016/j.lssr.2018.02.002

Tylka, A. J., Cohen, C. M. S., Dietrich, W. F., Lee, M. A., Maclennan, C. G., Mewaldt, R. A., et al. (2005). Shock geometry, seed populations, and the origin of variable elemental composition at high energies in large gradual solar particle events. *Astrophys. J.* 625, 474–495. doi:10.1086/429384

Tylka, A. J., Cohen, C. M. S., Dietrich, W. F., Krucker, S., McGuire, R. E., Mewaldt, R. A., et al. (2003). "Inspirehep," in Proceedingof the 28th International Cosmic Ray Conference (ICRC 2003) - INSPIRE, Tsukuba, Japan, August 2003, 3305.

Tylka, A. J., Cohen, C. M. S., Dietrich, W. F., Maclennan, C. G., McGuire, R. E., Ng, C. K., et al. (2001). Evidence for remnant flare suprathermals in the source population of solar energetic particles in the 2000 bastille day event. *Astrophys. J. Lett.* 558, L59–L63. doi:10.1086/323344

Tylka, A. J., and Dietrich, W. F. (2009). "A new and comprehensive analysis of proton spectra in ground-level enhanced (GLE) solar particle events," in Proceedings of 31st International Cosmic Ray Conference Lodz, Lodz, Poland, July 2009.

Tylka, A. J., and Lee, M. A. (2006). A model for spectral and compositional variability at high energies in large, gradual solar particle events. *Astrophys. J.* 646, 1319–1334. doi:10.1086/505106

Wang, Y.-M., Pick, M., and Mason, G. M. (2006). Coronal holes, jets, and the origin of ^{3}He-rich particle events. *Astrophys. J.* 639, 495–509. doi:10.1086/499355

Wiedenbeck, M. E., Mason, G. M., Cohen, C. M. S., Nitta, N. V., Gómez-Herrero, R., and Haggerty, D. K. (2013). Observations of solar energetic particles from ^{3}He-rich events over a wide range of heliographic longitude. *Astrophys. J.* 762, 54. doi:10.1088/0004-637X/762/1/54

Wild, J. P., Smerd, S. F., and Weiss, A. A. (1963). Solar bursts. *Annu. Rev. Astron. Astrophys.* 1, 291–366. doi:10.1146/annurev.aa.01.090163.001451

Xie, H., Cyr, O. C., Mäkelä, P., and Gopalswamy, N. (2019). Statistical study on multispacecraft widespread solar energetic particle events during solar cycle 24. *J. Geophys. Res.* 124, 6384–6402. doi:10.1029/2019JA026832

Zank, G. P., Li, G., and Verkhoglyadova, O. (2007). Particle acceleration at interplanetary shocks. *Space Sci. Rev.* 130, 255–272. doi:10.1007/s11214-007-9214-2

Zank, G. P., Rice, W. K. M., and Wu, C. C. (2000). Particle acceleration and coronal mass ejection driven shocks: A theoretical model. *J. Geophys. Res.* 105, 25079–25095. doi:10.1029/1999JA000455

Zhang, M., Cheng, L., Zhang, J., Riley, P., Kwon, R. Y., Lario, D., et al. (2023). A data-driven, physics-based transport model of solar energetic particles accelerated by coronal mass ejection shocks propagating through the solar coronal and heliospheric magnetic fields. *Astrophys. J. Suppl.* 266, 35. doi:10.3847/1538-4365/accb8e

frontiers | Frontiers in Astronomy and Space Sciences

TYPE Methods
PUBLISHED 29 September 2023
DOI 10.3389/fspas.2023.1282261

OPEN ACCESS

EDITED BY
David Knudsen,
University of Calgary, Canada

REVIEWED BY
Jeff Forbes,
University of Colorado Boulder,
United States
Yun Gong,
Wuhan University, China

*CORRESPONDENCE
Jens Oberheide,
joberhe@clemson.edu

†PRESENT ADDRESS
Stone M. Gardner, University of Alaska,
Fairbanks, AK, United States

RECEIVED 23 August 2023
ACCEPTED 19 September 2023
PUBLISHED 29 September 2023

CITATION
Oberheide J, Gardner SM and Neogi M (2023), Resolving the tidal weather of the thermosphere using GDC.
Front. Astron. Space Sci. 10:1282261.
doi: 10.3389/fspas.2023.1282261

Resolving the tidal weather of the thermosphere using GDC

Jens Oberheide*, Stone M. Gardner† and Mukta Neogi

Department of Physics and Astronomy, Clemson University, Clemson, SC, United States

NASA's Geospace Dynamics Constellation (GDC) mission is a six satellite constellation to make *in situ* measurements of important ionospheric and thermospheric variables to better understand the processes that govern Earth's near space environment. Scheduled for a 2029 launch into high inclination orbits ~82° at ~380 km, the satellite orbit planes will separate over time to provide almost continuous local solar time coverage every day towards the end of the 3 year baseline GDC mission. As such, the neutral temperature and neutral wind measurements of GDC will likely allow the heliophysics community to make significant progress towards resolving the tidal weather of the thermosphere, that is, day-to-day tidal variability, and how it is driven by meteorological processes near the surface and *in situ* forcing in the ionosphere-thermosphere system. To assess the GDC ability to accurately resolve the tides each day and when in the mission this can be achieved, we conduct an Observational Simulation System Experiment (OSSE) using SD-WACCM-X and the predicted GDC orbits. Our results show that GDC can provide closure on the tidal variability (mean, diurnal and semidiurnal, migrating and nonmigrating) at orbit height in mission phase 4 and throughout most parts of mission phase 3. We also perform Hough Mode Extension fitting of relevant tidal components to study possible connections between the GDC observations and the tides at 200 km, to assess synergies between GDC and the forthcoming DYNAMIC mission (scheduled to be co-launched with GDC) that will measure altitude-resolved winds and temperatures in the ~100–200 km height range.

KEYWORDS

GDC, tidal weather, OSSE, DYNAMIC, Hough mode extensions

1 Introduction

Each day, upward propagating atmospheric waves carry vast amounts of energy, around 10^{16}J (Jarvis, 2001), to the ionosphere-thermosphere (IT system). This value is comparable to the input of solar EUV and greater than typical auroral particle and Joule heating combined (Richmond and Lu, 2000; Newell et al., 2009). However, much of the wave spectrum is not well-sampled by observations nor realistically captured in global-scale models, leaving atmospheric waves as one of the largest sources of uncertainty in understanding the variability of the Earth's upper atmosphere and ionosphere, coupling of the lower and upper atmosphere, and the prediction of the atmosphere's response to space weather (Sassi et al., 2019). At present, the global-scale wave spectrum is only known in the mesosphere/lower thermosphere (MLT, <100 km) and above 250 km, in a limited latitude range equatorward of about 55°, and with a "climatological" time resolution of >1 month (Oberheide et al., 2011a) The heliophysics community does not have suitable global measurements in the all-important 100–200 km altitude range, where dissipation and

in situ forcing occur. Suitablerefers to the availability of day and nighttime measurements (full local solar time coverage) to resolve the tidal spectrum. Consequently, the 100–200 km altitude region remains the "thermospheric gap" where we know little about the dynamics. Equally important, the "tidal weather," that is, variability on timescales (days) relevant for space weather, is not known at any altitude above the stratopause up to the exosphere—but is expected to be on the same order as the monthly mean amplitudes as many wave sources are related to meteorological weather near the Earth's surface Oberheide et al. (2015b).

The importance of resolving the global wave spectrum, particularly the tides, on weather time scales was highlighted by the National Academies in the 2013 Decadal Survey (National Research Council, 2013) which put forward the Geospace Dynamics Constellation (GDC) and the DYNAMIC mission to study the meteorological driving of geospace, among other science questions. GDC is scheduled for a launch in 2029 with all *in situ* instruments onboard the six identical spacecraft selected. The specifics of the DYNAMIC mission are at the time of this paper not clear as the instruments have not yet been selected—but it is likely that they will include the capability to measure temperatures and winds in the 100–200 km height range, per 2013 Decadal Survey (National Research Council, 2013). We will thus focus on the GDC mission and its ability to resolve the tidal weather *in situ* around 380 km in the following and only briefly discuss approaches of how to connect GDC and DYNAMIC measurements of tides.

The GDC orbit geometry is complex, to allow measurements to evolve from local to regional to global scales over the course of the 3 year baseline mission (GDC Science and Technology Definition, 2021). In-track and cross-track horizontal winds are prime parameters of GDC, along with neutral temperature and other parameters NNH17ZDA004O-GDC. (2021). Per the NASA ephemeris description GDC Ephemeris. (2022), the GDC satellites will reach a maximum of 6 h local time separation (ascending nodes) in mission phase 3 after 12 months of science operations, 9 h (phase 4) after 22 months and 12 h towards the end of the mission. Science operations will start about 3 months post launch. The maximum local time separation of the spacecraft is unaffected by a potential downscoped (threshold) GDC mission of four spacecraft. In this paper, we conduct an Observational Simulation System Experiment (OSSE) using hourly output of 1 year of 2009 SD-WACCM-X simulations to resolve the mean, diurnal and semdiurnal tidal spectrum every day. Our results show that this is possible with a high level of accuracy during GDC mission phase 4, with degrading capabilities during the earlier parts of the GDC mission.

The manuscript is organized as follows. Section 2 overviews the observational requirements to resolve the tidal weather. Section 3 overviews key aspects of GDC and the SD-WACCM-X simulations and describes the OSSE. Section 4 provides the OSSE results and complements them with the results from the full model as a function of GDC mission phase. Section 5 provides Hough Mode Extension fits to evaluate the connection between GDC and DYNAMIC. Section 6 contains the conclusions.

2 Observational requirements to resolve tidal weather

2.1 Atmospheric tides

Atmospheric tides (Oberheide et al., 2015a) are global-scale oscillations in winds, temperature and many other parameters that attain substantial amplitudes (several tens of m/s, K) in the mesopause region around 90 km and above in the thermosphere. The most important tidal periods (in this order) are harmonics of a solar day: diurnal (24 h), semidiurnal (12 h), terdiurnal (8 h) and quarterdiurnal (6 h). Tides can propagate westward, eastward or remain stationary with horizontal wavelengths (along longitude) of order ~10,000 km, vertical wavelengths between ten to several hundred kilometers, and substantial changes in magnitude as function of latitude. Many tidal components are forced in the troposphere, through infrared absorption by tropospheric water vapor and latent heat release during cloud droplet formation in organized deep convective systems. As such, tides are more than likely to map surface weather variability into the space weather of the ionosphere: either through direct upward propagation into the thermosphere or through dynamo processes in Earth's E-region with subsequent mapping of polarization electric fields along magnetic field lines into the F-region (Immel et al., 2006; Forbes et al., 2009). The new COSMIC-2 constellation allows one to diagnose F-region plasma density tides every day (Oberheide, 2022) and shows that weather-like tidal plasma variations are ubiquitous. Further tidal sources are in the stratosphere/mesosphere, through ultraviolet absorption by ozone and several nonlinear fluid dynamical processes, and in the thermosphere, through far and extreme ultraviolet absorption and through interactions of the fluid with ions (Hagan et al., 2001; Häusler et al., 2013; Jones Jr. et al., 2013). An additional, poorly understood, pathway is the dissipation of convectively forced gravity waves that, according to modeling, produces body forces and heating in the 170–200 km altitude range that *in situ* force a spectrum of nonmigrating tides Vadas et al. (2014). In order to separate tidal variability imposed by surface weather from variability driven by nonlinearity, and solar and geomagnetic forcing from above, one needs to obtain the spectrum the tides on weather timescales (ideally, day-to-day).

The general form of a tidal oscillation at a particular latitude φ and altitude z is given in Eq. 1 and a wave crest occurs when Eq. 2 is satisfied.

$$A\cos\left(s\lambda - \sigma_m t - \Phi\right) \tag{1}$$

$$\Phi = s\lambda - \sigma_m t \tag{2}$$

$A = A(\varphi, z)$ is the tidal amplitude, $\Phi = \Phi(\varphi, z)$ is the tidal phase, t is universal time, λ is longitude, $s \geq 0$ is the zonal wavenumber (the number of wave crests that occur along a latitude circle) and σ_m is the tidal frequency. The wave propagates eastward (or remains standing for $s = 0$) for $\sigma_m > 0$ and westward for $\sigma_m < 0$. Using $\sigma_1 = (2\pi/24)$ hour^{-1} for the diurnal base frequency, the mth diurnal harmonic is expressed as $\sigma_m = m\sigma_1$, with $m = [\pm1, \pm2, \pm3, \pm4]$ for diurnal, semidiurnal, terdiurnal, quarterdiurnal tides, respectively.

Eq. 1 expressed in local solar time (LST, the natural time frame of reference of a satellite in low Earth orbit, $t_{LST} = t + \lambda/\sigma_1$) is as follows.

$$A_{m,s}\cos\left((s+m)\lambda - \sigma_m t_{LST} - \Phi_{m,s}\right) \tag{3}$$

Amplitude and phase depend on frequency and zonal wavenumber, now indicated by the m,s subscripts. Tides are ubiquitous and usually a whole spectrum of different tidal components (that is, (m,s) frequency/wavenumber pairs) is simultaneously excited. Their linear superposition (Eq. 4) is what is observed.

$$\sum_{m,s} A_{m,s}\cos\left((s+m)\lambda - \sigma_m t_{LST} - \Phi_{m,s}\right) \tag{4}$$

An important subset of the tides follow the apparent (from a ground-based observer perspective) westward motion of the Sun. For these so-called migrating tides, $s = -m$, $m < 0$ and Eq. 3 simplifies to

$$A_{-|m|,|m|}\cos\left(|m|\sigma_1 t_{LST} - \Phi_{-|m|,|m|}\right) \tag{5}$$

Eq. 5 shows that migrating tides have the same local solar time variation at all longitudes. The tide is called migrating diurnal tide if $(m,s) = (-1,1)$, migrating semidiurnal tide if $(m,s) = (-2,2)$, migrating terdiurnal tide if $(m,s) = (-3,3)$ and so on. Tidal components with $s \neq -m$ are called nonmigrating tides. Tidal components are usually identified by a two-letter, one-number nomenclature: the first letter indicates the period ("D": diurnal 24 h, "S": semidiurnal 12 h, "T": terdiurnal 8 h, "Q": quarterdiurnal 6 h), the second letter is the propagation direction ("W": westward, "E": eastward, "S": standing), and the number is the zonal wavenumber s. With that, the migrating semidiurnal tide $(m,s) = (-2,2)$ is SW2, the nonmigrating diurnal eastward propagating tide of zonal wavenumber 3 $(m,s) = (1,3)$ is DE3, and so on.

2.2 Observational requirements

The key science requirement is to attain wind and temperature data that allow one to diagnose the tidal spectrum (m,s) as a function of latitude and altitude, for periods $m = [\pm1,\pm2,\pm3,\pm4] = [\pm24,\pm12,\pm8,\pm6]$ hours and zonal wavenumbers $s = [0,6]$, and to do so on a daily basis. Harmonic fitting (Fourier decomposition) of Eq. 4 requires full local solar time and longitude coverage to delineate the tidal amplitudes $A_{m,s}$ and phases $\Phi_{m,s}$ as function of latitude and altitude. The longitude coverage requirement makes global observations from space essential, as a single ground-based instrument cannot separate between different zonal wavenumbers s. Suitable networks of ground-based instruments are not feasible due to the land/ocean distribution on Earth. The local solar time coverage requirement can been achieved by making use of spacecraft local solar time precession, that is, combining several weeks of observations into a "composite day" that covers all local solar times. However, this puts a severe limitation on the time resolution of tidal diagnostics from a single spacecraft. At any given latitude, a single spacecraft observes at two different local solar times each day: one on the ascending orbit node and one on the descending orbit node. These local solar

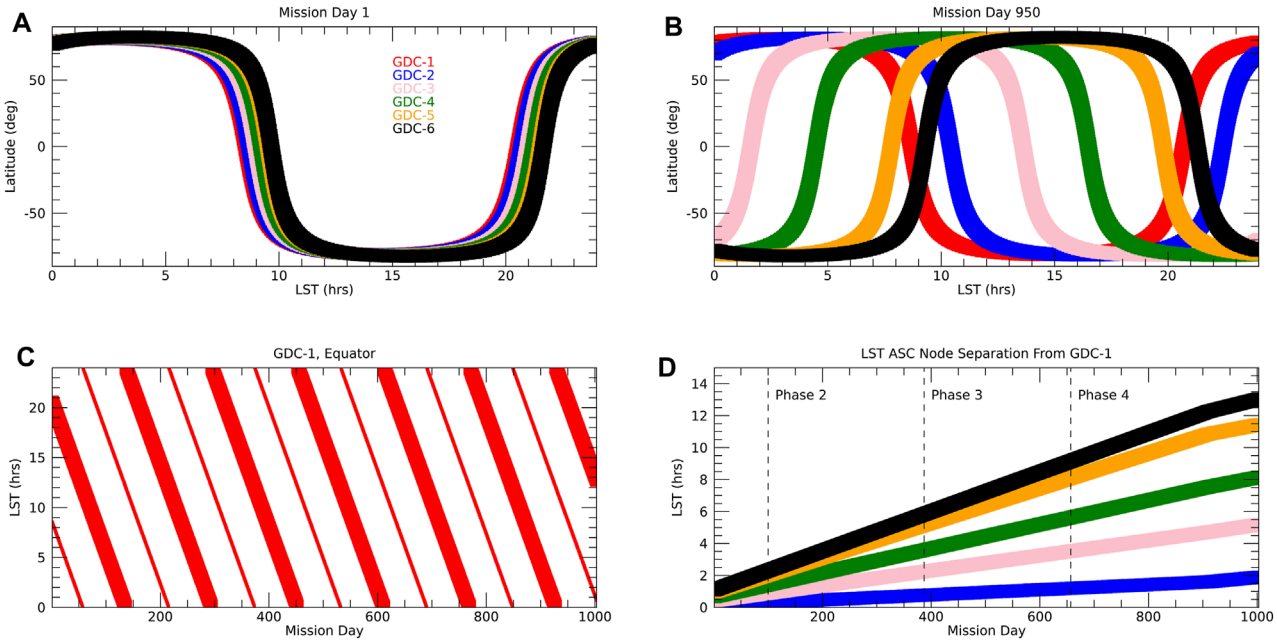

FIGURE 1
(A) Local solar time of the six GDC spacecraft as function of latitude for mission day 1. Mission day is relative to the beginning of GDC mission phase 1, about 3 months after launch. **(B)** Same as **(A)** but for mission day 950. **(C)** Local solar time precession of GDC-1 over the mission. Large symbols indicate ascending orbit nodes and small symbols indicate descending orbit nodes. **(D)** Local solar time separation between the spacecraft as function of mission day. Plotted is the difference for the ascending orbit node relative to GDC-1 with the same color code as in **(A)**.

times are largely independent of longitude (variations for a given day and orbit node are within a few minutes) and change from 1 day to another by several minutes towards earlier times, depending on orbit inclination.

For example, a single spacecraft in a 82° inclination orbit needs about 90 days for the ascending orbit node to precess 12 h in local solar time, which can easily be computed from first principles (Nielsen et al., 1958). The 12-h descending orbit node precession is 90 days, too. Consequently, one would need to combine 90 days of observations (for 82° inclination) to obtain the "composite day" 24 h local solar time coverage needed to diagnose $A_{m,s}$ and $\Phi_{m,s}$. Consequently, the time resolution of current state-of-the-art tidal diagnostics in the mesosphere/lower thermosphere region is 61 days (TIMED satellite) (Oberheide et al., 2006; Forbes et al., 2008), 41 days (low latitudes, ICON satellite) (Cullens et al., 2020; Forbes et al., 2022) and 135 days around 400 km (CHAMP satellite, inclination 87.3°) (Häusler and Lühr, 2009). Attempts to diagnose short-term tidal variability from a single satellite, without exceptions, rely on assumptions such as neglecting certain (m,s) pairs, setting *in situ* sources to zero, or others (Oberheide et al., 2002; Oberheide et al., 2015b; Lieberman et al., 2013; Pedatella et al., 2016; Gasperini et al., 2020). Such assumptions may be justified for certain altitude regimes and situations, for example, when multiple data sources indicate the predominance of a certain (m,s) tidal component, but become increasingly questionable, even speculative, throughout the thermosphere because of a lack of observations. The only solution to the problem is to increase the number of local solar times observed each day by flying multiple spacecraft in different orbital planes, as in the GDC constellation.

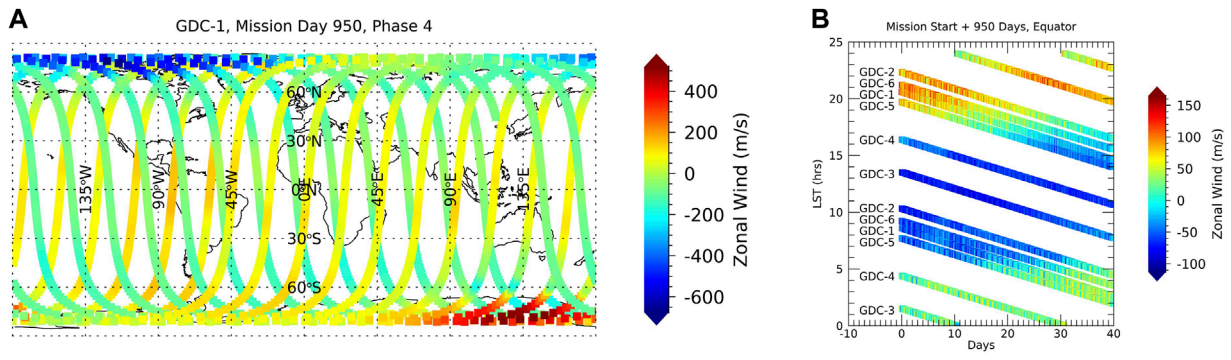

FIGURE 2
(A) Zonal wind from SD-WACCM-X sampled along the orbit track of GDC-1 for mission day 950. **(B)** Equatorial (±2.5° latitude) local solar time coverage and evolution of the six GDC spacecraft starting on mission day 950 with sampled zonal wind from SD-WACCM-X.

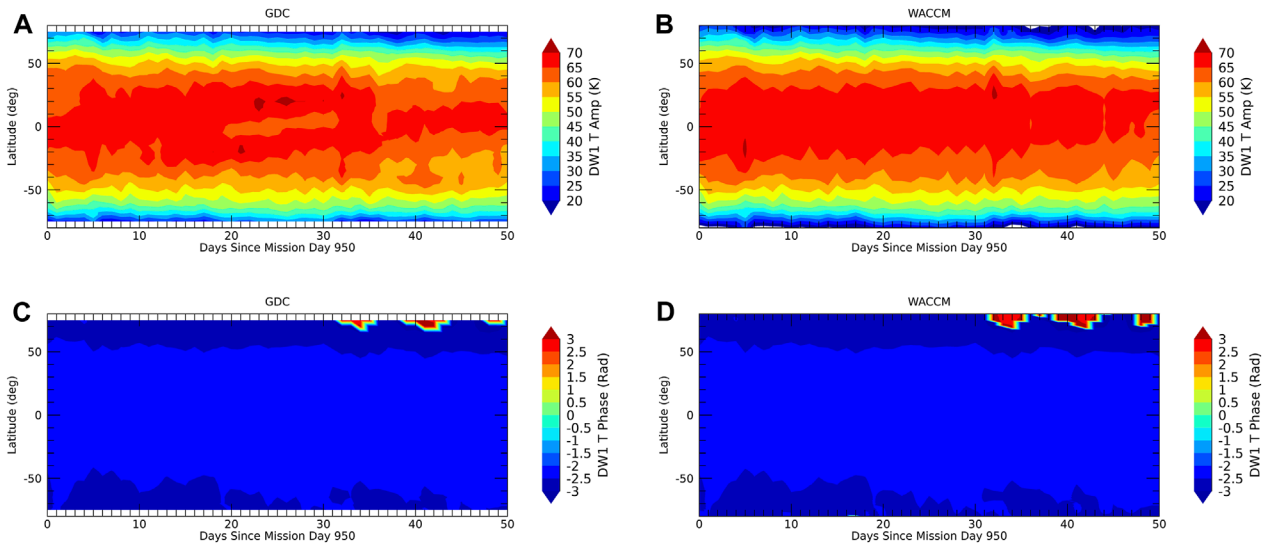

FIGURE 3
DW1. **(A)** GDC OSSE temperature amplitudes towards the very end of phase 4. **(B)** Same as **(A)** but from the full SD-WACCM-X model. **(C)** GDC OSSE temperature phases (rad, maximum at 0° longitude). **(D)** Same as **(C)** but from the full SD-WACCM-X model.

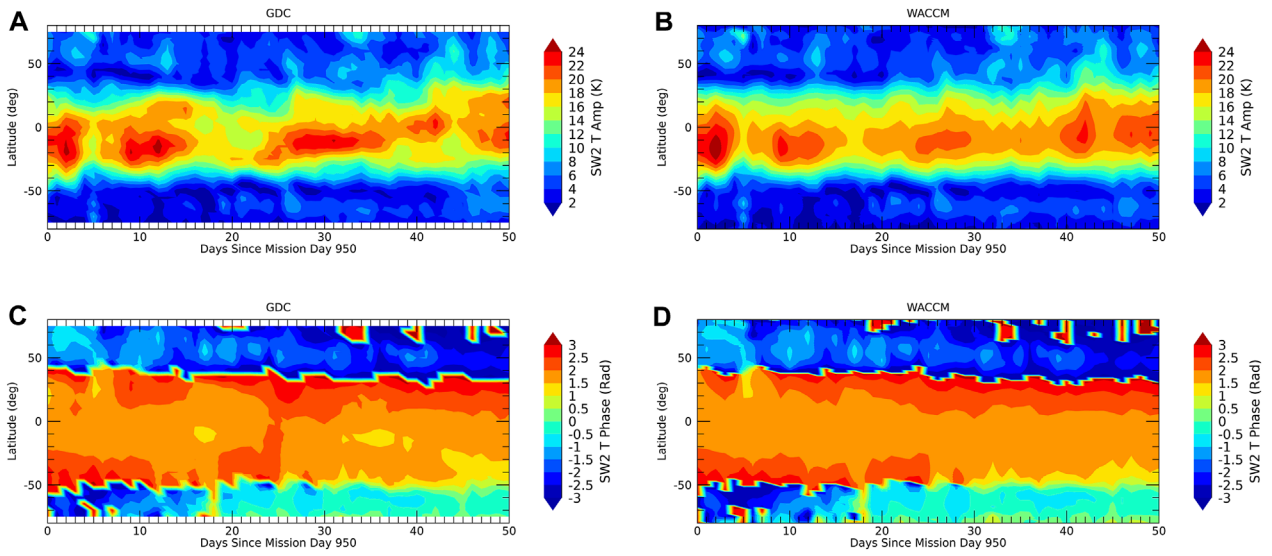

FIGURE 4
Same as Figure 3 but for SW2.

3 GDC, SD-WACCM-X, and OSSE

3.1 GDC

The six GDC satellites (numbered GDC-1 to GDC-6) will be launched into circular orbits at about 380 km and approximately 82° inclination, with some slight variations in the inclination between the different spacecraft to allow for differential orbit precession and thus a spreading of local solar time (LST) over the lifetime of the mission (Figure 1). As already mentioned in section 2, the LST for a given day, orbit node and latitude is almost longitude independent. Neutral temperatures and winds will be measured by the MoSAIC instrument onboard each satellite with a Program Element Appendix (PEA) (NNH17ZDA004O-GDC, 2021) expected performance of accuracy/precision of 20/10 m/s (winds) and 10/2{%} (temperature), and a cadence of 3 s. Further details of the MoSAIC instrument are beyond the scope of this paper and the reader is referred to future literature once the specifics of the instrument have been made public. The GDC ephemeris files (revision C) provided by NASA (GDC Ephemeris, 2022) assume a first mission day of 31 July 2028 and an end of mission on 30 April 2031, for a total of 1,003 days every 30 s "Mission day" is defined as day of science operations (starting with GDC phase 1) and excludes the approximately 3 months of commissioning after launch.

GDC has four phases for its science operations with phase 1 marking the beginning of full science operations. In phase 1, the orbital planes of the six spacecraft (and hence their LST of measurement) are close together, followed by phases 2, 3, and 4 with a more or less linear increase in LST separation. See Figure 1 for a high level summary of LST *versus* latitude toward the beginning and the end of the mission, and the evolution of LST over time, with the LST of the spacecraft ascending orbit nodes distributed over 12 h towards the end of the mission. Along with the descending orbit nodes, full LST coverage is achieved every day over most parts of phase 4. The GDC phases are further subdivided depending on where the spacecraft are placed on each orbit relative to each other, to optimize coverage for the local, regional, and global science objectives. The relative placement of the spacecraft on each orbit does not matter for the tides (but is accounted for in the OSSE) and the reader is referred to the NASA documentation (GDC Ephemeris, 2022) for further details. Figure 2A exemplifies the typical single day coverage of one GDC spacecraft, here shown as sampled SD-WACCM-X zonal winds. The equatorial LST coverage of the six spacecraft for the 40 days following mission day 950 towards the very end of phase 4 is shown in Figure 2B. Almost full local solar time coverage is maintained even in case of a four spacecraft threshold mission that consists of the removal of the GDC-3 and GDC-5 spacecraft (NNH17ZDA004O-GDC, 2021).

3.2 SD-WACCM-X

The Whole Atmosphere Community Climate Model with thermosphere-ionosphere eXtension (WACCM-X) is a whole atmosphere model extending from the surface to the upper thermosphere ($4.1*10^{-10}$ hPa, 500–700 km depending on solar activity) (Liu et al., 2018). The horizontal resolution is $1.9° \times 2.5°$ (lat × lon). The vertical resolution is variable, and is 0.25 scale heights above 0.96 hPa, with a finer resolution at lower altitudes. The 'Specific-Dynamics' or SD-WACCM-X version nudges MERRA-2 data up to 60 km (Smith et al., 2017). The ionosphere and thermosphere processes are largely adopted from TIEGCM. Solar and geomagnetic forcing are parameterized by F10.7 cm and either Kp or solar wind parameters. In the following, we use 1-hourly model output for the year 2009.

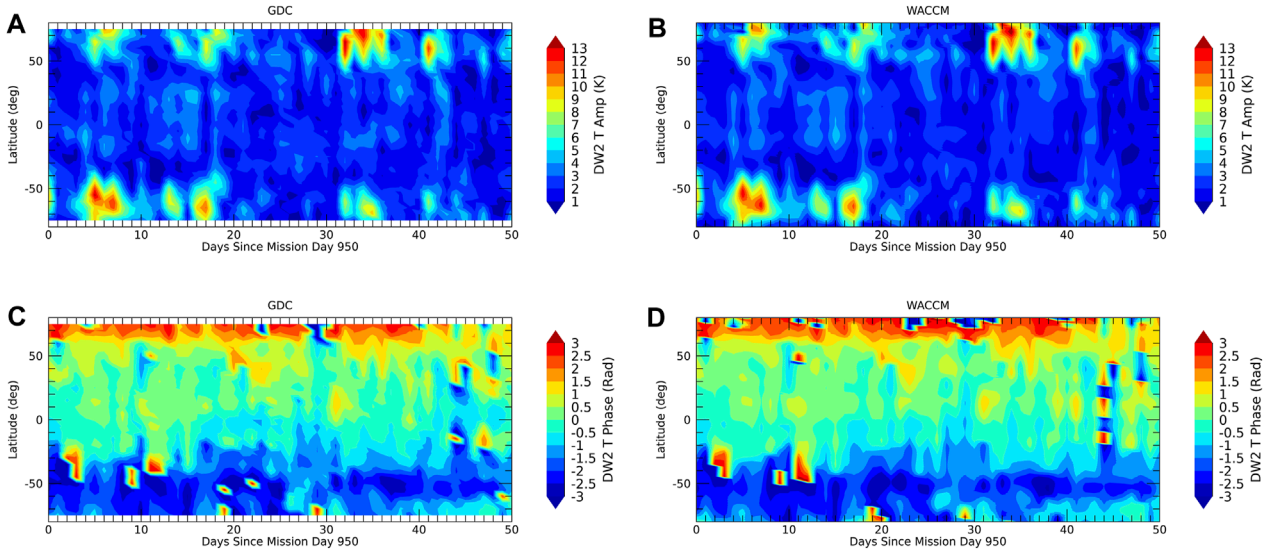

FIGURE 5
Same as Figure 3 but for DW2.

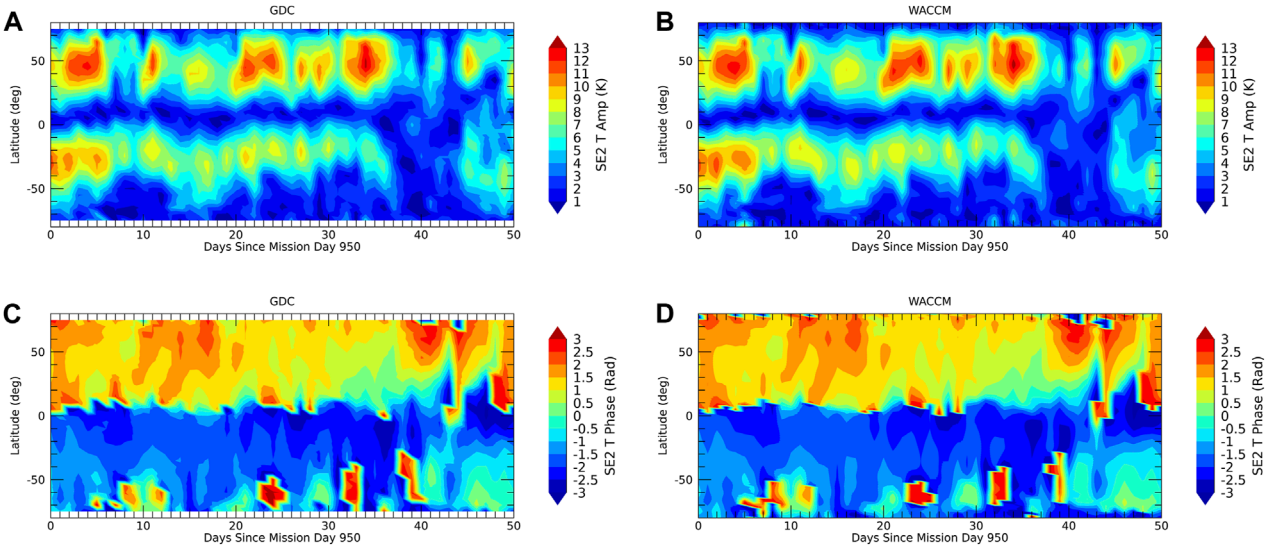

FIGURE 6
Same as Figure 3 but for SE2.

3.3 OSSE

The Observational Simulation System Experiment (OSSE) can be thought of as "flying the GDC spacecraft through the model," followed by a tidal diagnostic approach that would be applied in the same way once real data are available. The same 2009 SD-WACCM-X simulation was used throughout the OSSE. For example, 31 December 2029 in the ephemeris file would use 31 December 2009 from the model, and 1 January 2030 would use 1 January 2009; and so on.

"Flying the GDC spacecraft through the model" is a two step process and essentially a linear interpolation. First, the vertical pressure coordinate in the model is replaced by the daily mean, global mean geopotential height. Second, the longitude, latitude and altitude of each spacecraft is read from the ephemeris files (provided every 30 s) and the model temperature, zonal wind and meridional wind (T, u, v) at the model height closest to the spacecraft altitude are linearly interpolated in longitude, latitude and time, resulting in daily maps of GDC-sampled SD-WACCM-X such as exemplified in Figure 2A for GDC-1. Note that the anticipated T, u, v data from GDC will have a factor of 10 more data along the orbit track if their cadence is 3 s as prescribed by the PEA (NNH17ZDA004O-GDC, 2021). This, however, does not impact the results of our study because the 30 s sampling used reflects the approximate model

resolution and because of the global scale (1,000 s of km) of the tides.

The tidal diagnostic is also a two step process, composed of mapping T, u, v from the combined six spacecraft on a regular longitude × latitude × local solar time grid (5° × 5° × 1h) each day, followed by two-dimensional Fourier diagnostic to obtain the tidal amplitudes and phases as function of period, propagation direction and zonal wavenumber. First, the daily data of each spacecraft, separately for ascending and descending orbit nodes, are combined into ±2.5° latitude bins every 5°, sorted in longitude and then brought on a regular 5° longitude grid through harmonic regression (zonal wavenumber 0–6). When repeated for all six spacecraft, this results in regularly gridded (longitude and latitude) T, u, v fields at 12 different (but at irregular intervals) local solar times. Then, harmonic regression in local solar time (mean, diurnal, semidiurnal, terdiurnal, quaterdiurnal) is applied and one obtains T, u, v on a regular longitude × latitude × local solar time grid (5° × 5° × 1h). Second, the tidal spectrum at each latitude is easily obtained through standard 2D (local solar time, longitude) Fourier fitting.

The most critical part in our OSSE is the local solar time separation of the six GDC spacecraft because of the need for full (24 h) LST coverage to perform the 2D Fourier fitting. If the LSTs of the six spacecraft are well separated (i.e., Figure 2B), the harmonic regression in LST will work well. However, if the LSTs are not well separated, i.e., in the earlier parts of the mission (Figure 1), the regression will not work well and the resulting spectra will be aliased. The quality of the OSSE results, and thus the GDC ability to resolve the tidal weather of the thermosphere, can easily be assessed by comparing with the amplitudes and phases from the full model (the "truth"), which are straightforwardly computed using 2D Fourier analysis.

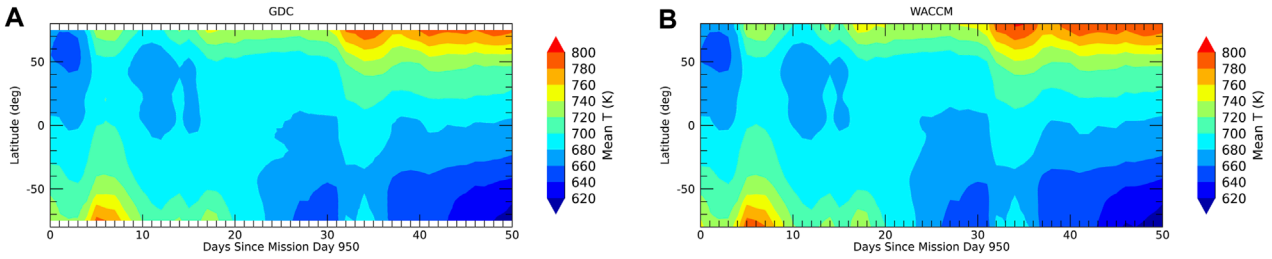

FIGURE 7
Same as Figure 3 but for the mean and without phases.

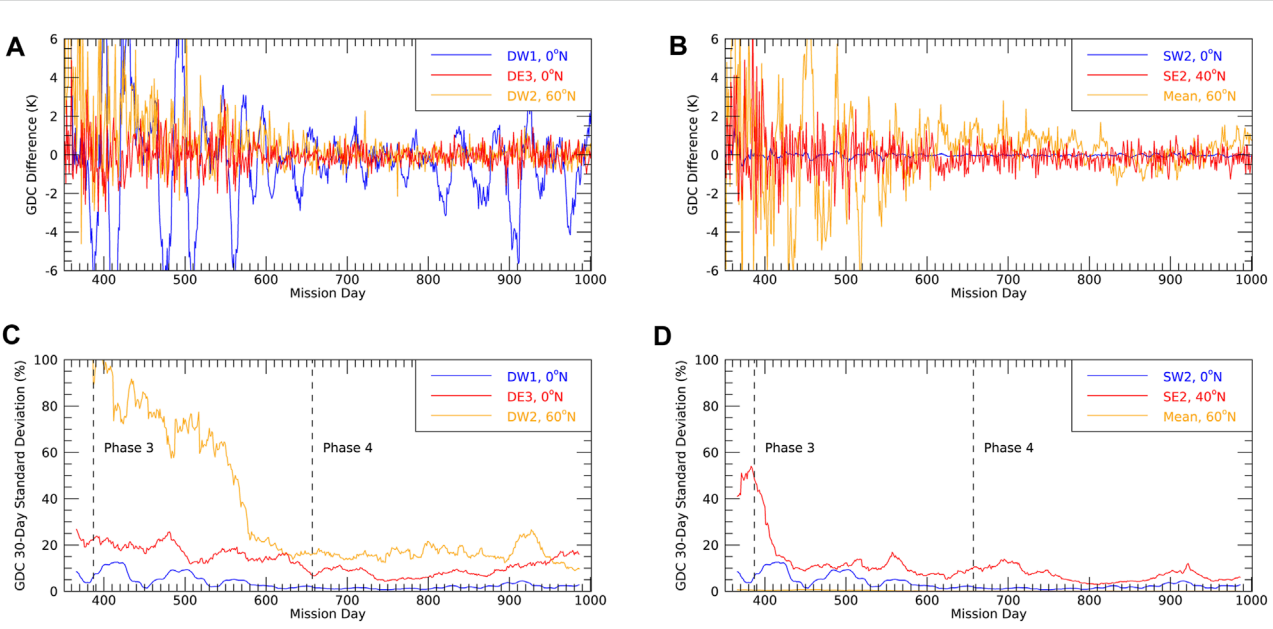

FIGURE 8
Tidal weather recovery during phases 3 and 4. **(A)** Difference between GDC and SD-WACCM-X amplitudes at peak latitudes in Kelvin: DW1, DE3, DW2. **(B)** As in **(A)** but for SW2, SE2, mean. **(C)** 30-day running mean standard deviation of **(A)** relative to the 30-day running mean SD-WACCM-X amplitude in percent. **(D)** As in **(C)** but for SW2, SE2, mean.

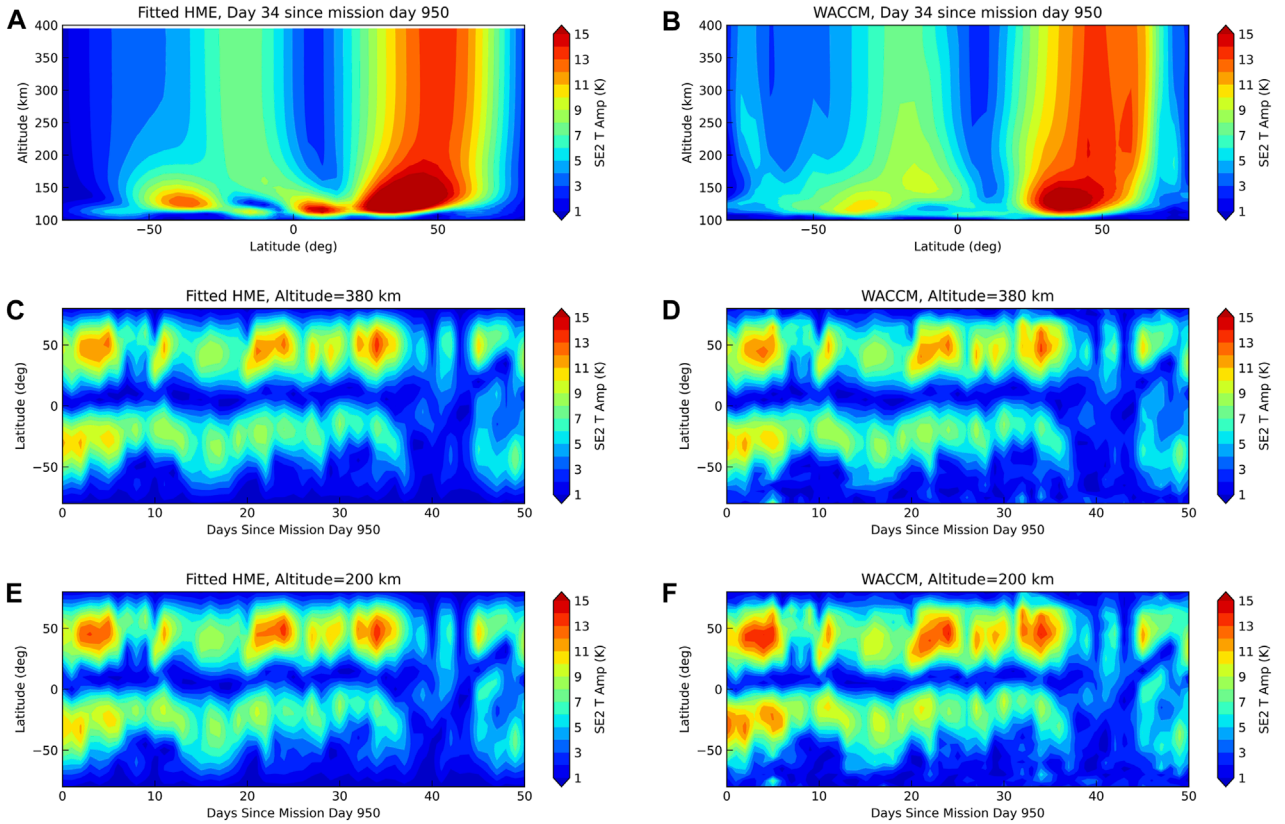

FIGURE 9
SE2. **(A)** Fitted HME amplitude for day 34 (since mission day 950). **(B)** As in **(A)** but from the full SD-WACCM-X model. **(C)** Fitted HME amplitude evolution at 380 km. **(D)** As in **(C)** but from the full SD-WACCM-X model. **(E)** Fitted HME amplitude evolution at 200 km. **(F)** As in **(E)** but from the full SD-WACCM-X model.

4 Results

In the following, we focus on temperature and a subset of two migrating (DW1, SW2) and two nonmigrating (DW2, SE2) tidal components and the mean. Results for other tidal temperature components above the noise level and representative zonal and meridional wind tides can be found in the Supplementary Material. DW2 and SW2 are the two biggest tides, while SE2 largely originates from tropospheric weather (Oberheide et al., 2011b), and DW2 is, according to theory, *in situ* forced in the high latitude thermosphere above 200 km through ion drag (Jones et al., 2013).

4.1 End of phase 4

The maximum LST spread is achieved towards the end of phase 4. Figures 3–7 show the evolution of amplitudes and phases from the OSSE (left column) *versus* the model "truth" (right column). Agreement is within one color scale and full recovery of the tidal weather at all latitudes and the mean can be achieved. A similar level of agreement is found for the wind tides and the other tidal components shown in the supplement.

4.2 Early phase 3 to end of phase 4

To study the impact of decreasing local solar time separation between the spacecraft, it is sufficient to study the differences between the OSSE and the "truth" at peak latitudes. This is shown in Figure 8 for DW2, DE3, DW2, SW2, SE2, and the mean for differences in Kelvin, and the 30-day running mean standard deviation of the differences relative to the 30-day running mean SD-WACCM-X amplitude in percent. In phase 4, differences are well within 1 K, with the exception of DW1 which can reach up to 4 K. However, the migrating tides DW1 and SW2 can be recovered within 5{%} during phase 4 and within 10{%} during phase 3 (including the early phase 3). The two eastward propagating DE3 and SE2 components can be recovered within 10–15{%} between the middle of phase 3 to the end of the mission. In early phase 3, the quality of the recovery rapidly decreases. DW2 is recovered within 20{%} during phase 4 and the last 2 months of phase 3 but not in earlier phases. The recovery of the mean is possible through phases 3 and 4, albeit with a somewhat larger error in the first half of phase 3. As a general finding, tidal recovery after mission day 600 (late phase 3) works well with increasing errors before that time with the specifics of the latter depending on the tidal component. Tidal diagnostics in phases 1 and 2 are not feasible on a day-to-day basis although combining several days/weeks of data might help to obtain tidal

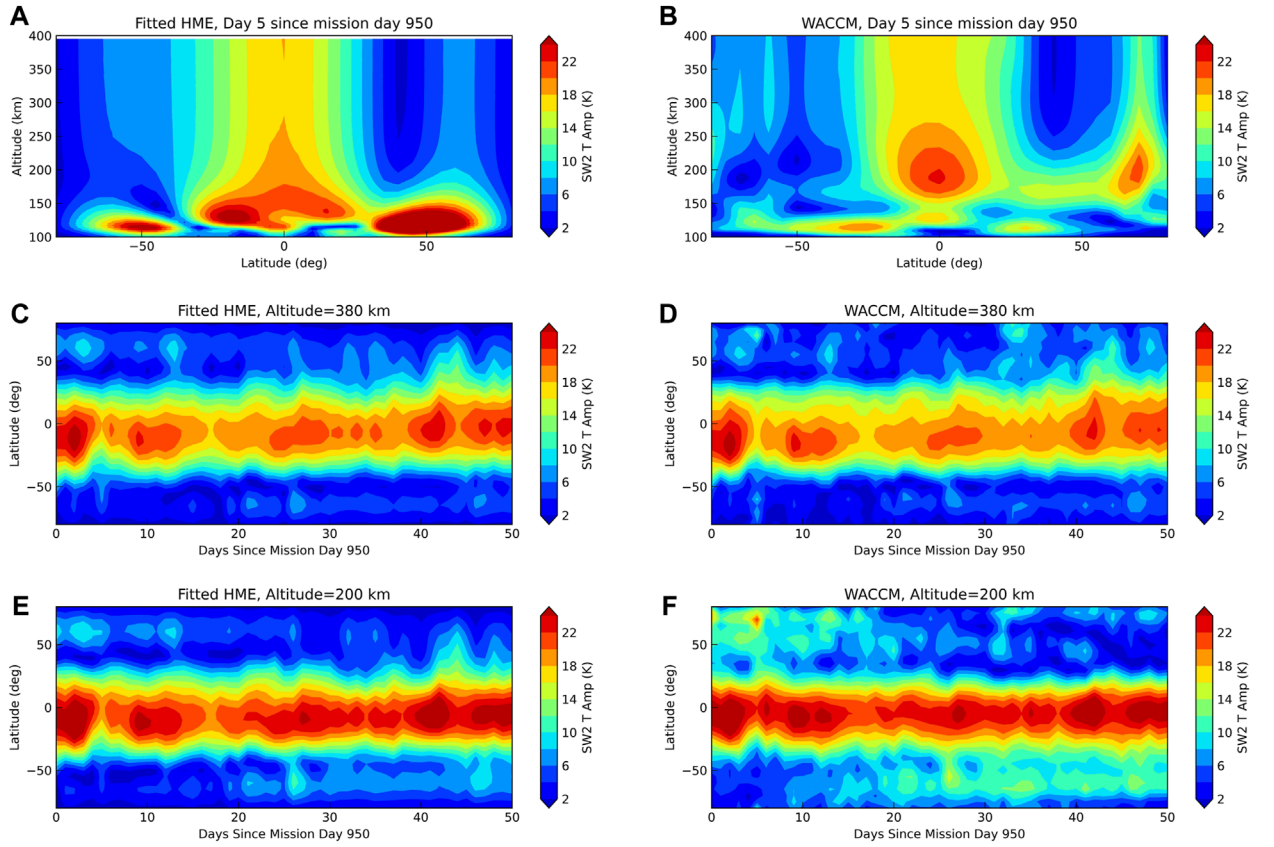

FIGURE 10
As Figure 9 but for the SW2 component.

definitions on time scales shorter than the orbit precession period. This is, however, beyond the scope of the current study.

5 Hough mode extension fits

Hough Mode Extensions (HME, Lindzen et al. (1977)) are modifications of the classical tidal theory to describe the latitude/altitude variation of upward propagating tides by accounting for dissipative processes that make the tidal equation inseparable. HMEs are computed using a linear tidal model and can be thought of as forming a complex vector space onto which tidal amplitudes and phases are projected by fitting the HMEs to observed tides in a given latitude/altitude range. The HMEs then provide the tidal amplitudes and phases at all latitudes and all altitudes, even those that have not been observed. The approach has been extensively used in the past to study upward propagation of tides from TIMED and ICON observations (Oberheide and Forbes, 2008; Oberheide et al., 2011a; Kumari and Oberheide, 2020; Forbes et al., 2022), and validated with CHAMP (Forbes et al., 2009; Häusler et al., 2013), HRDI and WINDII (Lieberman et al., 2013) and ground-based observations (Yuan et al., 2014). On the other hand, differences between *in situ* observations around 400 km with HME fit results to TIMED tidal temperatures and winds in the mesosphere/lower thermosphere were used to predict the existence of tidal sources in the thermosphere (Oberheide et al., 2009), i.e., through ion drag, that have by now been reproduced in dedicated general circulation model simulations (Jones Jr. et al., 2013).

In general, one can use HMEs to connect the *in situ* GDC observations with the tides in the 100–200 km height region of the atmosphere targeted by the DYNAMIC mission put forward in the 2013 Decadal Survey (National Research Council, 2013). As of this day, NASA plans to launch DYNAMIC at the same time as GDC, to do concurrent measurements (NNH23ZDA0190, 2023). HME fits to GDC will thus allow one to downward extend tides to 200 km and compare with DYNAMIC tides: a structurally good agreement would indicate that no thermospheric sources between 200–380 km exist and conclusively connect upward propagating tides from mostly tropospheric/stratospheric sources to GDC. If larger differences exist, they would indicate the presence of thermospheric sources, an important result on its own. To test this approach, we perform a number of HME fits to 380 km tides for GDC mission phase 4 utilizing the HMEs described by Forbes and Zhang. (2022) for solar minimum conditions (F10.7 cm = 75 sfu). For simplicity, the fits are performed on the SD-WACCM-X full model temperature tides, which is sufficient because of the close agreement between the GDC OSSE and the full model tides.

To exemplify the approach, Figure 9 shows an example for SE2, a tidal component with no known sources in the thermosphere that largely originates from latent heat release in deep convective systems in the tropical troposphere. HME fits to SE2 from TIMED observations have been shown to agree well with CHAMP *in situ* tidal diagnostics (Oberheide et al., 2011b). The fit results in the left column use the first six HMEs for SE2 (Forbes and Zhang, 2022), for F10.7 cm = 75 sfu, fitted between ±65° latitude and at 380 km altitude. To demonstrate the height structure, panel a) shows a day when the amplitudes were particularly large. The comparison with the full SD-WACCM-X amplitudes in panel c) indicates that the HME approach reproduces the "truth" fairly well down to approximately 200 km where the notional Decadal Survey DYNAMIC mission (National Research Council, 2013) would measure. This is also reflected in the good agreement between the HME and full model time evolutions at 380 km and 200 km, shown in panels c) to f). Larger differences start to emerge below 200 km due to the presence of higher order (shorter vertical wavelength) modes that dissipate more quickly when propagating upward: the latter cannot be accurately captured when fitting to 380 km altitude. There is also a high southern latitude amplitude maximum in the full model output that is not captured by the HMEs, indicating the presence of some *in situ* tidal forcing processes in the thermosphere, possibly related to ion drag. Overall, HMEs will be able to connect GDC and DYNAMIC tidal diagnostics for components that have no thermospheric sources, such as SE2, DE3 (not shown) and others, and close the 200–380 km measurement gap between the two missions.

A more complicated case is shown in Figure 10 for the SW2 component. SW2 in the thermosphere comes partly from upward propagation from the lower atmosphere and partly from *in situ* solar forcing with significantly different relative contributions at different altitudes due to forcing and dissipation (Forbes et al., 2011). As such, large differences between the HME fits and the full model exist below 200 km and also at higher latitudes between 200–380 km. Altitude-varying *in situ* forcing is not well-captured by HME fits, particularly at high latitudes, i.e., the 70°N amplitude maximum around 200 km in the full model is missing in the HME fits, with HMEs producing generally much to large signals below 150 km. Only low latitude *in situ* forced SW2 projects well into the HMEs in the 200–380 km range, producing the good temporal evolution agreement at low latitudes shown in panels c) to f). Consequently, the low latitude SW2 measured by DYNAMIC could be interpreted as the main source of the low latitude SW2 from GDC. Differences at high latitudes, however, persist and the HMEs would help to isolate the parts of the SW2 where additional tidal forcing and/or changes in tidal dissipation occur in the altitude range between DYNAMIC and GDC. This is particularly interesting for components such as DW2 and D0 that are hypothesized to come from high latitude ion drag forcing above 200 km (Jones Jr. et al., 2013) or from gravity wave dissipation around 200 km at low to mid latitudes (Vadas et al., 2014). DW2 and D0 from HME fits at 380 km (not shown) are quite small while the full model (Figure 5) shows large amplitudes at high latitudes (*in situ* forcing through GW dissipation is not fully captured in SD-WACCM-X due to the model resolution).

6 Conclusion

Our Observational Simulation System Experiment using SD-WACCM-X and the predicted GDC orbits demonstrate that GDC can resolve the day-to-day tidal variability (mean, diurnal and semidiurnal, migrating and nonmigrating) at orbit height in mission phase 4 and throughout most parts of mission phase 3. The quality of high latitude tidal recovery starts to deteriorate before mission day 600, about 2 months before the end of phase 3. We note that the mean state of thermosphere can also be recovered on a day-to-day basis throughout phases 3 and 4, including the mean meridional circulation. A more detailed study that includes Monte-Carlo simulations of measurement errors has to await final specifications of the instruments onboard GDC. However, the 3 s cadence of the wind and temperature measurements on each spacecraft and the 5° latitude binning used in the tidal diagnostics would produce approximately 3,600 data points each day for a given latitude bin that enter the further gridding on longitude and local solar time (15 orbits, six spacecraft, ascending and descending orbit nodes, 20 data points along track within 5°; $15 \times 6 \times 2 \times 20 = 3,600$). It is thus reasonable to predict that a targeted (NNH17ZDA004O-GDC, 2021) wind precision of 10 m/s and temperature precision of 2{%} (20 K) will result in amplitude errors that are well within 1 m/s (1 K). Our Hough Mode Extension fitting of relevant tidal components to GDC further supports the concept to fly GDC and DYNAMIC concurrently, with DYNAMIC capable of informing GDC about the sources of the observed tidal variability and for the capability of the combined measurements to further test current theories of *in situ* tidal forcing and dissipation.

Data availability statement

The datasets presented in this study can be found in online repositories. The names of the repository/repositories and accession number(s) can be found in the article/Supplementary Material.

Author contributions

JO: Conceptualization, Data curation, Formal Analysis, Funding acquisition, Investigation, Methodology, Project administration, Resources, Software, Supervision, Validation, Visualization, Writing–original draft, Writing–review and editing. SG: Formal Analysis, Investigation, Software, Visualization, Writing–review and editing. MN: Formal Analysis, Investigation, Software, Visualization, Writing–review and editing.

Funding

The author(s) declare financial support was received for the research, authorship, and/or publication of this article. JO and SG were partly supported through NASA grant 80NSSC22-K0018.

Conflict of interest

The authors declare that the research was conducted in the absence of any commercial or financial relationships that could be construed as a potential conflict of interest.

Publisher's note

All claims expressed in this article are solely those of the authors and do not necessarily represent those of their affiliated organizations, or those of the publisher, the editors and the reviewers. Any product that may be evaluated in this article, or claim that may be made by its manufacturer, is not guaranteed or endorsed by the publisher.

Supplementary material

The Supplementary Material for this article can be found online at: https://www.frontiersin.org/articles/10.3389/fspas.2023.1282261/full#supplementary-material

References

Cullens, C. Y., Immel, T. J., Triplett, C. C., Wu, Y. J., England, S. L., Forbes, J. M., et al. (2020). Sensitivity study for icon tidal analysis. *Prog. Earth Planet. Sci.* 7, 18. doi:10.1186/s40645-020-00330-6

Forbes, J. M., Bruinsma, S. L., Zhang, X., and Oberheide, J. (2009). Surface-exosphere coupling due to thermal tides. *Geophys. Res. Lett.* 36, 38748. doi:10.1029/2009GL038748

Forbes, J. M., Oberheide, J., Zhang, X., Cullens, C., Englert, C. R., Harding, B. J., et al. (2022). Vertical coupling by solar semidiurnal tides in the thermosphere from icon/mighti measurements. *J. Geophys. Res. Space Phys.* 127, e2022JA030288. doi:10.1029/2022ja030288

Forbes, J. M., Zhang, X., Bruinsma, S., and Oberheide, J. (2011). Sun-synchronous thermal tides in exosphere temperature from CHAMP and GRACE accelerometer measurements. *J. Geophys. Res. Space Phys.* 116, 16855. doi:10.1029/2011JA016855

Forbes, J. M., and Zhang, X. (2022). Hough mode Extensions (HMEs) and solar tide behavior in the dissipative thermosphere. *J. Geophys. Res. Space Phys.* 127, e2022JA030962. doi:10.1029/2022ja030962

Forbes, J. M., Zhang, X., Palo, S., Russell, J., Mertens, C. J., and Mlynczak, M. (2008). Tidal variability in the ionospheric dynamo region. *J. Geophys. Res. Space Phys.* 113, 12737. doi:10.1029/2007JA012737

Gasperini, F., Liu, H., and McInerney, J. (2020). Preliminary evidence of madden-julian oscillation effects on ultrafast tropical waves in the thermosphere. *J. Geophys. Res. Space Phys.* 125, e2019JA027649. doi:10.1029/2019ja027649

GDC Ephemeris (2022). GDC design reference mission predicted ephemeris description, revision C. Tech. rep., NASA.

GDC Science and Technology Definition (2021). Final report. Tech. rep., NASA.

Hagan, M. E., Roble, R. G., and Hackney, J. (2001). Migrating thermospheric tides. *J. Geophys. Res. Space Phys.* 106, 12739–12752. doi:10.1029/2000JA000344

Häusler, K., and Lühr, H. (2009). Nonmigrating tidal signals in the upper thermospheric zonal wind at equatorial latitudes as observed by CHAMP. *Ann. Geophys.* 27, 2643–2652. doi:10.5194/angeo-27-2643-2009

Häusler, K., Oberheide, J., Lühr, H., and Koppmann, R. (2013). "The geospace response to nonmigrating tides," in *Climate and weather of the sun-earth system (CAWSES): Highlights from a priority Program*. Editor F. J. Lübken (Dordrecht, Heidelberg, New York, London: Springer Atmospheric Sciences), 481–550. doi:10.1007/978-94-007-4348-9

Immel, T. J., Sagawa, E., England, S. L., Henderson, S. B., Hagan, M. E., Mende, S. B., et al. (2006). Control of equatorial ionospheric morphology by atmospheric tides. *Geophys. Res. Lett.* 33, L15108. doi:10.1029/2006GL026161

Jarvis, M. J. (2001). Bridging the atmospheric divide. *Science* 293, 2218–2219. doi:10.1126/science.1064467

Jones, M., Jr., Forbes, J. M., Hagan, M. E., and Maute, A. (2013). Non-migrating tides in the ionosphere-thermosphere: *in situ* versus tropospheric sources. *J. Geophys. Res. Space Phys.* 118, 2438–2451. doi:10.1002/jgra.50257

Kumari, K., and Oberheide, J. (2020). QBO, ENSO, and solar cycle effects in short-term nonmigrating tidal variability on planetary wave timescales from saber—an information-theoretic approach. *J. Geophys. Res. Atmos.* 125, e2019JD031910. doi:10.1029/2019jd031910

Lieberman, R. S., Oberheide, J., and Talaat, E. R. (2013). Nonmigrating diurnal tides observed in global thermospheric winds. *J. Geophys. Res. Space Phys.* 118, 7384–7397. doi:10.1002/2013JA018975

Lindzen, R. S., Hong, S. S., and Forbes, J. (1977). *Semidiurnal Hough mode extensions in the thermosphere and their application*. Washington, DC: Naval Research Laboratory.

Liu, H. L., Bardeen, C. G., Foster, B. T., Lauritzen, P., Liu, J., Lu, G., et al. (2018). Development and validation of the whole atmosphere community climate model with thermosphere and ionosphere extension (WACCM-X 2.0). *J. Adv. Model. Earth Syst.* 10, 381–402. doi:10.1002/2017MS001232

National Research Council (2013). *Solar and space Physics: A science for a technological society*. Washington, DC: The National Academies Press. doi:10.17226/13060

Newell, P. T., Sotirelis, T., and Wing, S. (2009). Diffuse, monoenergetic, and broadband aurora: the global precipitation budget. *J. Geophys. Res. Space Phys.* 114, 14326. doi:10.1029/2009JA014326

Nielsen, J. N., Goodwin, K., Frederick, R., and Mersman, W. A. (1958). Three-dimensional orbits of Earth satellites including effects of Earth oblateness and atmospheric rotation. Tech. Rep. MEMO 12-4-58A, NASA.

NNH17ZDA004O-GDC (2021). Program element Appendix (PEA) P geospace Dynamics constellation PEA-P. Tech. rep., NASA.

NNH23ZDA0190 (2023). Solar terrestrial probes Program dynamical neutral atmosphere-ionosphere coupling (DYNAMIC) AO. Tech. rep., NASA.

Oberheide, J. (2022). Day-to-Day variability of the semidiurnal tide in the F-region ionosphere during the january 2021 SSW from COSMIC-2 and ICON. *Geophys. Res. Lett.* 49, e2022GL100369. doi:10.1029/2022gl100369

Oberheide, J., Forbes, J. M., Häusler, K., Wu, Q., and Bruinsma, S. L. (2009). Tropospheric tides from 80 to 400 km: propagation, interannual variability, and solar cycle effects. *J. Geophys. Res. Atmos.* 114, 12388. doi:10.1029/2009JD012388

Oberheide, J., and Forbes, J. M. (2008). Tidal propagation of deep tropical cloud signatures into the thermosphere from TIMED observations. *Geophys. Res. Lett.* 35, L04816. doi:10.1029/2007GL032397

Oberheide, J., Forbes, J. M., Zhang, X., and Bruinsma, S. L. (2011a). Climatology of upward propagating diurnal and semidiurnal tides in the thermosphere. *J. Geophys. Res. Space Phys.* 116, 16784. doi:10.1029/2011JA016784

Oberheide, J., Forbes, J. M., Zhang, X., and Bruinsma, S. L. (2011b). Wave-driven variability in the ionosphere-thermosphere-mesosphere system from timed observations: what contributes to the "wave 4". *J. Geophys. Res. Space Phys.* 116, 15911. doi:10.1029/2010JA015911

Oberheide, J., Hagan, M. E., Roble, R. G., and Offermann, D. (2002). Sources of nonmigrating tides in the tropical middle atmosphere. *J. Geophys. Res. Atmos.* 107, ACL 6-1–ACL 6-14. doi:10.1029/2002JD002220

Oberheide, J., Hagan, M., Richmond, A., and Forbes, J. (2015a). "Dynamical meteorology – atmospheric tides," in *Encyclopedia of atmospheric sciences*. Editors G. R. North, J. Pyle, and F. Zhang (Oxford: Academic Press), 287–297. doi:10.1016/B978-0-12-382225-3.00409-6

Oberheide, J., Shihokawa, K., Gurubaran, S., Ward, W. E., Fujiwara, H., Kosch, M. J., et al. (2015b). The geospace response to variable inputs from the lower atmosphere: A review of the progress made by task group 4 of CAWSES-II. *Prog. Earth Planet. Sci.* 2, 2. doi:10.1186/s40645-014-0031-4

Oberheide, J., Wu, Q., Killeen, T. L., Hagan, M. E., and Roble, R. G. (2006). Diurnal nonmigrating tides from TIMED Doppler interferometer wind data: monthly climatologies and seasonal variations. *J. Geophys. Res. Space Phys.* 111, A10S03. doi:10.1029/2005JA011491

Pedatella, N. M., Richmond, A. D., Maute, A., and Liu, H. L. (2016). Impact of semidiurnal tidal variability during SSWs on the mean state of the ionosphere and thermosphere. *J. Geophys. Res. Space Phys.* 121, 8077–8088. doi:10.1002/2016JA022910

Richmond, A., and Lu, G. (2000). Upper-atmospheric effects of magnetic storms: A brief tutorial. *J. Atmos. Solar-Terrestrial Phys.* 62, 1115–1127. doi:10.1016/S1364-6826(00)00094-8

Sassi, F., McCormack, J. P., and McDonald, S. E. (2019). Whole atmosphere coupling on intraseasonal and interseasonal time scales: A potential source of increased predictive capability. *Radio Sci.* 54, 913–933. doi:10.1029/2019RS006847

Smith, A. K., Pedatella, N. M., Marsh, D. R., and Matsuo, T. (2017). On the dynamical control of the mesosphere–lower thermosphere by the lower and middle atmosphere. *J. Atmos. Sci.* 74, 933–947. doi:10.1175/JAS-D-16-0226.1

Vadas, S. L., Liu, H. L., and Lieberman, R. S. (2014). Numerical modeling of the global changes to the thermosphere and ionosphere from the dissipation of gravity waves from deep convection. *J. Geophys. Res. Space Phys.* 119, 7762–7793. doi:10.1002/2014JA020280

Yuan, T., She, C. Y., Oberheide, J., and Krueger, D. A. (2014). Vertical tidal wind climatology from full-diurnal-cycle temperature and Na density lidar observations at Ft. Collins, CO (41°N, 105°W). *J. Geophys. Res. Atmos.* 119, 4600–4615. doi:10.1002/2013JD020338

frontiers | Frontiers in Astronomy and Space Sciences

TYPE Methods
PUBLISHED 29 February 2024
DOI 10.3389/fspas.2024.1231840

OPEN ACCESS

EDITED BY
David Knudsen,
University of Calgary, Canada

REVIEWED BY
Joachim Vogt,
Jacobs University Bremen, Germany
Malcolm Dunlop,
Science and Technology Facilities Council, United Kingdom

*CORRESPONDENCE
Hassanali Akbari,
hassanali.akbari@nasa.gov

RECEIVED 31 May 2023
ACCEPTED 09 February 2024
PUBLISHED 29 February 2024

CITATION
Akbari H, Rowland D, Coleman A, Buynovskiy A and Thayer J (2024), Gradient calculation techniques for multi-point ionosphere/thermosphere measurements from GDC.
Front. Astron. Space Sci. 11:1231840.
doi: 10.3389/fspas.2024.1231840

Gradient calculation techniques for multi-point ionosphere/thermosphere measurements from GDC

Hassanali Akbari[1,2]*, Douglas Rowland[1], Austin Coleman[3], Anton Buynovskiy[3] and Jeffrey Thayer[3,4]

[1]NASA Goddard Space Flight Center, Greenbelt, MD, United States, [2]Department of Physics, Catholic University of America, Washington, DC, United States, [3]Ann and H. J. Smead Aerospace Engineering Sciences, University of Colorado at Boulder, Boulder, CO, United States, [4]Space Weather Technology, Research, and Education Center (SWx TREC), University of Colorado at Boulder, Boulder, CO, United States

The upcoming Geospace Dynamics Constellation (GDC) mission aims to investigate dynamic processes active in Earth's upper atmosphere and their local, regional, and global characteristics. Achieving this goal will involve resolving and distinguishing spatial and temporal variability of ionospheric and thermospheric (IT) structures in a quantitative manner. This, in turn, calls for the development of sophisticated algorithms that are optimal in combining information from multiple *in-situ* platforms. This manuscript introduces an implementation of the least-squares gradient calculation approach previously developed by J. De Keyser with the focus of its application to the GDC mission. This approach robustly calculates spatial and temporal gradients of IT parameters from *in-situ* measurements from multiple spacecraft that form a flexible constellation. The previous work by De Keyser, originally developed for analysis of Cluster data, focused on 3-D Cartesian geometry, while the current work extends the approach to spherical geometry suitable for missions in Low Earth Orbit (LEO). The algorithm automatically provides error bars for the estimated gradients as well as the scales over which the gradients are expected to be constant. We evaluate the performance of the software on outputs of high-resolution global ionospheric/thermospheric simulations. It is shown that the software will be a powerful tool to explore GDC's ability to answer science questions that require gradient calculations. The code can also be employed in support of Observing System Simulation Experiments to evaluate suitability of various constellation geometries and assess the impact of measurement sensitivities on addressing GDC's science objectives.

KEYWORDS

multi-point *in-situ* measurements, satellite constellation, Geospace Dynamics Constellation (GDC), ionospheric dynamics, gradient calculation

1 Introduction

Determining and disentangling the spatial and temporal variability of a field from sparse *in-situ* measurements is a long-standing problem in space physics. Addressing this problem, along with providing broader coverage in measurements, is commonly raised

as a major justification for designing and launching multi-platform satellite missions (e.g., Escoubet et al., 2001; Burch et al., 2016). The Geospace Dynamics Constellation (GDC) mission, that is currently in the formulation phase, is one of the latest of such missions. GDC's goal is to significantly increase our understanding of how the coupled ionosphere-thermosphere (IT) system reacts to external energy input from the Sun and the magnetosphere. Specifically, it will aim to address the following overarching science goals: 1) Understand how the high latitude ionosphere-thermosphere system responds to variable solar wind/magnetosphere forcing; and 2) Understand how internal processes in the global ionosphere-thermosphere system redistribute mass, momentum, and energy. Successfully addressing these objectives is challenging as the IT system is known to vary locally and globally, with scale-sizes ranging from sub-kilometer to thousands of kilometers and on timescales that range from seconds or minutes to hours or days.

Completely characterizing the dynamics of the IT system and determining the physical processes underlying its variability would ideally require a very dense (in altitude, longitude, and latitude) sampling of various plasma and neutral parameters over a wide range of spatial and temporal scales. As a practical matter, the number of spacecraft in such a constellation that can provide accurate comprehensive measurements is finite—for example, GDC will fly six spacecraft. This immediately introduces important challenges. On the one hand, relatively fine spatial and temporal resolutions, when compared to the physical scales, are required to properly capture the behavior of the system locally; and on the other hand, the global nature of the GDC mission would require a broad coverage of observing platforms in local time and longitude. Satisfying both conditions with a limited number of *in-situ* platforms can only be possible via a flexible constellation that evolves to observe the full range of relevant scales. A flexible satellite architecture, in turn, requires sophisticated algorithms that are themselves flexible and optimal in combining observations from individual points.

In this paper, we introduce a software package 'LSGC-AS-LEO 1.0', which is an implementation of the least-squares gradient calculation approach developed by De Keyser et al. (2007) and De Keyser (2008) with the focus on its application for the GDC mission. The gradients characterize variations of the field in space and time, helping to disentangle the spatial and temporal ambiguity in measurements in an inherently quantitative manner. In the following section, we briefly describe GDC's expected constellation architecture and its evolution during different phases of the mission. In Section 3, we present a brief overview of the gradient calculation technique. In Section 4, we evaluate the performance of the technique on simulated GDC measurements of the IT parameters, and discuss its significance for the GDC mission. Section 5 includes the summary, conclusions, and a description of the future steps.

2 GDC constellation architecture

GDC's constellation consists of six spacecraft in a circular orbit at the altitude of 350–400 km with an inclination of about 81–82°. At a given time, the spacecraft will sample plasma and neutral parameters on a relatively thin spherical shell, the altitude of which will slowly vary between 350 and 400 km due to orbital drag and subsequent reboosts via onboard propulsion. The satellites will be deployed via a single launch vehicle with small inclination differences. Over time, differential precession will lead to separation of the six orbital planes in local time, leading to an ever-widening instantaneous longitudinal coverage. Different phases of the mission can then be defined that are appropriate for the investigation of the IT processes over local (referred to as phase 1, with scale-lengths < 2 h in local time), regional (phase 2, with cross-track (primarily longitudinal at the equator) scale-lengths between 2 and 9 LT hours), and global (phase 3, towards the end of the mission with scale-lengths > 9 h in local time) scales.

Figure 1 shows the expected evolution of the satellite configuration during days 92 (top), 190 (middle), and 764 (bottom) from the start of the science phase of the mission. These correspond to the beginning of phase 1, end of phase 1, and sometime in the late regional/early global phase of the mission, respectively. Shown in each panel are instantaneous positions of all six spacecraft (shown as colored circles) for a scenario where the constellation is in the northern hemisphere and traveling northward. Thin vertical and horizontal lines show 5-degree increments in longitude and latitude. Dashed lines in colors matching each circle show the near future trajectory of that GDC spacecraft, demonstrating near-latitudinal direction around the equator, and predominantly longitudinal direction above ~75° geographic latitude. Figure 1 clearly demonstrates the dynamic nature of the constellation in space and time and the complexities that one may face when attempting to determine spatio-temporal variability of the ionosphere and thermosphere from GDC measurements. For example, the hexagonal shape of the constellation seen in Panel A1 near the equator may be suitable to simultaneously determine local variability in latitude, longitude, and time; while at higher latitudes (see Panel A6), where the trajectories of the individual spacecraft cross, little information can be obtained in latitude due to lack of broad latitudinal sampling. In this case, the form of the constellation which briefly approximates a 'pearls on a string' configuration would be better suited for investigating variability in longitude and time.

The variability in constellation architecture along with the need to monitor its ability to estimate gradients in both latitude and longitude at a given time motivated the creation of a quantity called the 'quality' (or 'Q') value and the associated 'Q-vector'. The Q-value can be defined as $Q_{val} = 1 + \frac{A}{A_e}$, in which A is the area of the spherical polygon formed by the satellite constellation at a given time after being projected onto a 2D surface using a Mercator projection, and A_e is the area of an equilateral polygon with the same perimeter. A maximum value of $Q_{val} = 2$ indicates a 'regularly' distributed constellation in space, while lower values imply that the sampling constellation is anisotropically distributed, which may result in less-than-optimal spread simultaneously in both latitude and longitude—for example, a minimum value of $Q_{val} = 1$ denotes a set of co-linear spacecraft. Since Q_{val} does not provide information on the 'direction' of anisotropy associated with a constellation, it can be complimented by a second quantity $Q_{dir} = \tan^{-1}\left(\frac{\Delta\text{lat}}{\Delta\text{long}}\right)$ which quantifies the direction of the skewness. Q_{dir} is defined as the inverse tangent of the ratio of the constellation's latitudinal spread to its longitudinal spread. For a constellation consisting of at least two spacecraft Q_{dir} is always defined and ranges from 0° to 90°. Q_{dir} values of 0° and 90° indicate that the constellation only samples along the longitudinal and latitudinal directions, respectively. Using both

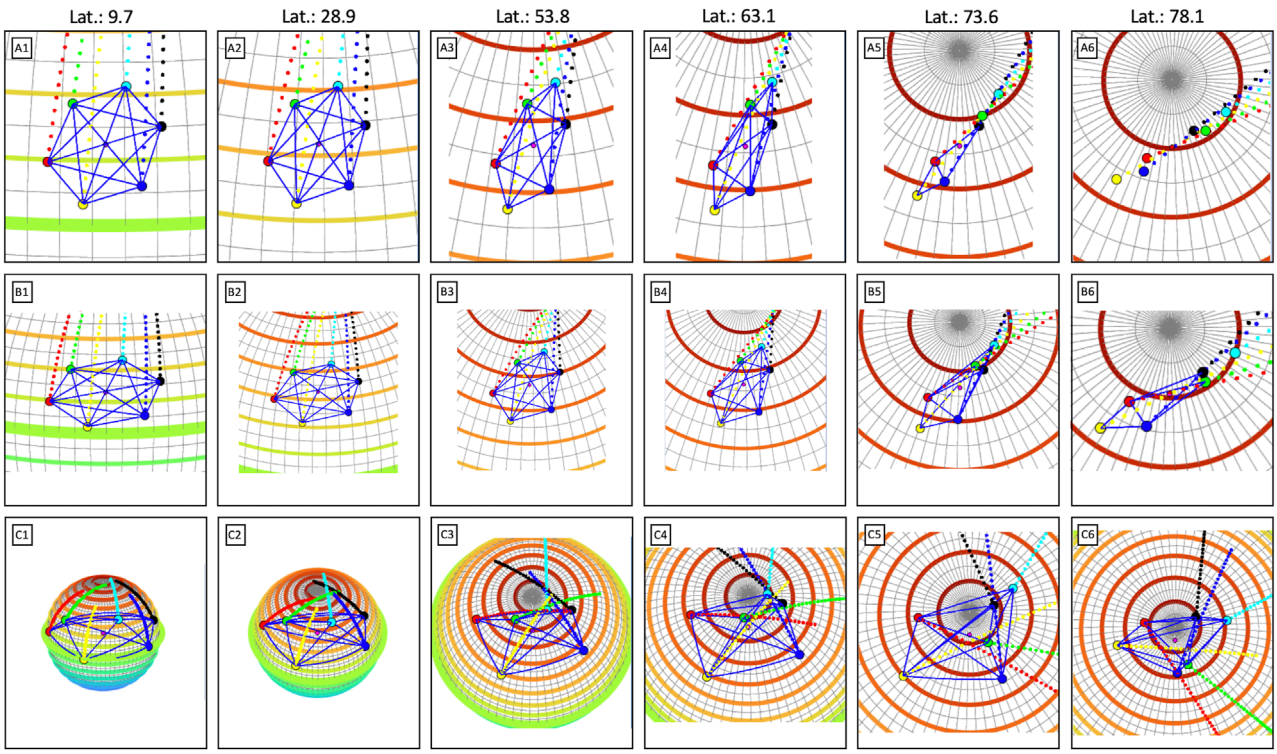

FIGURE 1
The expected evolution of the satellite configuration for days 92 (top), 190 (middle), and 764 (bottom) from the start of the science phase of the mission. Instantaneous positions of all six spacecraft (shown as colored circles) and the near future trajectory of that GDC spacecraft (shown as dashed lines in matching colors) are shown. Thin vertical and horizontal lines show 5-degree increments in longitude and latitude. The GDC ephemeris used here are from the 'Revision C' version, released in May 2022. The latest ephemeris is publicly available at https://ccmc.gsfc.nasa.gov/mission-planning/GDC/.

components of the Q-vector, i,e., Q_{val} and Q_{dir}, one can interpret the evolution of the constellation over time and its ability to provide sampling in different spatial directions. In the context of this work, Q-vector is used to monitor the constellation architecture and quantify the latitudinal and longitudinal spread of the spacecraft array. This provides insight into the array's ability to compute gradients in those specific directions. It is worth mentioning that a more mathematically rigorous approach to evaluate the effective constellation dimensions based on error considerations and through investigation of the eigenvalues and eigenvectors of the spacecraft position tensor was developed by Vogt et al. (2020). There, in the general 3-dimensional case, the eigenvalues give insight into the amount of variance in each of the principal directions of the spacecraft array, which are captured through the eigenvectors. The eigenvectors with the largest eigenvalues correspond to the directions most heavily sampled by the spacecraft array. The approach developed by Vogt et al. (2020) provides a more formal description of the constellation and will be adopted in the updated versions of the LSGC-AS-LEO. It is important to note that the assumption that an isotropic constellation is ideal for sampling is only strictly true when the gradients are isotropic. When this is not the case, ideal constellation configurations may have Q-values appropriate to the ratio of longitudinal to latitudinal gradients in the measured fields.

Figure 2 shows the trajectories of GDC spacecraft as a function of latitude and longitude (top panels) for three orbits corresponding to the beginnings of phases 1a (left), 2a (middle), and 3a (right). For each case, the magnitude and angle of the Q-vector is shown in the bottom panels as the constellation evolves in time. The drop in the magnitude of the Q-value is evident at high latitudes, consistent with the anisotropic constellation shape shown in Figure 1. As will be shown in Section 4, the ability of LSGC-AS-LEO 1.0 to fully determine both longitudinal and latitudinal variability in the IT system using GDC measurements may reduce for smaller Q-values below a threshold. Q-vector can, thus, be used as an empirical measure to optimize constellation design and provide an indication of where robust gradient calculations may be achievable.

Figure 1 and Figure 2 demonstrate the variability of GDC's constellation geometry as a function of latitude and mission phase. As a result of this variability, any approach that would aim to utilize multi-point measurements from GDC to characterize the dynamics of the IT system would ideally need to be general and flexible, without many assumptions on the sampling scheme, and at the same time ensure the optimum utilization of data from all satellites. Further, a successful approach would need to take into account spatial and temporal scales over which ionospheric and thermospheric structures evolve relative to the size of the constellation, and provide measures of reliability for its calculations. The least-squares gradient calculation with adaptive scaling (LSGC-AS method, De Keyser et al., 2007; De Keyser, 2008) is such an approach and is briefly described in the next section.

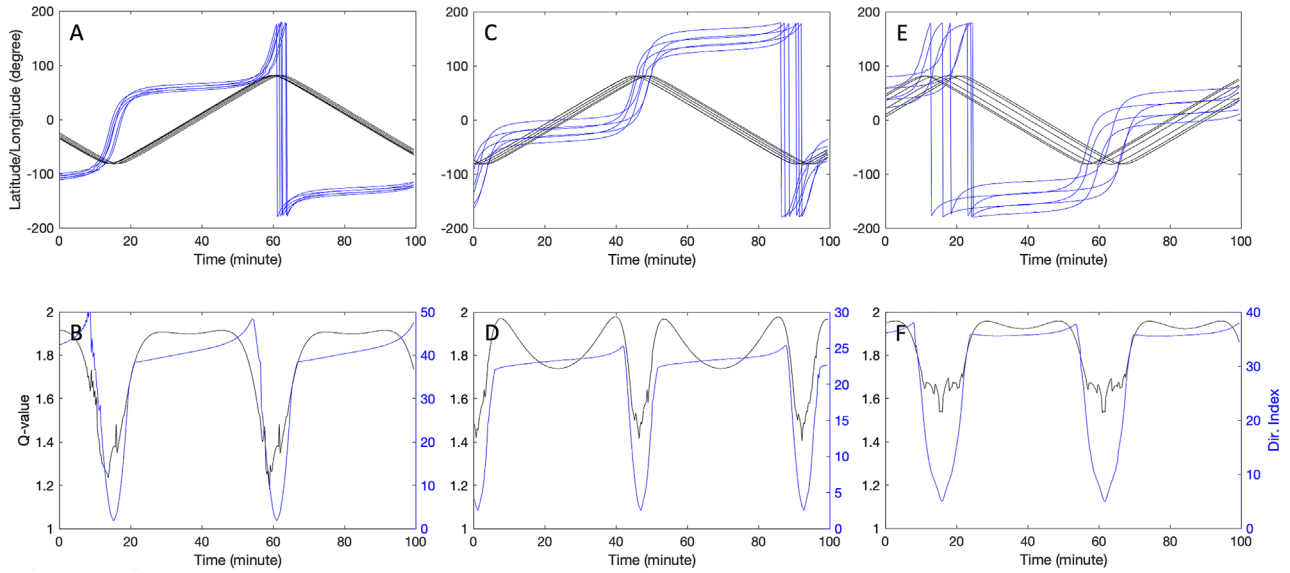

FIGURE 2
(A,C,E) GDC constellation latitudes (black) and longitudes (blue) for three orbits on the first days of phases 1a, 2a, and 3a, respectively. **(B,D,E)** parameters of the Q-vector for the orbits shown above.

3 Least-squares gradient calculation with adaptive scaling—overview

Optimally combining information from multi-point measurements to quantitatively determine the local dynamics of a measured field often proves to be challenging. This topic has been the subject of many previous works that have let to the development of different algorithms and tools (e.g., Chanteur, 1998; Harvey, 1998; Paschmann and Daly, 1998; Robert et al., 1998; Amm and Viljanen, 1999; Darrouzet et al., 2006; Denton et al., 2020; Dunlop and Lühr, 2020; Fiori, 2020; Torbert et al., 2020; Bard and Dorelli, 2021; Denton et al., 2022; Zhu et al., 2022). Mathematically, the problem can be translated to one involving calculation of gradients—once the gradients of a field are known with respect to space and time its local dynamics can be better understood. Precise calculations of gradients, however, are generally difficult due to a number of reasons, the most important of which are the presence of noise in data and under-sampled variations of the measured field in between the spacecraft. On the one hand, for estimated gradients to be accurate the spacecraft should form a close constellation to fully resolve variations of the sampled field; and on the other hand, for the estimated values to be meaningful the difference between sampled values should be large compared to the measurement noise—a condition which may require a larger separation between the spacecraft. It is balancing between the two constraints that necessitates the use of sophisticated algorithms for computing gradients. In addition, the spatial scales of variation in the sampled field may vary depending on the process being studied, or the location of the measurements, which introduces further complexity and a need for the algorithm to assess its own performance. Given the complexity of the task of calculating gradients, a significant amount of effort has gone towards developing appropriate algorithms and tools. Much of these works have been performed in support of the European Space Agency's (ESA) three-satellite Swarm mission (Friis-Christensen et al., 2008). For example, Ritter and Lühr (2006) and Ritter et al. (2013) were among the first to address current estimation in the context of a multi-satellite LEO mission. Vogt et al. (2009) and Vogt et al. (2013) provided tools and an error analysis framework for planar spacecraft configurations with special consideration of physical constraints to estimate out-of-plane contributions. Shen et al. (2012a) and Shen et al. (2012b) developed magnetic gradient estimation techniques with particular relevance to measurements in an environment dominated by field-aligned currents. Blagau and Vogt (2019) and Blagau and Vogt (2023) implemented relevant techniques in a publicly available software package based on Python. Of the mentioned works, those described by Shen et al. (2012b) and Vogt et al. (2020) stand out as general approaches to gradient calculations, both of which utilize some adaptation of the position tensor of the satellite configuration to compute spatial gradients in a least-squares sense. Very recently, in the past 2 years, a series of publications have emerged that introduce further methods to combine information from multiple *in-situ* platforms. These recent works include: Shen and Dunlop (2023), who introduced a geometrical method based on integral theorems to compute the linear gradients; Shen et al. (2021b), who developed a novel method to estimating both the linear and quadratic gradients using multiple spacecraft observation; Shen et al. (2021a) and Dunlop et al. (2021), who developed algorithms specifically for determining nonlinear magnetic gradients; and the book by Dunlop et al. (2021), that covers a number of multispacecraft techniques that were initially developed to analyze data from the Cluster mission (Escoubet et al., 2001). As mentioned before, here we implement the approach described by De Keyser et al. (2007) and De Keyser (2008), which is also a general gradient calculation tool, developed based on the concept of homogeneity scales in orthogonal directions, including in time. The method aims to ensure

the utilization of the maximum amount of information available and allows to assess the meaningfulness of the result by providing error estimates. This approach is briefly described below. The description only includes high-level intuition behind the approach and is not meant as a substitute for the detailed mathematical description in De Keyser et al. (2007) and De Keyser (2008).

Imagine a scalar field f sampled at $\boldsymbol{x}_i = [x_i; y_i; z_i; t_i]$, for $i = 1 \cdots N$, by an arbitrary number of satellites that form a flexible constellation. At a given time, f may be approximated in the vicinity of point $\boldsymbol{x}_0 = [x_0; y_0; z_0; t_0]$ via its Taylor series expansion: $f(\boldsymbol{x}) = f_0 + \Delta\boldsymbol{x}^\top \boldsymbol{g}_0 + \frac{1}{2}\Delta\boldsymbol{x}^\top \boldsymbol{H}_0 \Delta\boldsymbol{x} + \cdots$, where $\Delta\boldsymbol{x} = \boldsymbol{x} - \boldsymbol{x}_0$, $f_0 = f(\boldsymbol{x}_0)$, and $\boldsymbol{g}_0$ and $\boldsymbol{H}_0$ are the gradient and the Hessian at $\boldsymbol{x}_0$. If we assume that f changes linearly in the vicinity of $\boldsymbol{x}_0$, thus ignoring the terms of the Taylor expansion beyond the second term, we will reach the approximate equation $f_a(\boldsymbol{x}) = f_0 + \Delta\boldsymbol{x}^\top \boldsymbol{g}_0$. Using $f_a(\boldsymbol{x})$, the field can be estimated at each sampled point $\boldsymbol{x}_i$. Defining residues $r_i = f_a(\boldsymbol{x}_i) - f_i$ at each point, where f_i is the measured value at $\boldsymbol{x}_i$, and requiring the residues to be zero leads to a system of N equations for the five unknowns—with the unknowns being f_0 and four partial derivatives with respect to x, y, z, and t. Often times, gradients would be determined using data obtained in a period of time over which the field is continuously sampled via multiple *in-situ* platforms. For example, calculating gradients in a 30-s window where six satellites obtain measurements every three seconds would lead to 60 samples. In this case, $N = 60 \gg 5$ and the system is highly over determined. One may proceed to select five samples to uniquely determine the unknowns, but the outcome would likely depend on the choices as well as the amount of measurement noise in the system. Furthermore, this approach would not utilize the maximum amount of information available, nor would it provide any insight on the reliability of the estimates. A more suitable approach would be to utilize all the available data points and solve the over-determined system of equations using a weighted least squares minimization procedure. In this case, equation i, corresponding to sample $\boldsymbol{x}_i$, would be weighted inversely proportional to the total amount of error that is expected for the residue r_i. Once the weights are known, the system of equations may be written in the matrix form and solved via singular value decomposition. Error bars on the estimated gradients as well as the ill-conditioning degree of the problem can be obtained from an appropriate covariance matrix and singular values—for more details see De Keyser et al. (2007) and De Keyser (2008).

Much of the complexity of the weighted least-squares minimization approach mentioned above is condensed in obtaining proper weights, w_i, for each equation based on the expected error associated with the corresponding measured sample. The choice of weights as inverse of the total error is to ensure that measurements with large errors do not contribute much to the solution of the over-determined system of equations. In the absence of systematic errors, the error δf_i in estimating sample f_i via $f_a(\boldsymbol{x}_i)$ may include three components. One is the 'measurement error' which is the inherent uncertainty associated with the instrument that provides f_i; the second is the 'approximation error' (or the 'curvature error') which exists due to ignoring the nonlinear terms of the Taylor expansion in $f_a(\boldsymbol{x})$; and the third is the error due to the potential presence of unresolved small-scale fluctuations in the field. As described by De Keyser et al. (2007), the small-scale fluctuation error can be incorporated in a statistical sense, the measurement error can be modeled via a zero-mean random noise with a standard deviation specific to each instrument, and the approximation error can be modeled as $\delta f_a \propto f_c |\boldsymbol{x}_i - \boldsymbol{x}_0|_\beta^2$, where f_c is a constant related to the Hessian of the field at point $\boldsymbol{x}_0$ and $|\boldsymbol{x}_i - \boldsymbol{x}_0|_\beta$ is the normalized distance between the measurement point $\boldsymbol{x}_i$ and $\boldsymbol{x}_0$—such that the modeled approximation error increases with distance according to the third term of the Taylor expansion. Here, $|\boldsymbol{x}_i - \boldsymbol{x}_0|_\beta$ is not merely the physical distance between two points but one that takes into account the linearity of the field along each orthogonal direction (including time). In other words, $|\boldsymbol{x}_i - \boldsymbol{x}_0|_\beta = \sqrt{\Sigma_k \frac{(x_{ik} - x_{0k})^2}{l_k^2}}$, where the subscript k indicates components along an orthogonal direction k and l_k are homogeneity lengths defined below. To clarify this point imagine a scenario where the field f varies linearly over short scales along axis x but over large scales along axis y. In this case, approximating f along y via the first two terms of the Taylor expansion remains accurate over a longer distance when compared to x. As such, the approximation error would need to be scaled differently along x and y. To incorporate such conditions, De Keyser et al. (2007) utilized the concepts of 'homogeneity lengths'. The homogeneity length, l_k, is the distance along a direction k over which a linear variation is a good approximation to a function f. The geometry defined by all homogeneity lengths thus defines the homogeneity space in which the field can be reasonably modeled by the first two terms of the Taylor expansion with relatively small errors in the form of $\delta f_a \propto f_c |\boldsymbol{x}_i - \boldsymbol{x}_0|_\beta^2$. Beyond the homogeneity space the modeled approximation error would need to increased rapidly with $|\boldsymbol{x}_i - \boldsymbol{x}_0|_\beta$ such that the information obtained outside of the homogeneity space contribute minimally to the computation of gradients. This can be enforced via incorporating an additional term in the approximation error.

The homogeneity scales are properties of the physical field and change in space and time. In general, their determination is not trivial. De Keyser (2008) has described an approach to automatically determine the homogeneity scales from the measurements. The approach could be best understood by noting that solving the weighted over-determined system is equivalent to minimizing χ^2, where:

$$\chi^2 = \frac{1}{N} \sum_{i=1}^{N} \frac{r_i^2}{\delta f_i^2}$$

However, one should bear in mind that in the presence of measurement and curvature errors, minimizing χ^2 may not be a suitable target. In reality, the computations should be performed such that the residue r_i reflect the correct amount of expected error associated with the calculations at point x_i. In other words, one would reasonably expect that $r_i^2 \approx \delta f_i^2$, and thus $\chi^2 \approx 1$ (for $N \gg 1$). In fact, it can be shown mathematically that under certain assumptions χ^2 follows the χ^2-statistics, under which the most likely value for χ^2 is ~1.

The process of identifying the homogeneity scales, and consequently solving the over-determined system of equations, then starts from a set of initial guesses for the homogeneity scales, followed by the calculation of the total expected error for each measurement point, assigning weights to each equation, computing the gradients, determining χ^2, then updating the homogeneity scales based on the value of χ^2. This cycle may be incorporated in an optimization scheme to allow $\chi^2 \to 1$ after a number of iterations.

Several optimization approaches are introduced in De Keyser (2008). We have currently implemented the 'common rescaling' approach, which will be further discussed in the context of Figure 5. Future work will involve implementing the other approaches developed by De Keyser (2008) and exploring additional ones.

4 Implementation of the least-squares gradient calculation for the GDC mission

Motivated by the upcoming GDC mission, and with the goal of evaluating the ability of the satellite constellation to resolve local dynamics of the IT system, we have implemented the approach in an open-source software LSGC-AS-LEO 1.0, presently written in MATLAB. Despite the immediate focus of the software on GDC, LSGC-AS-LEO 1.0 is implemented in a general form, utilizing many settings that can be adjusted by the user, and as such it maintains the ability to support other missions with minimal updates to few functions. Here, we present and discuss typical outputs of the software on synthetic and simulated fields relevant to the IT system. Evaluating the results using simple synthetic test cases allows to validate the implementation, examine the robustness of the underlying algorithms, and further provides the opportunity to clarify certain important concepts of the algorithm described in Section 3 and in De Keyser et al. (2007) and De Keyser (2008). Additional test cases using realistic global simulations of the IT system along with GDC's proposed ephemeris data further allows showcasing the significance of the software for GDC's future measurements. Because GDC's measurements will occur in a narrow altitude region between 350 and 400 km, our implementation of the LSGC-AS algorithm is tailored to assume spherical coordinates, and to assume zero radial variation, i.e., all measurement points are sampled at the same altitude and all the gradient calculations are performed in the spherical coordinates. Extending this procedure to account for non-zero radial variations is straightforward.

For the first test case, imagine a synthetic thermospheric neutral temperature of the form

$$T_n = 1000 + 200\sin(1.5\theta - 40) + 200\sin(2\phi) + 0.1\left(\frac{t}{100}\right)^{2.1}$$

where θ, ϕ, and t are latitude, longitude, and time in units of degree, degree, and seconds, respectively. T_n is not meant to represent the actual neutral temperature in the thermosphere; instead it serves as a simple function with simultaneous variability in latitude, longitude, and time. Running the software with an appropriate label specifying the synthetic function results in the following actions: GDC's predicted ephemeris data over a predefined period of time are imported and used to sample the synthetic T_n with an adjustable cadence; a predefined level of measurement noise is then introduced to the sampled values; datapoints $[\boldsymbol{x}_i, f_i]$ from all or selected spacecraft gathered within a period of time centered at t_i are then passed onto a routine in order to determine the gradients at point $\boldsymbol{x}_i$. The gradients are calculated at an arbitrary 'evaluation point', which by default is defined at the geometric center of the constellation. An optimization routine is used that adaptively modifies the homogeneity scales such that computations result in an appropriate outcome for χ^2. Various settings that define the details of the computations are specified prior to running the routine. These include the initial guesses for homogeneity scales, f_c, the measurement noise level, available satellites, the phase and time of the GDC mission, the evaluation point, optimization method, measurement cadence, integration time, whether calculations are performed on f or $log(f)$, etc. The final result is an estimate of the value of T_n at the evaluation point, the longitudinal and latitudinal gradients of T_n at the evaluation point, the temporal rate of change of T_n at the evaluation point, and error bars for these quantities, as well as estimates for the homogeneity lengths.

Figure 3 shows the results of the gradient calculations for the synthetic function T_n sampled during the first 100 min of GDC's phase 1a. The input parameters to LSGC-AS-LEO that have been used to produce this and the following plots are summarized in Table 1. In the top panel of Figure 3, T_n, as seen by six individual satellites, are shown with thin black lines. The size of the constellation in phase 1a is small compared to the scales over which T_n varies in space and time, and as a result the six spacecraft measure relatively similar values—i.e., the black lines nearly overlay each other—with the exceptions at the highest latitudes near times 14 and 60 min. Also shown in Panel A are the true (red) and the estimated (blue) values of T_n at the evaluation point, here defined as the center of the constellation. The calculated latitudinal, longitudinal, and temporal gradients along with their expected errors (i.e., their $3-\sigma$ error bars) are shown in Panels B–D in blue. The calculated gradients closely follow the true gradients which are shown in red, with the exceptions at times ~14 and 60 min where $\nabla_{lat} T_n$ briefly deviates from the red curve and its error bars significantly increase. Noting the latitude and longitude of the evaluation point and the components of the Q-vector in Panels E and F, respectively, it becomes clear that the difficulty in determining $\nabla_{lat} T_n$ (the latitudinal vector component of the gradient) around times ~14 and 60 min is due to the shape of the constellation as the spacecraft approach the polar regions. As was shown in Panel A6 of Figure 1, at these times (primarily poleward of 75° geographic latitude in either hemisphere) the constellation spreads along longitude without much coverage in latitude, leading to poorly-constrained estimates for $\nabla_{lat} T_n$. This longitudinal elongation of the constellation is also reflected in Panel G which shows the condition number defined in De Keyser et al. (2007) as $cond = s^2_{min}/s^2_{max}$, where $s_{\min}$ and $s_{\min}$ are the minimum and maximum singular values obtained during the singular value decomposition of the over-determined system of equations. The condition number serves as a general measure of ill-conditioning of the problem and decreases by about an order of magnitude as the constellation elongates at higher latitudes, signaling large errors in parts of the calculations. Finally, the bottom two panels of Figure 3 demonstrate the performance of the implemented common rescaling optimization routine described in De Keyser (2008). The purpose of the optimization routine is to adaptively rescale the initial homogeneity lengths such that χ^2 approaches a predefined value, resulting in refinements to the error estimates as well as an estimate of the scale lengths over which the calculated gradient is expected to be accurate. In this case, in order for the error bars in Panels A–D to represent the $3-\sigma$ errors, optimization works to enforce $\chi^2 \sim 1/9$. Panels H and I show the calculated latitudinal homogeneity length and χ^2, respectively. While the initial homogeneity scales in latitude, longitude, and time has been chosen as $L_{lat} = 60°$, $L_{long} = 160°$, and $L_t = 30$ min, respectively,

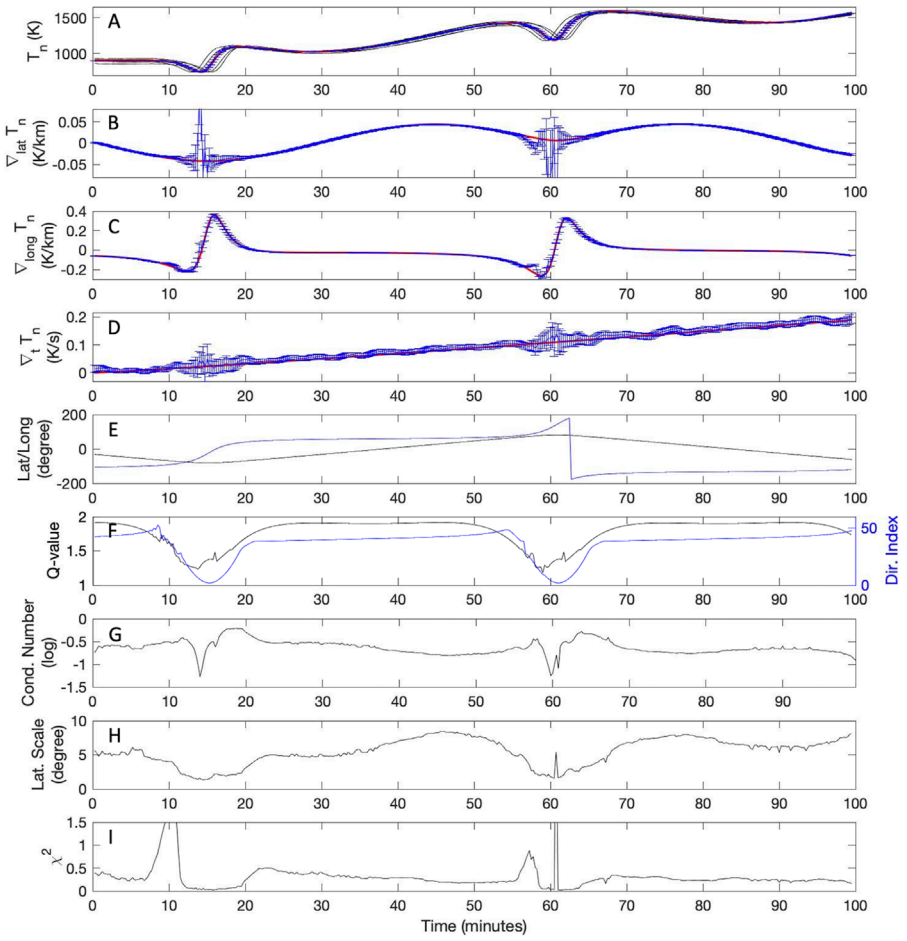

FIGURE 3
From top to bottom: **(A)** function values as observed by individual satellites (thin black lines), true (red), and reconstructed (blue) values of the function at the evaluation point, at the center of the constellation; **(B)** true (red) and estimated (blue) latitudinal gradients at the evaluation point; **(C)** true (red) and estimated (blue) longitudinal gradients at the evaluation point; **(D)** true (red) and the estimated (blue) temporal gradients at the evaluation point; **(E)** latitude (black) and longitude (blue) of the evaluation point; **(F)** components of the Q-vector; **(G)** condition number; **(H)** latitudinal homogeneity length L_{lat}; **(I)** χ^2. Synthetic function is sampled during the first 100 min of phase 1a, and is subjected to a small measurement noise of 0.1%. Other settings include: initial guesses for homogeneity length scales L_{lat}: 60°, L_{long}: 160°, L_t: 1,800 s; maximum 'time window' over which to combine samples MaxT: 2.5 min; Measurement cadence: 15 s. The input parameters to LSGC-AS-LEO that have been used to produce various plots in this paper are summarized in Table 1.

the optimization routine scales all the homogeneity lengths by a common factor that varies between ~7–50 as the constellation moves in space and sample different features of T_n. Most notably, as the constellation approaches the polar region between times 10–20 and 55–65 min the homogeneity scales decrease, consistent with larger variations in $\nabla_{long} T_n$.

It will be insightful to repeat the gradient calculation test described above with slight modifications. In the left panels of Figure 4 we show the results from a similar run in which the measurement error introduced to T_n is now significantly increased from 0.1% to 3% of f_i. This is an important test as GDC will include various particle and field instruments with different levels of measurement accuracy for which the performance of the gradient calculation need to be tested. As can be seen in Panels A–D, an immediate consequence of the elevated noise level is larger errors for the calculated gradients, which are also reflected by the increased error bars. This is not surprising since gradient calculations are highly sensitive to the presence of background noise. Further, it is seen that, unlike in Figure 3B, the incorrect latitudinal gradients between 13–19 and 59–62 min are no longer properly covered by the error bars—this is perhaps due to inaccurate choices of initial homogeneity scales or f_c. Nevertheless, the decreased condition number at these times can still serve as a cautionary flag regarding the accuracy of the results. In the right panels of Figure 4 we show the results from a similar run with yet another modification: the time axis now corresponds to the first 100 min of GDC's phase 2b. In this phase the constellation size (i.e., the average distance between spacecraft) increases. The individual spacecraft now sample different values of T_n with differences that are greater than the 3% background noise level—see Panel J. Consequently, the accuracy of the estimated gradients increases and their error bars significantly drop in Panels K–M. This is due to the reduced noise amplification nature of the gradient operator over longer distances, and applies to cases where the measurement error dominates over the approximation error.

TABLE 1 Input parameters to LSGC-AS to produce each of the example plots shown in Figures 3–9.

Input parameters to LSGC-AS runs	Figure 3	Figure 4 left	Figure 4 right	Figure 6	Figure 7 left	Figure 7 right	Figure 8	Figure 9
Mission phase	1a	1a	2a	1a	2a	2b	1a	2b
Noise level (%)	0.1	3	3	4	4	4	1	2
L_{lat} (degree)	60	60	60	10	10	10	10	50
L_{long} (degree)	160	160	160	50	50	50	20	50
L_t (second)	1800	1800	1800	2,500	2,500	2,500	500	2,500
Cadence (second)	15	15	15	20	20	20	20	20
MaxT (minute)	2.5	2.5	2.5	2	2	2	3	2.5

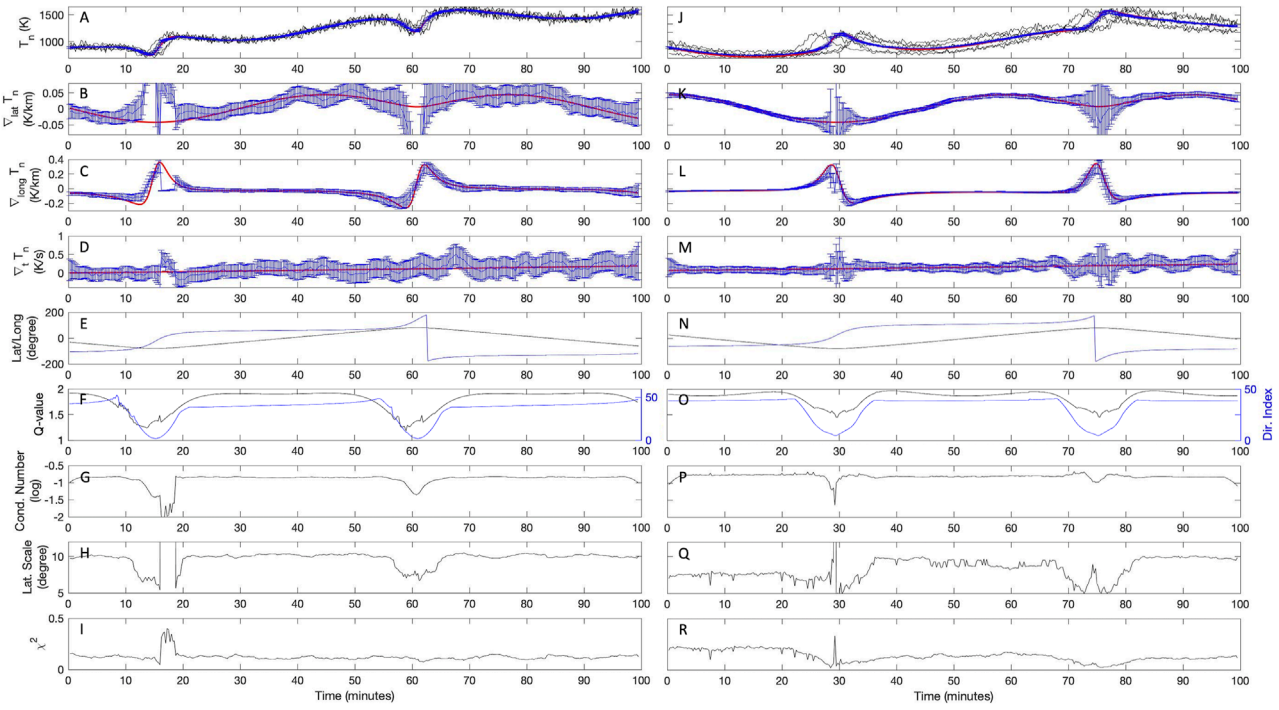

FIGURE 4
In the same format as that in Figure 3, but with increased added measurement noise level of 3%. The left and right panels correspond to the first 100 min of GDC's phases 1a and 2a, respectively.

Before wrapping up the evaluation of the gradient calculation approach on the synthetic field T_n, it would be helpful to revisit the impact of the optimization and the adaptive scaling of the homogeneity lengths from a different prospective. Consider the results shown in Figure 4J–R at the single time t_0 = 74.75 min. Here, the constellation approached the polar regions with the latitude of the evaluation point at 80.1°. At this time, about 120 samples $[\boldsymbol{x}_i, f_i]$, collected by all six spacecraft within 2.5 min from t_0, have been used to calculate the gradients shown in panels K–M. According to Panel H, the optimization has decreased the homogeneity lengths by a common factor of about 7, from the initial scales of L_{lat} = 60°, L_{long} = 160°, and L_t = 30 min. In Figure 5 we show the distribution of the residues $|r_i|$ for each datapoint $\boldsymbol{x}_i$ as a function of the normalized distance $|\boldsymbol{x}_i - \boldsymbol{x}_0|_\beta$. The absolute value of the residues are shown for

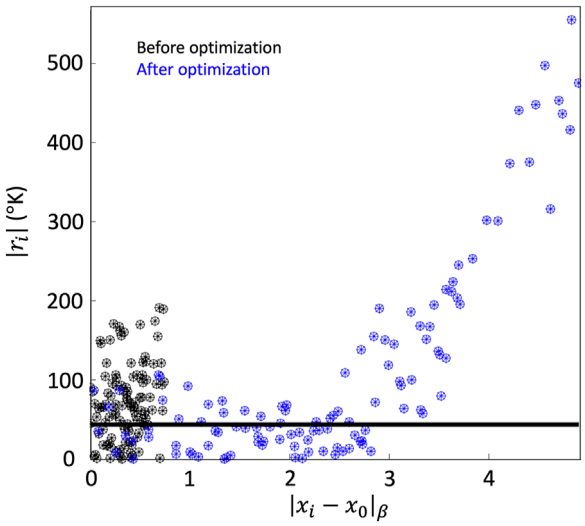

FIGURE 5
Absolute values of the residues as a function of the normalized distance for datapoints used to calculate gradients at time ~75 min (latitude ~80°) for the example shown on the right panels of Figure 4. Optimization results in reducing the homogeneity scales by a factor of ~7. As a result, $|\boldsymbol{x}_i - \boldsymbol{x}_0|_\beta$ increases, updating the weights assigned to each datapoint, and subsequently modifying the calculated ∇_{lat}, ∇_{long}, and ∇_t by −96, 97, −740%, respectively, while altering the distribution of the residues as a function of the normalized distance.

the following two cases: the black datapoints correspond to the case where the least-squares minimization problem is solved without the optimization procedure (thus, only according to the initial homogeneity lengths); whereas the blue datapoints correspond to the case where the optimization has been turned on (thus allowing the homogeneity lengths to be rescaled). For the case of adaptive scaling turned off, the least-squares minimization approach is successful in solving the over-determined system of equations such that the residues are small and on the order of the measurement noise added to f_i (shown by the horizontal black bar). Despite the reasonably small residues, however, we note that the gradients calculated using the initial homogeneity scales do not correctly represent the actual values—in other words, the calculated gradients are legitimate, yet inappropriate, solutions of the over-determined system. With adaptive scaling enabled, the homogeneity scales decrease, $|\boldsymbol{x}_i - \boldsymbol{x}_0|$ increases, and as a result only a fraction of the datapoint that are closest to evaluation point are effectively used to calculate the gradients. The calculated gradients in latitude, longitude, and time are then modified by −96, 97, and −740%, respectively, compared to the previous case which brings them very close to the true gradients. At the same time, we observe that the distribution of $|r_i|$ as a function of the normalized distance $|\boldsymbol{x}_i - \boldsymbol{x}_0|$ follows the following expected form: from the definition of $f_a(\boldsymbol{x})$ in Section 3, one would generally expect $|r_i| = |f_a(\boldsymbol{x}_i) - f_i| \approx \delta f_{m,i} + f_c|\boldsymbol{x}_i - \boldsymbol{x}_0|^2_\beta$, where $\delta f_{m,i}$ is the measurement error at point $\boldsymbol{x}_i$. Accordingly, in Figure 5 for smaller values of $|\boldsymbol{x}_i - \boldsymbol{x}_0|$ the residues are small, on the order of the measurement noise, while at larger distances $|r_i|$ increases rapidly due to larger approximation errors.

With the implementation of the least-squares gradient calculation approach validated via the synthetic example, we now turn to more realistic scenarios to test the ability of the software to determine the local dynamic of the ionosphere and thermosphere using GDC measurements. Figure 6A shows a frozen-in-time snapshot of the electron density as a function of geographic latitude and longitude from a three-dimensional TIEGCM simulation, featuring the Equatorial Ionization Anomaly (EIA). EIA is a dayside/dusk ionospheric feature that is formed from a phenomenon known as the Fountain/Appleton effect (Appleton, 1946). This phenomenon is a result of a vertical ion drift near the magnetic equator that is related to the E-region dynamo (Hanson and Moffett, 1966). This results in a concentration of plasma at ±20° in magnetic latitude with a depletion of plasma at the magnetic equator primarily in the F-region (200–450 km) (Rishbeth, 2000). The EIA is in a highly collisional domain and is coupled with the thermosphere, but due to the lack of spatial and temporal resolutions from data collected in previous missions, there are unanswered questions to the exact coupling mechanisms in this region. Here, we employ simulations of the EIA using NCAR's High-Resolution Thermosphere-Ionosphere-Electrodynamics General Circulation Model (HR-TIEGCM). HR-TIEGCM is a global 3D numerical model that can simulate the IT region from ~97 km to ~600 km with a longitude/latitude grid of 0.625° × 0.625°, a vertical resolution of 0.25 of a scale height, and a timestep of 60 s (Qian et al., 2014; Dang et al., 2021). This temporal and spatial resolution is on par with what the GDC mission will be capable of capturing.

Our goal in this example is to evaluate the performance of LSGC-AS-LEO 1.0 to calculate the spatial gradients associated with the EIA using GDC data. In order to properly display the calculated gradients in the context of the two-dimensional image on Panel A, we briefly ignore the temporal variations of the electron density and assume that temporal gradients are zero at all locations. Upon running the software, the simulated data are imported and interpolated every 20 s along the trajectories of the GDC spacecraft during the first few hours of phase 1a. 4% measurement noise is then introduced to the data, which is comparable to the expected performance (i.e., 2% accuracy, and 1% precision) of GDC's Atmospheric Electrodynamics probe for THERmal plasma (AETHER) instrument. The gradients are calculated with the initial homogeneity scales of $L_{lat} = 10°$, $L_{long} = 50°$, and $L_t = 2,500$ s. Overplotted on the electron density map on Panel A is the trajectory of the evaluation point (the continuous black curve), as well as the spatial gradient vectors (black arrows). One can verify that the gradient vectors always point nearly perpendicular to the electron density contours. Shown on the right panels, in a similar format as those in Figure 3, are the electron densities seen by individual satellites (Panel B), the latitudinal (C), longitudinal (D), and temporal (E) gradients, latitude and longitude of the evaluation point (F) at the center of the constellation, L_{lat} (G), and χ^2 (H). While in Panel A gradient vectors are calculated and shown for about 5 GDC orbits through the simulated field, the right panels only show time series for the first 120 min (~1.3 orbits) from the beginning of the interval starting at round −30° latitude and −106° longitude. The blue circles overplotted on the trajectory of the evaluation point in Panel A mark temporal timesteps of 10 min, allowing to compare the time series plots with the two-dimensional map in Panel A. The gradients are calculated accurately with the exception of the temporal gradients which suffer from

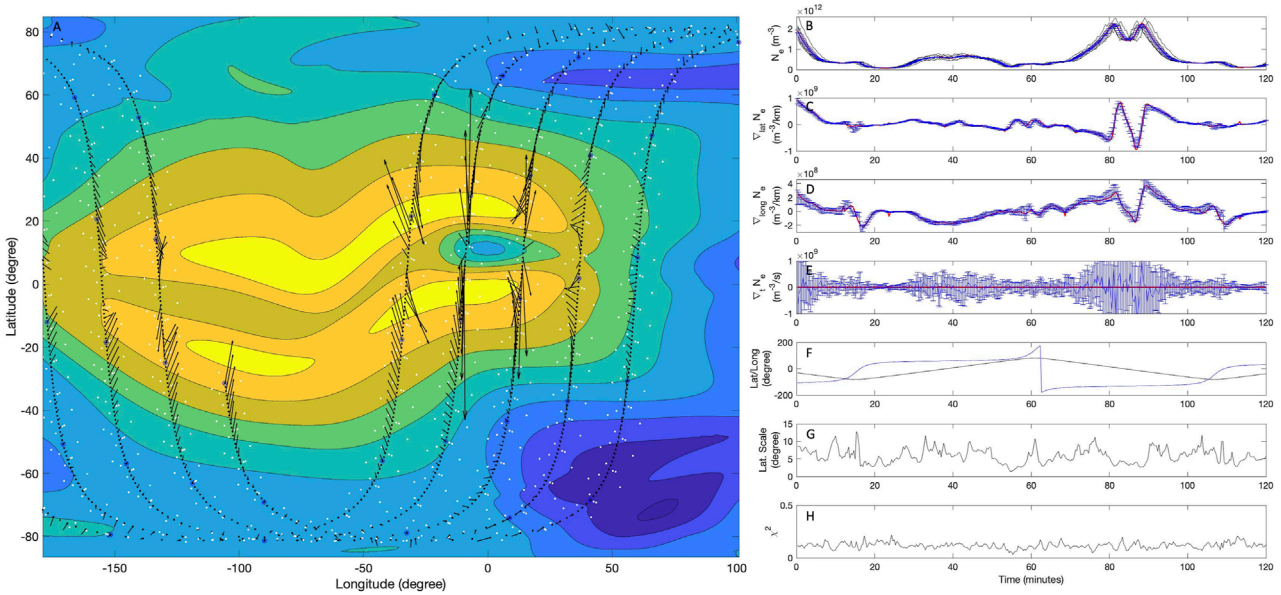

FIGURE 6
Results of the gradient calculation technique on simulated ionospheric electron density via TIEGCM. **(A)** 2d map showing the equatorial ionization anomaly, with gradient vectors calculated during GDC's phase 1a. The continuous black lines shows the trajectory of the evaluation point. For reference, the white dots show trajectories of individual satellites, representing the size of the constellation. **(B)** time series results of the computations are shown in a similar format as those in Figure 3. 4% measurement noise has been added to the sampled data. Other settings include: L_{lat}: 10°, L_{long}: 50°, L_t: 2,500 s, MaxT: 2 min; Measurement cadence: 20 s.

very large error bars. The reason for these error estimates will be discussed later when visiting Figure 7. The spatial gradients shown in Panels C and D allow us to visualize the underlying electron density field without referring to the two-dimensional map on Panel A. For example, from the large negative longitudinal gradients around time 40 min, one could conclude that the electron density peak seen in Panel B at that time is due to a primarily longitudinal structure. This can indeed be confirmed by visiting Panel A and noting that observed electron density enhancement around time 40 min is due the constellation traversing along the eastern edge of the EIA at the longitude of ~60° and the latitude range of −20 to +40°.

In Figure 7 we repeat a similar test as that in Figure 6 while focusing on the constellation architecture at later phases of the mission. Here, the left panels correspond to the first 100 min of phase 2a and the panels on the right correspond to the beginning of the phase 2b. The figures show electron densities observed by individual satellites (Panel A and F), the calculated gradients (B–D and G–I), and the latitude and longitude of the evaluation point (F and J). In both examples we allow the simulated electron density field to evolve in time, such that the true temporal gradient are non-zero. At the beginning of phase 2a, it appears that the spatial gradients associated with the EIA are often properly captured. However, by the beginning of phase 2b, the size of the constellation has increased such the certain smaller scale features are no longer resolved, and at times the sharpest gradients are underestimated—e.g., around time 140–150 and 185–195 min. As a consequence of these errors, the estimated electron density at the evaluation point, at the center of the constellation, also deviate from the true values in Panel F. With respect to the temporal gradients, in both Panels D and J, the estimated values are significantly greater than true gradients and are accompanied by very large error bars, indicating that the estimates are likely not meaningful.

The difficulty in determining $\nabla_t N_e$ in this case arises from several factors which include: 1) the constellation architecture during the chosen phases of the mission, including the large (~7 km/s) velocity of the satellites, that limits the duration of time over which a given spatial region is visited; 2) the ratio of the spatial gradients to $\nabla_t N_e$ at a given point; and 3) the relatively large measurement noise introduced to the samples. For example, consider the largest true temporal gradients in Figure 7D that reach a maximum of $\sim 4 \times 10^7 m^{-3}/s$ at time 64 min. If persisted during a 2-min interval over which the gradients are computed δN_e due to $\nabla_t N_e$ may reach to $\sim 5 \times 10^9 m^{-3}$. This is an order of magnitude smaller than the measurement noise introduced at these times, and two orders of magnitude smaller than δN_e due to the latitudinal gradients. Nevertheless, as will be shown in Figure 8, temporal gradients of IT parameters can still be reasonably obtained using LSGC-AS-LEO 1.0 and GDC data depending on a number of factor, including the phase of the mission, measurement noise level, and the form of the variations of the measured field. It should also be emphasized that in low-measurement-noise conditions (< 1%), applicable to high-precision electric and magnetic field data and their products such as $\boldsymbol{E} \times \boldsymbol{B}$ ion drifts, or plasma densities obtained from the background plasma frequency, even small temporal gradients can be reliably captured by the current approach. Finally, it should be noted that, as can be seen in the predicted GDC ephemerides (Rev C data files: https://ccmc.gsfc.nasa.gov/RoR_WWW/GDC_support/Proposer_Resources/GDC_EphemerisRevC.zip; description of data files: https://ccmc.gsfc.nasa.gov/static/files/GDC-SCI-DESC-0005RevC.

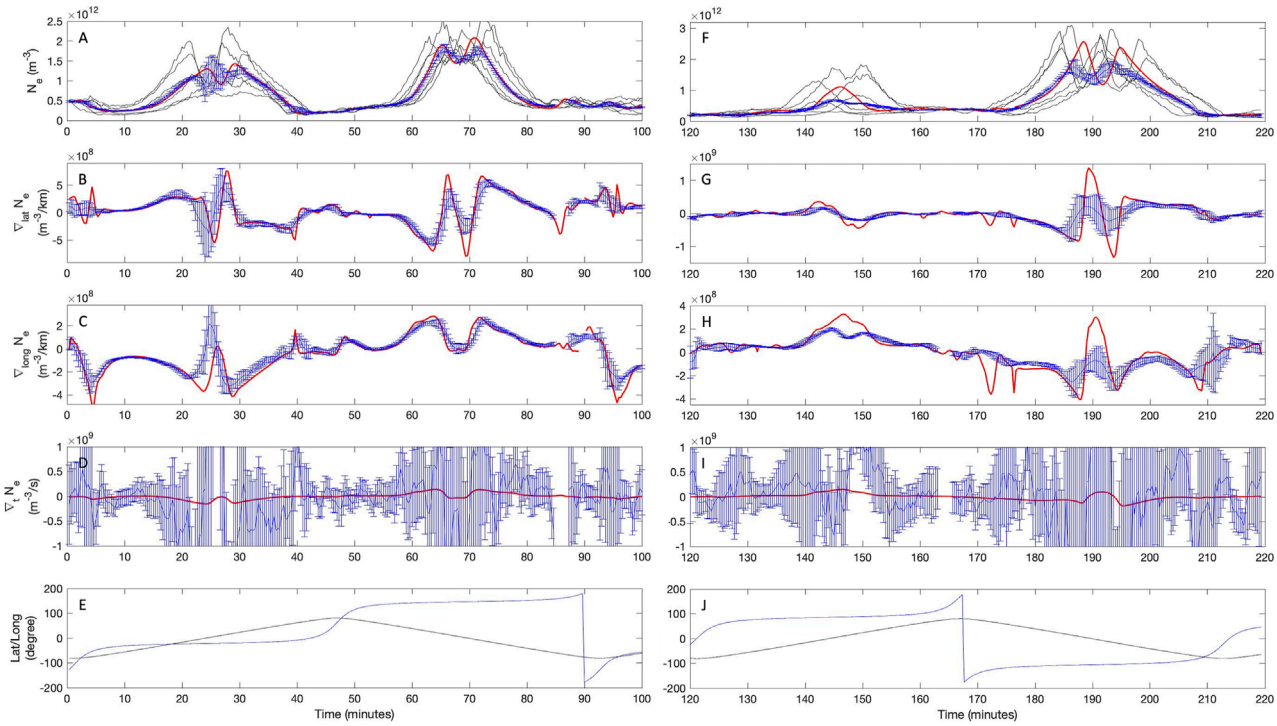

FIGURE 7
In a similar format as Figures 6B–F, the results of the gradient calculations on electron density but during the initial periods of GDC's phases 2a (left) and 2b (right). The increased size of the constellation is evident in the top panels as the individual satellites measures increasingly different values.

pdf), there are other sampling configurations (e.g., 'Follow the Leader' configurations in Phases 2 and 3) in which GDC will have longer revisit times, allowing the study of slow temporal variations.

In Figure 8 we return to the constellation geometry in phase 1a and evaluate the performance of the software in disentangling the spatial and temporal variability in a vector quantity: the zonal (U, shown on the left) and meridional (V, shown on the right) neutral winds as simulated by TIEGCM. Here, in order to demonstrate the ability of the approach to capture temporal gradients only 1% noise has been added to the simulated values. For reference, the expected performance of GDC's neutral wind measurements by the Modular Spectrometer for Atmosphere and Ionosphere Characterization (MoSAIC) instrument is the accuracy and precision of no more than 4.5 m/s. With this level of measurement noise, all the gradients are determined with reasonably small error bars, including periods of non-zero $\nabla_t U_n$ and $\nabla_t V_n$ between times ~120–150, as well as the most prominent variations of spatial gradients near the polar regions. While the specified 4.5 m/s accuracy of neutral wind measurement by the MoSAIC instrument translates to measurement noise levels as low as 2.25% in our example, an effective measurement noise of 1% or below is achievable by averaging multiple datapoints from MoSAIC that will be obtained within the 20-s measurement cadence used in our example shown in Figure 8. MoSAIC will provide independent samples of ion and neutral densities, temperatures, compositions, and velocities every two seconds or faster, providing a minimum of 10 samples within 20 s, providing the possibility to effectively reduce random measurement noise level by a factor of ~3, to below 1%.

It is important to recognize that the ability of a mission like GDC to measure gradients relies on a reasonably good match between the spatiotemporal separation of the satellites and the phenomena being studied. Early phases of the mission are best for studying small-scale, sharp variations, and later phases are best for studying larger-scale, more gradual variations. As an example consider the simulated neutral temperature field shown in Figure 9A. The image shows variation of T_n in space at a fixed time, with the minimum and maximum values of ~850 and 1200 K, respectively. For reference, the trajectory of the GDC constellation during the first orbit of phase 2b are also overplotted on the image. In the right panels of Figure 9, the gradients computed during phase 2b of the mission are shown to successfully capture the spatial variations of the underlying field. It should also be emphasized that, while the examples shown in Figures 3–9 demonstrate that the least-squares gradients calculation approach is a powerful tool capable of estimating the gradients of the IT parameters using GDC's future measurements, the utilization of the approach is not necessarily trivial or free from limitations and caveats. For example, the performance of the algorithm currently relies on appropriate choices for several parameters, such as the homogeneity lengths, the determination of which may prove to be difficult in a real scenario. Further, for the approach to be applicable in a routine and robust manner, the sensitivity of the chosen parameter values needs to be studied. Such investigations will be the subject of future works.

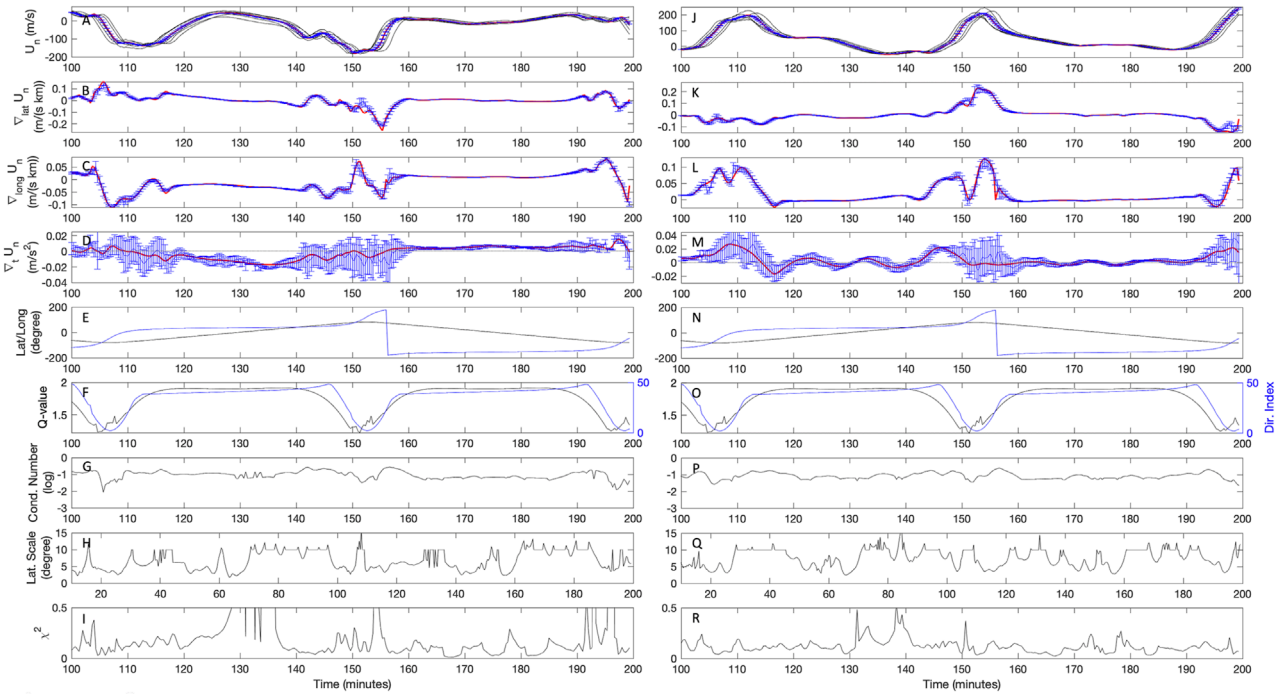

FIGURE 8
Results of the gradient computation on zonal (left) and meridional (right) neutral winds from TIEGCM simulations. 1% measurement noise has been added to the data sampled during the initial stages of the phase 1a. Other settings include: L_{lat}: 10°, L_{long}: 20°, L_t: 500 s, MaxT: 3 min; Measurement cadence: 20 s.

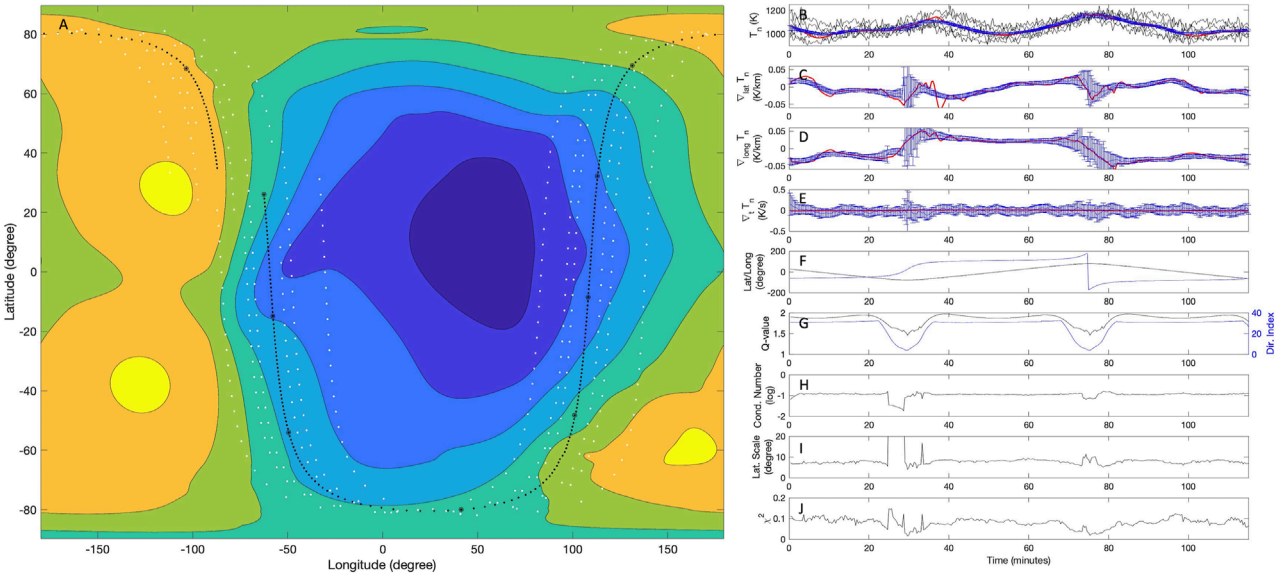

FIGURE 9
(A) shows a snapshot of the neutral temperature from TIEGCM as a function of latitude and longitude. For reference, the trajectory of the center of the constellation and those of the individual satellites during the first orbit of phase 2b are also shown via the black line and white dots, respectively. **(B–J)** show results of the gradient computation for neutral temperature measurements at the beginning of phase 2b, subject to 2% measurement noise—that is MoSAIC's expected accuracy and precision in determining the neutral gas temperature. Other settings include: L_{lat}: 50°, L_{long}: 50°, L_t: 2,500 s, MaxT: 2.5 min, Measurement cadence: 20 s.

5 Summary and conclusion

In preparation for the Geospace Dynamics Constellation mission, we have implemented the least-square gradient calculation approach described by De Keyser et al. (2007) and De Keyser (2008) in a open-source software LSGC-AS-LEO 1.0. Calculation of the gradients of the ionospheric and thermospheric parameters would allow to disentangle the spatial and temporal variability of the measured fields in an inherently quantitative manner. The approach that is implemented is flexible and, thus, highly suitable for GDC's dynamic constellation architecture. Via a number of examples, and by utilizing synthetic and simulated IT fields, we have validated the performance of the software and demonstrated its power to explore GDC's ability to resolve spatial and temporal structures that may exist in the ionosphere and the thermosphere. We have also established the usefulness of the software to evaluate suitability of various constellation geometries and assess the impact of measurement sensitivities on addressing GDC's science objectives. For example, from the test cases discussed one may draw the following several conclusions: 1) computation of the temporal gradients of neutral and plasma variables, while are sensitive to the measurement noise level, are possible with GDC measurements; 2) The spatial gradients of the equatorial ionization anomaly can be reasonably resolved during phase 1 of the mission, while at the later phases the gradients are likely to be underestimated. On the other hand, in the presence of measurement noise, computing the gradients of the neutral temperature would likely be more difficult in the earliest phases of the mission due to the small gradients and large homogeneity lengths involved; 3) Gradients of the neutral wind can be well determined in the earliest phases of the mission even at the highest latitudes where the constellation skews in longitude.

We will continue to enhance the software in several directions. The future work will include further refinements to the optimization scheme and implementation of direction-dependent scaling for the homogeneity lengths, implementation of constrains (e.g., divergence free or curl free) in the algorithm for vector fields, enhancement of computation efficiency, and performing additional tests on simulated data to further probe GDC's ability to address its science questions.

Data availability statement

LSGC-AS-LEO v1 has been uploaded to Zenodo and can be found at https://doi.org/10.5281/zenodo.10685218. Further inquiries can be directed to the corresponding author.

Author contributions

All authors listed have made a substantial, direct, and intellectual contribution to the work and approved it for publication.

Funding

This work was funded by NASA's Geospace Dynamics Constellation mission.

Conflict of interest

The authors declare that the research was conducted in the absence of any commercial or financial relationships that could be construed as a potential conflict of interest.

Publisher's note

All claims expressed in this article are solely those of the authors and do not necessarily represent those of their affiliated organizations, or those of the publisher, the editors and the reviewers. Any product that may be evaluated in this article, or claim that may be made by its manufacturer, is not guaranteed or endorsed by the publisher.

References

Amm, O., and Viljanen, A. (1999). Ionospheric disturbance magnetic field continuation from the ground to the ionosphere using spherical elementary current systems. *Earth, Planets Space* 51, 431–440. doi:10.1186/bf03352247

Appleton, E. V. (1946). Two anomalies in the ionosphere. *Nature* 157, 691. doi:10.1038/157691a0

Bard, C., and Dorelli, J. (2021). Neural network reconstruction of plasma space-time. *Front. Astronomy Space Sci.* 8, 732275. doi:10.3389/fspas.2021.732275

Blagau, A., and Vogt, J. (2019). Multipoint field-aligned current estimates with swarm. *J. Geophys. Res. Space Phys.* 124, 6869–6895. doi:10.1029/2018ja026439

Blagau, A., and Vogt, J. (2023). Swarmface: a python package for field-aligned currents exploration with swarm. *Front. Astronomy Space Sci.* 9, 1077845. doi:10.3389/fspas.2022.1077845

Burch, J., Moore, T., Torbert, R., and Giles, B. (2016). Magnetospheric multiscale overview and science objectives. *Space Sci. Rev.* 199, 5–21. doi:10.1007/s11214-015-0164-9

Chanteur, G. (1998). Spatial interpolation for four spacecraft: theory. *ISSI Sci. Rep. Ser.* 1, 349–370.

Dang, T., Zhang, B., Lei, J., Wang, W., Burns, A., Liu, H.-l., et al. (2021). Azimuthal averaging–reconstruction filtering techniques for finite-difference general circulation models in spherical geometry. *Geosci. Model Dev.* 14, 859–873. doi:10.5194/gmd-14-859-2021

Darrouzet, F., De Keyser, J., Décréau, P., Lemaire, J., and Dunlop, M. (2006). Spatial gradients in the plasmasphere from cluster. *Geophys. Res. Lett.* 33. doi:10.1029/2006gl025727

De Keyser, J. (2008). Least-squares multi-spacecraft gradient calculation with automatic error estimation. *Ann. Geophys. (Copernic. GmbH)* 26, 3295–3316. doi:10.5194/angeo-26-3295-2008

De Keyser, J., Darrouzet, F., Dunlop, M., and Décréau, P. (2007). Least-squares gradient calculation from multi-point observations of scalar and vector fields: methodology and applications with cluster in the plasmasphere. *Ann. Geophys. (Copernic. GmbH)* 25, 971–987. doi:10.5194/angeo-25-971-2007

Denton, R., Torbert, R., Hasegawa, H., Dors, I., Genestreti, K., Argall, M., et al. (2020). Polynomial reconstruction of the reconnection magnetic field observed by multiple spacecraft. *J. Geophys. Res. Space Phys.* 125, e2019JA027481. doi:10.1029/2019ja027481

Denton, R. E., Liu, Y.-H., Hasegawa, H., Torbert, R. B., Li, W., Fuselier, S., et al. (2022). Polynomial reconstruction of the magnetic field observed by multiple spacecraft with integrated velocity determination. *J. Geophys. Res. Space Phys.* 127, e2022JA030512. doi:10.1029/2022ja030512

Dunlop, M., Dong, X.-C., Wang, T.-Y., Eastwood, J., Robert, P., Haaland, S., et al. (2021a). Curlometer technique and applications. *J. Geophys. Res. Space Phys.* 126, e2021JA029538. doi:10.1029/2021ja029538

Dunlop, M. W., and Lühr, H. (2020). *Ionospheric multi-spacecraft analysis tools: approaches for deriving ionospheric parameters*. Berlin, Germany: Springer Nature.

Dunlop, M. W., Wang, T., Dong, X., Haarland, S., Shi, Q., Fu, H., et al. (2021b). Multispacecraft measurements in the magnetosphere. *Magnetos. Sol. Syst.*, 637–656. doi:10.1002/9781119815624.ch40

Escoubet, C., Fehringer, M., and Goldstein, M. (2001). <i>Introduction</i>The Cluster mission. *Ann. Geophys. (Copernic. GmbH)* 19, 1197–1200. doi:10.5194/angeo-19-1197-2001

Fiori, R. A. (2020). Spherical cap harmonic analysis techniques for mapping high-latitude ionospheric plasma flow—application to the swarm satellite mission. *Ionos. Spacecr. Analysis Tools Approaches Deriving Ionos. Param.*, 189–218. doi:10.1007/978-3-030-26732-2_9

Friis-Christensen, E., Lühr, H., Knudsen, D., and Haagmans, R. (2008). Swarm–an earth observation mission investigating geospace. *Adv. Space Res.* 41, 210–216. doi:10.1016/j.asr.2006.10.008

Hanson, W., and Moffett, R. (1966). Lonization transport effects in the equatorial f region. *J. Geophys. Res.* 71, 5559–5572. doi:10.1029/jz071i023p05559

Harvey, C. C. (1998). Spatial gradients and the volumetric tensor. *ISSI Sci. Rep. Ser.* 1, 307–322.

Paschmann, G., and Daly, P. W. (1998). Analysis methods for multi-spacecraft data. *ISSI Sci. Rep. Ser.* 1, 1608–280x.

Qian, L., Emery, B. A., Foster, B., Lu, G., Maute, A., Richmond, A. D., et al. (2014). The NCAR TIE-GCM: a community model of the coupled thermosphere/ionosphere system," in *Model. ionosphere–thermosphere Syst.* Eds., Editor J. Huba, R. Schunk, and G. Khazanov: John Wiley, 73–83. doi:10.1002/9781118704417.ch7

Rishbeth, H. (2000). The equatorial f-layer: progress and puzzles. *Ann. Geophys.* 18, 730–739. doi:10.1007/s005850000221

Ritter, P., and Lühr, H. (2006). Curl-b technique applied to swarm constellation for determining field-aligned currents. *Earth, planets space* 58, 463–476. doi:10.1186/bf03351942

Ritter, P., Lühr, H., and Rauberg, J. (2013). Determining field-aligned currents with the swarm constellation mission. *Earth, Planets Space* 65, 1285–1294. doi:10.5047/eps.2013.09.006

Robert, P., Dunlop, M. W., Roux, A., and Chanteur, G. (1998). Accuracy of current density determination. *Analysis methods Spacecr. data* 398, 395–418.

Shen, C., and Dunlop, M. (2023). Field gradient analysis based on a geometrical approach. *J. Geophys. Res. Space Phys.* 128, e2023JA031313. doi:10.1029/2023ja031313

Shen, C., Rong, Z., and Dunlop, M. (2012a). Determining the full magnetic field gradient from two spacecraft measurements under special constraints. *J. Geophys. Res. Space Phys.* 117. doi:10.1029/2012ja018063

Shen, C., Rong, Z., Dunlop, M., Ma, Y., Li, X., Zeng, G., et al. (2012b). Spatial gradients from irregular, multiple-point spacecraft configurations. *J. Geophys. Res. Space Phys.* 117. doi:10.1029/2012ja018075

Shen, C., Zhang, C., Rong, Z., Pu, Z., Dunlop, M. W., Escoubet, C. P., et al. (2021a). Nonlinear magnetic gradients and complete magnetic geometry from multispacecraft measurements. *J. Geophys. Res. Space Phys.* 126, e2020JA028846. doi:10.1029/2020ja028846

Shen, C., Zhou, Y., Ma, Y., Wang, X., Pu, Z., and Dunlop, M. (2021b). A general algorithm for the linear and quadratic gradients of physical quantities based on 10 or more point measurements. *J. Geophys. Res. Space Phys.* 126, e2021JA029121. doi:10.1029/2021ja029121

Torbert, R. B., Dors, I., Argall, M. R., Genestreti, K., Burch, J., Farrugia, C. J., et al. (2020). A new method of 3-d magnetic field reconstruction. *Geophys. Res. Lett.* 47, e2019GL085542. doi:10.1029/2019gl085542

Vogt, J., Albert, A., and Marghitu, O. (2009). Analysis of three-spacecraft data using planar reciprocal vectors: methodological framework and spatial gradient estimation. *Ann. Geophys.* 27, 3249–3273. doi:10.5194/angeo-27-3249-2009

Vogt, J., Blagau, A., and Pick, L. (2020). Robust adaptive spacecraft array derivative analysis. *Earth Space Sci.* 7, e2019EA000953. doi:10.1029/2019ea000953

Vogt, J., Sorbalo, E., He, M., and Blagau, A. (2013). Gradient estimation using configurations of two or three spacecraft. *Ann. Geophys.* 31, 1913–1927. doi:10.5194/angeo-31-1913-2013

Zhu, X., Cohen, I. J., Mauk, B. H., Nikoukar, R., Turner, D. L., and Torbert, R. B. (2022). A new three-dimensional empirical reconstruction model using a stochastic optimization method. *Front. Astronomy Space Sci.* 9, 91. doi:10.3389/fspas.2022.878403

frontiers | Frontiers in Astronomy and Space Sciences

TYPE Opinion
PUBLISHED 08 April 2024
DOI 10.3389/fspas.2024.1391990

OPEN ACCESS

EDITED BY
Katariina Nykyri,
National Aeronautics and Space Administration, United States

REVIEWED BY
Mario J. Pinheiro,
University of Lisbon, Portugal

*CORRESPONDENCE
Daniel Weimer,
dweimer@vt.edu

RECEIVED 26 February 2024
ACCEPTED 25 March 2024
PUBLISHED 08 April 2024

CITATION
Weimer D (2024), The significance of small-scale electric fields may be overestimated.
Front. Astron. Space Sci. 11:1391990.
doi: 10.3389/fspas.2024.1391990

The significance of small-scale electric fields may be overestimated

Daniel Weimer*

Center for Space Science and Engineering Research, Virginia Tech (retired), Blacksburg, VA, United States

KEYWORDS

electric fields, Joule heating, small-scale, mesoscale, structure, variability, conductivity, GDC

1 Introduction

It is well known that the electric fields and currents in the polar ionosphere have a significant role in the dissipation of energy through Joule heating. The resulting expansion of the thermosphere can have costly impacts on satellites in low-Earth orbit (Billett et al., 2024). In a paper by Codrescu et al. (1995) it was proposed that the variability in the high-latitude electric field could significantly increase the amount of energy that is dissipated through Joule heating, and therefore electric field models that do not include such variability will underestimate the total amount of heating. Since then, many papers have appeared about the topic of the additional heating that could be produced by the presence of the small-scale (<100 km) and meso-scale (100–500 km) (Sheng et al., 2022) fluctuations or structures in the electric field. Conference sessions and agency solicitations have also been devoted to this topic. The purpose of this paper is to suggest the possibility that these variations in the electric field may not be as significant as generally thought, and how future multispacecraft measurements could help to resolve the question.

2 Electric field variations

The electric fields (and heating) are generally the strongest when the Interplanetary Magnetic Field (IMF) is directed in a Southward direction, in parallel with the Earth's magnetic field in the polar regions. Under such conditions the electric field is generally points from dawn to dusk in the polar region, and towards the equator at auroral latitudes, corresponding to anti-sunward plasma flow in the polar cap and sunward plasma flow at the lower latitudes. An example of such electric fields measured on the DE-2 satellite with the Vector Electric Field Instrument (VEFI) (Maynard et al., 1981) is shown in Figure 1A. The electric field component that is shown is orientated in the direction of the satellite's motion. Often there may be short-duration jumps in the electric field of a "spiky" nature, as demonstrated in this figure.

The existence of these electric field spikes has been known since 1972 when Heppner (1972) had reported that the fluctuations are seen in the polar cap more often in the winter hemisphere than in the summer hemisphere. Maynard et al. (1982) reported that the large-magnitude electric field spikes are commonly seen in the polar cusp region, and also in the nightside auroral oval. This seasonal difference was also found by Heppner et al. (1993), as well as in a recent reanalysis of the DE-2 electric field data (Laakso and Pfaff, 2023). Figure 1 demonstrates the seasonal difference, as the example shown in Figure 1A was a winter pass and Figure 1B shows the electric fields measured in the summer, Northern hemisphere on

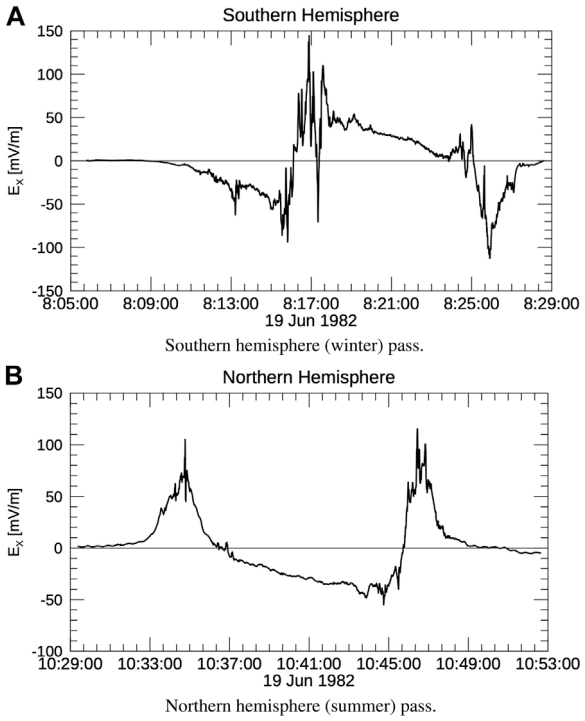

FIGURE 1
Electric field measured on the DE-2 satellite on consecutive polar passes 19 June 1982. The field component E_X is parallel to the direction of the satellite's velocity, with positive values being in the direction of the forward motion. **(A)** Southern hemisphere (winter) pass. **(B)** Northern hemisphere (summer) pass.

the same orbit. The summer hemisphere pass exhibits fewer of the large-magnitude fluctuations in comparison to the winter pass. Regarding the duration and magnitudes of the electric field spikes, Laakso and Pfaff (2023) had noted that "the observed events last between 0.1 and 60 s, corresponding to (north-south) widths of 1–500 km along the satellite trajectory." Magnitudes of electric field spikes in the range of 200–400 mV/m were found to be common in the data from the electric field instrument on the DE-2 satellite. These field strengths correspond to plasma drift velocities in the range of 5–8 km/s. Occasionally peaks of about 1 V/m were seen, correlating to a drift speed of 20 km/s. As noted by Pfaff et al. (2022), these velocities exceed the maximum range of the typical ion drift meter type of instrument that are common on ionospheric spacecraft, that usually have a limit of around 4 km/s. Ion drift meters often have sample rates that are lower than with double-probes such as VEFI, which sampled the electric field at 16 Hz.

3 Influence of conductivity

As already mentioned, the electric field variability is more pronounced on the night side and winter hemisphere. This behavior leads to the obvious conclusion that the electric field fluctuations have lager magnitudes when the ionospheric conductivity is low, and therefore results in less heating. Evans et al. (1983) had found that "the ionospheric level electric field intensity is highly correlated, often on a one-to-one basis, with the reciprocal of the height-integrated Pedersen conductivity, which in turn is controlled by the auroral electron precipitation." This anti-correlation between the electric field and conductivity was investigated in more detail by Mallinckrodt and Carlson (1985), Baker et al. (2004), and Zhu et al. (2018).

Cosgrove et al. (2009) looked into this situation and more detail, finding that "because small spatial-scale electric fields are likely polarization electric fields, and therefore negatively correlated with conductance (over space), they may not lead to underestimation of Joule heating." Furthermore, "the result emphasizes that it cannot be known whether small-spatial-scale variability leads to underestimation or overestimation of the Joule heating rate, until a careful measurement of the spatial correlation between conductance and electric field has been made" (Cosgrove et al., 2009).

4 Other considerations

Similar to the paper by Codrescu et al. (1995), efforts to model the effects of variability in the electric field often introduce such variations superimposed on a simulated, large-scale electric field model. The problem is that the conductivity in their calculations is often fixed, with the result that larger amounts of heating are found. Obviously, if the anti-correlated variations in the conductivity are not taken into consideration, then the results of such efforts are likely over-exaggerated, in agreement with (Cosgrove et al., 2009).

A similar problem is that the lifetimes of each electric field spike have not considered. Do these large-magnitude field spikes persist for a long time, or just a few seconds or less? Another way of putting it is in terms of their duty-cycle, or what percentage of time they exist at one location compared to being absent? How far do they extend in the transverse direction? The relevant papers generally do not consider that question, although the initial one by Codrescu et al. (1995) did admit that "E-field fluctuations are known to exist on a variety of temporal and spatial scales." Ignoring these properties can also lend to over-exaggeration of the heating effects, especially if the modeling calculations assume that the fluctuations are fixed in place and are long lasting.

Direct measurements of the Poynting flux from simultaneous vector electric and magnetic field measurements helps to diminish the problem of not knowing conductance values. These Poynting flux data are also subject to misinterpretation if momentary energy spikes that are detected are assumed to persist for the entire duration of the 20–30 min polar pass.

Weimer (2005a) presented an empirical model for calculating the Poynting flux entering the polar ionosphere, derived from combining models of the electric fields and field-aligned currents (Note that a later Weimer (2005b) paper updated the model calculations to use a spherical cap harmonic analysis, but the methods used to obtain the Poynting flux remained the same.). Through use of results from Burke (2008) and the JB2008 thermosphere model (Bowman et al., 2008), Weimer et al. (2011) had found that the total energy flowing into the ionosphere and thermosphere calculated with the 2005 model could account for the observed changes in the density of the global thermosphere in geomagnetic storm intervals. Despite the lack of small-scale

variations, there does not seem to be any missing energy in the 2005 model predictions.

5 Multispacecraft measurements

The lifetimes and dimensions of the small-scale electric field fluctuations cannot be determined with measurements from only one satellite, so multispacecraft measurements are required. NASA's future Geospace Dynamics Constellation (GDC) will be useful for this task, as measurements of electric fields and Poynting flux will be obtained at varied intervals of time and location. The Science and Technology Definition Team (STDT) Final Report for the GDC mission (https://lws.larc.nasa.gov/pdf_files/04%20GDC%20STDT%20Report%20FINAL.pdf) refers to a particularly useful orbital configuration known as "pearls on a string," with multiple satellites on the same orbital plane separated by short distances. In this orbital configuration, if an electric field spike is detected by one or two satellites but not on the following one, then its lifetime could be narrowed down. The expected motion of the electric field spikes, along with their associated aurora, could lead to some ambiguity in the lifetime measurements. But some spikes could disappear, to be replaced by others that have moved into the satellites' orbit. A careful analysis will be required to resolve some ambiguity. Ideally the initial separation in the GDC mission would be smaller than the 5-min that is illustrated in Figure 3.2 in the report by the STDT (2019). Multispacecraft measurements that are obtained on orbits separated in local time will be worthwhile for estimating the longitudinal spatial dimensions and motions of the small-scale variations.

Unfortunately, the currently planned configuration of the GDC satellites will not have onboard any double-probe type of electric field instrument, like the VEFI on DE-2. With plans for only a plasma drift instrument to measure the electric fields, the GDC capabilities will not be optimal for the detection of electric field spikes having the largest magnitudes (plasma drifts over 5 km/s) and smallest spatial sizes (Pfaff et al., 2022; Laakso and Pfaff, 2023).

6 Space weather models

To resolve the matter of the amount of heating generated by the small-scale electric field variations, the global, physics based ionosphere-theremosphere-magnetosphere models need further improvement. In order for to fully reconstruct the small-scale structure in the electric field, they would need to have spatial grid resolutions on the order of 10–50 km in both dimensions. The temporal variability of the electric fields in such models will need to be realistic, following from the results obtained from the future GDC mission. Modeling the conductivity variations on similar scales will be difficult, as the conductivity cannot be easily obtained. Conductivity variations that are derived from electron precipitation require that the precipitation inputs have the same spatial resolutions as the electric field, with appropriate dimensions and temporal scales.

7 Discussion

During the last 2 decades there has been a common viewpoint that postulates that the small-scale and mesoscale fluctuations in the polar electric fields provide a significant contribution to the amount of Joule heating that is dissipated in the ionosphere. The opinion expressed here is that this significance may be overestimated. Oftentimes the calculations that are presented to support this hypothesis ignore the relevant conductivity variations as well as assuming that the fluctuations persist for tens of minutes. Multispacecraft measurements, such as with the future GDC mission, will provide valuable evidence about the temporal and spatial characteristics of the small-scale fields and Poynting flux, with some limitations due to missing double-probes. These data will help to answer the questions about their significance.

Author contributions

DW: Visualization, Writing–original draft, Writing–review and editing.

Funding

The author(s) declare that no financial support was received for the research, authorship, and/or publication of this article.

Conflict of interest

The author declares that the research was conducted in the absence of any commercial or financial relationships that could be construed as a potential conflict of interest.

Publisher's note

References

Baker, J. B. H., Zhang, Y., Greenwald, R. A., Paxton, L. J., and Morrison, D. (2004). Height-integrated Joule and auroral particle heating in the night side high latitude thermosphere. *Geophys. Res. Lett.* 31. doi:10.1029/2004GL019535

Billett, D. D., Sartipzadeh, K., Ivarsen, M. F., Iorfida, E., Doornbos, E., Kalafatoglu Eyiguler, E. C., et al. (2024). The 2022 Starlink geomagnetic storms: global thermospheric response to a high-latitude ionospheric driver. *Space weather*. 22, e2023SW003748. doi:10.1029/2023SW003748

Bowman, B. R., Tobiska, W. K., Marcos, F. A., Huang, C. Y., Lin, C. S., and Burke, W. J. (2008). "A new empirical thermospheric density model JB2008 using new solar and geomagnetic indices," in AIAA/AAS Astrodynamics Specialist Conference Proceedings, Honolulu, HI, USA, August 2008, 19.

Burke, W. J. (2008). "Stormtime energy budgets of the global thermosphere," in *Mid-latitude ionospheric Dynamics and disturbances*. Editor P. M. Kintner (Washington, DC: NASA), 181, 235–246.

Codrescu, M. V., Fuller-Rowell, T. J., and Foster, J. C. (1995). On the importance of E-field variability for Joule heating in the high-latitude thermosphere. *Geophys. Res. Lett.* 22, 2393–2396. doi:10.1029/95GL01909

Cosgrove, R. B., Lu, G., Bahcivan, H., Matsuo, T., Heinselman, C. J., and McCready, M. A. (2009). Comparison of AMIE-modeled and Sondrestrom-measured Joule heating: a study in model resolution and electric field–conductivity correlation. *J. Geophys. Res.* 114. doi:10.1029/2008JA013508

Evans, D. S., Maynard, N. C., Troim, J., Jacobsen, T., and Egeland, A. (1983). Auroral vector electric field and particle comparisons 2. Electrodynamics of an arc. *J. Geophys. Res.* 82, 2235–2249. doi:10.1029/JA082i016p02235

Heppner, J. (1972). Electric field variations during substorms: OGO-6 measurements. *Planet. Space Sci.* 20, 1475–1498. doi:10.1016/0032-0633(72)90052-9

Heppner, J. P., Liebrecht, M. C., Maynard, N. C., and Pfaff, R. F. (1993). High-latitude distributions of plasma waves and spatial irregularities from de 2 alternating current electric field observations. *J. Geophys. Res. Space Phys.* 98, 1629–1652. doi:10.1029/92JA01836

Laakso, H., and Pfaff, R. (2023). Fast plasma drifts in the high latitude ionosphere. *Geophys. Res. Lett.* 50, e2023GL103566. doi:10.1029/2023GL103566

Mallinckrodt, A. J., and Carlson, C. W. (1985). On the anticorrelation of the electric field and peak electron energy within an auroral arc. *J. Geophy. Res.* 90, 399–408. doi:10.1029/JA090iA01p00399

Maynard, N., Bielecki, E., and Burdick, H. (1981). Instrumentation for vector electric field measurements from DE-b. *Space Sci. Instrum.* 5, 523–534.

Maynard, N. C., Heppner, J. P., and Egeland, A. (1982). Intense, variable electric fields at ionospheric altitudes in the high latitude regions as observed by DE-2. *Geophys. Res. Lett.* 9, 981–984. doi:10.1029/GL009i009p00981

Pfaff, R., Laakso, H., Bonnell, J. W., Cattell, C., Lu, G., Thayer, J., et al. (2022). Measuring the vector electric field in the ionosphere – important new scientific and space weather advances and a synopsis of double probes as an excellent instrument to measure electric fields on non-spinning satellites. *A White Pap. 2024-2033 Decadal Surv. Sol. Space Phys. (Heliophysics)*. Available at: https://surveygizmoresponseuploads.s3.amazonaws.com/fileuploads%2F623127%2F6920789%2F79-39d6663d3238e36b6b61e223c229605e_PfaffRobertF2.pdf.

Sheng, C., Deng, Y., Bristow, W. A., Nishimura, Y., Heelis, R. A., and Gabrielse, C. (2022). Multi-scale geomagnetic forcing derived from high-resolution observations and their impacts on the upper atmosphere. *Space weather*. 20, e2022SW003273. doi:10.1029/2022SW003273

STDT (2019). NASA science and Technology definition Team for the Geospace Dynamics constellation: final report. Available at: https://lws.larc.nasa.gov/pdf_files/04%20GDC%20STDT%20Report%20FINAL.pdf. (Accessed February 12 2019).

Weimer, D. R. (2005a). Improved ionospheric electrodynamic models and application to calculating Joule heating rates. *J. Geophys. Res.* 110, A05306. doi:10.1029/2004JA010884

Weimer, D. R. (2005b). Predicting surface geomagnetic variations using ionospheric electrodynamic models. *J. Geophys. Res.* 110, A12307. doi:10.1029/2005JA011270

Weimer, D. R., Bowman, B. R., Sutton, E. K., and Tobiska, W. K. (2011). Predicting global average thermospheric temperature changes resulting from auroral heating. *J. Geophys. Res.* 116, A01312. doi:10.1029/2010JA015685

Zhu, Q., Deng, Y., Richmond, A., and Maute, A. (2018). Small-scale and mesoscale variabilities in the electric field and particle precipitation and their impacts on joule heating. *J. Geophys. Res. Space Phys.* 123, 9862–9872. doi:10.1029/2018JA025771

frontiers | Frontiers in Astronomy and Space Sciences

TYPE Methods
PUBLISHED 06 May 2024
DOI 10.3389/fspas.2024.1379321

OPEN ACCESS

EDITED BY
Thomas Earle Moore,
Third Rock Research, United States

REVIEWED BY
Bertrand Bonfond,
University of Liège, Belgium
Jim Burch,
Southwest Research Institute (SwRI),
United States
Ruth Skoug,
Los Alamos National Laboratory (DOE),
United States

*CORRESPONDENCE
Gonzalo Cucho-Padin,
gonzaloaugusto.cuchopadin@nasa.gov

RECEIVED 31 January 2024
ACCEPTED 16 April 2024
PUBLISHED 06 May 2024

CITATION
Cucho-Padin G, Connor H, Jung J, Shoemaker M, Murphy K, Sibeck D, Norberg J and Rojas E (2024), A feasibility study of 4-D tomography of soft X-ray magnetosheath emissivities using multi-spacecraft measurements.
Front. Astron. Space Sci. 11:1379321.
doi: 10.3389/fspas.2024.1379321

A feasibility study of 4-D tomography of soft X-ray magnetosheath emissivities using multi-spacecraft measurements

Gonzalo Cucho-Padin[1,2]*, Hyunju Connor[3], Jaewoong Jung[3,4], Michael Shoemaker[5], Kyle Murphy[6], David Sibeck[1], Johannes Norberg[7] and Enrique Rojas[8]

[1]Space Weather Laboratory, NASA Goddard Space Flight Center, Greenbelt, MD, United States, [2]Department of Physics, Catholic University of America, Washington, DC, United States, [3]Geospace Physics Laboratory, NASA Goddard Space Flight Center, Greenbelt, MD, United States, [4]Astronomy Department, University of Maryland College Park, College Park, MD, United States, [5]Navigation and Mission Design Branch, NASA Goddard Space Flight Center, Greenbelt, MD, United States, [6]Independent Researcher, Thunder Bay, ON, Canada, [7]Finnish Institute of Meteorology, Helsinki, Finland, [8]Department of Earth and Atmospheric Sciences, Cornell University, Ithaca, NY, United States

Upcoming heliophysics missions utilize state-of-the-art wide field-of-view (FOV) imaging technology to measure and investigate the space plasma environment on a global scale. At Earth, remote sensing of soft X-ray emissions, which are generated via the charge exchange interaction between heavy solar wind ions and exospheric neutral atoms, is a promising means to investigate the global magnetosheath structure, its response to varying solar wind conditions, and the spatiotemporal properties of the dayside magnetic reconnection. Data analysis techniques such as optical tomography can provide additional structural and time-varying information from the observed target and thus enhance the mission's scientific return. In this work, we simulate multiple and simultaneous observations of the dayside magnetosphere using soft X-ray imagers located at long-distance vantage points to reconstruct the time-dependent, three-dimensional (3-D) structure of the magnetosheath using a dynamic tomographic approach. The OpenGCCM MHD model is used to simulate the time-varying response of the magnetosheath to solar wind conditions and, subsequently, generate synthetic soft X-ray images from multiple spacecraft vantage points separated along a common orbit. A detailed analysis is then performed to identify the nominal set of spacecraft that produces the highest fidelity tomographic reconstruction of the magnetopause. This work aims to (i) demonstrate, for the first time, the use of dynamic tomography to retrieve the time-varying magnetosheath structure and (ii) identify a nominal mission design for multi-spacecraft configurations aiming for optical tomography.

KEYWORDS

3-D/4-D tomography, soft X-Ray, magnetosheath, multi-spacecraft measurements, optical remote sensing

1 Introduction

Heliophysics and magnetospheric communities are highly interested in understanding the dynamics of the magnetopause, which hosts key processes such as the dayside magnetic reconnection, as it is crucial for transporting mass, energy, and momentum from the solar wind into the terrestrial magnetosphere (Dungey, 1961; Sibeck et al., 2018; Koga et al., 2019). Due to its relevance, several satellite-based missions (e.g., MMS, Cluster, THEMIS) have acquired data from the magnetosheath region and its internal boundary, the magnetopause, where magnetic reconnection typically occurs during steady solar wind conditions. Their *in situ* instruments have provided valuable information on the structure, composition, and shape of the magnetopause boundary and its dynamic response to variations of solar wind parameters. Nevertheless, these data are difficult to interpret owing to their limited spatial and temporal coverage. Since the magnetopause is so vast, *in situ* instruments can only observe small crossing regions a couple of times every day (e.g., for the case of the THEMIS mission), and the acquisition period is restricted to the orbital velocity, in most cases, resulting in a few minutes. Moreover, abrupt variability in the interplanetary magnetic field (IMF) orientation can considerably change the structure of the magnetopause, moving it earthward several Earth radii (R_E) from its nominal location (~10 R_E) (Aubry et al., 1970), a feature that *in situ* instruments cannot detect efficiently.

Recently, optical remote sensing of soft X-ray emissions from the terrestrial magnetosphere has sparked the interest of the scientific community as a means for global imaging of the dayside magnetosheath Robertson and Cravens (2003); Kuntz et al. (2015); Connor et al. (2021); Sibeck et al. (2018). At Earth, soft X-ray emissions, with photon energies ranging from 100 eV to 2 keV, are generated via the charge exchange interaction between high-charge state heavy solar wind ions (accumulated in the magnetosheath region) and exospheric hydrogen (H) atoms. For example, a ≈560 eV soft X-ray photon is produced when a solar wind ion O^{7+} picks up the electron of an H atom, as shown in the following equation:

$$O^{7+} + H \rightarrow O^{6+} + H^{+} + h\nu \quad (1)$$

In the next years, two space-based missions will observe the dayside magnetospheric region using wide field-of-view (FOV) soft X-ray imagers. The European Space Agency/Chinese Academy of Science (ESA/CAS) Solar wind Magnetosphere Ionosphere Link Explorer (SMILE) spacecraft mission will acquire images with its 15.5° × 26.5° wide FOV sensor from a highly elliptical polar orbit with an apogee of ≈19 R_E and 52-h orbital period (Branduardi-Raymont et al., 2018). On the other hand, NASA's Lunar Environment heliospheric X-ray Imager (LEXI) is an optical 9.1° × 9.1° FOV instrument that will be onboard a Lunar-based platform to image the dayside magnetosheath from a nearly circular and ecliptic orbit with a ≈ 60R_E radius, and for a total acquisition period of ≈7 days (Walsh et al., 2024).

To support this new generation of instruments, several data analysis and image processing algorithms were developed to infer the physical properties of the magnetospheric region from this 2-D imagery. Special interest has been posed in the detection of the magnetopause location as well as the description of its structural shape since the dayside magnetic reconnection occurs here. For example, Collier and Connor (2018) describe a technique that uses a simulated sweep of line-of-sight (LOS) measurements over the dayside magnetospheric region to identify tangent points over the magnetopause based on the analysis of soft X-ray intensity gradient. These points are then used to estimate the magnetopause's three-dimensional (3-D) curvature. Jorgensen et al. (2019a,b) show a methodology to fit 2-D soft X-ray images to an experimental functional form that ultimately allows identification of both magnetopause and bow shock positions at the subsolar line. Samsonov et al. (2022) used the tangential direction approach introduced by Collier and Connor (2018) to analyze synthetic SMILE data that includes realistic orbit, attitude, and Poisson-distributed noise in the 2-D images. Kim et al. (2024) describe a technique to estimate the subsolar magnetopause position from synthetic soft X-ray images acquired by LEXI that are contaminated with shot noise. A Gaussian low-pass filter is used to attenuate the noise, and a posterior analysis of intensity contrast along the Sun-Earth line is implemented to identify the magnetopause position.

In addition, several studies utilized optical tomography to reconstruct the 3-D structure of the magnetosheath soft X-ray emissivity from 2-D images. For example, Jorgensen et al. (2022) simulated synthetic images of the dayside magnetosphere as observed by the SMILE spacecraft and implemented the algebraic reconstruction technique (ART) to derive the 3-D structure of this region. An efficient tomographic reconstruction requires observations from several distinct vantage points around the target to reproduce its spatial structure; however, using a single image from the SMILE's instrument may not provide sufficient information for the reconstruction. For this reason, Jorgensen et al. (2022) evaluated the use of additional measurements from a second SMILE imager located at a similar geocentric distance but in the opposite hemisphere. This new satellite configuration yielded better results in estimating the 3-D soft X-ray emissivity. Wang et al. (2023) considered the limited view-angle problem in tomographic reconstructions for SMILE data and proposed a machine-learning-based tool to generate supplementary images from the magnetosheath. They trained a Generative Adversarial Network (GAN) using synthetic soft X-ray images derived from simulated magnetohydrodynamic (MHD) models of the magnetosphere under several solar wind conditions. The GAN was used to produce images from additional vantage points that support SMILE observations in reconstructing the magnetosheath emissivity. Recently, Cucho-Padin et al. (2024) proposed a technique that solves the single-image tomography problem by incorporating a 3-D physics-based model of soft X-ray emissivities in the reconstruction process. The algorithm, based on the maximum *a posteriori* (MAP) estimation approach, utilizes synthetic soft X-ray measurements as observed by the LEXI instrument to modify a given prior (reference) model. As a result, the MAP technique generates a new 3-D model of emissivities that exhibits high agreement with observational data and an expected physical spatial distribution.

All these efforts to estimate the magnetopause location and to reconstruct the 3-D structure of the magnetosheath from remote sensing observations have considered a temporally static magnetospheric region, which is unlikely under time-varying solar

wind conditions. In this context, this work will evaluate the efficiency of tomographic reconstructions of a varying magnetosheath using multi-spacecraft measurements. Specifically, we describe a technique for 4-D tomography to reconstruct the time-dependent magnetosheath structure utilizing simulated soft X-ray imagers onboard a two-satellite configuration. This work will support the design of future multi-spacecraft missions.

This manuscript is organized as follows. Section 2 introduces the mathematical formulation of our proposed tomographic technique to estimate time-dependent, 3-D distributions of soft X-ray emissivities based on remote sensing observations of the dayside magnetosphere. Section 3 presents the design of the spacecraft configuration used to simulate soft X-ray measurements and provides examples of dynamic tomographic reconstructions and the quantification of their effectiveness in reproducing the ground truth emissivities. Finally, Section 4 discusses possible sources of errors to be considered in a more realistic analysis and provides concluding remarks on this research work.

2 Methodology

2.1 Forward emission model

This work aims to determine the spatial distribution and temporal evolution of soft X-ray emissivities (denoted as P) within the magnetosheath region. These emissivities are generated by charge exchange interactions between heavy solar wind ions and neutral hydrogen atoms from the terrestrial exosphere (see Eq. 1). The soft X-ray emissivity, also referred to as volumetric emission rate (VER), is expressed as:

$$P = \alpha\, n_H n_{sw} \langle g \rangle \quad [\text{eV cm}^{-3}\text{sec}^{-1}] \tag{2}$$

Here, α is the efficiency factor in units of [eV cm^2], which includes solar wind charge exchange (SWCX) cross-sections, SWCX photon energies, and the ratio between the density of solar wind heavy ions to the density of solar wind protons (Whittaker and Sembay, 2016; Jung et al., 2022). Also, n_H indicates the density of exospheric H atoms in units of [atoms cm^{-3}], n_{sw} is the solar wind proton density in units of [ions cm^{-3}], and $\langle g \rangle = \sqrt{v_{sw}^2 + v_{th}^2}$ [cm sec^{-1}] represents the relative velocity of neutrals and ions calculated with the plasma bulk speed v_{sw} and thermal speed vth under the assumption of negligible neutral velocity (Walsh et al., 2016; Sibeck et al., 2018).

An appropriate space-based photometric detector can provide routine observations of P such that these measurements can be used systematically to estimate their spatial distribution through inversion techniques. A single observation of P from a platform located at planetocentric distance $\mathbf{r}$, viewing line-of-sight (LOS) look angle $\hat{\mathbf{n}}$, and acquired at time t can be expressed as:

$$I(\mathbf{r}, \hat{\mathbf{n}}, t) = \frac{1}{4\pi} \int_0^{L_{max}} P(\mathbf{r}, t)\, dl + I_{bkg}(\hat{\mathbf{n}}, t) \quad [\text{eV cm}^{-2}\text{sec}^{-1}\text{str}^{-1}] \tag{3}$$

where I represents the incoming and directional photon flux, the term $P(\mathbf{r}, t)$ is the volumetric emissivity considered isotropic such that the factor $1/4\pi$ effectively extracts the photon flux along $\hat{\mathbf{n}}$, and the line-integral is evaluated from the origin of the LOS or spacecraft location ($l = 0$) to an appropriate boundary from where terrestrial soft X-ray emissions become negligible ($l = L_{max}$). The term I_{bkg} denotes the astrophysical background along the LOS direction $\hat{\mathbf{n}}$ that can be removed using sophisticated background models or alternative measurements, e.g., from Chandra X-ray Observatory (Weisskopf, 2003), ROSAT (Trümper, 1982), and XMM-Newton Jansen et al. (2001), among others.

The linearity between measured photon flux (I) and the volumetric emissivities (P), as presented in Eq. 3, enables the formulation of a discrete inverse problem (i.e., tomography) whose computational solution estimates the time-dependent 3-D soft X-ray emissivities at the magnetosheath from an ensemble of photon flux measurements of that region. In this study, we closely follow the steps presented by Cucho-Padin et al. (2022) in the context of exospheric tomography to formulate and solve this soft X-ray inverse problem.

First, we select the solution domain as the 3-D space that will be observed by the photometric sensor in a given period of time. Then, we discretize this solution domain into N non-overlapping 3-D voxels. The shape of the solution domain and voxels (e.g., cubic, spherical, cylindrical, or custom form) does not affect the mathematical formulation provided here; however, its selection should consider the desired spatial resolution of emissivities as well as the amount of computational resources used to solve the inverse problem. We illustrate the tomographic technique here using spherical shapes without loss of generality. Thus, we define the voxel size by its radial Δr, azimuthal $\Delta\phi$, and polar $\Delta\theta$ distances and assume that the soft X-ray emissivity is constant within the voxel volume.

Second, we define a $[N \times 1]$ column vector $\mathbf{x}$ containing all volumetric emissivities. We then create a $[M \times 1]$ column vector $\mathbf{y}$ of background-free measurements such that the mth element of $\mathbf{y}$ is $y_m = I_m - I_m^{bkg}$. Next, we calculate the intersection of each y measurement's LOS with all voxels in the solution domain. This results in an ensemble of line sectors (dl) where each of them corresponds to a specific voxel. These dl values are used to form the $[1 \times N]$ row vector $\mathbf{L}[m]$, e.g., $\mathbf{L}[m] = [0, dl_{n=2}, \ldots, 0, 0, dl_{n=n}, \ldots, dl_{n=N}]$, where a zero value indicates no intersection between measurement's LOSs and the solution domain. This process is repeated with m LOSs to generate the $[M \times N]$ observation matrix $\mathbf{L}$. For the sake of clarification, the $\mathbf{L}$ matrix can be generated *a priori* when (i) voxel sizes and (ii) the measurement's LOS look angles ($\hat{\mathbf{n}}$) are known. The compact algebraic linear system that relates emissivities (x_n) and measurements (y_m) is given by

$$\mathbf{y} = \mathbf{L}\mathbf{x} + \mathbf{w}, \tag{4}$$

where $\mathbf{w}$ denotes a $[M \times 1]$ measurement noise vector inherent to the optical acquisition. Eq. 4 is known as the forward emission model when the vector of emissivities, $\mathbf{x}$, is provided. On the other hand, when values for photon flux measurements ($\mathbf{y}$), their LOS's look angles, and voxel sizes of the solution domain are provided, we have an inverse problem whose solution estimates values for emissivities. In the next subsection, we provide a technique to solve this inverse problem considering the time-dependent evolution of the magnetospheric region.

2.2 The dynamic inverse model

The rapid variability of IMF orientations may modify the global structure of the magnetosheath and magnetopause in timescales of tens of minutes. To investigate these dynamic processes, wide field-of-view soft X-ray technology is expected to have a high acquisition rate, e.g., one image every 5 min. Thus, the solution to the inverse problem defined in the previous section should be able to resolve volumetric emissivities from an ensemble of observations acquired during this short period of time.

To do so, we closely follow the statistical approach introduced by Norberg et al. (2023) in the context of ionospheric dynamic tomography. Thus, we first define a dynamic state-space framework that consists of two equations:

$$\mathbf{y}_k = \mathbf{L}_k \mathbf{x}_k + \mathbf{w}_k \tag{5}$$

$$\mathbf{x}_k = \mathbf{F}_{k-1} \mathbf{x}_{k-1} + \mathbf{q}_{k-1} \tag{6}$$

Here, Eq. 5 is the "measurement equation" and follows a similar structure as Eq. 4, the subscript k denotes the discrete time step, and the vector $\mathbf{w}_k$ is defined as a random vector with Gaussian distribution $\mathbf{w}_k \sim \mathcal{N}(\mathbf{0}, \mathbf{R}_k)$ (where $\mathcal{N}(\boldsymbol{\mu}, \boldsymbol{\Sigma})$ denotes a random vector that has a Gaussian probability distribution with mean vector $\boldsymbol{\mu}$ and covariance matrix $\boldsymbol{\Sigma}$). Furthermore, Eq. 6 is the "model evolution equation" where the $[N \times N]$ matrix $\mathbf{F}_{k-1}$ models the temporal evolution of the states, typically derived from principle physics, and the $[N \times 1]$ vector $\mathbf{q}$ is the process noise with an assumed Gaussian distribution $\mathbf{q}_k \sim \mathcal{N}(\mathbf{0}, \mathbf{Q}_k)$.

Based on the previous equations, we can define the probability distribution of the predicted state $\hat{\mathbf{x}}$ at time k given a set of measurements $\mathbf{y}$ acquired at time $k-1$ as $p(\mathbf{x}_k|\mathbf{y}_{k-1}) = \mathcal{N}(\hat{\mathbf{x}}_k, \hat{\mathbf{P}}_k)$ where

$$\hat{\mathbf{x}}_k = \mathbf{F}_{k-1} \bar{\mathbf{x}}_{k-1}, \tag{7}$$

$$\hat{\mathbf{P}}_k = \mathbf{F}_{k-1} \bar{\mathbf{P}}_{k-1} \mathbf{F}_{k-1}^{\mathrm{T}} + \mathbf{Q}_{k-1} \tag{8}$$

and the superscripts $(\bar{})$ and $(\hat{})$ indicate the prior estimation and the future prediction of a given variable, respectively. The matrix $\mathbf{P}$ is known as the covariance matrix of states. The diagonal elements contain the variance of the soft X-ray emissivity in each voxel contained in vector $\mathbf{x}$, and the off-diagonal elements indicate the covariance (or correlation) between a given pair of voxels.

Furthermore, if the probability distribution for the predicted state is (i) used as the prior distribution for the next time step k and (ii) updated with measurements also acquired at time k, we can obtain the posterior distribution defined as $p(\mathbf{x}_k|\mathbf{y}_k) = \mathcal{N}(\bar{\mathbf{x}}_k, \bar{\mathbf{P}}_k)$ where

$$\begin{aligned} \bar{\mathbf{x}}_k &= \bar{\mathbf{P}}_k \left(\mathbf{L}_k^{\mathrm{T}} \mathbf{R}_k^{-1} \mathbf{y}_k + \bar{\mathbf{P}}_k^{-1} \hat{\mathbf{x}}_k \right) \\ \bar{\mathbf{P}}_k &= \left(\mathbf{L}_k^{\mathrm{T}} \mathbf{R}_k^{-1} \mathbf{L}_k + \hat{\mathbf{P}}_k^{-1} \right)^{-1} \end{aligned} \tag{9}$$

Here, both $\bar{\mathbf{x}}_k$ and $\bar{\mathbf{P}}_k$ are presented in a space form and depend on their predicted versions. Also, the state-transition matrix $\mathbf{F}_{k-1}$ is assumed to be the identity matrix $\mathbf{I}$, which results in a purely random walk evolution model. For clarification, a random walk evolution model describes a simple process in which the next state only depends on the previous state and a fixed probabilistic variation which is provided in terms of variance. In our case, when $\mathbf{F}$ is equal to $\mathbf{I}$, Eqs 7, 8 become $\mathbf{x}_k = \mathbf{x}_{k-1}$ and $\mathbf{P}_k = \mathbf{P}_{k-1} + \mathbf{Q}_{k-1}$, respectively, which, in turn, shows that the variation from the previous state is given only by $\mathbf{Q}_{k-1}$. Ideally, matrix $\mathbf{F}$ could incorporate magneto-hydrodynamics to predict the temporal evolution of the dayside magnetospheric region; however, the process of discretizing the MHD equations into a matrix would increase the complexity of the inverse problem. Previous studies demonstrated that a random walk evolution framework, along with continuous observations of the states, yields good results that are superior to static reconstructions (Zhang et al., 2005; Butala et al., 2010).

The iterative implementation of Eq. 9 provides time-dependent estimations of the state $\bar{\mathbf{x}}_k$, and is known as Kalman filtering (KF). Typically, KF requires the use of the full covariance matrix $\mathbf{P}_k$ with N^2 elements. The high memory allocation needed for this process fostered the development of the TomoScand Gaussian Markov Random Field (TS-GMRF) approach (Norberg et al., 2023; 2018). In TS-GMRF, Eqs 7, 8 are simplified using $\mathbf{F}_{k-1} = \mathbf{I}$, and it is assumed that the predicted distribution (in Eq. 8) can be approximated with $\mathbf{Q}_{k-1}$, i.e., $\hat{\mathbf{P}}_k \approx \mathbf{Q}_{k-1}$. Also, the TS-GMRF approach constructs the matrix $\mathbf{Q}^{-1}$, known as the "precision matrix," using correlation lengths for the three dimensions (l_r, l_ϕ, l_θ), a standard deviation function $\boldsymbol{\sigma}(\mathbf{r})$, and an ensemble of sparse differential matrices that impose smoothness on the estimated state vector $\mathbf{x}_k$. Hence, when matrix $\mathbf{Q}^{-1}$ is provided, we can rewrite Eq. 9 as

$$\bar{\mathbf{x}}_k = \left(\mathbf{L}_k^{\mathrm{T}} \mathbf{R}_k^{-1} \mathbf{L}_k + \mathbf{Q}_{k-1}^{-1} \right)^{-1} \left(\mathbf{L}_k^{\mathrm{T}} \mathbf{R}_k^{-1} \mathbf{y}_k + \mathbf{Q}_{k-1}^{-1} \bar{\mathbf{x}}_{k-1} \right) \tag{10}$$

It is noteworthy that not only the precision matrix $\mathbf{Q}_k^{-1}$, but also the observation matrix $\mathbf{L}_k$ is sparse due to the measurement geometry, such as the resulting system in Eq. 10 remains sparse and allows exploiting this property for efficient computation.

For the sake of clarification, the correlation length (l) is defined as the maximum distance between two points in the solution domain (e.g., x^{r_1}, x^{r_2} at locations r_1 and r_2) where the covariance of their physical values drops to 10% of the variance, i.e., $l = \underset{l}{\operatorname{argmin}} \left(\operatorname{Cov}(x^{r_1}, x^{r_2}) - 10\% \times \operatorname{Var}(x^{r_1}) \right)$. The standard deviation function $\boldsymbol{\sigma}(r)$ used in constructing $\mathbf{Q}^{-1}$ is a $[N \times 1]$ vector that provides a standard deviation value to each voxel in the solution domain. Its mathematical definition is specific for the 3-D structure to be reconstructed and will be presented in Section 3. Also, the reader is referred to (Norberg et al., 2018; Cucho-Padin et al., 2022) for further details on implementing matrix $\mathbf{Q}^{-1}$.

2.3 Assessment of 3-D tomographic reconstructions

To assess the confidence of our time-dependent, 3-D tomographic retrievals of soft X-ray emissivities, we use the residual error and the Structural Similarity index (SSIM). The residual error is defined by

$$Res.Error = 100\% \times \frac{\|\mathbf{y}_k - \mathbf{L}_k \bar{\mathbf{x}}_k\|_2}{\|\mathbf{y}_k\|_2} \tag{11}$$

and denotes the agreement between the 3-D estimated emissivities $\bar{\mathbf{x}}_k$ and the input radiance data $\mathbf{y}_k$.

The SSIM index is defined as

$$SSIM = \frac{\left(2\mu_{\mathbf{x}_g}\mu_{\bar{\mathbf{x}}} + C_1\right)\left(2\sigma_{\mathbf{x}_g\bar{\mathbf{x}}} + C_2\right)}{\left(\mu^2_{\mathbf{x}_g} + \mu^2_{\bar{\mathbf{x}}} + C_1\right)\left(\sigma^2_{\mathbf{x}_g} + \sigma^2_{\bar{\mathbf{x}}} + C_2\right)} \tag{12}$$

where the terms $\mu_{\mathbf{x}_g}$ and $\sigma^2_{\mathbf{x}_g}$ denote the mean and variance of the ground truth vector $\mathbf{x}_g$, the terms $\mu_{\bar{\mathbf{x}}}$ and $\sigma^2_{\bar{\mathbf{x}}}$ indicate the mean and variance of estimated emissivity vector $\bar{\mathbf{x}}$, and the term $\sigma_{\mathbf{x}_g\bar{\mathbf{x}}}$ represents the covariance between $\mathbf{x}_g$ and $\bar{\mathbf{x}}$. Also, the constant values $C_1 = (K_1 D)^2$ and $C_2 = (K_2 D)^2$ where D is the dynamic range of $\mathbf{x}$, i.e., $D = \max(\mathbf{x}_g) - \min(\mathbf{x}_g)$, and we use $K_1 = 0.01$ and $K_2 = 0.03$ as recommended in (Wang et al., 2023; Cucho-Padin et al., 2024). The index SSIM has values from 0 to 1, where SSIM = 1 indicates that the two input vectors are identical.

3 Numerical experiments

In this section, we simulate soft X-ray photon flux acquired from a sensing platform with a high inclination and circular orbit around Earth during solar wind transient conditions. Also, we describe the proposed spacecraft ephemerides along with specifications of the proposed experiments.

3.1 Assumed magnetosheath soft X-ray emissions

We follow the next steps to generate the ground truth vector $\mathbf{x}_g$ of soft X-ray emissivities. First, we use the magnetohydrodynamic (MHD) Open Geospace General Circulation Model (OpenGGCM) simulation reported in (Connor et al., 2021) to obtain the global spatial distributions of protons in the inner and outer magnetospheric region during controlled solar wind conditions. Using linear interpolation, we extract the OpenGGCM plasma data in the region of X_{GSE}, Y_{GSE}, $Z_{GSE} \sim [-20, 20]R_E$ with a spatial resolution of 0.1 RE. This spatial configuration defines a rectangular grid that contains $N^R = 64,481,201$ voxels. In this proof-of-concept study, we aim to reconstruct the magnetosheath under varying solar wind magnetic conditions; thus, we conducted a 1-h MHD simulation with a 1-min resolution wherein the IMF suddenly varies from $[B_x, B_y, B_z] = [0, 0, 5]$ nT to $[B_x, B_y, B_z] = [0, 0, -5]$ nT at the 10th minute of the simulation. Values of solar wind density and velocity are assumed to be constants with values $n_{sw} = 10$ [cm^{-3}], $v_{sw} = 400$ [km sec^{-1}].

Second, we identify and extract the proton population from the inner magnetospheric region simulated by the MHD model. Since this region does not contain sufficient heavy solar wind ions, it will not yield significant soft X-ray emission. For this task, we utilized the approach described by Samsonov et al. (2022), which determines the location of the inner magnetosphere through the following equations:

$$\begin{aligned} p &< p\,(msp) + \Delta p \\ V_x &> V_x\,(sw) \times k_v, \end{aligned} \tag{13}$$

where $p(msp)$ is the thermal pressure of the magnetospheric region, $V_x(sw)$ is the solar wind along the x-axis, and the variables Δp and k_v are manually selected to adjust the comparison. For each 1-min MHD model, the thermal pressure of the magnetosphere is calculated, spanning values between 0.05 and 0.1 [nPa]. Also, $V_x(sw)$ is set to −400 [km sec^{-1}], and we assume $\Delta P = 0.2$ nPa and $k_v = 0.15$ as recommended in (Samsonov et al., 2022). If both conditions in Eq. 13 are matched, that location is considered part of the inner magnetosphere and should be removed from the analysis.

Third, we use a spherically symmetric neutral exosphere whose density distribution (n_H) is given by (Connor and Carter, 2019):

$$n_H(r) = n_0\left(\frac{10R_E}{r}\right)^3 \text{[atoms cm}^{-3}\text{]} \tag{14}$$

where n_0 is the hydrogen (H) density at 10 R_E subsolar point and equal to 25 [atoms cm^{-3}], and the term r denotes the planetocentric distance in units of R_E. Also, we adopt an efficiency factor $\alpha = 1 \times 10^{-15}$ [eV cm^2]. Finally, the global volumetric emissivity P can be directly calculated using Equation 2.

Figure 1 shows the temporal evolution of magnetosheath soft X-ray emissivities as a response to varying solar wind conditions, which will be denoted as $\mathbf{x}_{g_k}$ and will serve as the ground truth emissivities to be reconstructed. The top panel of Figure 1 shows the Bz component of the IMF. The bottom panel is subdivided into three rows displaying the ecliptic plane (XY_{GSE}) and a 3-D visualization of the emissivities at the (A) 5$^{\text{th}}$, (B) the 20$^{\text{th}}$ and (C) the 55$^{\text{th}}$ minute after the start of the simulation.

3.2 Spacecraft mission design

Model-free, time-dependent, and 3-D tomographic reconstructions of soft X-ray emissivities in the magnetospheric region require simultaneous observations from distinct vantage points that can provide sufficient spatial information about the target. In this context, we evaluate tomographic reconstructions using a two-satellite configuration based on the results reported by Jorgensen et al. (2022), which indicate that using two soft X-ray imagers significantly reduces the estimation error obtained with a single instrument. Also, in a realistic scenario, using two satellites would reduce the cost of implementing additional space-based platforms and imaging sensors.

Our design of a spacecraft orbit closely follows that one proposed by Sibeck et al. (2023) for the Solar-Terrestrial Observer for the Response of the Magnetosphere (STORM) mission concept, whose objective is to continuously track and quantify the flow of solar wind energy through the magnetosphere using a set of optical instruments that measure energetic neutral atom (ENA) from the ring current, far ultraviolet (FUV) emission from the auroral region, and soft X-ray emission mainly from the dayside magnetosheath. Our study focused on the analysis of the soft X-ray measurements. The STORM mission concept comprises a single spacecraft in a circular orbit with a radius of $30R_E$ and an inclination of 90° with respect to the ecliptic plane. The orbit's orientation is nearly fixed in the inertial frame, allowing the Sun-Earth direction to rotate 360° relative to the orbit over 6 months. The spacecraft is three-axis controlled, with one body axis always to the nadir and the other two axes controlled to keep the sun on one side of the vehicle. Further, the soft X-ray imager onboard the STORM mission has a square field-of-view (FOV) of 23 [deg] and a constant boresight direction canted 18.5 [deg] towards the sun

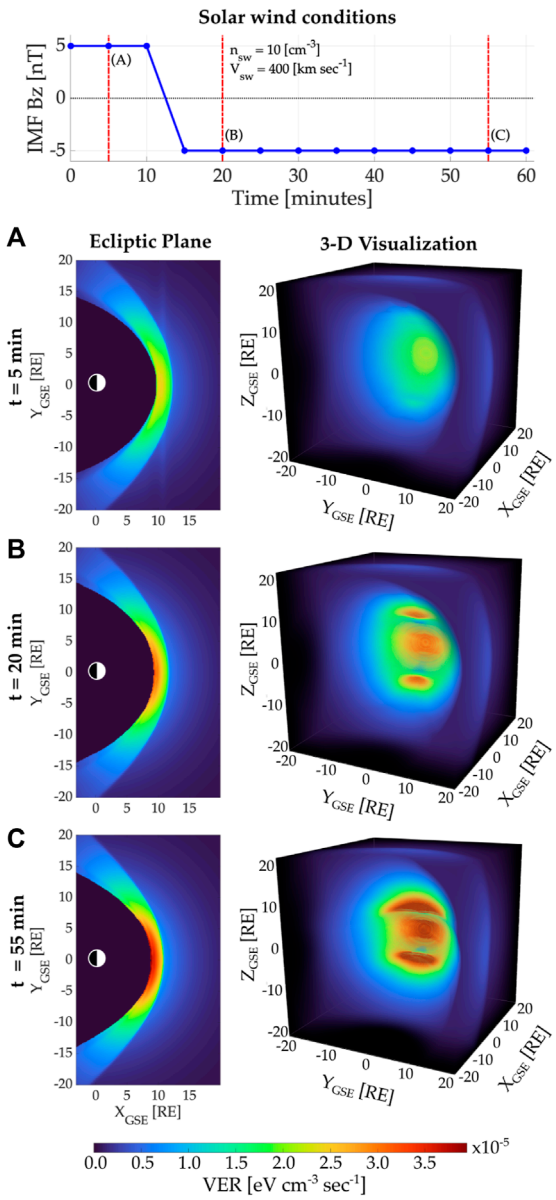

FIGURE 1
Temporal evolution of magnetosheath soft X-ray emissivities as a response to IMF conditions. The top panel displays IMF Bz values used in this study to simulate the magnetospheric model. The bottom panels show the ecliptic plane and 3-D visualization of the ground truth emissivities for three periods of time: **(A)** 5 min, **(B)** 20 min, and **(C)** 55 min after the start of the simulation.

direction in the spacecraft body frame. Aside from periods of low orbital beta angle (Sun near the plane of the orbit), this design allows nearly continuous imaging of the subsolar point at 10 R_E (nominal location of the magnetopause).

The objective of this manuscript is to conduct a comparison study of tomographic reconstructions of the dayside magnetosheath from soft X-ray observations acquired by two satellites in STORM-like orbits. For this, we simulated seven (7) spacecraft with different phase angles but similar longitudinal locations that will be arranged in pairs for the tomographic process. Figure 2 shows the distributions of these satellites named spacecraft 0 (SC0) to spacecraft 6 (SC6) along the circular orbit (gray curve). The phase angles between satellites are fixed, and their values (in units of degrees) with respect to SC0 are SC1: 60 [deg], SC2: 75 [deg], SC3: 90 [deg], SC4: 105 [deg], SC5: 120 [deg], and SC6: 180 [deg].

3.3 The impact of orbit selection on tomography feasibility

In this work, we assert that tomographic reconstruction can be performed if and only if the two imaging instruments observe a given target from different vantage points simultaneously. Although this condition is ensured by our design of the imager's boresight direction that allows nearly continuous observation of the subsolar point at 10 R_E, there are periods of time in which one or two imagers point sunward. To avoid contamination from direct sunlight, we define a Sun-Earth avoidance angle equal to 45 [deg]. In other words, if the angle created by the Sun-Earth line (X_{GSE}) and the LOS direction ($\hat{\mathbf{n}}$) of a pixel in a soft X-ray imager is smaller than 45 [deg], we consider that tomography is not possible for this satellite's 3-D position.

Based on the previous requirements, Figure 3 shows locations (in GSE spherical coordinates) where tomography is feasible using a pair of spacecraft for a period of 6 months. In each panel, the gray dots indicate the 1-h interval position of the SC0 (at $r \approx 30R_E$) during a complete translation around Earth. The blue dots show locations where SC0 and SCX (with X $\in [1,2,3,4,5,6]$) simultaneously acquire soft X-ray radiance data free from sunlight contamination, i.e., tomography is possible. The number of locations to perform tomography significantly reduces as the phase angle between SC0 and SCX reaches 180 [deg], especially near the low-latitude region, as shown in the bottom right panel (SC0 and SC6). In order to conduct a comparison study of tomographic estimations using these six two-satellite configurations, we selected two vantage points for SC0 where tomography is feasible with all the remaining spacecraft. They are named P1 and P2 and are depicted as red stars in all six panels. Their specific positions in GSE Cartesian coordinates are P1 = [4.846, −14.143, −26.085] R_E and P2 = [3.941, 14.679, 25.827] R_E.

Figure 4 shows additional analysis for tomographic feasibility using these two-satellite configurations. Each panel shows a histogram of the number of hours when tomography is possible (using SC0 and SCX) with respect to the ecliptic longitude. The histogram dataset has been generated from data shown in Figure 3 that were accumulated along a 10-deg bin in the longitudinal dimension. The total number of hours when tomography can be performed is included on the top left of each panel. In a period of 6 months, tomography can be conducted between 1736 h (using SC0 and SC6) and 2,503 h (using SC0 and SC1). In addition, the number of hours when tomography is feasible remains nearly consistent (at ~ 110 h) for all six cases when SC0 is located near the terminators (dawn and dusk regions or ecliptic longitudes around ±90 [deg]).

Furthermore, the total number of hours in a 6-month period is ~4,320, which indicates that each spacecraft configuration can perform tomography between 40% and 57% of this period. Nevertheless, due to the geometry constraints, continuous

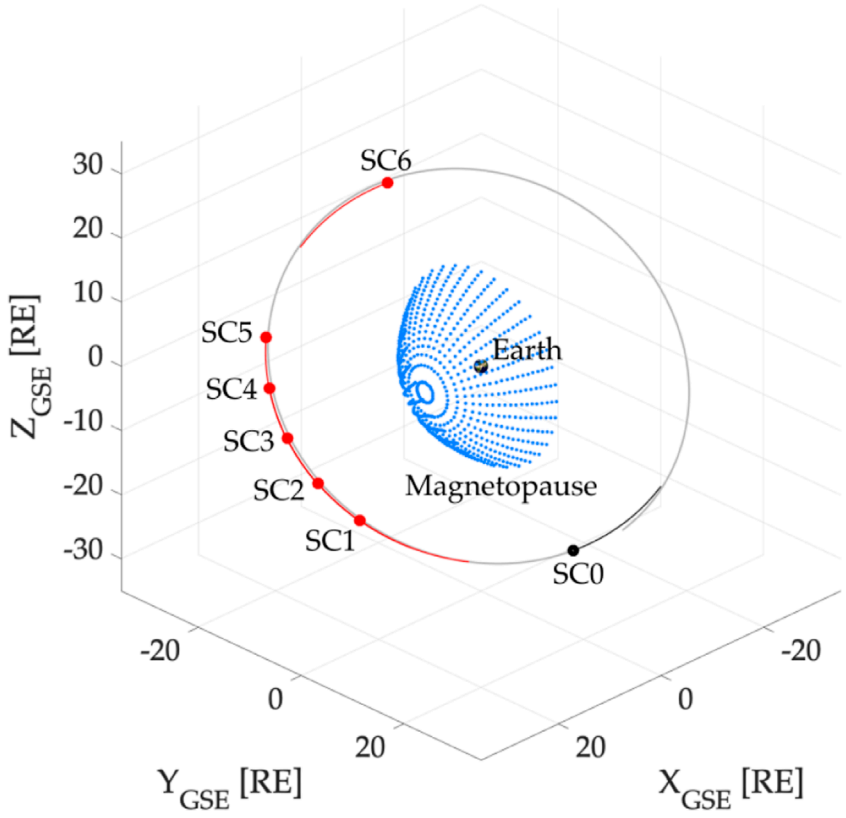

FIGURE 2
The spacecraft mission has been designed to have a circular orbit (grey solid line) with a radius of 30 RE and an inclination of 90° with respect to the ecliptic plane. The black dot shows the location of spacecraft 0 (SC0), and the red dots show the location of spacecraft one to 6 (SC1 – SC6). Blue dots show an example of a temporally static dayside magnetopause. In this study, we evaluate the feasibility of tomographic estimation of soft X-ray emissivities using ensembles of two spacecraft with SC0 as the reference satellite.

acquisition along a longitudinal bin for ~120 h and covering all latitudes is possible only near the terminators, as shown in Figure 3.

3.4 Four-dimensional tomographic reconstructions of soft X-ray emissivities

In this subsection, we define the experiments needed to evaluate the efficiency of the tomographic results using a two-satellite configuration. Also, we describe the generation of synthetic soft X-ray images and the details of implementing the dynamic tomographic approach.

3.4.1 Experiment settings

We established six experiments with each pair of satellites (SC0/SCX) that include dynamic tomographic reconstructions of the ground truth soft X-ray emissivities from two vantage points (P1 and P2) every 5 min for a 1-h period. Note that the ground truth emissivities ($\mathbf{x}_g$) have a 1-min resolution (see specifications in Section 3.1, while our tomographic reconstructions will be performed every 5 min since this is the expected integration time (t_{int}) achieved by the soft X-ray imager (Cucho-Padin et al., 2024).

Figure 5 shows examples of viewing geometry for tomographic reconstruction using a two-satellite configuration. Each row shows the acquisition geometry using the SC0/SCX configuration when the SC0 is at a given vantage point PY (with Y $\in [1,2]$). The black and red solid lines indicate the imaging sensors' boresight of SC0 and SCX, respectively. Note that, in all cases, the intersection of boresights occurs near the subsolar point at 10 R_E.

3.4.2 Generation of synthetic measurements

To generate synthetic soft X-ray images for each experiment, we first define the pixel resolution of the imaging sensor to be 0.25×0.25 [deg^2], similar to that specified for NASA's LEXI experiments in (Cucho-Padin et al., 2024). This value, along with the sensor's FOV of 23 [deg], yields a 2-D image of 92×92 pixels. Next, for each pixel, we calculate its 3-D position and LOS direction ($\hat{\mathbf{n}}$) and intersect them with the rectangular grid of ground truth emissivities ($\mathbf{x}_{g_k}$) to generate the observation matrix $\mathbf{L}_k^R$ with size $[M \times N^R]$, where $M = 92 \times 92 \times 2 = 16,298$ measurements, $N^R = 64,481,201$ voxels (see Section 3.1) and the super index R indicates the use of the rectangular grid. Following the forward emission model presented in Eq. 5 and considering that, in this study, soft X-ray measurements are noise-free and background-free, we can calculate the vector of observations as follows $\mathbf{y}_k^R = \mathbf{L}_k^R \mathbf{x}_{g_k}$. Note that we considered the satellites' displacement during the 5-min acquisition period such that all observation matrices $\mathbf{L}_k^R$ are different when $k \in [1, 13]$.

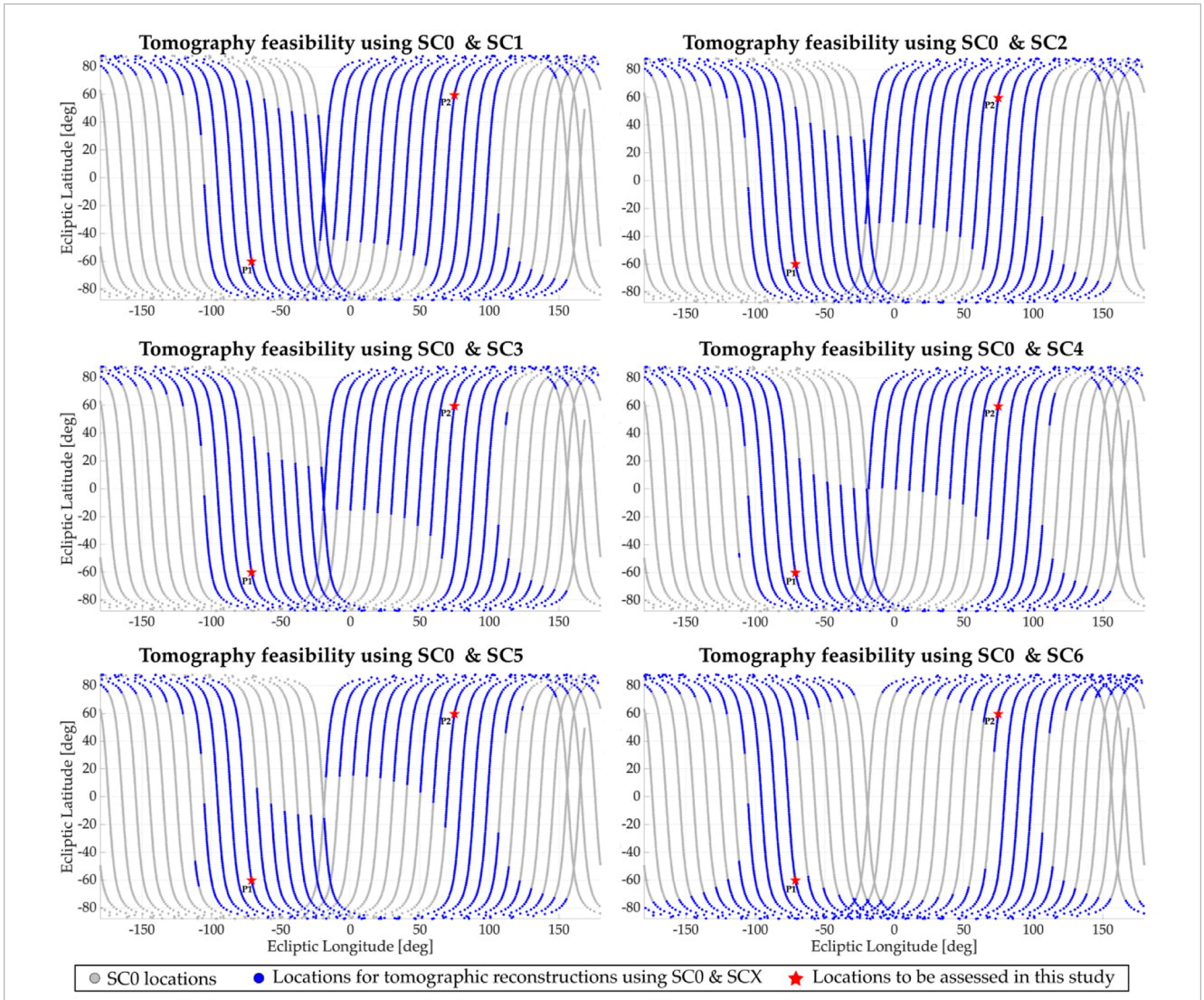

FIGURE 3
Each panel shows the locations of SC0 during a complete translation of the satellite around Earth (6-month period). The blue dots indicate positions where a tomographic reconstruction of the magnetosheath emissivity is possible using both SC0 and SCX ($X \in \{1,2,3,4,5,6\}$). Gray dots indicate locations where tomography is not feasible since one or both sensors are contaminated by direct sunlight. The red stars (named P1 and P2) indicate vantage points for SC0 where tomographic reconstructions using SC0/SCX data are evaluated in this study.

Figure 6 shows an example of a 3-D viewing geometry to generate synthetic soft X-ray measurements. In this case, SC0 is located at vantage point P1, and the SC3 position corresponds to a phase angle of 90 [deg] with respect to SC0. The 3-D soft X-ray emissivities (VER) displayed in the left panel correspond to the start of the simulation ($k = 1$). The green pyramids represent the sensor FOV of 23 [deg], and the two panels on the right show the synthetic images acquired from each spacecraft. Due to the extension of the FOV, the imaging sensors are able to capture features of the high-altitude cusp (see SC3's image at coordinates [-10,10] [deg]). For the sake of clarification, these two $[92 \times 92]$ pixel images, sorted in a single column vector, form the set of measurements $\mathbf{y}_{k=1}^{R}$ corresponding to the SC0/SC3 configuration. Our MHD simulations of the magnetosphere and their corresponding soft X-ray emissivities have been calculated for a 1-h period with a 1-min resolution and can be identified by their timestamps $t = \{0, 1, 2, \ldots, 60\}$; however, tomographic reconstructions do not follow this temporal sequence as they will be executed every 5 min. The following array shows the correspondence between time t, associated with the MHD simulations, and the time k used in our estimation approach: $\{(k = 1, t = 0), (k = 2, t = 5), \ldots, (k = 5, t = 20), \ldots, (k = 12, t = 55), (k = 13, t = 60)\}$.

3.4.3 Tomographic inversion process

In this study, we utilized a solution domain that was smaller and had lower spatial resolution than the ground truth rectangular grid, which is more appropriate for this testing stage. For the selection, we considered the following requirements: (i) the volume of this region should include the actual coverage reached by the FOV of both instruments from all vantage points used in the experiments, and (ii) the voxel sizes of this region should secure

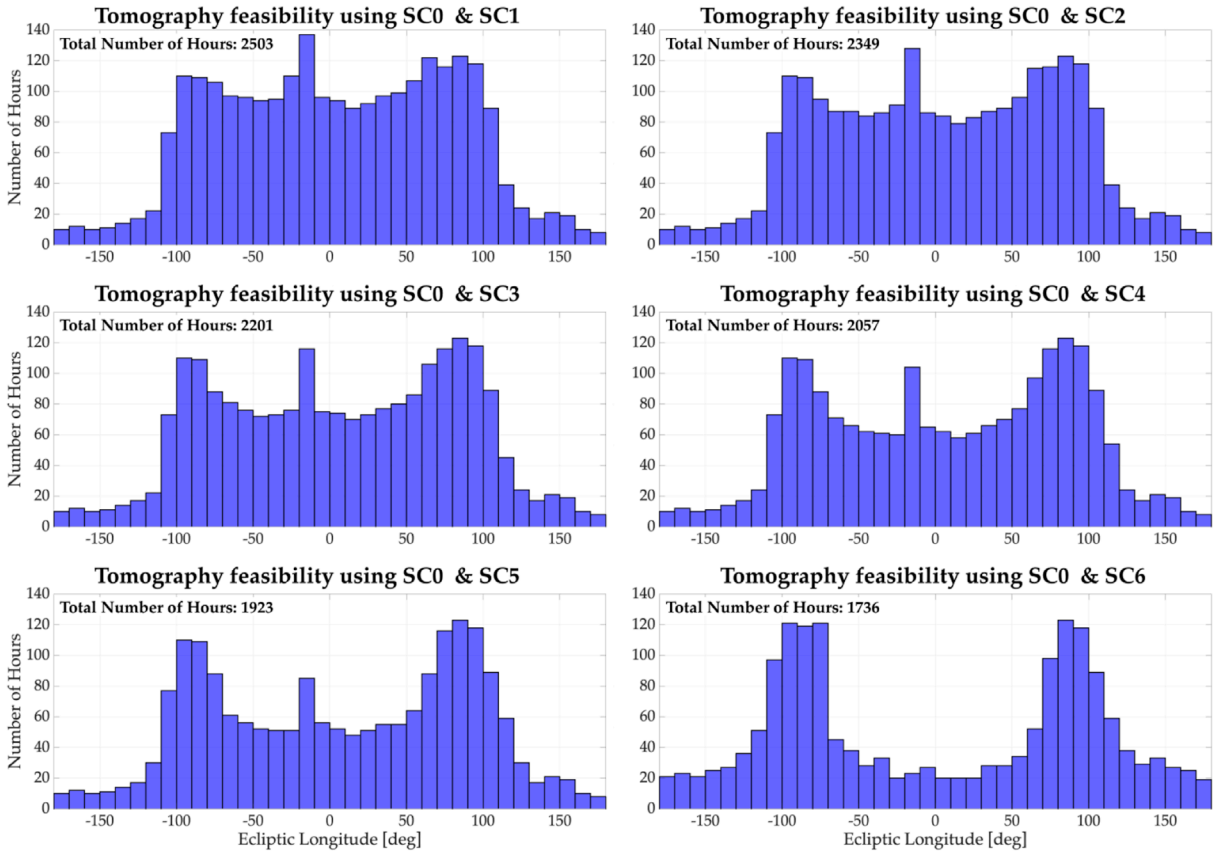

FIGURE 4
Each panel shows a histogram of the number of hours when tomographic reconstruction is possible using SC0 and SCX (X ∈ {1,2,3,4,5,6}) per longitudinal bin (10° widths). The dataset used for each panel corresponds to a complete translation of the satellite around Earth, i.e., a 6-month period.

the correct interpretation of spatial gradients in the soft X-ray emissivity distributions. Thus, our solution domain is a spherical region with the following dimensions in GSE coordinates: radial (r) ∈ $[3.75, 20.05]R_E$, azimuthal (ϕ) ∈ [-110, 100] degrees, and co-latitudinal (θ) ∈ [0, 180] degrees. Also, this region is divided into spherical voxels with sizes $\Delta r = 0.1R_E$, $\Delta\phi = \Delta\theta = 10$ [deg]. The number of voxels per dimension is $N_r = 163, N_\phi = 22$, and $N_\theta = 18$, and the total number of voxels for this spherical grid is $N^S = 64,548$. This spherical grid contains most of the soft X-ray emissivities produced on Earth while discarding zones not observed by the optical sensors in the proposed experiments.

We then intersect each pixel's LOS with the spherical grid to generate the observation matrix $\mathbf{L}_k^S$ and define the inverse problem as $\mathbf{y}_k^R = \mathbf{L}_k^S \bar{\mathbf{x}}_k$ where the only unknown is $\bar{\mathbf{x}}_k$ (the super index S indicates the use of the spherical grid). Note that using measurements obtained from a high-resolution grid, $\mathbf{y}_k^R$, imposes a scaling problem in our study that is worth investigating to determine the trade-off between reconstruction errors (e.g., expected over- and underestimation of retrieved emissivities) and the effective usage of computational resources.

The tomographic reconstructions start at $k = 1$ and, according to Eq. 10, it requires an estimated vector of emissivities for $k-1$, $\bar{\mathbf{x}}_0$. For this, we created a prior reference of emissivities using Shue et al. (1998) and Jelínek et al. (2012) models to identify the location of the magnetopause and bow shock, respectively, from the solar wind conditions used to generate the ground truth emissivities at $k = 1$. Then, we fill out the magnetosheath and outer magnetospheric regions with soft X-ray emissivities using the parametric formulation described by Jorgensen et al. (2019a) (see Eq. (8) in the reference) and with parameter values $A_1 = 3.2285 \times 10^5$ eV cm^{-3} s^{-1}, $B = -1.7985 \times 10^5$ eV cm^{-3} s^{-1}, α= 2.4908, $\beta = -1.6458$, $A_2 = 1.3588 \times 10^{-5}$ eV cm^{-3} s^{-1}. These parameters are identical to those shown as an example in (Jorgensen et al., 2019a). It is noteworthy that we do not intend to provide similar emissivities to the ground truth at $k = 1$ since our method will correct those values and their spatial distributions with the input measurements.

To generate the covariance matrix of measurements, $\mathbf{R}_k$, we consider that soft X-ray observations, $\mathbf{y}_k$, are primarily contaminated by Poisson-distributed shot noise, i.e., $y_k \sim Poiss(\lambda)$ where λ acts as the mean and variance of the probability distribution. Since the statistical tomography approach introduced in Section 2 establishes that all random vectors involved in the inverse problem should follow a Gaussian probability distribution, we use the approximation $Poiss(\lambda) \approx \mathcal{N}(\lambda, \lambda)$ for each measurement (see Feller (1968); Hajek (2015); Cucho-Padin et al. (2024); Butala et al. (2010) for further details). Additionally, we consider that each measurement is independent of the others such that their covariance is zero, and the

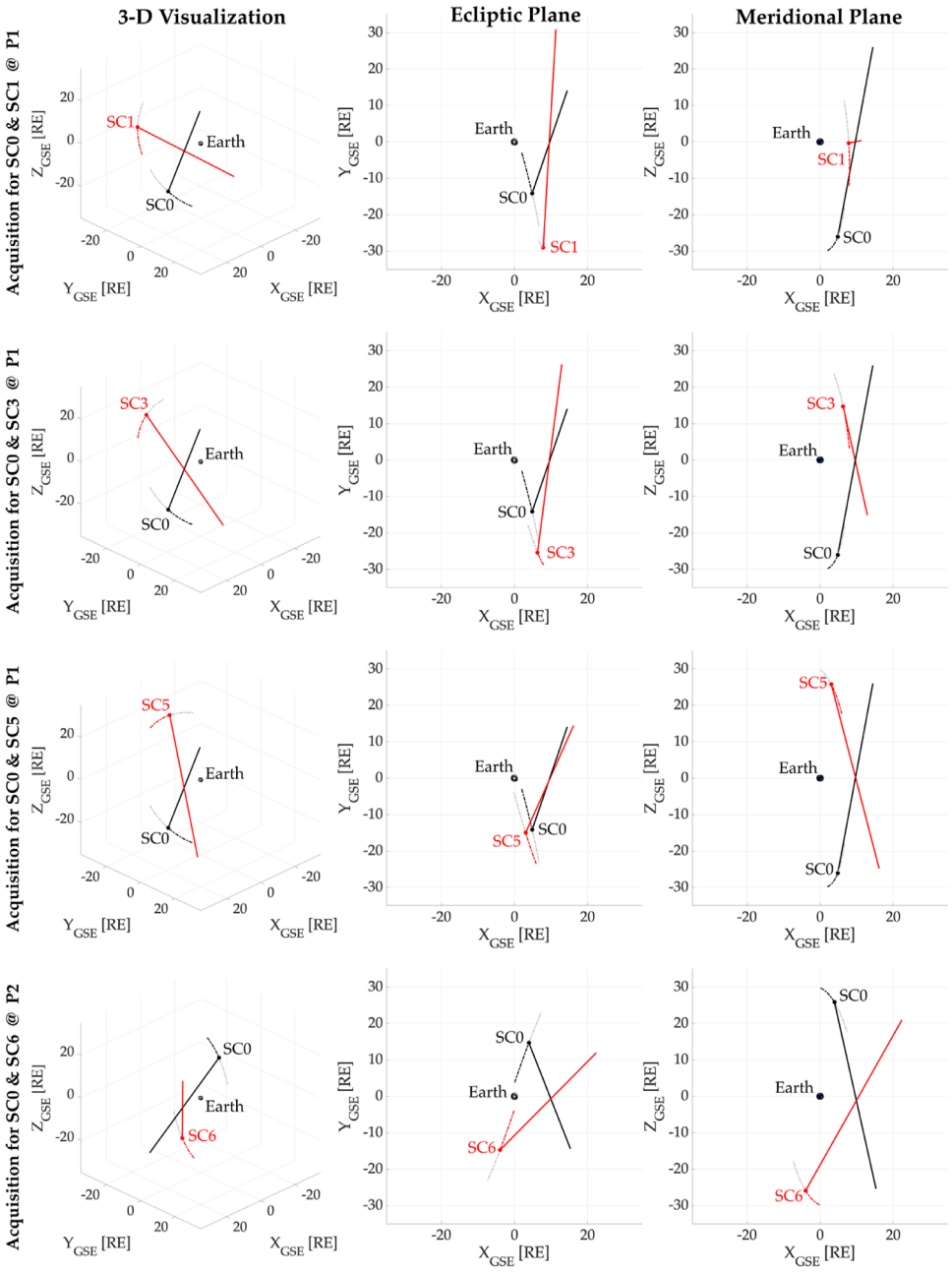

FIGURE 5
Examples of viewing geometry for tomographic reconstruction of the magnetosheath emissivity. Each row shows the locations (dots) and orbits (curved solid lines) of SC0 and SCX. The solid straight lines represent the boresight of the soft X-ray imagers in the satellites.

value of λ is the actual y measurement as it is the high-probability realization of $Poiss(\lambda)$. As a result, $\mathbf{R}_k$ is defined as a diagonal matrix whose variance elements are the values of $\mathbf{y}_k$, i.e., $\mathbf{R}_k = \mathrm{diag}(\mathbf{y}_k)$.

To generate the precision matrix $\mathbf{Q}_{k-1}^{-1}$, we closely follow the implementation provided in Eqs 7-9 in (Cucho-Padin et al., 2022). This formulation requires (i) 3-D correlation lengths and (ii) a standard deviation function, $\boldsymbol{\sigma}_{k-1}$. We selected correlation lengths that have been previously tested and used in Cucho-Padin et al. (2024) in the context of magnetosheath tomography with values $l_r = l_\phi = l_\theta = 4[R_E]$. On the other hand, the implementation of the function $\boldsymbol{\sigma}_{k-1}$ follows the piece-wise approach reported by Norberg et al. (2023) (see Eq. 9 in the reference), which provides values of standard deviation to voxels along radial profiles within the solution domain and can be expressed as follows.

$$\boldsymbol{\sigma}(r)_{k-1} = \begin{cases} \sigma_1 \times \exp\left(\left(r - r_{k-1}^{mp}\right)/\beta_1\right), & r^{min} < r < r_{k-1}^{mp} \\ \sigma_2(r), & r_{k-1}^{mp} < r < r_{k-1}^{peak} \\ \sigma_3 \times \exp\left(-\left(r - r_{k-1}^{peak}\right)/\beta_2\right), & r_{k-1}^{peak} < r < r^{max}. \end{cases} \tag{15}$$

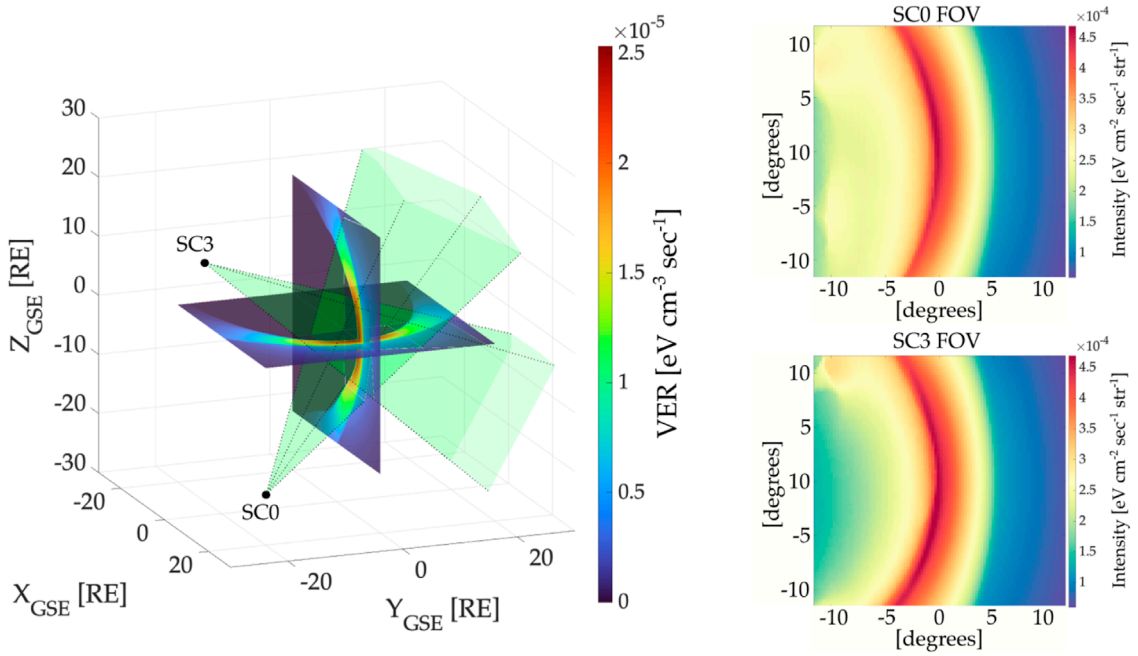

FIGURE 6
Example of 3-D viewing geometry for tomographic reconstructions of magnetosheath emissivities. In the left panel, the colored slices represent the meridional and ecliptic planes of the soft X-ray volumetric emissivities. The black dots indicate the location of the spacecraft 0 and three at time $t = 0$. The green pyramids represent the instrument FOV, whose interception occurs near the subsolar point at 10 R_E. The right panel shows two synthetic 2-D images observed by the SC0 (top sub-panel) and the SC3 (bottom sub-panel) as a result of evaluating Eq. 3 along the pixels' LOS.

To explain the spatial structure of $\boldsymbol{\sigma}(r)_{k-1}$, we also define the 3-D matrix $\mathbf{x}_{k-1}(r,\phi,\theta)$ with size $[N_r \times N_\phi \times N_\theta]$, which is the 3-D spatial rearrangement of elements in vector $\mathbf{x}_{k-1}$. Thus, in Eq. 15, the terms r^{min} and r^{max} denote the minimum and maximum radius of the solution domain with values 3.75 and 20.05 R_E, respectively. The term r^{mp}_{k-1} is the estimated location of the magnetopause, which is calculated as the position of the highest first derivative along a radial profile of $\mathbf{x}$, i.e., $r^{mp} = \underset{r}{\text{argmax}}\{\partial \mathbf{x}_{k-1}(r,\phi=\phi_0,\theta=\theta_0)/\partial r\}, \forall r \in [r^{min}, r^{max}]$ (Cucho-Padin et al., 2024). The value of r^{peak}_{k-1} indicates the location of the highest emissivity in $\mathbf{x}_{k-1}$ that is within the magnetosheath region, i.e., $r^{peak}_{k-1} = \underset{r}{\text{argmax}}\{\mathbf{x}_{k-1}(r,\phi=\phi_0,\theta=\theta_0)\}, \forall r \in [r^{min}, r^{max}]$. Also, the terms σ_1 and σ_3 are scalar factors with values equal to $\eta \times \mathbf{x}_{k-1}(r = r^{mp}_{k-1}, \phi=\phi_0, \theta=\theta_0)$ and $\eta \times \mathbf{x}_{k-1}(r = r^{peak}_{k-1}, \phi=\phi_0, \theta=\theta_0)$, respectively, and the term $\sigma_2(r)$ has the form $\sigma_2(r) = \eta \times \mathbf{x}_{k-1}(r,\phi=\phi_0,\theta=\theta_0), \forall r \in [r^{mp}, r^{peak}]$. The latter three terms show that standard deviation values are based on certain emissivity values of $\mathbf{x}_{k-1}$ that are modified by the factor η. This factor defines how much the estimated emissivity for time step k might vary from its previous value at time step $k-1$. In this study, we empirically set $\eta = 0.3$ for all the conducted experiments. Further, the term β_1 defines the exponential growth of the standard deviation of soft X-ray emissivities in the inner magnetospheric region and has been set to $\beta_1 = 5$ based on our previous experiments. The term β_2 defines the exponential decay of the standard deviation of emissivities outside the magnetosheath and follows the expression $\beta_2 = \underset{r}{\text{argmin}}\{\mathbf{x}_{k-1}(r) - \mathbf{x}_{k-1}(r^{peak}/e)\}, \forall r \in [r^{peak}, r^{max}]$, which essentially describes the scale height of emissivities beyond of the magnetosheath.

Once all matrices and vectors indicated on the right-hand side of Eq. 10 are provided, we can estimate $\bar{\mathbf{x}}_k$. Then, the process is repeated to obtain $\bar{\mathbf{x}}_{k+1}$ using (i) a new set of observations $\mathbf{y}_{k+1}$, (ii) the corresponding observation matrix $\mathbf{L}_{k+1}$, and covariance matrix of measurements $\mathbf{R}_{k+1}$, (iii) the previous solution $\bar{\mathbf{x}}_k$, and (iv) a new precision matrix $\mathbf{Q}_k^{-1}$ derived from values of $\bar{\mathbf{x}}_k$ according to Eq.15.

3.4.4 Tomographic results

In this section, we present three examples of tomographic reconstructions whose viewing geometry is depicted in the three first rows of Figure 5.

Figure 7 shows the tomographic reconstruction of the magnetosheath soft X-ray emissivities using the SC0/SC1 configuration when the SC0 is located at vantage point P1. Each row shows results corresponding to periods of time: (A) $t = 5$ min, $k = 2$, (B) $t = 20$ min, $k = 5$, and (C) $t = 55$ min, $k = 12$. The first column shows the ecliptic plane of the reconstruction, and the white lines display the boundaries of the spherical grid used as the solution domain. The second column shows a 3-D visualization in GSE Cartesian coordinates. The third column shows plots comparing volumetric emissivities along the Sun-Earth line from 3.75 to 20.05 R_E geocentric distance. Here, the blue and red lines show the ground truth and reconstructed emissivities, respectively.

A visual comparison between our tomographic retrievals of soft X-ray emissivities (in the first column) and the ground truth values (presented in Figure 1) for the same time steps shows the ability of our algorithm to capture the temporal evolution

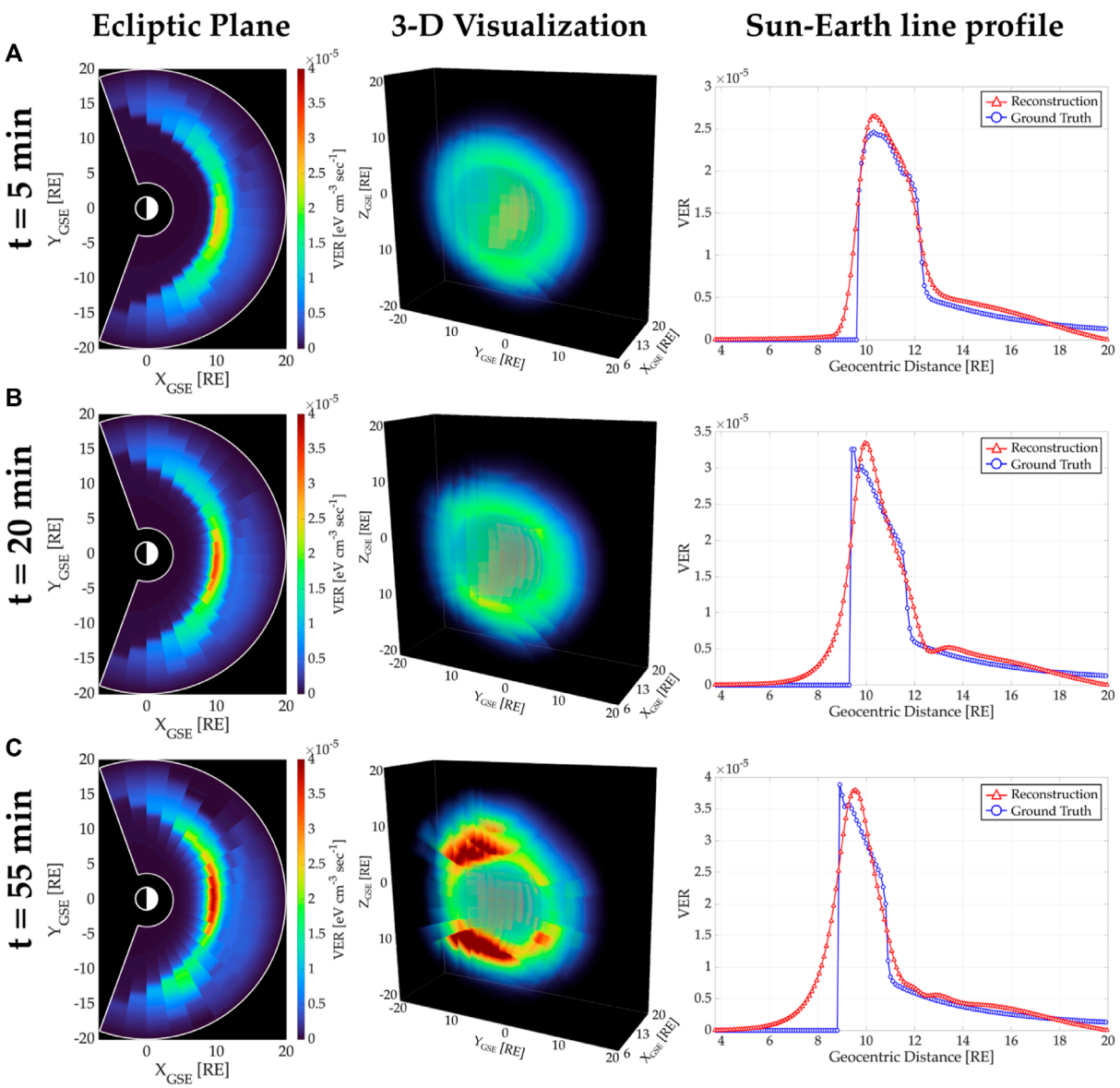

FIGURE 7
Tomographic reconstruction of the magnetosheath soft X-ray emissivities using the SC0/SC1 configuration when the SC0 is at vantage point P1. Each row corresponds to periods of time: **(A)** t =5 min, **(B)** t =20 min, and **(C)** t =55 min. The first column shows the ecliptic plane of reconstructions, the second column displays a 3-D visualization, and the third column depicts the Sun-Earth line profile of reconstructed and ground truth emissivities.

of the magnetosheath density, especially near the Sun-Earth line. The 3-D structure for time step $k = 12$ (second column, row C) shows that our methodology can reconstruct the dense high-altitude cusps even though the sensors' FOV does not fully cover them. The structures of reconstructed radial profiles (red lines in the third column) show not only the influence of our assumed exponential standard deviation function $\boldsymbol{\sigma}(r)$ but also the algorithm's ability to use observational data to yield expected emissivity spatial distributions. We acknowledge that our methodology cannot reproduce a precise structure of the magnetosheath nor the exact values of VER in the voxels since the reconstruction process is affected by the spherical geometry of our solution domain and its limited extension. Furthermore, the method is unable to yield sharp gradients in the emissivity distributions (as in the blue line), and further investigation should be done to improve the function $\boldsymbol{\sigma}(r)$ and/or to include a total variation approach (that allows piece-wise reconstruction) within the precision matrix $\mathbf{Q}_{k-1}^{-1}$. A quantitative comparison of reconstructed values with the ground truth emissivities is provided in Section 3.4.5.

With an identical format to Figure 7, 8 depicts dynamic tomographic reconstructions of the magnetosheath soft X-ray emissivities using the SC0/SC3 configuration when the SC0 is located at vantage point P1. Although the first column shows a good agreement between reconstructed and ground truth emissivity values and their spatial distributions, there is an evident depletion of emissivities at $t = 55$ min (row C) starting around noon and

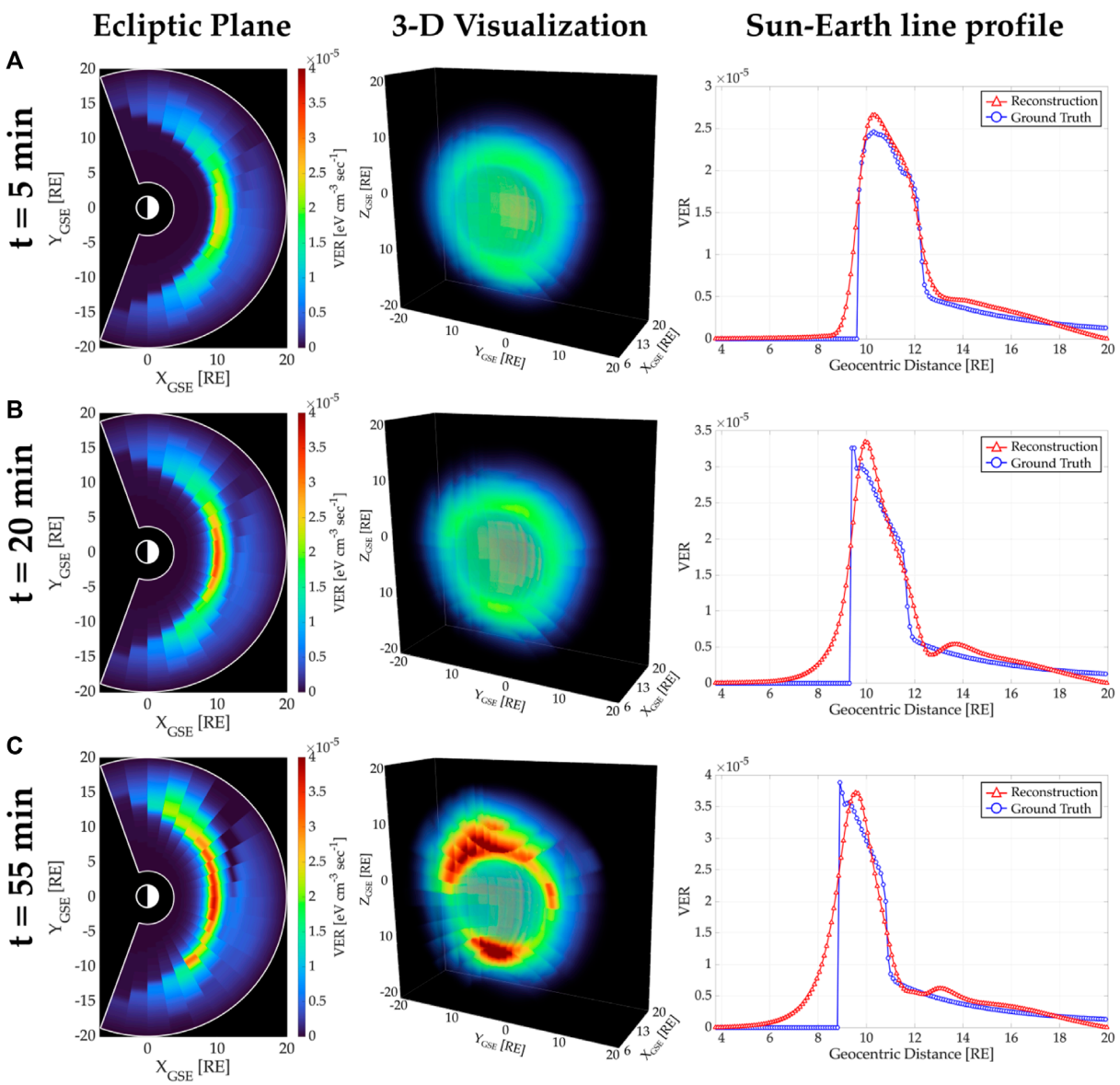

FIGURE 8
Tomographic reconstruction of the magnetosheath soft X-ray emissivities using the SC0/SC3 configuration when the SC0 is at vantage point P1. Each row corresponds to periods of time: **(A)** t =5 min, **(B)** t =20 min, and **(C)** t =55 min. The first column shows the ecliptic plane of reconstructions, the second column displays a 3-D visualization, and the third column depicts the Sun-Earth line profile of reconstructed and ground truth emissivities.

propagating towards the dusk region with an increased radial distance. This depletion is also observable in the reconstructed Sun-Earth line profile (red line in the right plot) around 12 R_E. On the other hand, the ecliptic plane (left plot) also shows enhancement of emissivities within the magnetosheath near the dawn region (~[9,-10] R_E in the XY_{GSE} plane). In order to analyze these features, we have conducted additional experiments testing several sizes of the solution domain and the voxels. The reader can observe examples of them in our previous published work (Cucho-Padin et al., 2024; 2022) in the context of static soft X-ray and exospheric tomography. Thus, these features are likely related to the usage of a solution domain smaller than the one used to generate the synthetic measurements. This condition imposes a problem in the estimated distribution of volumetric emissivities in those voxels along the measurement LOSs. In tomography, this issue is typically solved when LOSs crossing a given voxel have different angular directions, interconnecting the voxel neighborhood and ultimately providing an adequate distribution of emissivities among them. However, the LOSs from a single sensor are almost parallel, and using two sensors for the reconstructions yields only two distinct LOS directions passing through any voxel in the solution domain. Besides these limitations, the structure of the magnetosheath can be clearly identified, as well as its spatial displacement as a response to the solar wind conditions, which is the aim of this study.

Figure 9 displays dynamic tomographic reconstructions of the magnetosheath soft X-ray emissivities using the SC0/SC5

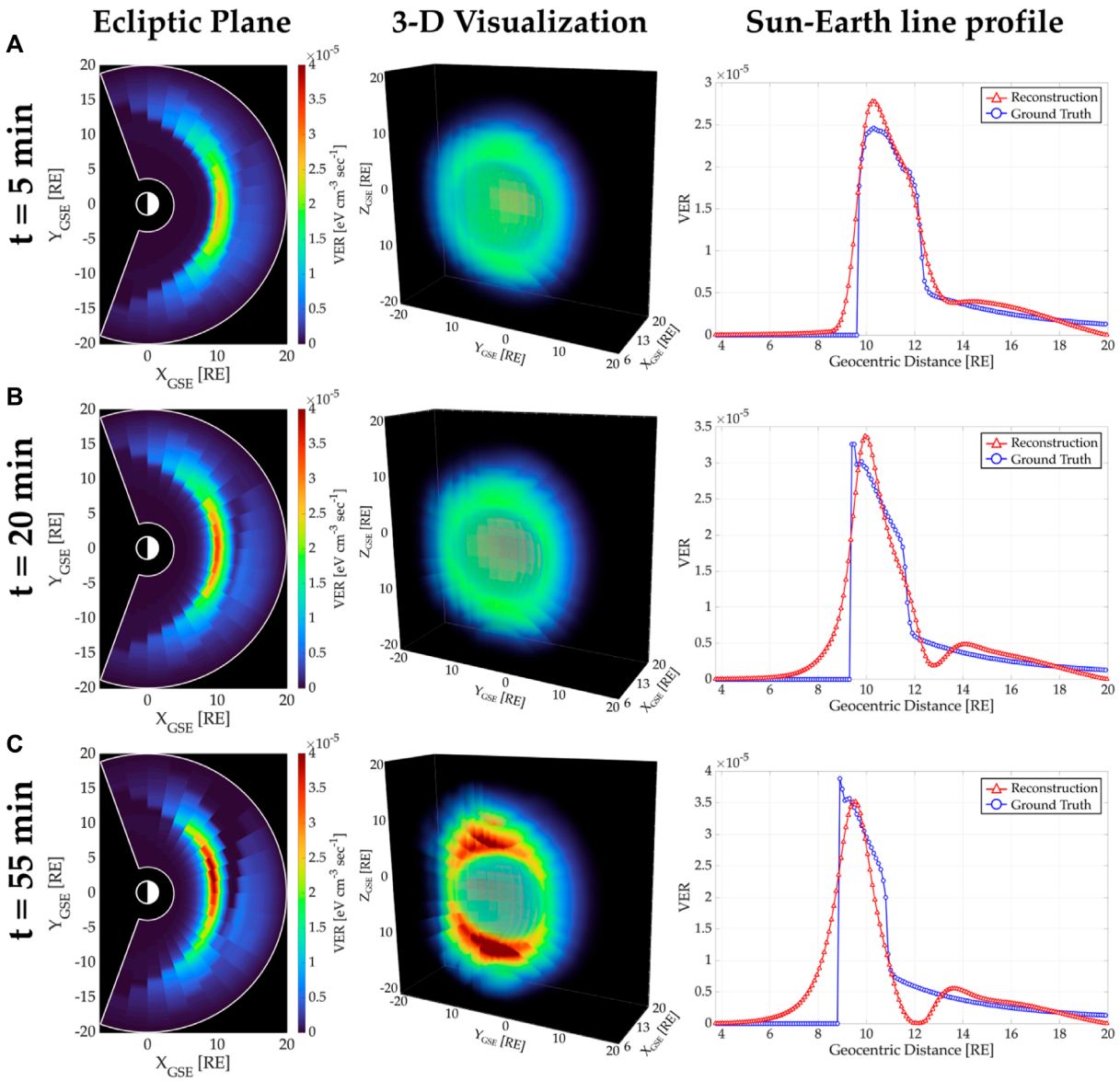

FIGURE 9
Tomographic reconstruction of the magnetosheath soft X-ray emissivities using the SC0/SC5 configuration when the SC0 is at vantage point P1. Each row corresponds to periods of time: **(A)** t =5 min, **(B)** t =20 min, and **(C)** t =55 min. The first column shows the ecliptic plane of reconstructions, the second column displays a 3-D visualization, and the third column depicts the Sun-Earth line profile of reconstructed and ground truth emissivities.

configuration when the SC0 is located at vantage point P1. This configuration produces a stronger depletion of emissivities than that one presented in Figure 8 (see row (C). This depletion adversely affects the Sun-Earth line region, as shown in the third column in row (C), around 12 R_E geocentric distance. Nevertheless, the emissivity values and their spatial distribution within the magnetosheath still exhibit good agreement with the temporal variation of the ground truth.

Another crucial factor affecting the estimation of soft X-ray emissivities is the spatial distribution of LOSs within the solution domain. Figure 10 depicts the LOS density per voxel at the ecliptic plane for the experiments shown in Figures 7–9. In each panel in Figure 10, a colored pixel corresponds to the number of LOSs passing through a spherical voxel in the XY_{GSE} plane. The specific time step for these plots is $k = 5$, and there is no significant variation in the LOS distributions during the 1-h analysis period. Note that the range of LOS density shown in the color bars differs from panel to panel.

The region observed by the SC0/SC5 configuration is the smallest among these three experiments owing to its viewing geometry (see the third row in Figure 5). Moreover, these two-satellite observations exhibit a non-uniform distribution with a preference towards radial distances $r > 10R_E$. The reduced number of observations of the inner magnetospheric region ($r < 10R_E$) justifies the low efficiency of our algorithm to reconstruct the high gradient structure displayed in the ground truth emissivities (see third column in Figures 7–9).

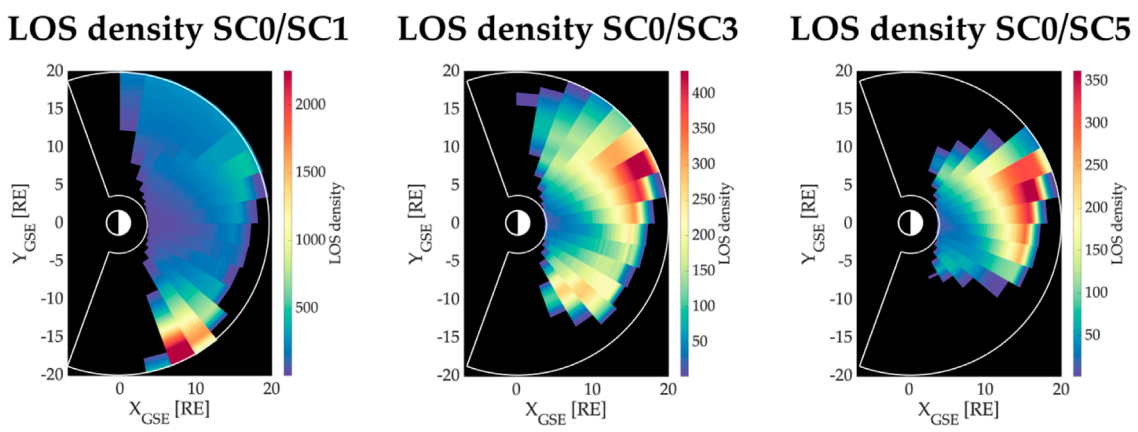

FIGURE 10
Line-of-sight density per voxels at the ecliptic plane for time step $k = 5$. The colors indicate the number of LOSs passing through each voxel in the ecliptic plane and provide information regarding the spatial distribution of measurements crossing the solution domain.

3.4.5 Assessment of tomographic reconstructions

In order to evaluate our tomographic retrievals of soft X-ray emissivities, we interpolated the resulting values reported in a spherical grid to the high-resolution rectangular grid used for the ground truth. To do so, we used the 3-D interpolation built-in function with the "spline" method in the MATLAB software. Then, we calculated the residual error (Eq. 11) and the Structural Similarity (SSIM) index (Eq. 12) for each reconstruction using definitions provided in Section 2.3. In each panel of Figure 11, the dashed blue line with circular markers and the dotted blue line with square markers show the SSIM values derived from the tomographic reconstructions performed with the SC0/SCX configuration when SC0 is at vantage points P1 and P2, respectively. Similarly, the dashed red line with circular markers and the dotted red line with square markers depict the residual errors obtained from reconstructions at vantage points P1 and P2, respectively.

In all panels, the SSIM index shows minimal variation for the first 10 min of the simulation ($k \in [0,3]$) but shows a monotonically decrease after that period. This feature is highly correlated to the response of the magnetosphere to the sudden change in the B_z component of the IMF. Indeed, the analysis of the MHD simulations reveals a fast Earthward movement of the magnetosheat starting at $t = 10$ min. In addition, the decreasing trend in the SSIM values is also linked to the displacement of the magnetosheath occurring in less than 5 min, which is our selected reconstruction cadence. Based on the Kalman filtering algorithm used in our approach, each reconstruction depends on current measurements and a previously estimated model that, in our case, was obtained 5 min before. As a result, our tomographic estimations exhibit a spatial delay in the 3-D structure imposed by the previous model.

Table 1 shows the averaged values of SSIM and residual error (e_{res}) for each spacecraft configuration. Specifically, we calculated (i) the total average of the indexes that include the results of the 13 dynamic reconstructions, (ii) the average of the indexes for the almost static period of the magnetosheath, i.e., $k \leq 3$, and (iii) the average of the indexes for the period when the magnetosheath moves Earthward, i.e., $k > 3$. Values in bold font indicate the maximum SSIM and the minimum e_{res} per row, which serves to identify the spacecraft configuration that produces the best tomographic reconstructions in our experiments.

3.4.6 Magnetopause location derived from 3-D tomographic reconstructions

In addition, we have calculated the location of the magnetopause (the inner boundary of the magnetosheath) along the Sun-Earth line using the approach presented in (Cucho-Padin et al., 2024), which utilizes a radial profile of reconstructed emissivities and calculates its first derivative along it. The radial position with the highest derivative is considered the current position of the magnetopause (MP). Figure 12 shows the calculation of the MP location (in units of R_E) for each dynamic reconstruction. In each panel, the black line with circular markers denotes the ground truth location of the magnetopause extracted from the MHD simulation. The blue line with square markers and the red line with triangular markers indicate the MP radial positions using the SC0/SCX configuration from vantage points P1 and P2, respectively. Since the radial resolution in the spherical grid and the axial resolution in the rectangular grid are identical with value $\Delta r = \Delta x = 0.1 R_E$, the error in magnetopause location can only adopt discrete values as in $e_k^{mp} = \text{abs}(r_g^{mp} - \bar{r}_k^{mp}) = \gamma \times 0.1\ R_E, \forall \gamma \in [0,1,2,\dots]$, where r_g^{mp} is the ground truth radial location of the magnetopause within the Sun-Earth line, and $\bar{r}_k^{mp}$ is the derived MP location from the tomographic results. In all panels, the error in the MP location is equal to or smaller than 0.1 R_E during the first 10 min ($t \leq 10, k \leq 3$) of the simulation, as the magnetosheath structure is almost static during this time period. On the other hand, after the value of the B_z component changes from five to −5 nT ($t > 10, k > 3$), tomographic reconstructions do not provide the exact position of the MP, but capture the Earthward MP motion.

An alternative method to quantify the error in the magnetopause location is calculating the average of the error using the formula $\bar{e}^{mp} = (\Sigma_{k=k_i}^{k_f} e_k^{mp})/(k_f - k_i + 1)$. Table 2 shows (i) the total averaged e^{mp} that considers the error in the 13 reconstructions, (ii) the averaged e_k^{mp} for the period when the magnetosheath is almost static ($k \leq 3$), and (iii) the averaged e_k^{mp} when the magnetosheath dynamically respond to the abrupt variation of B_z ($k > 3$). Values

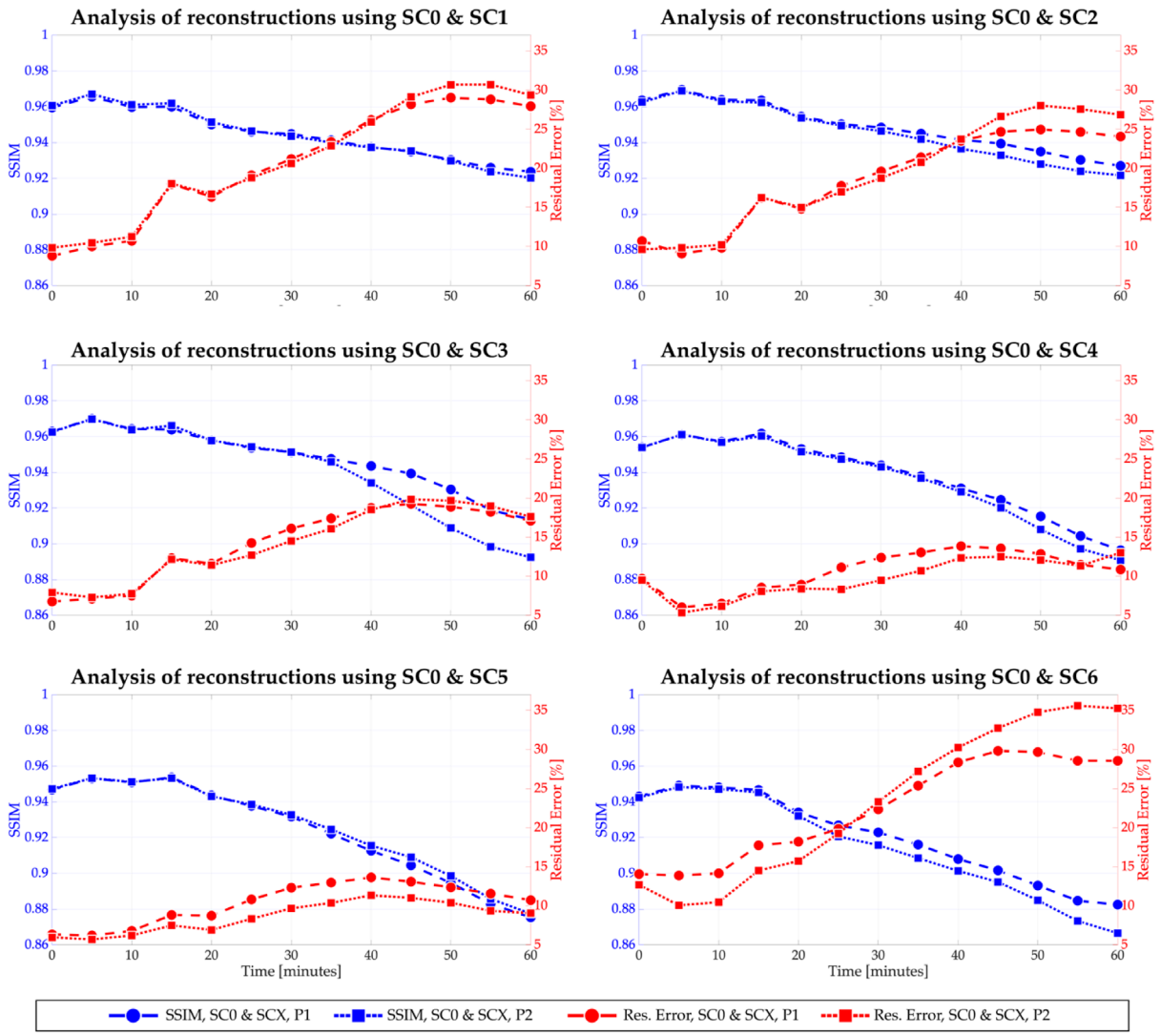

FIGURE 11
Assessment of tomographic reconstructions. Each panel shows the calculated SSIM and residual error values for the time-dependent tomographic reconstructions. The dashed blue line with circular markers and the dotted blue line with square markers show the SSIM values obtained from the tomographic reconstruction conducted with SC0 and SCX at the vantage points P1 and P2, respectively. Similarly, the dashed red line with circular markers and the dotted red line with square markers show the residual error values calculated from tomographic reconstructions conducted with SC0 and SCX at the vantage points P1 and P2, respectively.

in bold font emphasize the satellite configuration that produces the smallest error.

4 Discussion and conclusion

This work aims to (i) demonstrate the capability of a statistically-based tomographic approach to reconstruct the time-dependent and 3-D soft X-ray magnetospheric emissivities and (ii) support the design of multi-spacecraft missions that include wide FOV imagers aiming for optical tomography. For this purpose, we simulated the response of the terrestrial magnetosphere to varying solar wind conditions using the MHD OpenGGCM model. The resulting magnetospheric plasma model, along with an assumed neutral exosphere, was used to generate the ground truth emissivities. Then, we designed orbits for a set of two-satellite configurations that can provide simultaneous soft X-ray observations of the dayside magnetosphere. Finally, we used these 2-D images and a dynamic tomographic technique based on Kalman Filtering and Gaussian Markov Random Field theory to reconstruct the 3-D soft X-ray emissivity distributions. In order to determine the spacecraft configuration that achieves the lowest reconstruction error, we calculated the SSIM index and the residual error for each experiment.

In this study, we did not include background soft X-ray contamination nor Poisson-distributed shot noise in the reconstruction process, as our main scope is to introduce the 4-D tomographic technique and a methodology for multi-spacecraft orbit selection based on the tomographic results. Nevertheless, in a realistic scenario, we need to

TABLE 1 Assessment of tomographic reconstruction based on SSIM and residual error values.

Value/configuration	SC0/SC1(%)	SC0/SC2(%)	SC0/SC3(%)	SC0/SC4(%)	SC0/SC5(%)	SC0/SC6(%)
Tot. Avg. SSIM (P1)	0.94 ± 4.3	**0.95 ± 3.9**	0.95 ± 4.1	0.94 ± 5.2	0.92 ± 4.0	0.92 ± 4.5
Avg. SSIM (k ≤ 3, P1)	0.96 ± 0.5	**0.97 ± 0.5**	0.97 ± 0.6	0.96 ± 0.5	0.95 ± 0.5	0.95 ± 0.5
Avg. SSIM (k > 3,P1)	0.94 ± 4.6	**0.94 ± 4.0**	0.94 ± 4.3	0.93 ± 4.2	0.92 ± 4.5	0.91 ± 5.1
Tot. Avg. SSIM (P2)	0.94 ± 4.3	**0.95 ± 4.0**	0.94 ± 4.4	0.94 ± 5.2	0.93 ± 3.6	0.91 ± 5.0
Avg. SSIM (k ≤ 3, P2)	0.96 ± 0.5	0.96 ± 0.5	**0.97 ± 0.5**	0.96 ± 0.5	0.95 ± 0.5	0.95 ± 0.5
Avg. SSIM (k > 3, P2)	0.94 ± 4.5	**0.94 ± 4.3**	0.93 ± 4.4	0.93 ± 5.0	0.92 ± 4.1	0.90 ± 5.2
Tot. Avg. Res. Error (P1)	20.6 ± 25	18.6 ± 23	14.3 ± 18	10.7 ± 13	**10.3 ± 10**	22.4 ± 35
Avg. Res. Error (k ≤ 3, P1)	9.8 ± 9	9.9 ± 9	7.1 ± 8	7.4 ± 12	**6.4 ± 9**	14.0 ± 5
Avg. Res. Error (k > 3, P1)	33 ± 27	21.2 ± 21	16.4 ± 23	11.7 ± 15	**11.5 ± 13**	24.8 ± 37
Tot. Avg. Res. Error (P2)	21.1 ± 24	19.3 ± 25	14.2 ± 18	9.8 ± 14	**8.6 ± 12**	23.2 ± 38
Avg. Res. Error (k ≤ 3, P2)	10.5 ± 9	9.9 ± 8	7.7 ± 9	7.0 ± 11	**6.0 ± 7**	11.1 ± 12
Avg. Res. Error (k > 3, P2)	24.3 ± 27	22.1 ± 27	16.2 ± 21	10.6 ± 16	**9.4 ± 15**	26.9 ± 36

include several sources of uncertainty as those listed below.

1. The image sensor's responsivity, along with a selected integration time, determines the total number of digital counts to be used in the reconstructions. A low responsivity and/or short integration time would yield a digital image with a low number of counts that can be highly affected by shot noise, thus, precluding the characterization of spatial structures in the observed scene.
2. The point spread function (PSF) of the imaging sensor may induce systematic error in 3-D tomographic retrievals as the PSF distorts object shapes in the scene. An adequate deconvolution algorithm is needed to extract this effect (Schmitz, M. A. et al., 2020).
3. The pointing knowledge determines the accuracy of the spacecraft to point towards a given target. In tomography, an error in the pointing knowledge directly affects the generation of the observation matrix, $\mathbf{L}_k$, as it highly depends on the precision of the LOS directions, $\hat{\mathbf{n}}$.

A thorough study of the effect of the listed factors on the tomographic reconstruction of a static magnetosheath is provided in (Cucho-Padin et al., 2024).

Tomographic results displayed in Figures 7–9 present artifacts that are highly related to (i) the use of a smaller solution domain than the one used to generate the measurements (see Section 3.4.4), (ii) the difference between the reconstruction cadence (5 min) and the speed of the magnetosheath Earthward movement, and (iii) the non-uniform distribution of LOSs passing through the solution domain.

In a real scenario, the actual extension of the region with terrestrial soft X-ray emitters is unknown and can deviate from those estimated by MHD models. On the other hand, the solution domain, needed for the tomography approach, requires fixed dimensions that depend on computational resources, such as RAM memory, to allocate vectors and matrices in Eq. 10, and/or the number of cores for the inversion process. Hence, it is likely that the region selected as the solution domain does not cover the entire soft X-ray emission zone. Our study simulates this scenario providing crucial insights about the spatial distribution of retrieved emissivities.

The reconstruction cadence is restricted by the selection of the integration time, which in turn depends on the number of digital counts required in the output image to reduce the effect of the shot noise. In our simulations, the integration time was selected as 5 min because, with this duration, the upcoming LEXI and SMILE missions are expected to capture soft X-ray images with a strong signal-to-noise ratio. The MHD simulations of the magnetosphere exhibited a rapid and Earthward movement of the magnetosheat that was not reproduced accurately using our proposed technique. However, the specific analysis of the magnetopause location at the Sun-Earth line (Section 3.4.6), needed to understand dayside magnetic reconnection dynamics, reveals that our estimations follow the displacement pattern for all experiments as shown in Figure 12. Also, the maximum average error in magnetopause location reported in Table 2 is 0.36 R_E.

The LOS distributions within the solution domain displayed in Figure 10 serve to identify covered regions where tomography reconstruction is more effective. The black pixels are regions not observed by both sensors, and their estimations will highly depend on the previous model, $\bar{\mathbf{x}}_{k-1}$. On the other hand, colored pixels indicate regions to be updated mainly through measured data. For the sake of clarification, regions not fully observed by the sensors but within the neighborhood of observed voxels will still be modified by data to some extent as our methodology (TS-GMRF) interconnects voxels and imposes smoothness among them (see Section 2).

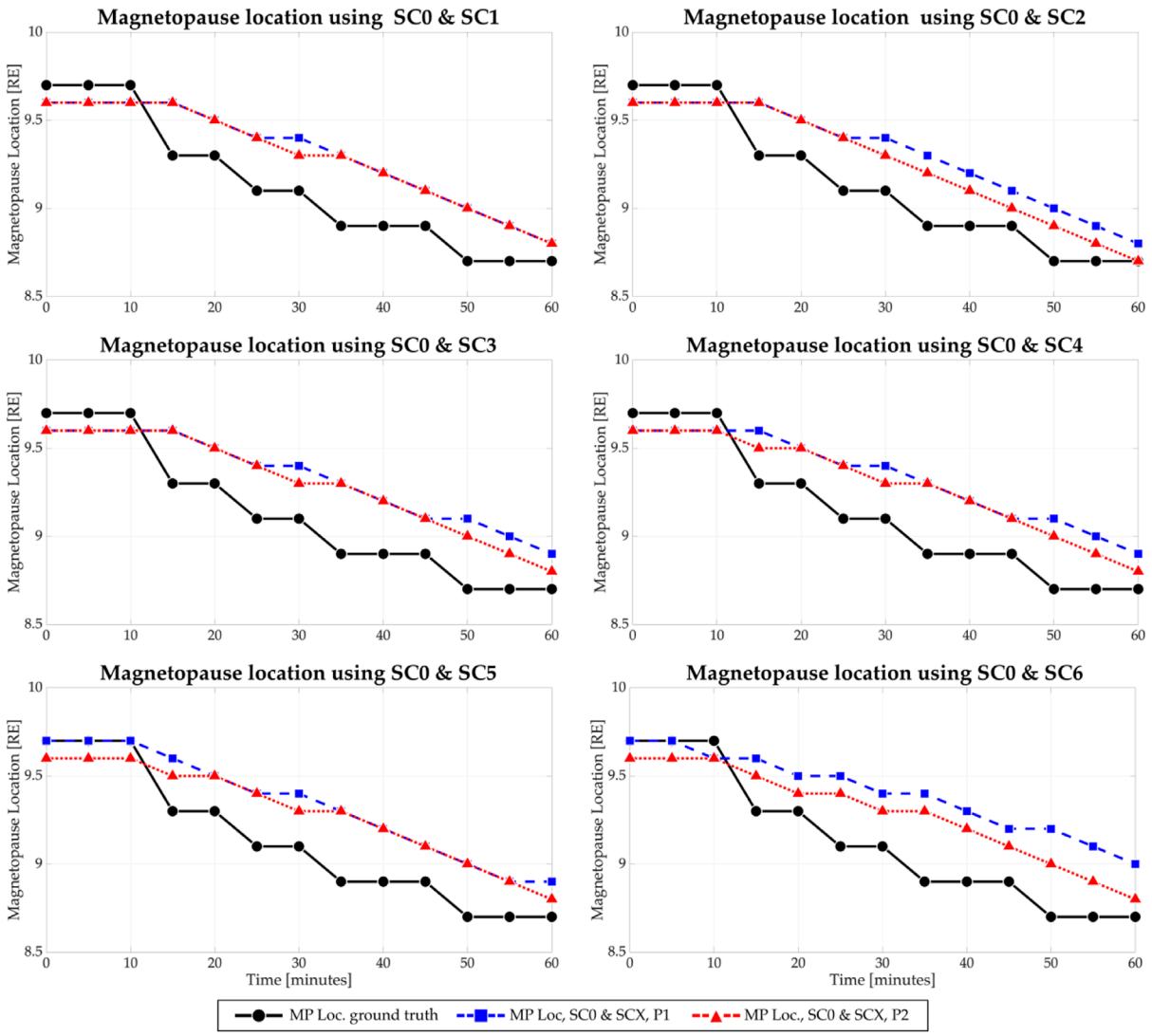

FIGURE 12
Magnetopause location derived from tomographic reconstructions. In each panel, the solid black line with circular markers indicates the ground truth magnetopause location derived from the MHD magnetospheric model. The dashed blue line with square markers and the dotted red line with triangular markers indicate the magnetopause location derived from tomographic reconstructions using SC0 and SCX at vantage points P1 and P2, respectively.

TABLE 2 Error in the magnetopause location.

Value/configuration	SC0/SC1 (%)	SC0/SC2 (%)	SC0/SC3 (%)	SC0/SC4 (%)	SC0/SC5 (%)	SC0/SC6 (%)
Tot. Avg. e^{mp} (P1)	0.22 ± 4	0.22 ± 4	0.25 ± 6	0.25 ± 6	**0.21 ± 6**	0.28 ± 5
Avg. e_k^{mp} (k ≤ 3, P1)	0.10 ± 0	0.10 ± 0	0.10 ± 0	0.10 ± 0	**0.00 ± 0**	0.03 ± 2
Avg. e_k^{mp} (k > 3,P1)	0.26 ± 6	**0.26 ± 5**	0.29 ± 6	0.29 ± 7	0.27 ± 5	0.36 ± 6
Tot. Avg. e^{mp} (P2)	0.22 ± 4	**0.17 ± 4**	0.22 ± 4	0.21 ± 4	0.21 ± 4	0.20 ± 4
Avg. e_k^{mp} (k ≤ 3, P2)	0.10 ± 0	0.10 ± 0	0.10 ± 0	0.10 ± 0	0.10 ± 0	0.10 ± 0
Avg. e_k^{mp} (k > 3, P2)	0.20 ± 5	**0.19 ± 5**	0.25 ± 5	0.24 ± 4	0.24 ± 5	0.23 ± 5

Although the experiments reported in this study are based on a single dynamic MHD model of the magnetosphere, we can still infer that our technique is robust enough to reconstruct soft X-ray emissivities corresponding to an MHD model whose input solar wind parameters produce (1) at most an Earthward displacement of 0.2 Re/minute of the magnetopause location, and (2) sufficient

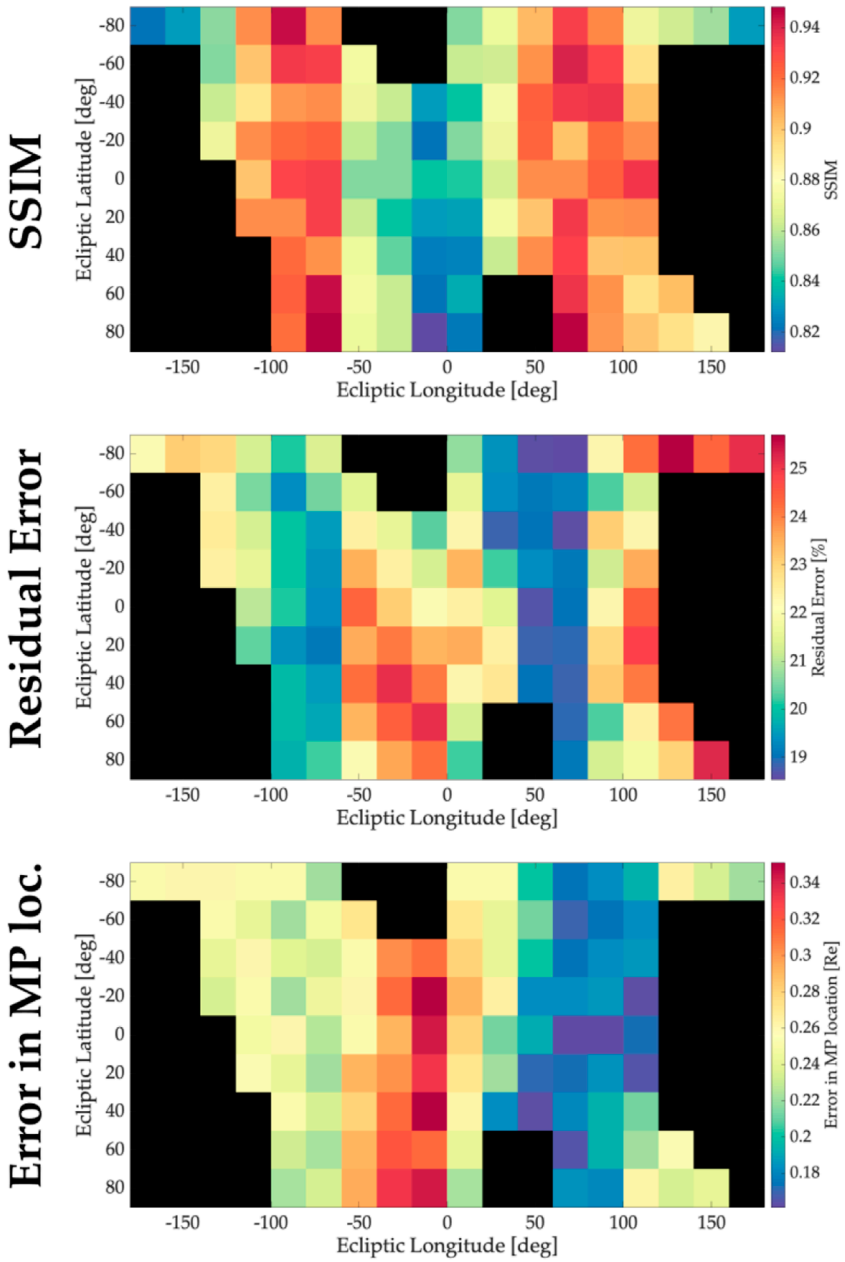

FIGURE 13
Average values of SSIM, residual errors in reconstructions, and errors in magnetopause location for the SC0/SC2 configuration during a 6-month period.

soft-X ray emitters to handle an appropriate signal to noise ratio. The latter is specifically related to the solar wind density and should be large enough to produce a soft X-ray intensity greater than 1 [eV/cm2/sec/str] along a pixel line-of-sight (see Figure 6) under the assumption of zero noise. The two abovementioned constraints allow us to generate an extensive combination of input solar wind conditions in which our tomography methodology is efficient.

In this study, we have used the methodology provided by Samsonov et al. (2022) to extract the inner magnetospheric region of the MHD model since solar wind ions would not populate this zone and would not create soft X-ray emitters. Nevertheless, the sudden depletion of soft X-ray emissivities to zero values in the inner magnetosphere (see Figure 1) is likely to be an artifact of this method. A more sophisticated analysis for inner magnetospheric extraction has been used in (Sibeck et al., 2018) (see Figure 58, left panel) and displays a gradual variation of soft X-ray emitters in the same region. Therefore, our dynamic tomography approach, which essentially supports this progressive change in the emissivity (the first component of Eq. (15)), might provide better results under a more realistic scenario.

Our study presented a quantitative comparison of reconstruction errors for each experiment. This has been conducted

using the SSIM index and the residual error of the estimated emissivities. According to Table 1, the highest SSIM values are achieved by the SC0/SC2 configuration, and the lowest residual errors are yielded when the SC0/SC5 configuration is used. Additionally, we quantified the error in magnetopause location, whose detection is one of the main goals of estimating the 3-D structure of emissivities. According to Table 2, the lowest averaged error in MP location is achieved by the SC0/SC5 configuration. Also, the lowest averaged error in MP location during the dynamic stage of the magnetosphere is obtained when the SC0/SC2 configuration is used. Other factors to be considered in the selection of the best spacecraft configuration for soft X-ray tomography are (1) the total number of hours in a 6-month period in which tomography is possible (see Figure 3) and (2) the coverage of LOS within the solution domain (displayed in Figure 10 for the SC0/SC5 case). Hence, the configuration SC0/SC2 has ~22% more hours to perform tomography in a 6-month period than SC0/SC5. Similarly, the SC0/SC2 configuration enables the two imaging sensors to cover ~32% more 3-D voxels (in the solution domain) than SC0/SC5. In sum, we found that the configuration SC0/SC2, with phase angle 75 [deg], is the best configuration among the seven presented in this study to provide a low error in the tomographic reconstruction of soft X-ray emissivities, a low error in detecting the magnetopause location, and a large number of hours during a 6-month period to perform tomography.

Finally, we evaluate our tomography methodology for the selected SC0/SC2 configuration over the 6-month period orbit. To do so, we have divided the spherical shell with radius 30 R_E, where the spacecraft transits, into $20° \times 20°$ pixels and perform the 60-min dynamic tomographic reconstruction for the SC0's location that is closest to the center of a given pixel. In Figure 13, we report the average values ($k \in [1, 13]$) for the SSIM index, residual error in the reconstructions, and error in the magnetopause location. High values of SSIM indexes and low values of the residual errors in reconstructions are mainly located near the terminators at any latitude. These results agree with static reconstructions reported in (Cucho-Padin et al., 2024), wherein the best SSIM was obtained from tomographic reconstructions of the magnetosheath that have the sensor's line-of-sight almost perpendicular to the Sun-Earth line. On the other hand, we note that estimation in the magnetopause location is also better in the terminators, with a preference toward the dusk region. Since our MHD simulations only account for changes in the Bz component of the IMF, it is not expected to have significant asymmetries in the soft X-ray emissivities along the longitudes; therefore, this effect is likely linked to the acquisition geometry which is not entirely symmetric for conjugate longitudes.

Data availability statement

The raw data supporting the conclusion of this article will be made available by the authors, without undue reservation.

Author contributions

GC-P: Conceptualization, Formal Analysis, Investigation, Methodology, Software, Visualization, Writing–original draft, Writing–review and editing. HC: Data curation, Methodology, Supervision, Writing–review and editing, Investigation. JJ: Data curation, Writing–review and editing, Investigation, Methodology. MS: Data curation, Writing–review and editing. KM: Methodology, Supervision, Writing–review and editing. DS: Methodology, Supervision, Writing–review and editing, Funding acquisition. JN: Formal Analysis, Supervision, Validation, Writing–review and editing. EV: Formal Analysis, Methodology, Validation, Writing–review and editing.

Funding

The author(s) declare financial support was received for the research, authorship, and/or publication of this article. This work was supported by NASA's HUSPI program, and the NASA Goddard Space Flight Center through Cooperative Agreement 80NSSC21M0180 to Catholic University, Partnership for Heliophysics and Space Environment Research (PHaSER). Hyunju Connor gratefully acknowledges the NASA grant (80MSFC20C0019).

Conflict of interest

The authors declare that the research was conducted in the absence of any commercial or financial relationships that could be construed as a potential conflict of interest.

Publisher's note

All claims expressed in this article are solely those of the authors and do not necessarily represent those of their affiliated organizations, or those of the publisher, the editors and the reviewers. Any product that may be evaluated in this article, or claim that may be made by its manufacturer, is not guaranteed or endorsed by the publisher.

References

Aubry, M. P., Russell, C. T., and Kivelson, M. G. (1970). Inward motion of the magnetopause before a substorm. *J. Geophys. Res. (1896-1977)* 75, 7018–7031. doi:10.1029/JA075i034p07018

Branduardi-Raymont, G., Wang, C., Escoubet, C. P., Adamovic, M., Agnolon, D., Berthomier, M., et al. (2018). Smile definition study report (red book).

Butala, M. D., Hewett, R. J., Frazin, R. A., and Kamalabadi, F. (2010). Dynamic three-dimensional tomography of the solar corona. *Sol. Phys.* 262, 495–509. doi:10.1007/s11207-010-9536-1

Collier, M. R., and Connor, H. K. (2018). Magnetopause surface reconstruction from tangent vector observations. *J. Geophys. Res. Space Phys.* 123 (10), 189–210. doi:10.1029/2018JA025763

Connor, H. K., and Carter, J. A. (2019). Exospheric neutral hydrogen density at the nominal 10 $R_{<i>E</i>}$ subsolar point deduced from xmm-Newton X-ray observations. *J. Geophys. Res. Space Phys.* 124, 1612–1624. doi:10.1029/2018JA026187

Connor, H. K., Sibeck, D. G., Collier, M. R., Baliukin, I. I., Branduardi-Raymont, G., Brandt, P. C., et al. (2021). Soft x-ray and ena imaging of the earth's dayside magnetosphere. *J. Geophys. Res. Space Phys.* 126, e2020JA028816. doi:10.1029/2020JA028816

Cucho-Padin, G., Connor, H., Jung, J., Walsh, B., and Sibeck, D. G. (2024). Finding the magnetopause location using soft x-ray observations and a statistical inverse method. *Earth Planet. Phys.* 8, 184–203. doi:10.26464/epp2023070

Cucho-Padin, G., Kameda, S., and Sibeck, D. G. (2022). The earth's outer exospheric density distributions derived from procyon/laica uv observations. *J. Geophys. Res. Space Phys.* 127, e2021JA030211. doi:10.1029/2021JA030211

Dungey, J. W. (1961). Interplanetary magnetic field and the auroral zones. *Phys. Rev. Lett.* 6, 47–48. doi:10.1103/PhysRevLett.6.47

Feller, W. (1968). *An introduction to probability theory and its applications*. New York, USA: Wiley.

Hajek, B. (2015). *Random processes for engineers*. Cambridge: Cambridge University Press.

Jansen, F., Lumb, D., Altieri, B., Clavel, J., Ehle, M., Erd, C., et al. (2001). Xmm-Newton observatory ∗ - i. the spacecraft and operations. *A&A* 365, L1–L6. doi:10.1051/0004-6361:20000036

Jelínek, K., Němeček, Z., and Šafránková, J. (2012). A new approach to magnetopause and bow shock modeling based on automated region identification. *J. Geophys. Res. Space Phys.* 117. doi:10.1029/2011JA017252

Jorgensen, A. M., Sun, T., Wang, C., Dai, L., Sembay, S., Wei, F., et al. (2019b). Boundary detection in three dimensions with application to the smile mission: the effect of photon noise. *J. Geophys. Res. Space Phys.* 124, 4365–4383. doi:10.1029/2018JA025919

Jorgensen, A. M., Sun, T., Wang, C., Dai, L., Sembay, S., Zheng, J., et al. (2019a). Boundary detection in three dimensions with application to the smile mission: the effect of model-fitting noise. *J. Geophys. Res. Space Phys.* 124, 4341–4355. doi:10.1029/2018JA026124

Jorgensen, A. M., Xu, R., Sun, T., Huang, Y., Li, L., Dai, L., et al. (2022). A theoretical study of the tomographic reconstruction of magnetosheath x-ray emissions. *J. Geophys. Res. Space Phys.* 127, e2021JA029948. doi:10.1029/2021JA029948

Jung, J., Connor, H. K., Carter, J. A., Koutroumpa, D., Pagani, C., and Kuntz, K. D. (2022). Solar minimum exospheric neutral density near the subsolar magnetopause estimated from the xmm soft x-ray observations on 12 november 2008. *J. Geophys. Res. Space Phys.* 127, e2021JA029676. doi:10.1029/2021JA029676

Kim, H., Connor, H. K., Jung, J., Walsh, B. M., Sibeck, D., Kuntz, K. D., et al. (2024). Estimating the subsolar magnetopause position from soft x-ray images using a low-pass image filter. *Earth Planet. Phys.* 8, 1–11. doi:10.26464/epp2023069

Koga, D., Gonzalez, W. D., Souza, V. M., Cardoso, F. R., Wang, C., and Liu, Z. K. (2019). Dayside magnetopause reconnection: its dependence on solar wind and magnetosheath conditions. *J. Geophys. Res. Space Phys.* 124, 8778–8787. doi:10.1029/2019JA026889

Kuntz, K. D., Collado-Vega, Y. M., Collier, M. R., Connor, H. K., Cravens, T. E., Koutroumpa, D., et al. (2015). The solar wind charge-exchange production factor for hydrogen. *Astrophysical J.* 808, 143. doi:10.1088/0004-637X/808/2/143

Norberg, J., Käki, S., Roininen, L., Mielich, J., and Virtanen, I. I. (2023). Model-free approach for regional ionospheric multi-instrument imaging. *J. Geophys. Res. Space Phys.* 128, e2022JA030794. doi:10.1029/2022JA030794

Norberg, J., Vierinen, J., Roininen, L., Orispää, M., Kauristie, K., Rideout, W. C., et al. (2018). Gaussian markov random field priors in ionospheric 3-d multi-instrument tomography. *IEEE Trans. Geoscience Remote Sens.* 56, 7009–7021. doi:10.1109/TGRS.2018.2847026

Robertson, I. P., and Cravens, T. E. (2003). X-ray emission from the terrestrial magnetosheath. *Geophys. Res. Lett.* 30. doi:10.1029/2002GL016740

Samsonov, A., Carter, J. A., Read, A., Sembay, S., Branduardi-Raymont, G., Sibeck, D., et al. (2022). Finding magnetopause standoff distance using a soft x-ray imager: 1. magnetospheric masking. *J. Geophys. Res. Space Phys.* 127, e2022JA030848. doi:10.1029/2022JA030848

Schmitz, M. A., Starck, J.-L., Ngole Mboula, F., Auricchio, N., Brinchmann, J., Vito Capobianco, R. I., et al. (2020). Euclid: nonparametric point spread function field recovery through interpolation on a graph laplacian. *Astronomy Astrophysics* 636, A78. doi:10.1051/0004-6361/201936094

Shue, J.-H., Song, P., Russell, C. T., Steinberg, J. T., Chao, J. K., Zastenker, G., et al. (1998). Magnetopause location under extreme solar wind conditions. *J. Geophys. Res. Space Phys.* 103, 17691–17700. doi:10.1029/98JA01103

Sibeck, D. G., Allen, R., Aryan, H., Bodewits, D., Brandt, P., Brown, G., et al. (2018). Imaging plasma density structures in the soft x-rays generated by solar wind charge exchange with neutrals. *Space Sci. Rev.* 214, 79. doi:10.1007/s11214-018-0504-7

Sibeck, D. G., Murphy, K. R., Porter, F. S., Connor, H. K., Walsh, B. M., Kuntz, K. D., et al. (2023). Quantifying the global solar wind-magnetosphere interaction with the solar-terrestrial observer for the response of the magnetosphere (storm) mission concept. *Front. Astronomy Space Sci.* 10. doi:10.3389/fspas.2023.1138616

Trümper, J. (1982). The rosat mission. *Adv. Space Res.* 2, 241–249. doi:10.1016/0273-1177(82)90070-9

Walsh, B. M., Collier, M. R., Kuntz, K. D., Porter, F. S., Sibeck, D. G., Snowden, S. L., et al. (2016). Wide field-of-view soft x-ray imaging for solar wind-magnetosphere interactions. *J. Geophys. Res. Space Phys.* 121, 3353–3361. doi:10.1002/2016JA022348

Walsh, B. M., Kuntz, K. D., Busk, S., Cameron, T., Chornay, D., Chuchra, A., et al. (Forthcoming 2024). The lunar environment heliophysics x-ray imager (lexi) mission. *Space Sci. Rev.*

Wang, R. C., Li, D., Sun, T., Peng, X., Yang, Z., and Wang, J. Q. (2023). A 3d magnetospheric ct reconstruction method based on 3d gan and supplementary limited-angle 2d soft x-ray images. *J. Geophys. Res. Space Phys.* 128, e2022JA030424. doi:10.1029/2022JA030424

Weisskopf, M. (2003). The chandra x-ray observatory: an overview. *Adv. Space Res.* 32, 2005–2011. doi:10.1016/S0273-1177(03)90639-9

Whittaker, I. C., and Sembay, S. (2016). A comparison of empirical and experimental o7+, o8+, and o/h values, with applications to terrestrial solar wind charge exchange. *Geophys. Res. Lett.* 43, 7328–7337. doi:10.1002/2016GL069914

Zhang, Y., Ghodrati, A., and Brooks, D. H. (2005). An analytical comparison of three spatio-temporal regularization methods for dynamic linear inverse problems in a common statistical framework. *Inverse Probl.* 21, 357–382. doi:10.1088/0266-5611/21/1/022

frontiers | Frontiers in Astronomy and Space Sciences

TYPE Original Research
PUBLISHED 30 May 2024
DOI 10.3389/fspas.2024.1394655

OPEN ACCESS

EDITED BY
Ankush Bhaskar,
Vikram Sarabhai Space Centre, India

REVIEWED BY
Bhargav Vaidya,
Indian Institute of Technology Indore, India
Vishal Upendran,
Lockheed Martin Solar and Astrophysics Laboratory (LMSAL), United States

*CORRESPONDENCE
Kyle R. Murphy,
kylemurphy.spacephys@gmail.com

RECEIVED 01 March 2024
ACCEPTED 26 April 2024
PUBLISHED 30 May 2024

CITATION
Murphy KR, Shoemaker MA, Sibeck DG, Schiff C, Connor H, Porter FS and Zesta E (2024), Target and science visibility of the solar-terrestrial observer for the response of the magnetosphere (STORM) global imaging mission concept.
Front. Astron. Space Sci. 11:1394655.
doi: 10.3389/fspas.2024.1394655

Target and science visibility of the solar-terrestrial observer for the response of the magnetosphere (STORM) global imaging mission concept

Kyle R. Murphy[1,2]*, Michael A. Shoemaker[3], David G. Sibeck[3], Conrad Schiff[3], Hyunju Connor[3], Fredrick S. Porter[3] and Eftyhia Zesta[3]

[1]Independent Researcher, Thunder Bay, ON, Canada, [2]Department of Physics, Lakehead University, Thunder Bay, ON, Canada, [3]Goddard Space Flight Center, Greenbelt, MD, United States

Imaging missions in Earth Science, Heliophysics, and Astrophysics have made fundamental advancements in science and have helped to further our understanding of our natural environment. Here we review the Solar-Terrestrial Observer for the Response of the Magnetosphere (STORM) mission concept, a global solar wind-magnetosphere imaging mission and investigate how often STORM can observe and image its key science targets; the magnetopause, ring current, and auroral oval. We introduce a novel analysis which defines STORM's plasma targets as discrete sample points in space, these points are collectively called point groups. These point groups are used in conjunction with fields-of-view of STORM's imagers to quantify target visibility, how often the mission can observe each of its targets. The target visibility is combined with a statistical investigation of historical solar wind and geomagnetic data, and a k-folds/Monte Carlo analysis to quantify STORM's science visibility. That is how often specific targets can be observed during elevated solar wind and geomagnetic conditions such that detailed science investigations can be completed to address STORM's science objectives. This analysis is further expanded to potential dual-spacecraft mission configurations to determine the nominal inter-orbit phasing which maximizes target and science visibility. Overall, we find that the target and science visibility of a single spacecraft mission is large, in the 100s and 1000s of hours/events, while the target and science visibility peak for a dual-spacecraft mission where the two spacecraft are ~85^{O} out of phase.

KEYWORDS

imaging, dungey cycle, magnetosphere, solar wind, reconnection, system science, dual spacecraft

1 Introduction

The interaction between the solar wind and Earth's magnetosphere is complex. It spans time scales of minutes to days, spatial scales from km's to several Earth radii, and encompasses plasma and neutral regimes throughout the magnetosphere, ionosphere, and atmosphere. This complex interaction is truly that of a system of systems (e.g., Borovsky and Valdivia, 2018), and while we have been able to gain valuable insight into the global system

from *in situ* measurements strategically designed to study key aspects of the individual systems, a system science approach is required to fully understand and piece together the dynamics and cross-coupling of this complex interaction (Sibeck et al., 2023a).

System science refers to understanding a group of interacting, interconnected, or interrelated elements that form a unified whole. In system science, understanding the dynamics of a complex system requires not only the analysis of how different components of the system are coupled but also the dynamics of the individual components forming the system. Without a deep understanding of the individual components of a system, there is no way to develop a complete understanding of the dynamics of the larger and more complex system as a whole (Lin et al., 2012). A good analogy, which very clearly depicts this, are global Heliophysics models. Such models are pieced or coupled together from individual smaller models to form global models which simulate the dynamics of the solar wind, magnetosphere, ionosphere, and upper atmosphere (e.g., the Solar Wind Modelling Framework, Gombosi et al., 2021; or the Multiscale Atmosphere-Geospace Environment, Lin et al., 2021).

The next era of discovery in Heliophsyics, and in particular, in the solar wind-magnetosphere interaction, requires global observations capable of probing both the individual components and cross-coupling of these components at the same time in order to address the system science nature of this interaction. Such observations are only possible with either a fleet of spacecraft providing *in situ* observations throughout the magnetosphere and in the solar wind, or via global imaging platforms, which provide a comprehensive picture of most if not all of the system. A fleet or constellation of spacecraft, such as the Magnetospheric Constellation mission concept (Kepko, 2018), can provide distributed *in situ* observations of local plasma, and electric and magnetic fields over global scales. However, to probe the necessary spatial scales across key regimes, such a constellation would require a vast number of spacecraft, which poses a complex technical and engineering task, the scale of which has never been attempted, may not be feasible, and could be highly cost-prohibitive. Global imaging, while unable to probe local electrodynamics, is capable of observing plasma dynamics of key regions from scales of several 100s of km to several 10s of Earth Radii with a higher density of observations than any potential *in situ* mission or fleet of spacecraft (e.g., each pixel in each image acts like a virtual spacecraft). Furthermore, global end-to-end imaging of the solar wind-magnetosphere interaction provides a robust and cost-effective method to quantify the physics of local and cross-scale processes necessary to develop a system science understanding of this complex system.

In this paper we expand on the Solar-Terrestrial Observer for the Response of the Magnetosphere (STORM) mission concept (Sibeck et al., 2018) to explore how often such a mission can observe its key science targets. Further, we build on the STORM mission concept by considering a dual-spacecraft imaging mission to identify the nominal phasing between two identically instrumented spacecraft in a shared orbit which together would provide the largest number of observation intervals of key science targets. In subsequent sections we review the STORM mission concept, including the science objectives, orbits of a single and dual spacecraft mission, and identify the key science targets, this is followed by an analysis of how often targets are observed, and how often these observations can be used to address STORM's science objectives. We conclude with a summary of our findings and discussion of the STORM mission concept.

2 Mission concept

The STORM mission is a global imaging mission concept designed to quantify the solar wind-magnetosphere interaction (Sibeck et al., 2018; Sibeck et al., 2023a; Sibeck et al., 2023b). STORM utilizes a comprehensive suite of imaging and *in situ* instruments to simultaneously observe the solar wind input to the magnetosphere system and the subsequent response of key plasma regimes including the magnetopause, magnetotail, local and global aurora, and ring current from a circular 30 R_E, 9.65 days period orbit inclined ~90° to the ecliptic plane. This orbit places STORM in the solar wind for extended time periods, thereby allowing the onboard magnetometer (MAG) and plasma instrument (IES) to make *in situ* observations of the dynamic solar wind magnetic field and ion/electron plasma while the soft X-ray (XRI), aurora (FUV), and ring current (ENA) imagers observe the response of the magnetosphere to solar wind dynamics. Working together this suite of instruments addresses four science objectives:

A. Energy Transfer at the Dayside Magnetopause
B. Energy Circulation and Transfer through the Magnetotail
C. Energy Sources and Sinks for the Ring Current
D. Energy Feedback from the Inner Magnetosphere

These four science objectives are strategically linked such that STORM comprehensively tracks the end-to-end circulation of energy through the coupled solar wind-magnetosphere system. In this way STORM is the first ever complete and standalone system science observatory.

To address STORM's four objectives, the mission must observe key solar wind and magnetosphere targets during specific geomagnetic and solar wind conditions such that detailed science investigations can be completed. We term these two observing requirements target visibility and science visibility. STORM's key observables and targets are the magnetopause, observed by XRI, the auroral oval, observed by FUV, the ring current, observed by ENA, and the solar wind plasma and interplanetary magnetic field (IMF) observed by IES and MAG. A detailed description of STORM's science traceability, which links STORM's four science objectives to physical parameters and observables (targets) and project instrument performances (including the fields-of-view of the imagers) can be found in Sibeck et al. (2023a). Figure 1 shows STORM's orbit, fields-of-view (FOV) and targets for each of the imagers represented by discrete sample points collectively called point groups, and the position of STORM (labeled SC0) and the location of six potential secondary spacecraft (SC1-SC6). These secondary spacecraft are used to determine the inter-spacecraft phasing that maximizes science visibility and science return in a notional dual-spacecraft mission.

Panel (a) of Figure 1 illustrates STORM's 30 R_E circular orbit (9.65 day period), the spacecraft motion along the orbit, and the field of view of the XRI, FUV, and ENA imagers. The spacecraft orbit is based on the STORM mission design and Design Reference Mission (DRM), which assumed a nominal 30 R_E circular orbit inclined 90° to the ecliptic, with an August 2026 launch and insertion into

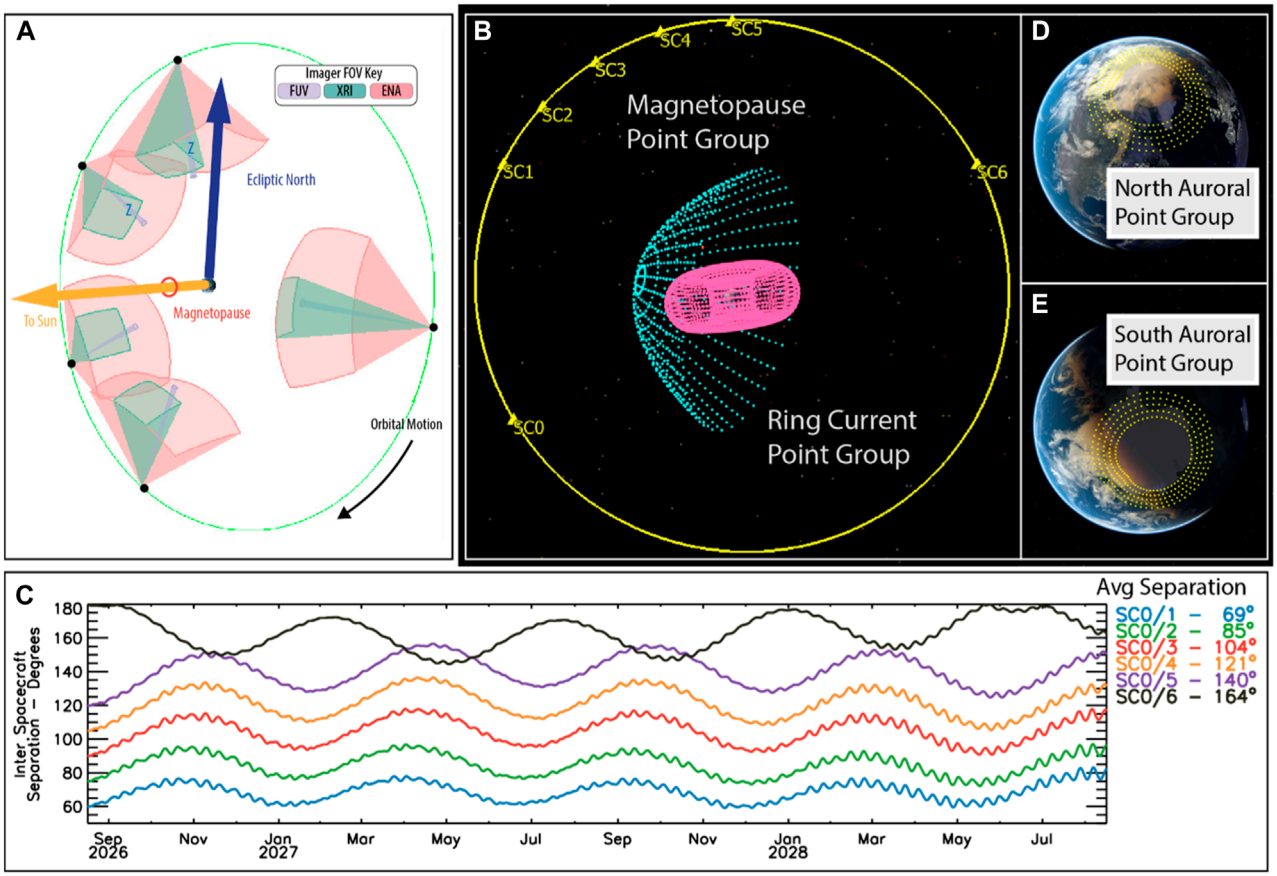

FIGURE 1
Overview of the STORM's orbit and mission design. **(A)** STORM's orbit during a period of high β-angle (orbital plane close to perpendicular to the sun-Earth line) and the fields-of-view of the FUV, XRI, and ENA imagers. **(B)** The phasing between a nominal single STORM spacecraft (SC0) and six potential secondary spacecraft (SC1-6) initially spaced at 60°, 75°, 90°, 105°, 120°, and 180° along a shared orbit. Also illustrated are the magnetopause (teal) and ring current (pink) point groups used to define target and science visibility. **(C)** The variation in the spacecraft phasing throughout the two-year science mission as a result of external forces experienced by the spacecraft. The margin shows the average separation of each spacecraft with SC0 over the nominal two-year mission. **(D)** The northern and **(E)** southern hemisphere auroral point groups used to define the visibility of the auroral oval and auroral target and science visibility.

science orbit in mid-August 2026 corresponding roughly with solar max of solar cycle 25. A spacecraft in such an orbit is perturbed strongly by the third-body gravitational effects from the Moon and Sun, which causes both periodic and secular changes to the orbital elements. The periodic changes include variations of approximately ±1° in inclination. The eccentricity grows secularly over time (lowering perigee which eventually leads to atmospheric reentry) unless maintained by station-keeping maneuvers. Previous mission design efforts (Shoemaker et al., 2022) showed that a spacecraft in STORM's orbit can maintain a 30 ± 1 R_E radius orbit for up to 4 years without any station-keeping, even when perturbed by both natural (e.g., solar radiation pressure, third-body gravity) and manmade (e.g., momentum unload, science orbit insertion error) causes. For the string-of-pearls constellation of satellites assumed in the present study (Figure 1B), the individual spacecraft would be acted upon differently from one another by third-body gravitational effects (i.e., differential perturbation), such that their relative orbital changes over time cause their along-track separations to vary. Figure 1C shows the relative separation angle between each spacecraft and SC0, when the orbital dynamics are modeled with the gravitational effects from the Sun (point-mass), Moon (point-mass), Earth (10 × 10 spherical harmonics), and solar radiation pressure. The initial orbital state for each spacecraft is identical, aside from initial true anomaly (to give the phase angle separation) and the semi-major axis. The initial semi-major axis for SC1-6 was adjusted by several hundred km to achieve the relative angular separation profiles shown in Figure 1C. This initial configuration allows the along-track separation to be naturally maintained within approximately ± 15° from a mean value over the two-year analysis span, without the need for active station keeping. Panels (b, d, and e) of Figure 1 show the position of six secondary spacecraft (labeled SC1 through six in panel b) and define the magnetopause, ring current, and north and south auroral point groups the represent STORM's targets.

The point groups (Figure 1B, D, E) represent the physical location of the magnetopause, ring current, and aurora. The magnetopause point group is defined using the magnetopause shape from Sibeck et al. (1991) under nominal solar wind conditions. The ring current point group is defined by the surface of a toroid with inner and outer radius of 2.5 and 6.5 R_E. The auroral point is defined as an elongated ellipse which encompasses the upper and

lower limits of the auroral oval as observed by previous studies (e.g., Frey et al., 2004; Milan et al., 2009b; Milan et al., 2019). Together these point groups along with the FOV of the imagers are used to define when and what portion of the magnetopause, ring current, and auroral ovals are observed. This quantifies STORM's target visibility. Coupled with a statistical analysis of historical solar and geomagnetic data this information is used to determine how often STORM can address each science objective, thus quantifying STORM's science visibility. In the following section we describe the methodology used to define both target and science visibility and quantify the target and science visibility for each of STORM's imagers and science objectives.

3 Target visibility

STORM's target visibility is quantified through detailed analysis of the DRM, imager FOVs, and the point groups discussed in the previous section. STORM's DRM simulates the spacecraft launch, insertion into the final 30 R_E circular orbit, spacecraft motion along the orbit, orbit evolution and all spacecraft maneuvers through a nominal two-year mission. The DRM also fully models the spacecraft including the position of each instrument, the spacecraft attitude, and the FOVs of the imagers and thus models in a precise way what fraction of each point group the corresponding imager is able to observe at any given point throughout the mission. Specifically, for each point group, we use a binary classification which labels a point as inside the FOV of an imager (1) or outside the FOV of the imager (0). When considering coincident observation by two spacecraft a point is classified as observed if it is in the FOV of an imager on either spacecraft. This is done for the entirety of a nominal 2-year mission at 1 h cadence (the cadence of the DRM). The ratio of observed points labeled with a '1' to the total number of points within a point group is the fraction of the point group observed by an imager at any given point in time.

For the magnetopause, we define a subset of the point group which encompasses the magnetopause nose as our target. This is because the motion of the magnetopause nose is a key observable for addressing several of STORM's science objectives (Sibeck et al., 2023a). The larger point group, while not used in subsequent analysis, is useful for quantifying target and science visibility of potential secondary objectives such as the dynamics of the Kelvin-Helmholtz stability along the magnetopause flanks. For the ring current we consider the entirety of the torus point group shown in Figure 1B. For the aurora, the two point covering the northern and southern auroral oval, are each subdivided by clock-angle into four subgroups which define dayside, dusk, night-side, and dawn auroral point groups. Additional statistics are composed by combining the north and south auroral point groups into a single auroral point group that can be observed regardless of the hemisphere. For the magnetopause nose and auroral point groups, if 98% of the points are observed we define those targets as being visible. For the ring current point group if 95% of the point group is observed the target is defined as visible. These, extremely conservative, thresholds are set so that if a small number of points on the edges of the point group are not visible, we do not define the target as not being visible.

Figure 2 shows the results of the target visibility analysis for a single spacecraft STORM mission (SC0 in Figure 1B) through the initial 6 months of a nominal science phase. In this initial 6-month period the STORM spacecraft visits all magnetic local times. The target visibility is calculated at the hourly cadence of DRM. Evident in Figure 2 is that ENA has the largest target visibility, followed by XRI, and the FUV. This is not surprising as ENA's observations of the ring current are rarely impeded, and most visibility dropouts result from spacecraft sun-avoidance maneuvers required to keep the sun out of the FOV of the imagers. XRI has the second highest visibility through the 6-month period. XRIs target, the magnetopause nose, can be impeded by the Earth throughout various portions of STORM's orbit, for example, when the spacecraft is on the night side. As expected FUV has the lowest target visibility since twice during every 9.65 day orbit the STORM spacecraft is in or near the equatorial place where FUV is unable to observe the high-latitude aurora.

Figure 3 expands on the analysis of Figure 2 and the number of hours each target can be observed over the entirety of a two-year science mission for a single STORM spacecraft (SC0) and each paired combination of SC0 and SC1 through SC6. Over the course of a two-year mission a single STORM spacecraft observes the magnetopause nose for over 11,000 h; the ring current for over 15,000 h; the auroral oval for nearly 2000 h; and the four sectors of the aurora oval for nearly 3,000 h each. For a dual spacecraft mission the hours of observing the ring current slightly increase and remains relatively constant for any spacecraft pair. Observations of the magnetopause increase significantly with a dual spacecraft mission. This is because with two spacecraft, the number of times when neither can observe magnetopause is drastically reduced. For auroral observations, the addition of a second spacecraft nearly doubles the total number of hourly intervals when an auroral target can be observed. For the four auroral sectors the number of hourly target visibility intervals peaks for SC0 and SC2 which are separated on average by 85°. For the full auroral oval, target visibility peaks for SC0 and SC1 which are separated by an average 69°.

In the following section we combine the target visibility derived here with a statistical analysis of solar wind and geomagnetic observations during solar cycles 23 and 24 to quantify STORM's science visibility for each objective. That is, how many hourly intervals exist when STORM observes the necessary targets during appropriate solar wind and geomagnetic conditions so that the science objectives can be addressed.

4 Science visibility

STORM's science visibility builds on the analysis which quantified the target visibility to provide a detailed statistical estimation of the number of hourly intervals during which STORM can address each of its four science objectives. This is accomplished by first identifying the necessary solar wind, magnetosphere, and geomagnetic thresholds required to address a specific mission objective. A synthetic time series of these solar wind, magnetosphere, and geomagnetic variables is then generated using historical data that has been epoch-advanced to mimic the solar cycle phase we believe STORM will be launched during. This synthetic time-series is combined with the target visibility to

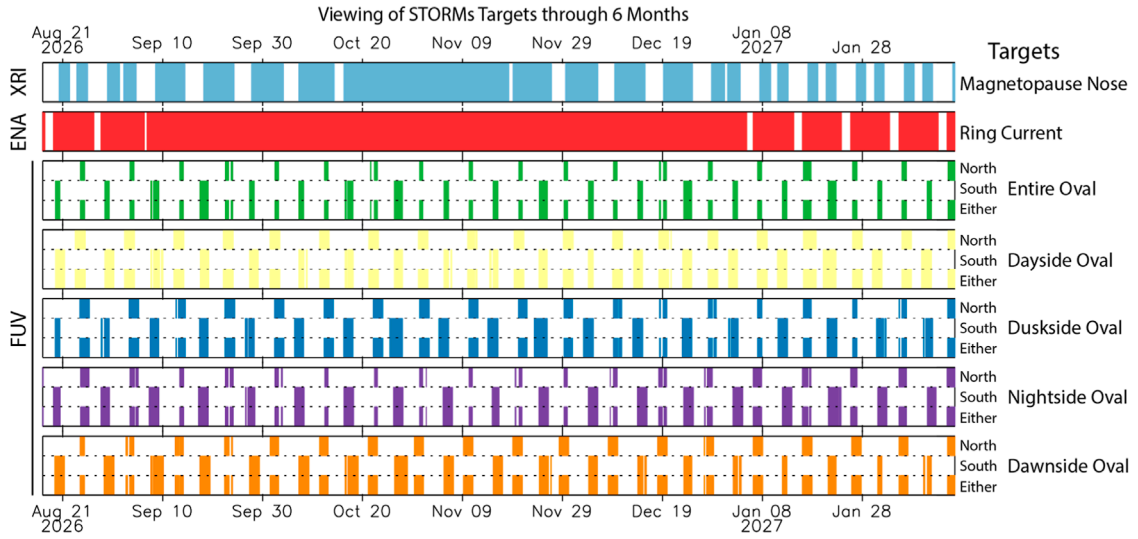

FIGURE 2
Target visibility of each of STORM's key observables. From top to bottom, the magnetopause nose (observed by XRI), the ring current (observed by ENA), the auroral oval and its four sectors, day, dusk, night, and dawn (observed by FUV). Note the auroral oval target visibility is broken down by hemisphere and also further combined to show visibility regardless of hemisphere.

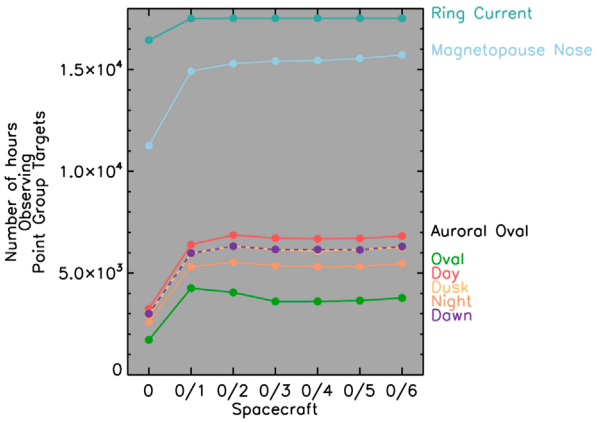

FIGURE 3
Target visibility for each of STORM's targets for a single spacecraft mission and six potential dual spacecraft missions (x-axis).

quantify when and how often specific thresholds are met or exceeded such that a science objective can be addressed. Specific thresholds include, for instance, the onset of a geomagnetic substorm or storm or an enhanced southward interplanetary magnetic field which can initiate dayside reconnection.

As an example, we can consider science objective A–Energy Transfer at the Dayside Magnetopause. As part of objective A STORM will use the XRI and FUV instruments to determine how dayside reconnection controls the flow of solar wind energy into the magnetosphere and the spatial and temporal properties of this interaction as a function of solar wind conditions (Sibeck et al., 2023a). To address these two questions XRI must observe the magnetopause nose and FUV must observe the dayside auroral oval during periods of elevated solar wind flux and southward IMF (Sibeck et al., 2023a). Here we use a threshold solar wind flux (SWF) of 2.5 × 10^8 $cm^{-2}s^{-1}$ and southward IMF of 5 nT (or −5 nT B_z). These solar wind thresholds allow XRI to track the motion of the magnetopause driven by reconnection at cadence sufficient to distinguish bursty reconnection from fast/slow steady reconnection (Sibeck et al., 2018; Sibeck et al., 2023a) and FUV to track proton auroral precipitation associated with magnetopause reconnection (Frey et al., 2002).

Figure 4 shows the culmination of this analysis using synthetic solar wind data from solar cycle 24 over a nominal two-year science mission. Panels (a) and (b) show the target visibility of the magnetopause nose and dayside auroral oval (c.f., Figure 1), and panel (c) shows when the two target visibilities overlap. Panels (d) and (e) show the synthetic IMF Bz and SWF time series during a two-year period around solar max of solar cycle 24 from the 1-h OMNI dataset (King and Papitashvili, 2005). We use a two-year period around solar max as this would be the nominal launch window and science mission phase of STORM. In panels (d) and (e) the dashed lines show the IMF Bz and solar wind flux thresholds. In panel (d) the circles identify hourly periods when IMF Bz exceeds its threshold and the FUV instrument can observe the dayside auroral oval. In panel (e) the circles identify when both IMF Bz and solar wind flux exceed their respective thresholds and the XRI instrument can observe the magnetopause nose. The text in the right margin of Figure 4 summarizes the total number of target visibility hours, and science target visibility hours for objective A.

The analysis shown in Figure 4 provides a single estimate of the number of science visibility hours for Objective A quantified from a two-year synthetic solar wind time series taken from historical data. However, the solar wind is quite variable such that the estimated science visibility can change based on the two-year time period selected, where within the solar cycle the synthetic timeseries came

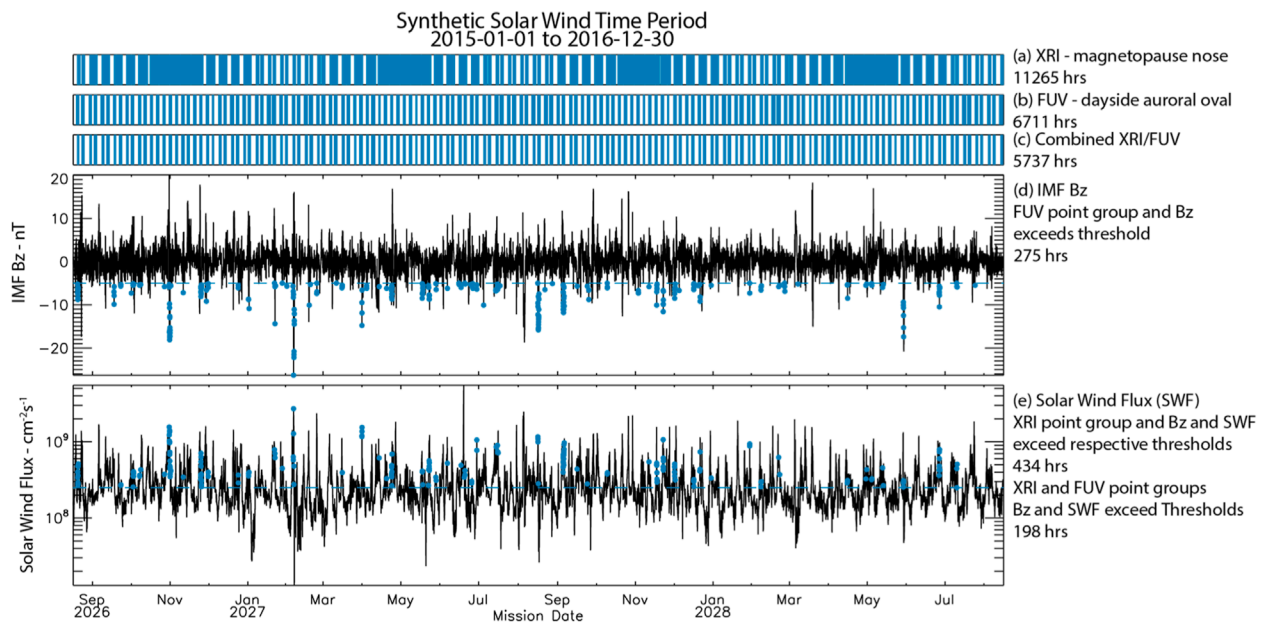

FIGURE 4
Target and science visibility for Objective A through a nominal two-year mission. **(A–C)** The target visibility of the magnetopause, dayside auroral oval, and times when both targets can be observed by STORM. **(D, E)** the synthetic IMF and solar wind flux time series used to define the science criteria for Objective A, the dashed lines show the thresholds of −5 nT and 2.5×10^8 $cm^{-2}s^{-1}$. The circles indicate times when the thresholds are exceeded and the target can be observed, these are periods of science visibility. The text in the margin summarizes the target and science visibility for Objective A.

from and from what solar cycle. To account for this variability, we use a k-folds or Monte Carlo framework which allows us to statistically estimate the science visibility as well as provide error bounds on this estimate. In short, ten synthetic solar wind timeseries are randomly sampled from a specified time interval. For each of these synthetic timeseries the science visibility is quantified as in Figure 4. The average and standard deviation of the mean of these ten estimates are then used to provide an overall estimate and error in the estimate of the science visibility.

Nominally STORM will launch around solar max, thus for this analysis we consider two-time intervals, solar max of solar cycle 23 and solar max of solar cycle 24. The max of solar cycle 23 and 24 are defined as 2000-03-03 and 2014-01-01 which lie close to the peak number of sunspots during each solar cycle. From these dates ten random time shifts of ±1 year are applied producing ten synthetic time series around the max of solar cycle 23 and 24 which are then used to complete the k-folds analysis. Figure 5 summarizes this k-folds analysis for science visibility for objective A for a single spacecraft mission and potential dual spacecraft missions. There are a larger number of hourly science visibility observing intervals during solar cycle 23 than solar cycle 24. This is not surprising as solar cycle 24 was unusually quiet. Science visibility also peaks for the SC0/2 dual spacecraft mission, consistent with the peak in target visibility in Figure 3. Important to note though is that there are several hundreds of hours of science visibility during solar cycle 24 to address science objective A with a single spacecraft mission even during an unusually quiet solar cycle.

STORM addresses its overall science goal by addressing the four objectives described in Section 2 Mission Concept. A detailed description of these science objectives, background regarding unanswered questions, how STORM distinguished between proposed interaction modes, determines occurrence patterns for each mode, and quantifies the significance of each mode, as well as the measurement requirements to address each objective and the dynamics of each mode were given by Sibeck et al. (2023a). Table 1 summarizes these details for each objective and identifies the physical process STORM is investigating, and the required instrument, target, and solar wind and/or geomagnetic conditions necessary to study that process. These identified instruments, targets, and solar wind and/or geomagnetic conditions are used to quantify the science visibility for each of STORM's objectives in the same way as for the detailed example for Objective A presented above. The same data set that was used for Objective A is used to generate a list of geomagnetic storms through solar cycles 23 and 24 using the methodology outlined in Murphy et al. (2018). This storm list is used to define an additional synthetic time series that separates all times into storm-times or quiet-times and further subdivides storm-times into either main phase or recovery phase. To generate a time-series of synthetic substorm onsets we use the Newell and Gjerloev (2011) substorm list through solar cycle 23 and 24 and tag each hour as either having or not having a substorm onset. This binary time-series is used to generate a synthetic time-series of whether a substorm onset occurs during any hour of the nominal two-year science mission. Figures 5–8 show the results of the science visibility and k-folds analysis for each objective and physical process detailed in Table 1.

Figure 6 shows the science visibility of Objective B Energy Circulation and Transfer Through the Magnetotail. This is achieved by determining how magnetotail reconnection regulates the circulation of energy from the dayside, through the magnetotail, and

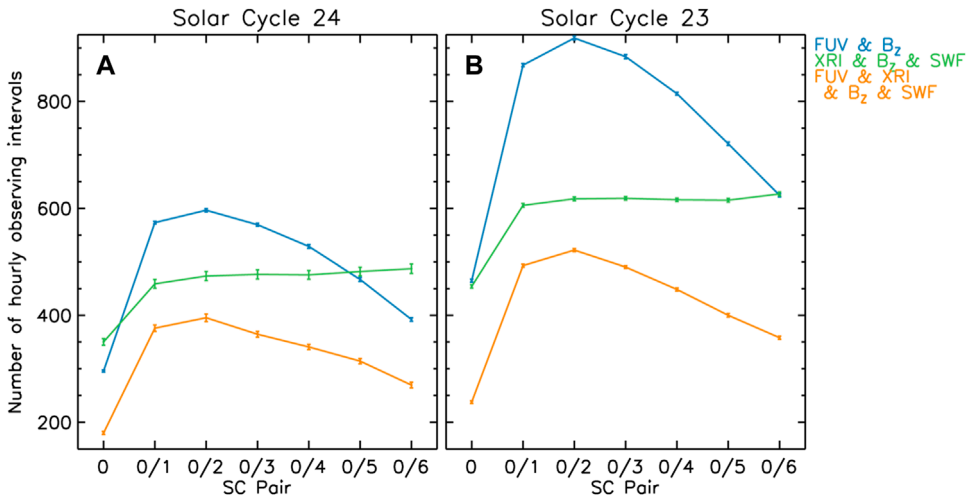

FIGURE 5
Science visibility for Objective A during **(A)** solar cycle 24 and **(B)** solar cycle 23. Blue–FUV observes dayside aurora and Bz < –5 nT; green XRI observes the magnetopause nose and Bz < –5 nT and SWF > 2.5 × 10^8 $cm^{-2}s^{-1}$; orange FUV observes dayside aurora, XRI observes magnetopause nose, and Bz < –5 nT and SWF > 2.5 × 10^8 $cm^{-2}s^{-1}$.

into the inner magnetosphere (Dungey, 1961) and by quantifying the occurrence and significance of differing reconnection modes (Sibeck et al., 2023a). In the tail, night side reconnection is the physical mechanism releasing stored energy. This energy is released by the onset of a substorm and localized brightening of the aurora. Subsequently, and depending on the solar wind and magnetosphere conditions this auroral brightening and substorm can evolve into a set of sawtooth substorms or extended periods of steady magnetospheric convection (DeJong et al., 2007; 2009). If the auroral brightening is localized the mode is characterized as a pseudo-breakup, a substorm like event where tail reconnection is believed to quenched or limited (Rostoker, 1998). Substorms, pseudo-breakups, sawtooth events, and steady magnetosphere convection are the different tail reconnection modes STORM will study to address Objective B. To do this STORM must observe substorm onsets with FUV so that the drivers of these various modes can be identified (c.f., Sibeck et al., 2023a). Coupled with XRI, FUV observations of these modes can further be used to determine how and whether these different tail reconnection modes return magnetic flux to the dayside magnetosphere (Dungey, 1961; Dungey, 1961). The top panel of Figure 6 shows the number of substorms that STORM FUV will observe in both single and dual-spacecraft configurations. The bottom panel shows the subset of these substorms during which XRI can also observe the magnetopause nose and hence flux returned to the dayside magnetopause. As with Objective A, the peak in science visibility of Objective B occurs for the SC0/2 spacecraft pair and the science visibility is higher during the more active solar cycle 23. Of note is that a single spacecraft mission observes a significant number of substorms on its own; ~800 with FUV and ~300 with both FUV and XRI.

STORM's Objective C will follow the energy released from magnetotail reconnection into the inner magnetosphere to quantify the sources and sinks and of ring current energization. To quantify the source of ring current energy, STORM must observe the ring current during geomagnetic storms and substorms, periods of ring current energization (Sibeck et al., 2023a). To quantify the sinks of ring current energy, including charge exchange, precipitation driven by wave-particle interactions (e.g., electromagnetic ion cyclotron waves, EMIC, etc.), and direct loss through the magnetosphere, STORM must observe the dusk side auroral oval in combination with an enhanced ring current (e.g., geomagnetic storm periods), and the magnetopause boundary in combination with an enhanced ring current. These observations will allow STORM to initially determine the dominant sink of ring current energy and subsequently quantify the relative efficiency of the three sinks (c.f., Figure 6; Sibeck et al., 2023b). Figure 7 shows the science visibility for each of these scenarios. Panels (a) and (b) of Figure 7 quantify STORM's science visibility during geomagnetic storms. Panel (a) depicts the number of hours ENA observes the ring current (ring current dynamics during storms) and the subset of these periods when FUV also observes the dusk side auroral oval (EMIC wave driven ring current loss). Panel (b) shows the average percentage of a geomagnetic storm, and the storm main and recovery phases where ENA observes the ring current. A single spacecraft STORM mission observes a significant number (~2000) of hourly intervals during geomagnetic storms. This roughly doubles for a dual spacecraft mission. In terms of "how much of a geomagnetic storm can be observed?" this is generally above 90%, that is ENA can observe the ring current for 90% of storms and storm main or recovery phases. Panel (c) shows the number of hourly intervals ENA observes the ring current and FUV observes the night-side auroral oval and a substorm occurs (substorm energization of the ring current). A single spacecraft mission observes ~800-1,000 substorms and a dual spacecraft mission observes as many as ~1,600-2000 substorms, depending on the solar cycle. Finally, panel (d) shows the number of 6-min intervals during which XRI observes the magnetopause nose, ENA observes the ring current, and the IMF Bz < –10 nT and SWF > 2 × 10^8 $cm^{-2}s^{-1}$. The increased Bz threshold is necessary for the magnetopause to penetrate the inner magnetosphere (Staples et al.,

10.3389/fspas.2024.1394655

TABLE 1 Summary of the physical processes, required instrument, target, and solar wind and geomagnetic conditions required to address each of STORM's four science objectives. * A lower SWF threshold is required as these ojbectives can be addressed using XRI with a lower cadence then required for Objective A.

Obj	Physical Process	Required Instrument	Target	Solar Wind, and/or Geomagnetic Condition defining Science Visibility conditions
A	Energy Transfer at the Dayside Magnetopause			
	Dayside Magnetopause Erosion	XRI	MP Nose	SWF > 2.5×10^8 $cm^{-2}s^{-1}$
				B_z < −5 nT
		FUV	DS Auroral Oval	B_z < −5 nT
B	Energy Circulation and Transfer Through the Magnetotail			
	Nightside magnetotail reconnection and substorms	FUV	NS Auroral Oval	Substorm Onset
	Nightside flux return to the dayside following nightside reconnection/substorm	XRI/FUV	NS Auroral Oval	Substorm Onset
			MP Nose	SWF > 2×10^8 $cm^{-2}s^{-1}$ *
C	Energy Sources and Sinks for the Ring Current			
	Ring current enhancement during geomagnetic storms	ENA	Ring Current	Geomagnetic Storm
	Ring current enhancement during substorms	ENA/FUV	Ring Current	Substorm onset
			NS Auroral Oval	
	Ring current loss via charge exchange vs. wave induced precipitation	ENA/FUV	Ring Current	Geomagnetic Storm
			Dusk Auroral Oval	
	Ring current loss through the magnetopause	ENA/XRI	Ring Current	Bz < −10 nT
			MP Nose	SWF > 2×10^8 $cm^{-2}s^{-1}$ *
D	Energy Feedback from the Inner Magnetosphere			
	Ring current effects on night-side reconnection and substorm onset	ENA/FUV	Ring Current	Substorm onset
			NS Auroral Oval	Dst < −20 nT
	Ring current effects on magnetopause position	ENA/XRI	Ring Current	Dst < −50 nT
			MP Nose	

2022) such that ring current loss through the magnetopause may be quantified; the number of intervals peaks for a dual spacecraft mission but remains high with ~500 and ~1,500 intervals for solar cycle 24 and 23, respectively.

Objective C investigates the dynamics of the energization of the inner magnetosphere; however, it is also important to consider the effects that the inner magnetosphere can have on other plasma systems. In particular a strong storm-time ring current may affect the position of the magnetopause (Tsyganenko and Sibeck, 1994; García and Hughes, 2007; Samsonov et al., 2016) and the latitude of substorm onset and the amount of open flux required to initiate tail reconnection (Milan et al., 2009a). Objective D will investigate energy feedback from the inner magnetosphere and the effects a strong ring-current has on the day and nightside magnetosphere. To investigate ring current feedback on the magnetopause XRI must observe the magnetopause nose, as ENA observes an enhanced ring current, defined here as Dst < −50 nT. These parameters define the science visibility for ring current feedback on the dayside magnetosphere which is shown in Figure 8 panel (a). To investigate the effect that the ring current has on nightside reconnection requires observations of an enhanced ring current with varying intensities and substorms onset. To achieve this the science visibility requires ENA to observe an enhanced ring current, defined as periods when Dst < -20 nT, and FUV must observe the

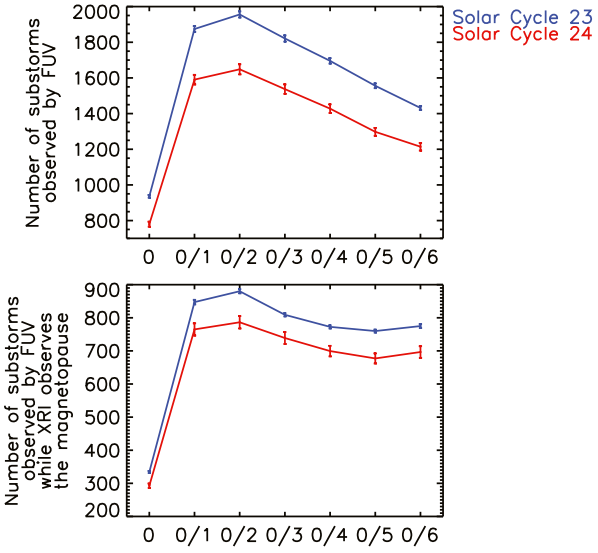

FIGURE 6
Science visibility for STORM's Objective **(B) (A)** The number of substorms observed by FUV and **(B)** the number of substorms observed by FUV when XRI observes the magnetopause nose for single and dual spacecraft missions (x-axis). The science visibility is estimated from both solar cycle 23 and 24 (blue and red).

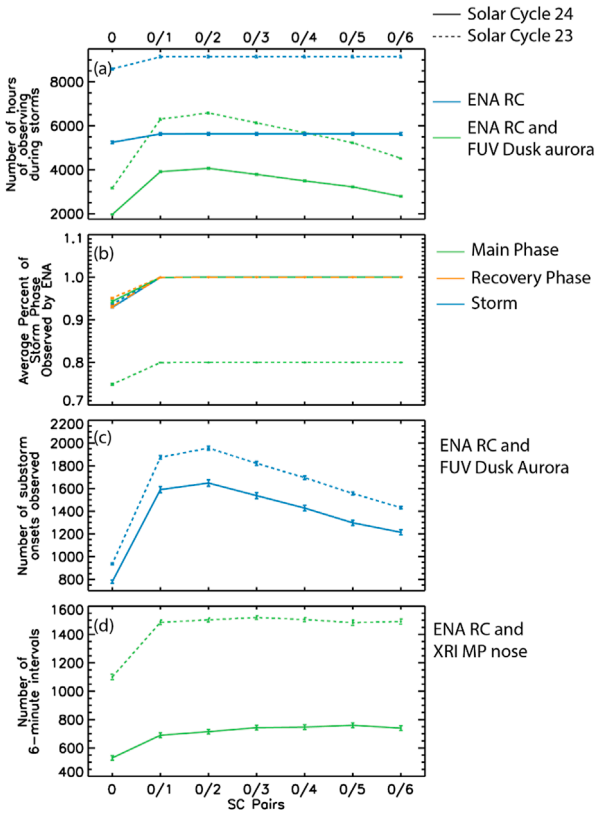

FIGURE 7
Science visibility for STORM's Objective C during solar cycle 23 (dashed) and 24 (solid) for a single and dual spacecraft mission (x-axis). **(A)** Number of hours observing the ring current (blue) and ring current/dusk auroral oval (green). **(B)** Percentage of storm (blue) and storm main (green) and recovery (orange) phases that ENA observes the ring current. **(C)** Number of substorms during an enhanced ring current when FUV can observe substorm onset and ENA can observed the ring current. **(D)** Number of 6-min intervals during an enhanced ring current when the ring current and magnetopause nose can be observed.

nightside auroral oval during a substorm. This science visibility is shown in Figure 8 panel (b). Note the difference in the Dst thresholds for these two science visibilities, different thresholds were specifically chosen as it is postulated that a larger ring current is required to affect the dayside magnetopause due to larger magnetic field strengths at the magnetopause then in the night-side tail during periods of extreme tail stretching observed before substorm onset. Overall, STORM has a significant number of events to address Objective D, with a minimum of ~200 h to address dayside feedback and ~400 substorms to address nightside feedback, both during periods when the ring current is enhanced. As with the other objectives, more events are observed for solar cycle 23 then solar cycle 24, and for a dual spacecraft mission consisting of SC0 and 2. In the next section we provide a brief summary of the results presented here and perspective looking forward to the future.

5 Summary and perspective

Earth Science, Heliophysics, and Astrophysics imaging missions have enabled fundamental scientific advances. In Earth Science, the advent of scientific imaging transformed meteorology. For example, the Geostationary Operational Environmental Satellite (GOES) family of satellites have provided continuous and reliable environmental information used to support weather forecasting, storm tracking, and research (Hawkings et al., 1996). The importance of such observations was demonstrated during the GOES I-M era with the successful tracking and monitoring of hurricanes Hugo and Andrew (Hawkings et al., 1996). In Astrophysics, imagers and telescopes have been the corner stone of scientific research for centuries. Following the space age, space-borne telescopes have been used characterize the cosmic microwave background (Hinshaw et al., 2013), study the aurora on other planets (Clarke et al., 1998), and identify exoplanets (Borucki, 2016). In solar physics, imagers are commonly used to monitor activity on the sun and its relation to space weather (Darnel et al., 2022) and for scientific research, including the Solar TErrestrial RElations Observatory (STEREO) mission designed to capture stereographic images of coronal mass ejections (Kaiser et al., 2008). In magnetospheric physics, imaging has been used to study the auroral (Mende, 2016), ring current (Brandt, 2002), and plasmaspheric (Goldstein et al., 2003) dyanmics. These observations have provided fundamental insight into solar wind-magnetosphere coupling, linking dayside reconnection to auroral precipitation (Frey et al., 2003), and inner-magnetospheric dynamics, via stereographic images of the terrestrial ring current (Goldstein and McComas, 2018).

This paper detailed the target and science visibility of the Solar-Terrestrial Observer for the Response of the Magnetosphere

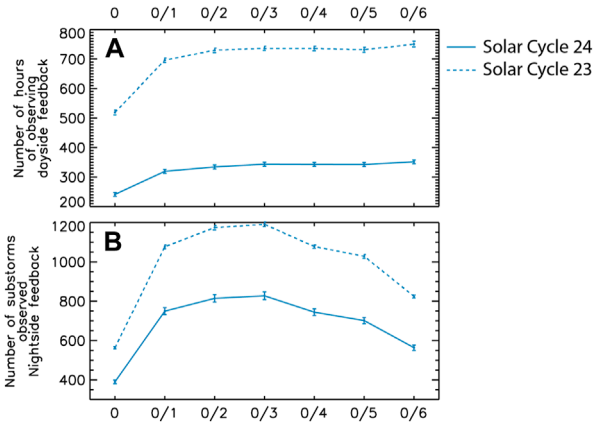

FIGURE 8
Science visibility for STORM's Objective D estimated from solar cycle 23 (dashed) and 24 (solid) as a function of single and dual spacecraft mission configurations (x-axis). **(A)** The number of hourly intervals when STORM can investigate inner-magnetosphere feedback on the dayside magnetopause. **(B)** The number of substorm during which STORM can investigate feedback of the inner magnetosphere on nightside reconnection and substorm dynamics.

(STORM) mission concept. STORM's overarching science goal is to study the system science of and flow of energy in the solar wind-magnetosphere system. STORM achieves this by observing key plasma regimes and systems associated with the Dungey cycle and coupled solar wind-magnetosphere system. This is referred to as STORM's target visibility, how often a specific target can be observed, and is illustrated in Figures 3, 4. STORM's science visibility quantifies the number of intervals (typically hourly intervals) when STORM can address its science objectives and overarching science goal, e.g., when the solar and geomagnetic conditions are sufficient to conduct science. This science visibility is derived for a single spacecraft and six spacecraft pairs which could form a potential dual spacecraft mission (c.f., Figure 1B). These target and science visibility was determined through a detailed analysis of the Design Reference Mission (DRM), instrument FOVs, and target locations, combined with a statistical analysis of historical solar wind conditions during solar cycles 23 and 24 (an active and quiet solar cycle). The analysis demonstrating how the science visibility is quantified is illustrated in Figures 4, 5; Figures 5–8 show the science visibility for each of STORM's four science objectives (Section 2—Mission Concept).

Overall, Figure 3 demonstrates that STORM observes each of its required targets, the magnetopause, the auroral oval and dusk, dawn, day, and night sectors, and the ring current for significant portions of the mission. The auroral oval is observed for a minimum of 2000 h and increases to ~3,000 h for each sector. The magnetopause is observed for a minimum of ~11,000 h and the ring current a minimum of ~16,000 h. These numbers increase for a dual spacecraft mission and peak for the SC0/2 pair, which are on average 85° out of phase (in a shared orbit Figure 1B). Regarding science visibility (Figures 5–8), STORM has several hundreds of intervals to address each of its objectives with a single spacecraft. The science visibility is larger during solar cycle 23 than 24, which is not surprising given the subdued nature of solar cycle 24 (Basu, 2013). Like STORMs target visibility, the science visibility peaks (in general) for spacecraft pair SC0/2 and provides the largest number of observations of the aurora and its four sectors which subsequently also creates a peak in the science visibility.

It is important to remind the reader that a statistical analysis of historical solar wind data around solar max of solar cycles 23 and 24 was used to quantify and estimate an error in the science visibility for each objective. This was done using a k-folds or Monte Carlo technique (described in Section 4—Target Visibility). This statistical analysis was performed to account for the non-normal and non-periodic distribution of solar wind and geomagnetic conditions required to address STORM's science and gives a more accurate representation of the science visibility then assuming a fixed distribution of events. For example, the rate of geomagnetic storms peaks during solar max; however, geomagnetic storms are not periodic and do not occur with a fixed frequency. The k-folds/Monte Carlo technique accounts for this and provides a more robust estimation of the expected science visibility and its errors (or variation–see Section 4 for details). Of note are the errors in the science visibility shown in Figures 5–8. They are small compared to the estimated science visibility, such that, in general, the science visibility does not vary significantly when considering a two-year period around solar max, which may potentially shift forward or backward by up to a year. There is larger variation in science visibility as a function of solar cycle and there is likely to be variation with solar phase. However, STORM would nominally launch around solar max and so the science visibility was calculated for that period of the solar cycle. Finally, both solar cycle 23 and 24 were used to determine science visibility in order to provide an upper and lower estimate from an active and quiet solar cycle.

In short, a single spacecraft STORM mission launched during a quiet solar cycle has a significant number of science visibility intervals. This would provide hundreds of intervals to address STORM's overarching science goals and each of the four science objectives allowing researchers to conduct case studies of particular events as well as statistical studies to determine the spatial and temporal characteristics of the fundamental phenomena coupling the solar wind and magnetosphere and leading the redistribution of energy throughout the magnetosphere. A dual spacecraft mission significantly increases science visibility and allows for stereographic imaging and tomography (see Cucho-Padin et al. this issue) which a single spacecraft can only do statistically. However, a dual spacecraft mission would significantly increase the overall complexity and budget as compared to a single spacecraft mission. Without a target budget value it is impossible to settle on a final STORM design, single vs. dual spacecraft. Recent NASA Medium Class Explore (MIDEX) announcements of opportunity have had budgets which align with a single STORM spacecraft mission and would allow STORM to fully address its objectives. However, if budgets increase it may be possible to consider a dual spacecraft mission and investigate the three-dimensional structure and dynamics of magnetopause and ring current via tomographic techniques, while observing STORM's targets for significant periods of time. Regardless, STORM would be the first stand-alone and complete system science mission capable of studying the end-to-end dynamics of the coupled solar wind-magnetosphere system and resulting flow of energy in the Dungey cycle (Sibeck et al., 2023b).

Data availability statement

The raw data supporting the conclusion of this article will be made available by the authors, without undue reservation.

Author contributions

KM: Conceptualization, Data curation, Formal Analysis, Funding acquisition, Investigation, Methodology, Project administration, Resources, Software, Supervision, Validation, Visualization, Writing–original draft, Writing–review and editing. MS: Conceptualization, Formal Analysis, Investigation, Methodology, Software, Visualization, Writing–original draft, Writing–review and editing. DS: Conceptualization, Methodology, Resources, Visualization, Writing–original draft, Writing–review and editing. CS: Conceptualization, Investigation, Methodology, Visualization, Writing–original draft, Writing–review and editing. HC: Conceptualization, Investigation, Methodology, Visualization, Writing–original draft, Writing–review and editing. FP: Conceptualization, Investigation, Methodology, Visualization, Writing–original draft, Writing–review and editing. EZ: Conceptualization, Formal Analysis, Investigation, Methodology, Visualization, Writing–original draft, Writing–review and editing.

Funding

The author(s) declare that financial support was received for the research, authorship, and/or publication of this article. This work is supported in part by a NASA GSFC IRAD.

Conflict of interest

The authors declare that the research was conducted in the absence of any commercial or financial relationships that could be construed as a potential conflict of interest.

Publisher's note

All claims expressed in this article are solely those of the authors and do not necessarily represent those of their affiliated organizations, or those of the publisher, the editors and the reviewers. Any product that may be evaluated in this article, or claim that may be made by its manufacturer, is not guaranteed or endorsed by the publisher.

References

Basu, S. (2013). The peculiar solar cycle 24 – where do we stand? *J. Phys. Conf. Ser.* 440, 012001. doi:10.1088/1742-6596/440/1/012001

Borovsky, J. E., and Valdivia, J. A. (2018). The Earth's magnetosphere: a systems science overview and assessment. *Surv. Geophys.* 39 (5), 817–859. doi:10.1007/s10712-018-9487-x

Borucki, W. J. (2016). KEPLER Mission: development and overview. *Rep. Prog. Phys.* 79 (3), 036901. doi:10.1088/0034-4885/79/3/036901

Brandt, P. C., Mitchell, D. G., Ebihara, Y., Sandel, B. R., Roelof, E. C., Burch, J. L., et al. (2002). Global IMAGE/HENA observations of the ring current: examples of rapid response to IMF and ring current-plasmasphere interaction. *J. Geophys. Res.* 107 (A11), 1359. doi:10.1029/2001JA000084

Clarke, J. T., Ballester, G., Trauger, J., Ajello, J., Pryor, W., Tobiska, K., et al. (1998). Hubble Space Telescope imaging of Jupiter's UV aurora during the Galileo orbiter mission. *J. Geophys. Res. Planets* 103 (E9), 20217–20236. doi:10.1029/98JE01130

Darnel, J. M., Seaton, D. B., Bethge, C., Rachmeler, L., Jarvis, A., Hill, S. M., et al. (2022). The GOES-R solar UltraViolet imager. *Space weather.* 20 (4). doi:10.1029/2022SW003044

DeJong, A. D., Cai, X., Clauer, R. C., and Spann, J. F. (2007). Aurora and open magnetic flux during isolated substorms, sawteeth, and SMC events. *Ann. Geophys.* 25 (8), 1865–1876. doi:10.5194/angeo-25-1865-2007

DeJong, A. D., Ridley, A. J., Cai, X., and Clauer, C. R. (2009). A statistical study of BRIs (SMCs), isolated substorms, and individual sawtooth injections. *J. Geophys. Res. Space Phys.* 114 (A8). doi:10.1029/2008JA013870

Dungey, J. W. (1961). Interplanetary magnetic field and the auroral zones. *Phys. Rev. Lett.* 6 (2), 47–48. doi:10.1103/PhysRevLett.6.47

Frey, H. U., Meade, S. B., Immel, T. J., Fuselier, S. A., Claflin, E. S., Gérard, J.-C., et al. (2002). Proton aurora in the cusp. *J. Geophys. Res.* 107 (A7), 1091. doi:10.1029/2001JA900161

Frey, H. U., Mende, S. B., Angelopoulos, V., and Donovan, E. F. (2004). Substorm onset observations by IMAGE-FUV. *J. Geophys. Res.* 109 (A10), A10304. doi:10.1029/2004JA010607

Frey, H. U., Phan, T. D., Fuselier, S. A., and Mende, S. B. (2003). Continuous magnetic reconnection at Earth's magnetopause. *Nature* 426 (6966), 533–537. doi:10.1038/nature02084

García, K. S., and Hughes, W. J. (2007). Finding the Lyon-Fedder-Mobarry magnetopause: a statistical perspective. *J. Geophys. Res. Space Phys.* 112 (A6). doi:10.1029/2006JA012039

Goldstein, J., and McComas, D. J. (2018). The big picture: imaging of the global geospace environment by the TWINS mission. *Rev. Geophys.* 56 (1), 251–277. doi:10.1002/2017RG000583

Goldstein, J., Sandel, B. R., Forrester, W. T., and Reiff, P. H. (2003). IMF-driven plasmasphere erosion of 10 July 2000. *Geophys. Res. Lett.* 30 (3), 1146. doi:10.1029/2002gl016478

Gombosi, T. I., Chen, Y., Glocer, A., Huang, Z., Jia, X., Liemohn, M. W., et al. (2021). What sustained multi-disciplinary research can achieve: the space weather modeling framework. *J. Space Weather Space Clim.* 11, 42. doi:10.1051/swsc/2021020

Hawkings, J., Staton, C. P., Paquett, J. A., Barbieri, L. P., Suranno, M. A., Reynolds, R., et al. (1996) *GOES I-M databook*.

Hinshaw, G., Larson, D., Komatsu, E., Spergel, D. N., Bennett, C. L., Dunkley, J., et al. (2013). Nine-year wilkinson microwave anisotropy probe (wmap) observations: cosmological parameter results. *Astrophysical J. Suppl. Ser.* 208 (2), 19. doi:10.1088/0067-0049/208/2/19

Kaiser, M. L., Kucera, T. A., Davila, J. M., St. Cyr, O. C., Guhathakurta, M., and Christian, E. (2008). The STEREO mission: an introduction. *Space Sci. Rev.* 136 (1–4), 5–16. doi:10.1007/s11214-007-9277-0

Kepko, L. (2018). "Magnetospheric constellation: leveraging space 2.0 for big science," in *Igarss 2018 - 2018 IEEE international geoscience and remote sensing symposium*, 285–288. doi:10.1109/IGARSS.2018.8519475

King, J. H., and Papitashvili, N. E. (2005). Solar wind spatial scales in and comparisons of hourly Wind and ACE plasma and magnetic field data. *J. Geophys. Res.* 110 (A2), A02104. doi:10.1029/2004JA010649

Lin, D., Sorathia, K., Wang, W., Merkin, V., Bao, S., Pham, K., et al. (2021). The role of diffuse electron precipitation in the formation of subauroral polarization streams. *J. Geophys. Res. Space Phys.* 126 (12). doi:10.1029/2021JA029792

Lin, Y., Duan, X., Zhao, C., and Xu, L.Da. (2012) *Systems science*. Boca Raton: CRC Press. doi:10.1201/b13095

Mende, S. B. (2016). Observing the magnetosphere through global auroral imaging: 2. Observing techniques. *J. Geophys. Res. Space Phys.* 121 (10), 10,638–10,660. doi:10.1002/2016JA022607

Milan, S. E., Grocott, A., Forsyth, C., Imber, S. M., Boakes, P. D., and Hubert, B. (2009a). A superposed epoch analysis of auroral evolution during substorm growth, onset and recovery: open magnetic flux control of substorm intensity. *Ann. Geophys.* 27 (2), 659–668. doi:10.5194/angeo-27-659-2009

Milan, S. E., Hutchinson, J., Boakes, P. D., and Hubert, B. (2009b). Influences on the radius of the auroral oval. *Ann. Geophys.* 27 (7), 2913–2924. doi:10.5194/angeo-27-2913-2009

Milan, S. E., Walach, M.-T., Carter, J. A., Sangha, H., and Anderson, B. J. (2019). Substorm onset latitude and the steadiness of magnetospheric convection. *J. Geophys. Res. Space Phys.* 124 (3), 1738–1752. doi:10.1029/2018JA025969

Murphy, K. R., Watt, C. E. J., Mann, I. R., Jonathan Rae, I., Sibeck, D. G., Boyd, A. J., et al. (2018). The global statistical response of the outer radiation belt during geomagnetic storms. *Geophys. Res. Lett.* 45 (9), 3783–3792. doi:10.1002/2017GL076674

Newell, P. T., and Gjerloev, J. W. (2011). Evaluation of SuperMAG auroral electrojet indices as indicators of substorms and auroral power. *J. Geophys. Res. Space Phys.* 116 (A12). doi:10.1029/2011JA016779

Rostoker, G. (1998). On the place of the pseudo-breakup in a magnetospheric substorm. *Geophys. Res. Lett.* 25 (2), 217–220. doi:10.1029/97GL03583

Samsonov, A. A., Gordeev, E., Tsyganenko, N. A., Šafránková, J., Němeček, Z., Šimůnek, J., et al. (2016). Do we know the actual magnetopause position for typical solar wind conditions? *J. Geophys. Res. A Space Phys.* 121 (7), 6493–6508. doi:10.1002/2016JA022471

Shoemaker, M. A., Folta, D. C., and Sibeck, D. G. (2022). "Application of tisserand's criterion and the lidov-kozai effect to STORM's trajectory design," in *AAS/AIAA astrodynamics specialist conference*.

Sibeck, D. G., Allen, R., Aryan, H., Bodewits, D., Brandt, P., Branduardi-Raymont, G., et al. (2018). Imaging plasma density structures in the soft X-rays generated by solar wind charge exchange with neutrals. *Space Sci. Rev.* 214 (4), 79. doi:10.1007/s11214-018-0504-7

Sibeck, D. G., Lopez, R. E., and Roelof, E. C. (1991). Solar wind control of the magnetopause shape, location, and motion. *J. Geophys. Res.* 96 (A4), 5489. doi:10.1029/90JA02464

Sibeck, D. G., Murphy, K. R., Porter, F. S., Connor, H. K., Walsh, B. M., Kuntz, K. D., et al. (2023a). Quantifying the global solar wind-magnetosphere interaction with the Solar-Terrestrial Observer for the Response of the Magnetosphere (STORM) mission concept. *Front. Astronomy Space Sci.* 10. doi:10.3389/fspas.2023.1138616

Sibeck, D. G., Murphy, K. R., Porter, F. S., Walsh, B., Connor, H., Kuntz, K., et al. (2023b). Imaging the end-to-end dynamics of the global solar wind-magnetosphere interaction. *Bull. AAS*. doi:10.3847/25c2cfeb.9b87eed9

Staples, F. A., Kellerman, A., Murphy, K. R., Rae, I. J., Sandhu, J. K., and Forsyth, C. (2022). Resolving magnetopause shadowing using multimission measurements of phase space density. *J. Geophys. Res. Space Phys.* 127 (2), e2021JA029298. doi:10.1029/2021JA029298

Tsyganenko, N. A., and Sibeck, D. G. (1994). Concerning flux erosion from the dayside magnetosphere. *J. Geophys. Res.* 99 (A7), 13425–13436. doi:10.1029/94ja00719

frontiers | Frontiers in Astronomy and Space Sciences

TYPE Perspective
PUBLISHED 05 August 2024
DOI 10.3389/fspas.2024.1430099

OPEN ACCESS

EDITED BY
Yoshizumi Miyoshi,
Nagoya University, Japan

REVIEWED BY
Jean-Francois Ripoll,
CEA DAM Île-de-France, France

*CORRESPONDENCE
Martin O. Archer,
m.archer10@imperial.ac.uk

RECEIVED 09 May 2024
ACCEPTED 22 July 2024
PUBLISHED 05 August 2024

CITATION
Archer MO, Shi X, Walach M-T, Hartinger MD, Gillies DM, Di Matteo S, Staples F and Nykyri K (2024), Crucial future observations and directions for unveiling magnetopause dynamics and their geospace impacts. *Front. Astron. Space Sci.* 11:1430099. doi: 10.3389/fspas.2024.1430099

Crucial future observations and directions for unveiling magnetopause dynamics and their geospace impacts

Martin O. Archer[1]*, Xueling Shi[2,3], Maria-Theresia Walach[4], Michael D. Hartinger[5,6], D. Megan Gillies[7,8], Simone Di Matteo[9,10], Frances Staples[11] and Katariina Nykyri[10]

[1]Department of Physics, Imperial College London, London, United Kingdom, [2]Department of Electrical and Computer Engineering, Virginia Tech, Blacksburg, VA, United States, [3]High Altitude Observatory, National Center for Atmospheric Research, Boulder, CO, United States, [4]Physics Department, Lancaster University, Lancaster, United Kingdom, [5]Space Science Institute, Boulder, CO, United States, [6]Department of Earth, Planetary, and Space Sciences, University of California Los Angeles, Los Angeles, CA, United States, [7]Department of Physics and Astronomy, University of Calgary, Calgary, AB, Canada, [8]Department of Chemistry and Physics, Mount Royal University, Calgary, AB, Canada, [9]Physics Department, The Catholic University of America, Washington, DC, United States, [10]NASA-Goddard Space Flight Center, Greenbelt, MD, United States, [11]Department of Atmospheric and Oceanic Sciences, University of California Los Angeles, Los Angeles, CA, United States

The dynamics of Earth's magnetopause, driven by several different external/internal physical processes, plays a major role in the geospace energy budget. Given magnetopause motion couples across many space plasma regions, numerous forms of observations may provide valuable information in understanding these dynamics and their impacts. *In-situ* multi-point spacecraft measurements measure the local plasma environment, dynamics and processes; with upcoming swarms providing the possibility of improved spatiotemporal reconstruction of dynamical phenomena, and multi-mission conjunctions advancing understanding of the "mesoscale" coupling across the geospace "system of systems." Soft X-ray imaging of the magnetopause should enable boundary motion to be directly remote sensed for the first time. Indirect remote sensing capabilities might be enabled through the field-aligned currents associated with disturbances to the magnetopause; by harnessing data from satellite mega-constellations in low-Earth orbit, and taking advantage of upgraded auroral imaging and ionospheric radar technology. Finally, increased numbers of closely-spaced ground magnetometers in both hemispheres may help discriminate between high-latitude processes in what has previously been a "zone of confusion." Bringing together these multiple modes of observations for studying magnetopause dynamics is crucial. These may also be aided by advanced data processing techniques, such as physics-based inversions and machine learning methods, along with comparisons to increasingly sophisticated geospace assimilative models and simulations.

KEYWORDS

magnetopause, surface waves, MHD waves, auroral ionosphere, field-aligned currents, ground, instruments, techniques

1 Introduction

Earth's magnetopause, depicted in Figure 1A, is the interface of the solar–terrestrial interaction, hence mediates the flow of mass, momentum, and energy between the solar wind and geospace. As this interaction is responsible for the myriad of phenomena that can severely impact vital infrastructure, collectively known as space weather, understanding physical processes at the magnetopause and their system-wide effects is of utmost importance. The magnetopause is observed to be in almost continual motion. Alongside magnetic reconnection (Dungey, 1961), the wave-like motion of the magnetopause constitutes one of the major energy transfer mechanisms in the solar–terrestrial interaction (Axford, 1964). These magnetopause motions affect auroral, ionospheric, outer radiation belt, and trapped magnetospheric plasmas — either directly or indirectly through associated ultra-low frequency (ULF) waves (e.g., Sibeck, 1990; Elkington, 2006).

The boundary location in steady state is dictated by a balance of pressures (thermal, magnetic, and dynamic) on both sides of the magnetopause. Imbalances which lead to magnetopause motion are typically thought of as being externally driven, e.g., by variations in the upstream flow pressure (Potemra et al., 1989; Sibeck et al., 1989; Francia et al., 1999; Viall et al., 2009), the velocity shear as the solar wind flows around the magnetosphere (Kelvin-Helmholtz Instability, KHI; Chandrasekhar, 1961; Faganello and Califano, 2017; Masson and Nykyri, 2018), or reconnection with the interplanetary magnetic field altering the dayside magnetic flux (Hill and Rassbach, 1975; Matlsev and Lyatsky, 1975). However, internal processes such as the drift-mirror instability may also generate pressure changes that drive boundary dynamics (Constantinescu et al., 2009; Nykyri et al., 2021). Several of these driving processes may occur simultaneously and even modify one another, making observations hard to disentangle (e.g., Ma et al., 2014; Di Matteo et al., 2022).

The wave-like motion of the magnetopause is well approximated by magnetohydrodynamic surface wave theory (see recent review of Archer et al., 2024). The interplay of inertial, damping, and restoring forces on the dayside magnetopause predicts a ~5–10 min response to direct driving (Smit, 1968; Freeman et al., 1995; Børve et al., 2011; Horaites et al., 2023) alongside resonant ~10–20 min standing surface waves from ionospheric reflection (Chen and Hasegawa, 1974; Plaschke and Glassmeier, 2011; Archer and Plaschke, 2015). In contrast, on the magnetopause flanks where KH-waves dominate, periodicities are shorter ~1–7 min (Lin et al., 2014; Kavosi and Raeder, 2015). Corresponding wavelengths along the boundary span a wide spatial range, ~1–15 R_E (Lin et al., 2014).

Since magnetopause dynamics couple across many regions of geospace, there are numerous means of directly and indirectly observing the processes occurring and their consequences. In this paper we outline current and future observational capabilities at Earth, grouped by different target regions of geospace. We highlight new/improved directions to the field for unveiling magnetopause dynamics across different modes of observation and how these may aid our understanding of the boundary's global importance to the geospace energy budget.

2 Solar wind – magnetosphere interface

2.1 Multi-point *in-situ* measurements

In-situ spacecraft provide measurements of the physical conditions present at their location, such as particle distributions/moments and (DC/AC) electric/magnetic fields. Single spacecraft cannot unambiguously separate variations in space and time. Four spacecraft are the minimum required to uniquely resolve 3D structure (Paschmann and Daly, 1998), methods for which have been applied to the Cluster, MMS, and THEMIS missions. These typically assume first-order derivatives and planar structures over spacecraft separation scales. For studying magnetopause dynamics, the times the boundary passed over each spacecraft allow estimation of its local thickness and motion (Paschmann et al., 2005; Plaschke et al., 2009). Furthermore, simultaneous observations around the moving boundary allow comparison of spatial patterns against theory (e.g., Hasegawa et al., 2004; Plaschke et al., 2013; Archer et al., 2019; 2021).

Multi-spacecraft missions to date have typically focused on one scale at a time (e.g., fluid/ion for Cluster, ion/electron for MMS), achieved through precisely-controlled formations. In contrast, upcoming missions such as HelioSwarm (Klein et al., 2023) and the Plasma Observatory concept (Retinò et al., 2022) instead propose semi-autonomous swarms of 7+ spacecraft broadly separated across a variety of plasma scales. Swarms will allow unprecedented spatiotemporal reconstruction of magnetopause dynamics, e.g., KH roll-up vortices as in Figure 1C, while also probing important cross-scale physics.

While multi-spacecraft missions provide great detail of local structures and physical processes, geospace constitutes a "system of systems" with many different plasma populations that feedback on one another leading to more complex emergent/collective dynamical behaviour (Kepko, 2018; Kepko et al., 2023). This highlights the need for simultaneous observations across multiple spatial scales to understand how collective interactions produce "mesoscale" phenomena (~1–3 R_E in the magnetosphere) that mediate the global solar–terrestrial interaction.

Conjunctions between existing missions have revealed some of these feedbacks and mesoscale structuring relevant to magnetopause dynamics. For example, foreshock and magnetosheath transients emerge from interactions of large-scale solar wind structures with the quasi-parallel bow shock and reflected suprathermal foreshock ion populations, leading to many localised disturbances of the boundary and impacts throughout geospace (e.g., Archer et al., 2012; 2013; Nykyri et al., 2019; Wang et al., 2020a; Escoubet et al., 2020). Currently an extraordinary number of spacecraft orbit Earth, meaning many opportunities for multi-mission conjunctions exist. Indeed, Figure 1B highlights how March 2024 regularly offered simultaneous observations upstream of the bow shock, near the magnetopause at different local times, and at different *L*-shells within the magnetosphere.

Unfortunately, sparse conjunctions do not provide sufficient measurements to resolve all key processes across the "system of systems". Furthermore, care must be taken when comparing/combining measurements across different missions/instruments. Mission concepts for ~40 distributed

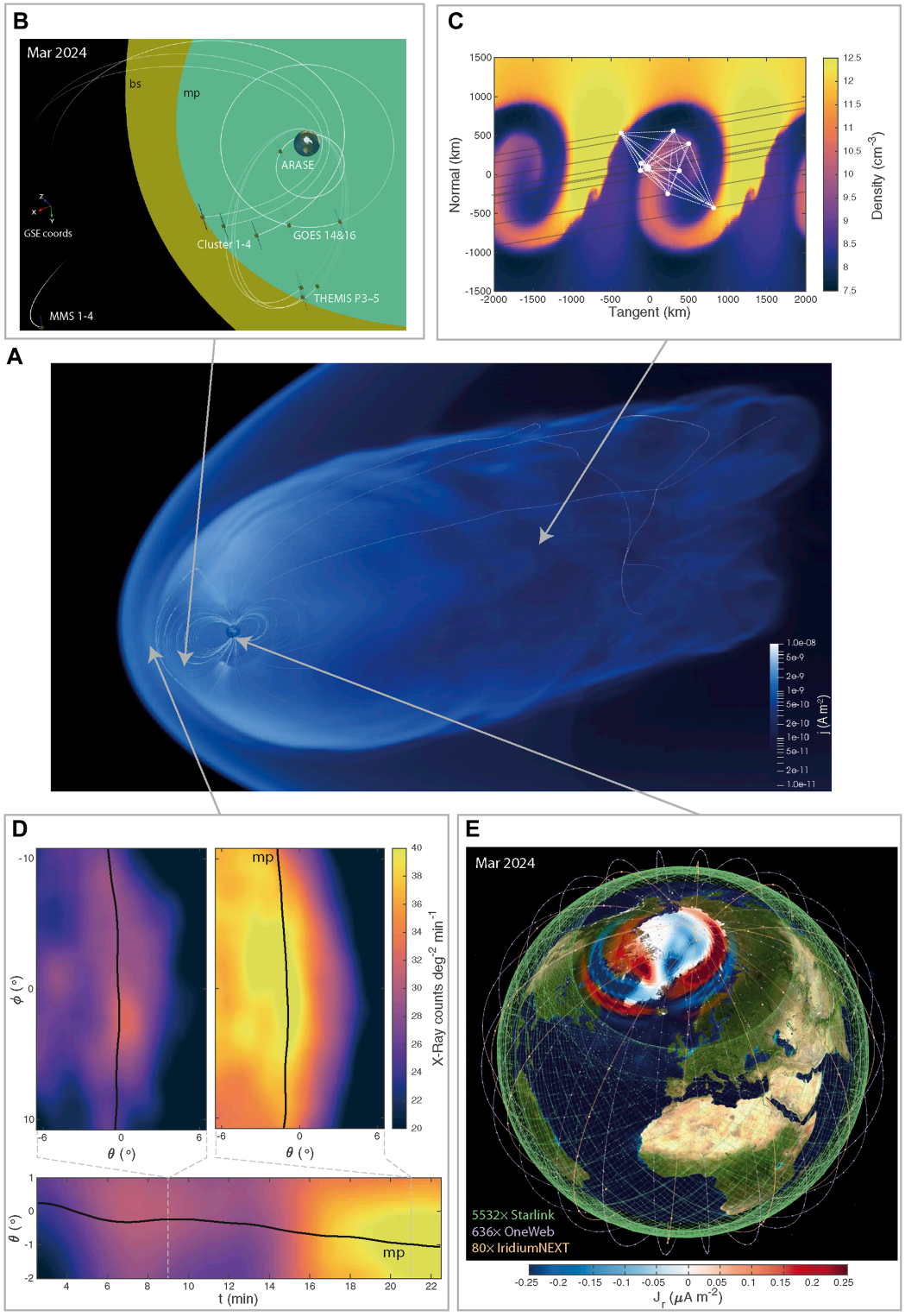

FIGURE 1
Current and future observational capabilities for studying magnetopause dynamics from space. **(A)** Visualisation of the magnetosphere from a Gorgon global MHD simulation (e.g., Mejnertsen et al., 2017). Displayed are volumetric current densities throughout the simulation, along with magnetic field lines in the meridional plane. **(B)** Example of an orbital conjunction from current *in-situ* missions ideal for investigating magnetopause dynamics. **(C)** Diagram of HelioSwarm skimming Kelvin-Helmholtz vortices from a local MHD simulation with 100 km velocity shear layer and no magnetic shear (Ma et al., 2017). **(D)** Simulated SMILE soft X-ray images (top panels) and time evolution along the Sun-Earth line (bottom panels) using data from Samsonov et al. (2024). The counts have been processed using multidimensional kernel density estimation, applying Epanechnikov kernels of optimal bandwidth from Silverman's rule (Silverman, 1986). A proxy for the magnetopause (black) is identified as the median of the marginal distributions. **(E)** Orbits of the Starlink, OneWeb, and Iridium NEXT constellations in low Earth orbit along with field-aligned currents associated with magnetopause surface waves from an SWMF global MHD simulation of the magnetospheric response to a solar wind density pulse (Archer et al., 2023).

identical spacecraft separated over "mesoscales" have been suggested to address this (Kepko, 2018; Kepko et al., 2023). These would have clear applications in building a global picture of magnetopause dynamics, revolutionising our understanding of the boundary's role in controlling mass, momentum, and energy transfer.

2.2 Soft X-rays

Large-scale imaging of the dynamic solar–terrestrial interaction from space is an emerging direction that clearly complements *in-situ* spacecraft and ground-based measurements. Several upcoming missions aim to image the dayside magnetosphere in soft X-rays from solar wind charge exchange, including the joint ESA-CAS SMILE mission (Branduardi-Raymont and Wang, 2022; Wang and Branduardi-Raymont, 2022), and smallsats Geo-X (Ezoe et al., 2020) and LEXI (Walsh et al., 2024). A heavy solar wind ion in the magnetosheath/cusps gains an electron in a high-energy state from a neutral exospheric atom, subsequently relaxing by emitting an X-ray photon (Cravens et al., 2001; Robertson and Cravens, 2003). Soft X-ray emissivities are predicted to peak at the tangent to the magnetopause (Sibeck et al., 2018), potentially enabling boundary dynamics to be tracked in both space and time.

Methods to determine the location of the magnetopause from X-ray images are not trivial, typically assuming some global shape (Samsonov et al., 2022; Wang and Sun, 2022). Furthermore, under typical to moderate solar wind driving, rather low photon counts are expected. Spatiotemporal binning can help increase signal-to-noise, though bins of scales comparable to typical dayside magnetopause motion ($1° \times 1° \times 5$ min) still result in very noisy images (e.g., Samsonov et al., 2022; 2024). While this may be mitigated by longer integration times and/or larger pixels, it would render boundary dynamics indeterminable.

More advanced techniques are likely required to improve scientific return. For example, data-driven density estimation techniques little used in our field may help (e.g., Archer et al., 2015; 2017). Instead of sharp fixed pixels, density estimation sums over smooth functions centred on each observation. This has convergence and continuity benefits over binning, and methods for data-driven scaling of bandwidths already exist (Silverman, 1986). Figure 1D shows our application to simulated data from Samsonov et al. (2024), demonstrating clear improvements.

3 Magnetosphere–ionosphere interface

Information about disturbances to the magnetopause are communicated to the auroral ionosphere along magnetic field lines by field-aligned currents (FACs), carried by precipitating magnetospheric electrons (ions) and/or upwelling ionospheric ions (electrons) for upward (downward) currents (Elphic, 1988; Sibeck, 1990). Recent high-resolution global MHD simulations, shown in Figure 1E (Archer et al., 2023), suggest magnetopause surface waves' FACs have large latitudinal extents (~10°) via non-resonant coupling between the compressional and Alfvén modes, peaking at the inner edge of the magnetopause transition (typically a few degrees equatorward of the Open–Closed Boundary, OCB; Kozyreva et al., 2019). These FACs open the possibility of remote sensing magnetopause motion at the magnetosphere–ionosphere interface. Current LEO spacecraft (e.g., Swarm, Friis-Christensen et al., 2008; POES; Evans and Greer, 2000; DMSP; Kilcommons et al., 2017; Redmon et al., 2017; and CASSIOPE; Yau and James, 2015) enable observations of magnetic field, electric field, precipitating particle, and/or drift velocity perturbations; all of which may be associated with magnetopause dynamics (e.g., Horvath and Lovell, 2021). However, due to orbital mechanics, single satellites in LEO provide a predominantly spatial cut and cannot capture the ~1–20 min periodicities at a fixed point in space associated with magnetopause motion. GDC's 6-spacecraft will enable temporal evolution of important magnetosphere–ionosphere–thermosphere coupling processes to be captured (Akbari et al., 2024). In early mission phases when orbital planes at high-latitudes are closest in longitude — best for studying magnetopause-related dynamics — resolvable timescales will be limited by the spacing/time between satellites to ~2–4 min. Mega-constellations with many satellites in the same orbital plane are required to capture the full range of magnetopause periodicities at the magnetosphere–ionosphere interface.

In recent years, commercial mega-constellations with 10's–1000s of satellites have been launched into LEO. Figure 1E shows orbits of the three largest to date: Iridium, OneWeb, and Starlink. The AMPERE project has successfully demonstrated engineering magnetometers aboard the polar-orbiting Iridium constellation (orange) can provide FAC observations across the polar cap through spherical fits to measured perturbations (Anderson et al., 2000; Waters et al., 2019). This has provided great insight into the variability of Region-1 and -2 FACs (Milan et al., 2017), though the 30° spacecraft separation within each of the 6 orbital planes means only periodicities >16 min are resolvable. Larger mega-constellations might be leveraged in a similar way, enabling FACs from magnetopause dynamics to be captured. OneWeb (purple) also has polar orbits, but twice as many orbital planes as Iridium and only ~7° separation within these. Thus OneWeb might provide ~2 min resolution polar maps with double the azimuthal fidelity. Starlink (green) occupy mostly ~50° inclined orbits, but a minority of orbits do cross the polar cap. The sheer number of Starlink satellites means it could still yield improved coverage/resolution to Iridium. Of course these possibilities would involve significant technical challenges and further developed processing methods, but could significantly advance our global monitoring of the dynamic solar–terrestrial interaction from space.

4 Ionosphere

4.1 Auroral imaging

Magnetopause disturbances can, through the precipitating magnetospheric particles carrying their FACs, lead to production/modulation of auroral emission in the ionosphere (e.g., Craven et al., 1986; Sibeck et al., 1999; Kozyreva et al., 2019). Aurorae are monitored from both ground and space, providing yet further means of remote sensing magnetopause dynamics.

This is a historic era for ground-based auroral science, with unprecedented all-sky imager (ASI) coverage operating coast-to-coast across the high latitude North American landscape, as shown

in Figure 2A (orange/yellow circles). The THEMIS-ASI network of 21 imagers (Donovan et al., 2006; 2008; Mende et al., 2008) has provided comprehensive panchromatic "white light" imaging since 2008, capturing qualitative images of auroral morphology from local to continent-wide scales (quantitative data can be derived by combining with meridian scanning photometers; Gabrielse et al., 2021). Since particle species cannot be differentiated in panchromatic data, aurorae are assumed caused by precipitating electrons. At 9 THEMIS-ASI sites are the REGO red-line imagers, which observe a key oxygen auroral emission (Liang et al., 2016). TREx, another continent-wide network across 6 locations (Gillies et al., 2019), instead features co-located monochromatic ASIs at major auroral emissions (blue-line, near-infrared, and RGB "true colour"). This enables electron flux and mean precipitation energy to be derived, yielding vital information on particle sources and their connection to the magnetosphere (Liang et al., 2022; 2024; Gillies et al., 2023). The THEMIS-ASIs are being replaced with RGB imagers to complement the SMILE mission, with the 19 new SMILE-ASIs completing by summer 2025 (Carter et al., 2024). Of course, ground-based auroral imagery is only possible during clear night skies, which for dayside magnetopause signatures limits studies to winter seasons.

In addition to ground-based imagers, space-based ones such as on IMAGE (Mende et al., 2000b; a,c), Polar (Torr et al., 1995), DMSP (Paxton et al., 2002), the upcoming SMILE (Branduardi-Raymont and Wang, 2022) and proposed MAAX (Halford et al., 2024) have the benefit of observing large areas and at wavelengths (e.g., UV-band) not observable from the ground. Furthermore, UV auroral observations are possible at all times, independent of light pollution. However, space-based auroral images are less detailed, due to trade-offs between spatial coverage and integration times, as well as orbital configuration. While DMSP auroral images build up over ~25 min polar crossings, meaning spatiotemporal ambiguity affects potential magnetopause signatures, both Polar and IMAGE were spinning allowing ~1–2 min cadence images, suitable for resolving auroral impacts of long-period magnetopause waves (e.g., Liou et al., 2008). SMILE's UVI will cover the entire auroral oval for the first time since 2005, allowing global auroral dynamics to be captured at 1 min and ~50–150 km resolution, augmented by more detailed imagery from the ground.

Figure 2B shows simulated FACs associated with magnetopause surface waves which may lead to auroral signatures (Archer et al., 2023). While auroral bright spots have been linked to the magnetopause (Lundin and Evans, 1985; Kozyreva et al., 2019) and recently plasmapause (He et al., 2020; Horvath and Lovell, 2021), it is not clear if surface waves' FACs are sufficient to generate emission or simply modulate existing aurorae. Insight might be gained through comparison with field line resonances, whose similar periodic FACs do produce aurorae (Samson et al., 1996; Milan et al., 2001; Gillies et al., 2018).

4.2 Radar

Closure of magnetopause disturbances' FACs through ionospheric Pedersen currents are associated with electric field oscillations and $\mathbf{E}\times\mathbf{B}$ plasma drifts, resulting in so-called Travelling Convection Vortices (TCVs, Friis-Christensen et al., 1988; Bristow et al., 1995) which may be detected by radar observations (e.g., Walsh et al., 2015; Shi et al., 2020).

SuperDARN (e.g., Ruohoniemi et al., 1989; Ruohoniemi and Greenwald, 1996; Chisham et al., 2007; Nishitani et al., 2019, etc.) consists of ground-based high-frequency coherent scatter radars which measure line-of-sight Doppler shifts of ionospheric irregularities. The network has expanded over the past 2 decades/solar cycles across high- (blue/red fans in Figure 2A) and mid-latitudes, enabling coverage for typical but also disturbed geomagnetic conditions (Nishitani et al., 2019; Walach and Grocott, 2019; Walach et al., 2021). Historically, ULF waves have been studied at individual radars, where comparing measurements across multiple beams (see Figure 2C for simulated single-beam observations) can track 2-D wave propagation providing insights into drivers (Fenrich et al., 1995; James et al., 2013). Because a full scan of the SuperDARN field-of-view took ~1–2 min though, signatures due to faster magnetopause dynamics (e.g., KH-waves) could not be fully captured over large-scales. However, exciting upgrades to digital radar systems (e.g., McWilliams et al., 2023) are enabling imaging at 3.5 s resolution. As these improvements roll out, the overlapping fields-of-view might allow unprecedented large-scale observations of TCVs due magnetopause dynamics through high-order spherical fits to velocity measurements (Ruohoniemi et al., 1989).

In addition to coherent scatter radars, Incoherent Scatter Radar (ISR, cyan stars in Figure 2A), e.g., EISCAT (Rietveld et al., 2019; Stamm et al., 2021), PFISR (Nicolla and Heinselman, 2007), and RISR, (Gillies et al., 2016), is another valuable tool for remote sensing magnetopause dynamics from the ionosphere. Buchert et al. (1999) and Wang et al. (2020b) used ISR measurements showing ULF waves with periods from 1–10 min significantly modulate the ionospheric electron density at a range of altitudes, ultimately affecting ionospheric conductance. While ISR's spatial coverage is limited for resolving the spatial scales and propagation of magnetopause dynamics, its ability to offer insights into altitude profiles of multiple ionospheric parameters becomes invaluable. These are aspects poorly explored both in magnetopause dynamical theory/simulations and observations at present.

4.3 Global navigation satellite systems (GNSS)

Ionospheric total electron content (TEC), the columnar number density, is most widely obtained using remote-sensing techniques between GNSS satellites and ground-receivers (magenta dots in Figure 2A). Observed TEC fluctuations with periods 10–1000 s have been linked to ULF waves in the polar cap (e.g., Watson et al., 2016), auroral zone (e.g., Pilipenko et al., 2014), and mid-/low-latitude regions (e.g., Yizengaw et al., 2018). These have amplitudes as large as 7 TECU (Watson et al., 2015). Pilipenko et al. (2014) explored several possible mechanisms of higher latitude ULF wave driven TEC fluctuations, two of which may be related to magnetopause surface waves and have been invoked in other studies. These are wave-modulated precipitation of energetic electrons affecting ionospheric conductivities (Buchert et al., 1999; Wang et al., 2020b), and periodic vertical plasma flows due

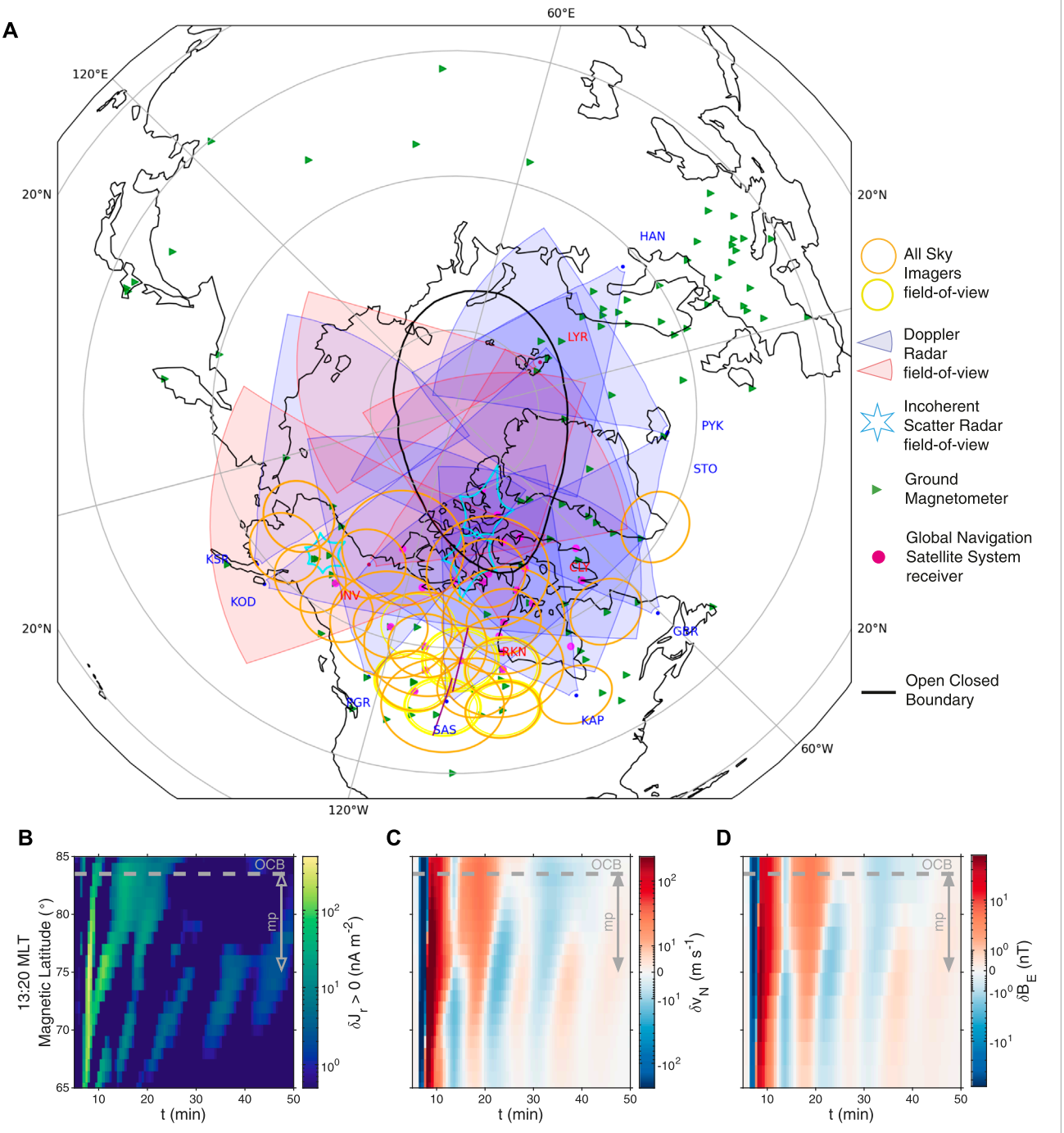

FIGURE 2
Current observational capabilities for remote sensing magnetopause dynamics and their impacts from the ground. **(A)** Orthographic map showing ground-based instruments in the high-latitude northern hemisphere in geographic coordinates (20° latitudinal spacing). These include SuperDARN radars (red/blue fans), SuperMAG ground magnetometers (green triangles), All Sky Imagers (orange/yellow circles), Incoherent Scatter Radar (cyan stars), spectrograph fields (purple lines), and Chain GNSS receivers (magenta dots). The Open–Closed Boundary (OCB) from the Tsyganenko (1995) model under median conditions is shown as the thick black line. Panels **(B–D)** Potential dayside ground-based signatures of magnetopause surface waves from the same global MHD simulation as in Figure 1E. Displayed are magnetic latitude–time plots (keograms) of perturbations in upwards field-aligned currents **(B)**, North–South ionospheric velocity **(C)**, and East–West ground magnetic field **(D)** near the noon sector. The OCB (dashed grey lines) and projected extent of the magnetopause (double-headed arrows) from the simulation are also displayed (note global simulation numerics lead to more smeared out boundary layers than in reality).

to waves' FACs (Belakhovsky et al., 2016; Kozyreva et al., 2020). TEC observations are complicated by satellite orbits and line-of-sight, with standard conversions from "slant" to "vertical" TEC (e.g., Kozyreva et al., 2020) assuming homogeneity over ~10° — invalid for even large-scale surface waves (Archer et al., 2023). Further modelling to better understand the physical

processes behind TEC fluctuations and any observational biases are needed for GNSS to become a valuable remote-sensing tool for magnetopause dynamics.

5 Ground magnetic field

The magnetic field at Earth's surface includes contributions from magnetosphere–ionosphere currents. Global networks of ground-based magnetometers of varying spatial separations (> 200 km, green triangles in Figure 2A) have been some of the earliest and most widely used tools for understanding how magnetopause disturbances lead to FACs/waves (Friis-Christensen et al., 1988; Sibeck, 1990; Araki, 1994; Motoba et al., 2007), ultimately impacting the global magnetosphere–ionosphere–thermosphere system (e.g., Shi et al., 2022). While unable to detect phenomena < 100 km (Hughes and Southwood, 1976), they have a few important advantages over other instruments. They can operate continuously without concern for sunlight, cloud cover, and ionospheric backscatter. Closely spaced magnetometers can also resolve important mesoscales from the ground (Engebretson and Zesta, 2017). Furthermore, ground magnetometers do not move in the geocentric frame, thus the interpretation of their data is less complicated than satellites (e.g., Anderson et al., 1989).

Studies of high-latitude ULF waves have been described as a "zone of confusion" with structuring whose relation out to the magnetosphere is ambiguous (Pilipenko et al., 2015; 2018; see also Figure 2D). Unambiguously linking wave power enhancements with magnetopause surface waves (e.g., Glassmeier, 1992), or other wave activity (e.g., Araki and Nagano, 1988; Lyatsky and Sibeck, 1997), may require closely spaced networks of magnetometers to identify the polarization changes and wave power variations predicted by simulations (Archer et al., 2023). 2D networks in both hemispheres spanning the cusp and auroral zones would further help discriminate wave modes; e.g., enabling natural experiments for isolating surface wave signatures from telluric currents (Weygand et al., 2023), variations in ionospheric conductance (e.g., Hartinger et al., 2017), and asymmetries in upstream driving conditions (e.g., Oliveira et al., 2020; Shi et al., 2020; Di Matteo and Sivadas, 2022; Villante et al., 2022).

Finally, magnetotelluric survey networks (e.g., USArray's EarthScope sites; Schultz, 2010) consist of small arrays taking simultaneous geoelectric and geomagnetic field measurements temporarily (typically ~3 weeks, but variable), subsequently moving locations. They have a few unique capabilities relevant for surface wave diagnostics (Hartinger et al., 2020; Shi et al., 2022). They are typically deployed in more spatially dense networks than typical magnetometer networks (< 70 km) thus capture finer-scale features. They provide information about ground conductivity, which can be used to discriminate magnetosphere–ionosphere currents from telluric currents. They also yield additional geoelectric field measurements, enabling the waves' hazard to power systems to be considered. However, their spatial coverage at any given time is much more limited and site locations may not always be optimal for studying the magnetopause's effects on the ground.

6 Discussion

This is an exciting time for studying magnetopause dynamics, with many new/emerging observational capabilities in both *in-situ* and remote sensing measurements. Each of these enables us to probe the physical processes occurring at the boundary and their impacts upon geospace. While each observational method has its own unique benefits and drawbacks, bringing them together simultaneously will start to provide a holistic view of the magnetopause's controlling role in mediating the solar–terrestrial interaction — from local physics, through to emergent mesoscale features, and ultimately the collective global response/impact. It is crucial this unprecedented observational coverage be maintained through sustained funding for extended mission/instrumentation operations.

Along with this unprecedented diversity and coverage of measurements, data processing methods will become more important than ever. Inversion techniques applied to multi-point measurements offer unique opportunities to resolve the temporal evolution and spatial structure of different wave modes, which may otherwise be convolved in original datasets complicating their physical interpretation (Archer et al., 2023). For example, distributed 2D networks of ground-based magnetometers have long been used to obtain magnetospheric field-aligned, ionospheric Pedersen and Hall, and now even telluric currents via the Spherical Elementary Current System technique (e.g., Shi et al., 2022; Weygand et al., 2023). Similar methods are now also being applied to SuperDARN observations (e.g., Fenrich et al., 2019). These approaches may further be boosted through machine learning capabilities (Camporeale, 2019; Nguyen et al., 2022; Grimmich et al., 2023), allowing more sophisticated data analysis across "big data" for the identification of signals related to magnetopause surface waves and dynamics (e.g., Cicone et al., 2016; Murphy et al., 2020; Di Matteo et al., 2021), especially in nonlinear and nonstationary contexts (Piersanti et al., 2018; Stallone et al., 2020). Finally, data mining and assimilation (Tsyganenko and Sitnov, 2007; Merkin et al., 2016; Alzate et al., 2023) into maturing "system of systems" models (e.g., Zhang et al., 2019; Sorathia et al., 2020; 2023; Gombosi et al., 2021) can aid the interpretation of this unprecedented, but still scattered, data collection enabling the global context to be inferred.

The techniques and physical insights gained from studying Earth's magnetopause might also translate to different space plasma environments where fewer observational methods are possible, such as the other planetary magnetopauses (e.g., Masters et al., 2009; Boardsen et al., 2010; Montgomery et al., 2023) or solar coronal structures like loops (Nakariakov et al., 2016). Here similar dynamical processes are thought to occur but over vastly different scales, morphologies, and/or plasma conditions.

Data availability statement

The original contributions presented in the study are included in the article/supplementary material, further inquiries can be directed to the corresponding author.

Author contributions

MA: Conceptualization, Funding acquisition, Visualization, Writing–original draft, Writing–review and editing. XS: Conceptualization, Visualization, Writing–original draft, Writing–review and editing. M-TW: Conceptualization, Writing–original draft, Writing–review and editing. MH: Conceptualization, Writing–original draft, Writing–review and editing. DG: Conceptualization, Writing–original draft, Writing–review and editing. SD: Conceptualization, Writing–original draft, Writing–review and editing. FS: Conceptualization, Writing–review and editing. KN: Funding acquisition, Writing–review and editing.

Funding

The author(s) declare that financial support was received for the research, authorship, and/or publication of this article. This work was supported by the International Space Science Institute (ISSI) in Bern, through ISSI International Team project #546 "Magnetohydrodynamic Surface Waves at Earth's Magnetosphere (and Beyond)." MA was supported by UKRI (STFC/EPSRC) Stephen Hawking Fellowship EP/T01735X/1 and UKRI Future Leaders Fellowship MR/X034704/1. XS was supported by National Aeronautics and Space Administration (NASA) awards 80NSSC21K1677 and 80NSSC21K1683, National Science Foundation (NSF) awards AGS-1935110, AGS-2025570, and AGS-2307205. M-TW was supported by UKRI (STFC) Ernest Rutherford Fellowship ST/X003663/1. MH was supported by NASA awards 80NSSC21K1683 and 80NSSC23K0903, and NSF awards AGS-2307204 and AGS-2027210. SD was supported by NASA award 80NSSC21K0459. FS was supported by NASA award 80NSSC21K0448.

Acknowledgments

We acknowledge the 3DView online tool (Génot et al., 2018) used to create Figure 1B. We acknowledge the pyDARN package (Shi et al., 2022) used to create Figure 2A. For the purpose of open access, the author(s) has applied a Creative Commons attribution (CC BY) licence to any Author Accepted Manuscript version arising.

Conflict of interest

The authors declare the absence of any commercial or financial relationships that could be construed as a potential conflict of interest.

The author(s) declared that they were an editorial board member of Frontiers, at the time of submission. This had no impact on the peer review process and the final decision.

Publisher's note

References

Akbari, H., Rowland, D., Coleman, A., Buynovskiy, A., and Thayer, J. (2024). Gradient calculation techniques for multi-point ionosphere/thermosphere measurements from GDC. *Front. Astron. Space Sci.* 11, 1231840. doi:10.3389/fspas.2024.1231840

Alzate, N., Di Matteo, S., Morgan, H., Seaton, D. B., Miralles, M. P., Balmaceda, L., et al. (2023). Data mining for science of the sun-earth connection as a single system. *Front. Astronomy Space Sci.* 10, 1151785. doi:10.3389/fspas.2023.1151785

Anderson, B. J., Engebretson, M. J., and Zanetti, L. J. (1989). Distortion effects in spacecraft observations of MHD toroidal standing waves: theory and observations. *J. Geophys. Res.* 94, 13425–13445. doi:10.1029/JA094iA10p13425

Anderson, B. J., Takahashi, K., and Toth, B. A. (2000). Sensing global Birkeland currents with iridium® engineering magnetometer data. *Geophys. Res. Lett.* 27, 4045–4048. doi:10.1029/2000GL000094

Araki, T. (1994). A Physical model of the geomagnetic sudden commencement. *Geophys. Monogr. Ser.* 81, 183–200. doi:10.1029/GM081p0183

Araki, T., and Nagano, H. (1988). Geomagnetic response to sudden expansions of the magnetosphere. *J. Geophys. Res. Space Phys.* 93, 3983–3988. doi:10.1029/JA093iA05p03983

Archer, M. O., Hartinger, M. D., Plaschke, F., Southwood, D. J., and Rastaetter, L. (2021). Magnetopause ripples going against the flow form azimuthally stationary surface waves. *Nat. Commun.* 12, 5697. doi:10.1038/s41467-021-25923-7

Archer, M. O., Hartinger, M. D., Rastaetter, L., Southwood, D. J., Heyns, M., Eggington, J. W. B., et al. (2023). Auroral, ionospheric and ground magnetic signatures of magnetopause surface modes. *J. Geophys. Res. Space Phys.* 128, e2022JA031081. doi:10.1029/2022JA031081

Archer, M. O., Hartinger, M. D., Walsh, B. M., and Angelopoulos, V. (2017). Magnetospheric and solar wind dependences of coupled fast-mode resonances outside the plasmasphere. *J. Geophys. Res. Space Phys.* 122, 212–226. doi:10.1002/2016JA023428

Archer, M. O., Hartinger, M. D., Walsh, B. M., Plaschke, F., and Angelopoulos, V. (2015). Frequency variability of standing alfvén waves excited by fast mode resonances in the outer magnetosphere. *Geophys. Res. Lett.* 42, 10150–10159. doi:10.1002/2015GL066683

Archer, M. O., Hietala, H., Hartinger, M. D., Plaschke, F., and Angelopoulos, V. (2019). Direct observations of a surface eigenmode of the dayside magnetopause. *Nat. Commun.* 10, 615. doi:10.1038/s41467-018-08134-5

Archer, M. O., Horbury, T. S., and Eastwood, J. P. (2012). Magnetosheath pressure pulses: generation downstream of the bow shock from solar wind discontinuities. *J. Geophys. Res. Spoace Phys.* 117, A05228. doi:10.1029/2011JA017468

Archer, M. O., Horbury, T. S., Eastwood, J. P., Weygand, J. M., and Yeoman, T. K. (2013). Magnetospheric response to magnetosheath pressure pulses: a low pass filter effect. *J. Geophys. Res. Space Phys.* 118, 5454–5466. doi:10.1002/jgra.50519

Archer, M. O., Pilipenko, V. A., Li, B., Sorathia, K., Nakariakov, V. M., Elsden, T., et al. (2024). Magnetopause MHD surface wave theory: progress & challenges. *Front. Astron. Space Sci.* 11. In press. doi:10.3389/fspas.2024.1407172

Archer, M. O., and Plaschke, F. (2015). What frequencies of standing surface waves can the subsolar magnetopause support? *J. Geophys Res.* 120, 3632–3646. doi:10.1002/2014JA020545

Axford, W. I. (1964). Viscous interaction between the solar wind and the earth's magnetosphere. *Planet. Space Sci* 12, 45–53. doi:10.1016/0032-0633(64)90067-4

Belakhovsky, V., Pilipenko, V., Murr, D., Fedorov, E., and Kozlovsky, A. (2016). Modulation of the ionosphere by pc5 waves observed simultaneously by gps/tec and eiscat. *Earth, Planets Space* 68, 102–113. doi:10.1186/s40623-016-0480-7

Boardsen, S. A., Sundberg, T., Slavin, J. A., Anderson, B. J., orth, H., Solomon, S. C., et al. (2010). Observations of Kelvin-Helmholtz waves along the dusk-side boundary of Mercury's magnetosphere during MESSENGER's third flyby. *Gephys. Res. Lett.* 37, L12101. doi:10.1029/2010GL043606

Børve, S., Sato, H., Pécseli, H. L., and Trulsen, J. K. (2011). Minute-scale period oscillations of the magnetosphere. *Ann. Geophys.* 29, 663–671. doi:10.5194/angeo-29-663-2011

Branduardi-Raymont, G., and Wang, C. (2022). *The SMILE mission*. Singapore: Springer Nature Singapore, 1–22. doi:10.1007/978-981-16-4544-0_39-1

Bristow, W. A., Sibeck, D. G., Jacquey, C., Greenwald, R. A., Sofko, G. J., Mukai, T., et al. (1995). Observations of convection vortices in the afternoon sector using the SuperDARN HF radars. *J. Geophys. Res. Space Phys.* 100, 19743–19756. doi:10.1029/95JA01301

Buchert, S. C., Fujii, R., and Glassmeier, K.-H. (1999). Ionospheric conductivity modulation in ULF pulsations. *J. Geophys. Res. Space Phys.* 104, 10119–10133. doi:10.1029/1998JA900180

Camporeale, E. (2019). The challenge of machine learning in space weather: nowcasting and forecasting. *Space weather.* 17, 1166–1207. doi:10.1029/2018SW002061

Carter, J. A., Dunlop, M., Forsyth, C., Oksavik, K., Donovon, E., Kavanagh, A., et al. (2024). Ground-based and additional science support for SMILE. *Earth Planet. Phys.* 8, 275–298. doi:10.26464/epp2023055

Chandrasekhar, S. (1961). *Hydrodynamic and hydromagnetic stability*. Oxford, UK: Oxford University Press.

Chen, L., and Hasegawa, A. (1974). A theory of long-period magnetic pulsations: 2. impulse excitation of surface eigenmode. *J. Geophys. Res.* 79, 1033–1037. doi:10.1029/JA079i007p01033

Chisham, G., Lester, M., Milan, S. E., Freeman, M. P., Bristow, W. a., Grocott, a., et al. (2007). A decade of the super dual auroral radar network (SuperDARN): scientific achievements, new techniques and future directions. *Surv. Geophys.* 28, 33–109. doi:10.1007/s10712-007-9017-8

Cicone, A., Liu, L., and Zhou, H. (2016). Adaptive local iterative filtering for signal decomposition and instantaneous frequency analysis. *Appl. Comput. Harmon. Analysis* 41, 384–411. doi:10.1016/j.acha.2016.03.001

Constantinescu, O. D., Glassmeier, K.-H., Plaschke, F., Auster, U., Angelopoulos, V., Baumjohann, W., et al. (2009). THEMIS observations of duskside compressional Pc5 waves. *J. Geophys. Res. Space Phys.* 114, A00C25. doi:10.1029/2008JA013519

Craven, J. D., Frank, L. A., Russell, C. T., Smith, E. J., and Lepping, R. P. (1986). *Solar Wind-Magnetosphere Coupling (Tokyo, Japan: terra Sci.), chap. Global auroral responses to magnetospheric compressions by shocks in the solar wind*, 367–380.

Cravens, T. E., Robertson, I. P., and Snowden, S. L. (2001). Temporal variations of geocoronal and heliospheric X-ray emission associated with the solar wind interaction with neutrals. *J. Geophys. Res. Space Phys.* 106, 24883–24892. doi:10.1029/2000JA000461

Di Matteo, S., and Sivadas, N. (2022). Solar-wind/magnetosphere coupling: understand uncertainties in upstream conditions. *Front. Astronomy Space Sci.* 9, 333. doi:10.3389/fspas.2022.1060072

Di Matteo, S., Viall, N. M., and Kepko, L. (2021). Power spectral density background estimate and signal detection via the multitaper method. *J. Geophys. Res. Space Phys.* 126, e28748. doi:10.1029/2020ja028748

Di Matteo, S., Villante, U., Viall, N., Kepko, L., and Wallace, S. (2022). On differentiating multiple types of ULF magnetospheric waves in response to solar wind periodic density structures. *J. Geophys. Res. Space Phys.* 127, e2021JA030144. doi:10.1029/2021ja030144

Donovan, E., Liu, W., Liang, J., Spanswick, E., Voronkov, I., Connors, M., et al. (2008). Simultaneous THEMIS *in situ* and auroral observations of a small substorm, *Geophys. Res. Lett.*, 35, L17S18. doi:10.1029/2008GL033794

Donovan, E., Mende, S., Jackel, B., Frey, H., Syrjäsuo, M., Voronkov, I., et al. (2006). The THEMIS all-sky imaging array—system design and initial results from the prototype imager. *J. Atmos. Solar-Terrestrial Phys.* 68, 1472–1487. doi:10.1016/j.jastp.2005.03.027

Dungey, J. W. (1961). Interplanetary magnetic field and the auroral zones. *Phys. Rev. Lett.* 6, 47–48. doi:10.1103/PhysRevLett.6.47

Engebretson, M., and Zesta, E. (Editors) (2017). *Ground magnetometer array planning: report of a workshop*. Minneapolis, USA: Augsburg College. http://space.augsburg.edu/GroundMagnetometerWorkshopReport.pdf

Elkington, S. R. (2006). "A review of ULF interactions with radiation belt electrons,". Editors K. Takahashi, P. J. Chi, R. E. Denton, and R. L. Lysak (John Wiley & Sons), 169.*Magnetospheric ULF waves: synthesis and new directions*

Elphic, R. C. (1988). Multipoint observations of the magnetopause: results from ISEE and AMPTE. *Adv. Space Res.* 8, 223–238. doi:10.1016/0273-1177(88)90135-4

Escoubet, C. P., Hwang, K.-J., Toledo-Redondo, S., Turc, L., Haaland, S. E., Aunai, N., et al. (2020). Cluster and MMS simultaneous observations of magnetosheath high speed jets and their impact on the magnetopause. *Front. Astron. Space Sci.* 6, 78. doi:10.3389/fspas.2019.00078

Evans, D. S., and Greer, M. S. (2000) "*Polar orbiting environmental satellite space environment monitor—2: instrument descriptions and archive data documentation*,". Boulder, CO, USA: NOAA.

Ezoe, Y., Funase, R., Nagata, H., Miyoshi, Y., Kasahara, S., Nakajima, H., et al. (2020). "GEO-X (GEOspace x-ray imager),". *Space telescopes and instrumentation 2020: ultraviolet to gamma ray*. Editors J.-W. A. den Herder, S. Nikzad, and K. Nakazawa (SPIE: International Society for Optics and Photonics), 11444. doi:10.1117/12.25607801144428

Faganello, M., and Califano, F. (2017). Magnetized Kelvin–Helmholtz instability: theory and simulations in the earth's magnetosphere context. *J. Plasma Phys.* 83, 535830601. doi:10.1017/S0022377817000770

Fenrich, F. R., Gillies, D. M., Donovan, E., and Knudsen, D. (2019). Flow velocity and field-aligned current associated with field line resonance: SuperDARN measurements. *J. Geophys. Res. Space Phys.* 124, 4889–4904. doi:10.1029/2019JA026529

Fenrich, F. R., Samson, J. C., Sofko, G., and Greenwald, R. A. (1995). ULF high- and low-m field line resonances observed with the super dual auroral radar network. *J. Geophys. Res. Space Phys.* 100, 21535–21547. doi:10.1029/95JA02024

Francia, P., Lepidi, S., Villante, U., Di Giuseppe, P., and Lazarus, A. J. (1999). Geomagnetic response at low latitude to continuous solar wind pressure variations during northward interplanetary magnetic field. *J. Geophys. Res. Space Phys.* 104, 19923–19930. doi:10.1029/1999JA900229

Freeman, M. P., Freeman, N. C., and Farrugia, C. J. (1995). A linear perturbation analysis of magnetopause motion in the Newton-Busemann limit. *Ann. Geophys.* 13, 907–918. doi:10.1007/s00585-995-0907-0

Friis-Christensen, E., Lühr, H., Knudsen, D., and Haagmans, R. (2008). Swarm – an earth observation mission investigating geospace. *Adv.Space Res.* 41, 210–216. doi:10.1016/j.asr.2006.10.008

Friis-Christensen, E., McHenry, M. A., Clauer, C. R., and Vennerstrøm, S. (1988). Ionospheric traveling convection vortices observed near the polar cleft: a triggered response to sudden changes in the solar wind. *Geophys. Res. Lett.* 15, 253–256. doi:10.1029/GL015i003p00253

Gabrielse, C., Nishimura, T., Chen, M., Hecht, J. H., Kaeppler, S. R., Gillies, D. M., et al. (2021). Estimating precipitating energy flux, average energy, and Hall auroral conductance from THEMIS all-sky-imagers with focus on mesoscales. *Front. Phys.* 9, 744298. doi:10.3389/fphy.2021.744298

Génot, V., Beigbeder, L., Popescu, D., Dufourg, N., Gangloff, M., Bouchemit, M., et al. (2018). Science data visualization in planetary and heliospheric contexts with 3DView. *Planet. Space Sci.* 150, 111–130. doi:10.1016/j.pss.2017.07.007

Gillies, D. M., Donovan, E., Hampton, D., Liang, J., Connors, M., Nishimura, Y., et al. (2019). First observations from the TREx spectrograph: the optical spectrum of STEVE and the picket fence phenomena. *Geophys. Res. Lett.* 46, 7207–7213. doi:10.1029/2019GL083272

Gillies, D. M., Knudsen, K., Rankin, R., Milan, S., and Donovan, E. (2018). A statistical survey of the 630.0-nm optical signature of periodic auroral arcs resulting from magnetospheric field line resonances. *Geophys. Res. Lett.* 45, 4648–4655. doi:10.1029/2018GL077491

Gillies, D. M., Liang, J., Gallardo-Lacourt, B., and Donovan, E. (2023). New insight into the transition from a SAR arc to STEVE. *Geophys. Res. Lett.* 50, e2022GL101205. doi:10.1029/2022GL101205

Gillies, R. G., van Eyken, A., Spanswick, E., Nicolls, M., Kelly, J., Greffen, M., et al. (2016). First observations from the RISR-C incoherent scatter radar. *Radio Sci.* 51, 1645–1659. doi:10.1002/2016RS006062

Glassmeier, K.-H. (1992). Traveling magnetospheric convection twin-vortices: observations and theory. *Ann. Geophys.* 10.

Gombosi, T. I., Chen, Y., Glocer, A., Huang, Z., Jia, X., Liemohn, M. W., et al. (2021). What sustained multi-disciplinary research can achieve: the space weather modeling framework. *J. Space Weather Space Clim.* 11, 42. doi:10.1051/swsc/2021020

Grimmich, N., Plaschke, F., Archer, M. O., Heyner, D., Mieth, J. Z. D., Nakamura, R., et al. (2023). Study of extreme magnetopause distortions under varying solar wind conditions. *J. Geophys. Res. Space Phys.* 128, e2023JA031603. doi:10.1029/2023JA031603

Halford, A., Liemohn, M., Ridley, A., Welling, D., Immel, T., Connor, H., et al. (2024) "Magnetospheric Auroral Asymmetry eXplorer: observing the auroral to uncover how energy flows in space-A Phase A SMEX Mission concept,". Abstract No. EGU24-2058. Göttingen, Germany: Copernicus Meetings.

Hartinger, M. D., Shi, X., Lucas, G. M., Murphy, B. S., Kelbert, A., Baker, J. B. H., et al. (2020). Simultaneous observations of geoelectric and geomagnetic fields produced by magnetospheric ULF waves. *Geophys. Res. Lett.* 47, e2020GL089441. doi:10.1029/2020GL089441

Hartinger, M. D., Xu, Z., Clauer, C. R., Yu, Y., Weimer, D. R., Kim, H., et al. (2017). Associating ground magnetometer observations with current or voltage generators. *J. Geophys. Res. Space Phys.* 122, 7130–7141. doi:10.1002/2017JA024140

Hasegawa, H., Fujimoto, M., Phan, T.-D., Rème, H., Balogh, A., Dunlop, M. W., et al. (2004). Transport of solar wind into Earth's magnetosphere through rolled-up Kelvin–Helmholtz vortices. *Nature* 430, 755–758. doi:10.1038/nature02799

He, F., Guo, R.-L., Dunn, W. R., Yao, Z.-H., Zhang, H.-S., Hao, Y.-X., et al. (2020). Plasmapause surface wave oscillates the magnetosphere and diffuse aurora. *Nat. Commun.* 11, 1668. doi:10.1038/s41467-020-15506-3

Hill, T. W., and Rassbach, M. E. (1975). Interplanetary magnetic field direction and the configuration of the day side magnetosphere. *J. Geophys. Res.* 80, 1–6. doi:10.1029/JA080i001p00001

Horaites, K., Rintamäki, E., Zaitsev, I., Turc, L., Grandin, M., Cozzani, G., et al. (2023). Magnetospheric response to a pressure pulse in a three-dimensional hybrid-vlasov simulation. *J. Geophys. Res. Space Phys.* 128, e2023JA031374. doi:10.1029/2023JA031374

Horvath, I., and Lovell, B. C. (2021). Subauroral flow channel structures and auroral undulations triggered by kelvin-helmholtz waves. *J. Geophys. Res. Space Phys.* 126, e2021JA029144. doi:10.1029/2021JA029144

Hughes, W. J., and Southwood, D. J. (1976). The screening of micropulsation signals by the atmosphere and ionosphere. *J. Geophys. Res.* 81, 3234–3240. doi:10.1029/JA081i019p03234

James, M. K., Yeoman, T. K., Mager, P. N., and Klimushkin, D. Y. (2013). The spatio-temporal characteristics of ULF waves driven by substorm injected particles. *J. Geophys. Res. Space Phys.* 118, 1737–1749. doi:10.1002/jgra.50131

Kavosi, S., and Raeder, J. (2015). Ubiquity of kelvin–helmholtz waves at earth's magnetopause. *Nat. Commun.* 6, 7019. doi:10.1038/ncomms8019

Kepko, L. (2018). "Magnetospheric constellation: leveraging space 2.0 for big science," in *Igarss 2018 - 2018 IEEE international geoscience and remote sensing symposium*, 285–288. doi:10.1109/IGARSS.2018.8519475

Kepko, L., Gabrielse, C., Gkioulidou, M., Nykyri, K., Sibeck, D., Turner, D., et al. (2023). Magnetospheric constellation (MagCon). *Bull. AAS* 55. doi:10.3847/25c2cfeb.0e470159Available at: https://baas.aas.org/pub/2023n3i200.

Kilcommons, L. M., Redmon, R. J., and Knipp, D. J. (2017). A new DMSP magnetometer and auroral boundary data set and estimates of field-aligned currents in dynamic auroral boundary coordinates. *J. Geophys. Res. Space Phys.* 122, 9068–9079. doi:10.1002/2016JA023342

Klein, K. G., Spence, H., Alexandrova, O., Argall, M., Arzamasskiy, L., Bookbinder, J., et al. (2023). Helioswarm: a multipoint, multiscale mission to characterize turbulence. *Space Sci. Rev.* 219, 74. doi:10.1007/s11214-023-01019-0

Kozyreva, O., Pilipenko, V., Lorentzen, D., Baddeley, L., and Hartinger, M. (2019). Transient oscillations near the dayside open-closed boundary: evidence of magnetopause surface mode? *J. Geophys. Res. Space Phys.* 124, 9058–9074. doi:10.1029/2018JA025684

Kozyreva, O. V., Pilipenko, V. A., Bland, E. C., Baddeley, L. J., and Zakharov, V. I. (2020). Periodic modulation of the upper ionosphere by ULF waves as observed simultaneously by superdarn radars and gps/tec technique. *J. Geophys. Res. Space Phys.* 125, e2020JA028032. doi:10.1029/2020JA028032

Liang, J., Donovan, E., Jackel, B., Spanswick, E., and Gillies, M. (2016). On the 630 nm red-line pulsating aurora: red-line Emission Geospace Observatory observations and model simulations. *J. Geophys. Res. Space Phys.* 121, 7988–8012. doi:10.1002/2016JA022901

Liang, J., Gillies, D., Donovan, E., Parry, H., Mann, I., Connors, M., et al. (2022). On the green isolated proton auroras during Canada thanksgiving geomagnetic storm. *Front. Astron. Space Sci.* 9, 1040092. doi:10.3389/fspas.2022.1040092

Liang, J., Gillies, D. M., Spanswick, E., and Donovan, E. F. (2024). Converting TREx-RGB green-channel data to 557.7 nm auroral intensity: methodology and initial results. *Earth Planet. Phys.* 8, 258–274. doi:10.26464/epp2023063

Lin, D., Wang, C., Li, W., Tang, B., Guo, X., and Peng, Z. (2014). Properties of Kelvin-Helmholtz waves at the magnetopause under northward interplanetary magnetic field: statistical study. *J. Geophys. Res. Space Phys.* 119, 7485–7494. doi:10.1002/2014JA020379

Liou, K., Takahashi, K., Newell, P. T., and Yumoto, K. (2008). Polar ultraviolet imager observations of solar wind-driven ULF auroral pulsations. *Geophys. Res. Lett.* 35, L16101. doi:10.1029/2008GL034953

Lundin, R., and Evans, D. S. (1985). Boundary layer plasmas as a source for high-latitude, early afternoon, auroral arcs. *Planet. Space Sci.* 33, 1389–1406. doi:10.1016/0032-0633(85)90115-1

Lyatsky, W. B., and Sibeck, D. G. (1997). Surface waves on the low-latitude boundary layer inner edge and travelling convection vortices. *J. Geophys. Res. Space Phys.* 102, 17643–17647. doi:10.1029/97JA00323

Ma, X., Delamere, P., Otto, A., and Burkholder, B. (2017). Plasma transport driven by the three-dimensional Kelvin-Helmholtz instability. *J. Geophys. Res. Space Phys.* 122, 10382–10395. doi:10.1002/2017JA024394

Ma, X., Otto, A., and Delamere, P. A. (2014). Interaction of magnetic reconnection and Kelvin-Helmholtz modes for large magnetic shear: 1. Kelvin-Helmholtz trigger. *J. Geophys. Res. Space Phys.* 119, 781–797doi. doi:10.1002/2013JA019224

Masson, A., and Nykyri, K. (2018). Kelvin-Helmholtz instability: lessons learned and ways forward. *Space Sci. Rev.* 214, 71. doi:10.1007/s11214-018-0505-6

Masters, A., Achilleos, N., Bertucci, C., Dougherty, M. K., Kanani, S. J., Arridge, C. S., et al. (2009). Surface waves on Saturn's dawn flank magnetopause driven by the Kelvin–Helmholtz instability. *Planet. Space Sci.* 57, 1769–1778. doi:10.1016/j.pss.2009.02.010

Matlsev, Y. P., and Lyatsky, W. B. (1975). Field-aligned currents and erosion of the dayside magnetosphere. *Planet. Space Sci.* 23, 1257–1260. doi:10.1016/0032-0633(75)90149-X

McWilliams, K. A., Detwiller, M., Kotyk, K., Krieger, K., Rohel, R., Billett, D. D., et al. (2023). Borealis: an advanced digital hardware and software design for superdarn radar systems. *Radio Sci.* 58, e2022RS007591. doi:10.1029/2022RS007591

Mejnertsen, L., Eastwood, J. P., Hietala, H., Schwartz, S. J., and Chittenden, J. P. (2017). Global MHD simulations of the earth's bow shock shape and motion under variable solar wind conditions. *J. Geophys. Res. Space Phys.* 123, 259–271. doi:10.1002/2017JA024690

Mende, S. B., Harris, S. E., Frey, H. U., Angelopoulos, V., Russell, C. T., Donovan, E., et al. (2008). The THEMIS array of ground-based observatories for the study of auroral substorms, *Space Sci. Rev.*, 141, 357–387. doi:10.1007/s11214-008-9380-x

Mende, S. B., Heetderks, H., Frey, H. U., Lampton, M., Geller, S. P., Abiad, R., et al. (2000a). Far ultraviolet imaging from the IMAGE spacecraft. 2. Wideband FUV imaging. *Space Sci. Rev.* 91, 271–285. doi:10.1023/A:1005227915363

Mende, S. B., Heetderks, H., Frey, H. U., Lampton, M., Geller, S. P., Habraken, S., et al. (2000b). Far ultraviolet imaging from the IMAGE spacecraft. 1. System design. *Space Sci. Rev.* 91, 243–270. doi:10.1007/978-94-011-4233-5_8

Mende, S. B., Heetderks, H., Frey, H. U., Stock, J. M., Lampton, M., Geller, S. P., et al. (2000c). "Far ultraviolet imaging from the IMAGE spacecraft. 3. Spectral imaging of lyman- and OI 135.6 nm," in *The IMAGE mission*. Editor J. L. Burch (chap: Springer Netherlands), 287–318. doi:10.1007/978-94-011-4233-5_103

Merkin, V. G., Kondrashov, D., Ghil, M., and Anderson, B. J. (2016). Data assimilation of low-altitude magnetic perturbations into a global magnetosphere model. *Space weather.* 14, 165–184. doi:10.1002/2015SW001330

Milan, S. E., Clausen, L. B. N., Coxon, J. C., Carter, J. A., Walach, M.-T., Laundal, K., et al. (2017). Overview of solar wind–magnetosphere–ionosphere–atmosphere coupling and the generation of magnetospheric currents. *Space Sci. Rev.* 206, 547–573. doi:10.1007/s11214-017-0333-0

Milan, S. E., Sato, N., Ejiri, M., and Moen, J. (2001). Auroral forms and the field-aligned current structure associated with field line resonances. *J. Geophys. Res. Space Phys.* 106, 25825–25833. doi:10.1029/2001JA900077

Montgomery, J., Ebert, R. W., Allegrini, F., Bagenal, F., Bolton, S. J., DiBraccio, G. A., et al. (2023). Investigating the occurrence of Kelvin-Helmholtz instabilities at Jupiter's dawn magnetopause. *Geophys. Res. Lett.* 50, e2023GL102921. doi:10.1029/2023GL102921

Motoba, T., Fujita, S., Kikuchi, T., and Tanaka, T. (2007). Solar wind dynamic pressure forced oscillation of the magnetosphere-ionosphere coupling system: a numerical simulation of directly pressure-forced geomagnetic pulsations. *J. Geophys. Res. Space Phys.* 112, A11204. doi:10.1029/2006JA012193

Murphy, K. R., Inglis, A. R., Sibeck, D. G., Watt, C. E. J., and Rae, I. J. (2020). Inner magnetospheric ULF waves: the occurrence and distribution of broadband and discrete wave activity. *J. Geophys. Res. Space Phys.* 125, e27887. doi:10.1029/2020JA027887

Nakariakov, V. M., Pilipenko, V., Heilig, B., Jelínek, P., Karlický, M., Klimushkin, D. Y., et al. (2016). Magnetohydrodynamic oscillations in the solar corona and Earth's magnetosphere: towards consolidated understanding. *Space Sci. Rev.* 200, 75–203. doi:10.1007/s11214-015-0233-0

Nguyen, G., Aunai, N., de Welle, B. M., Jeandet, A., Lavraud, B., and D, F. (2022). Massive multi-mission statistical study and analytical modeling of the earth's magnetopause: 1. a gradient boosting based automatic detection of near-earth regions. *J. Geophys. Res. Space Phys.* 127, e2021JA029773. doi:10.1029/2021JA029773

Nicolla, M. J., and Heinselman, C. J. (2007). Three-dimensional measurements of traveling ionospheric disturbances with the poker flat incoherent scatter radar. *Geophys. Res. Lett.* 34, L21104. doi:10.1029/2007GL031506

Nishitani, N., Ruohoniemi, J. M., Lester, M., Baker, J. B. H., Koustov, A. V., Shepherd, S. G., et al. (2019). Review of the accomplishments of mid-latitude super dual auroral radar network (superdarn) hf radars. *Prog. Earth Planet. Sci.* 6, 27. doi:10.1186/s40645-019-0270-5

Nykyri, K., Begtson, M., Angelopoulos, V., Nishimura, Y., and Wing, S. (2019). Can enhanced flux loading by high-speed jets lead to a substorm? multipoint detection of the christmas day substorm onset at 08:17 UT, 2015. *J. Geophys. Res. Space Phys.* 124, 4314–4340. doi:10.1029/2018JA026357

Nykyri, K., Johnson, J., Kronberg, E., Turner, D., Wing, S., Cohen, I., et al. (2021). Magnetospheric Multiscale observations of the source region of energetic electron microinjections along the duskside, high-latitude magnetopause boundary layer. *Geophys. Res. Lett.* 48, e2021GL092466. doi:10.1029/2021GL092466

Oliveira, D. M., Hartinger, M. D., Xu, Z., Zesta, E., Pilipenko, V. A., Giles, B. L., et al. (2020). Interplanetary shock impact angles control magnetospheric ULF wave activity: wave amplitude, frequency, and power spectra. *Geophys. Res. Lett.* 47, e90857. doi:10.1029/2020GL090857

Paschmann, G., and Daly, P. W. (1998) "Analysis methods for multi-spacecraft data," in *ISSI scientific reports*. Bern, Switzerland: International Space Science Institute.

Paschmann, G., Haaland, S., Sonnerup, B. U. O., Hasegawa, H., Georgescu, E., Klecker, B., et al. (2005). Characteristics of the near-tail dawn magnetopause and boundary layer. *Ann. Geophys.* 23, 1481–1497. doi:10.5194/angeo-23-1481-2005

Paxton, L. J., Morrison, D., Zhang, Y., Kil, H., Wolven, B., Ogorzalek, B. S., et al. (2002). Validation of remote sensing products produced by the special sensor ultraviolet scanning imager (ssusi): a far uv-imaging spectrograph on dmsp f-16. Optical spectroscopic techniques, remote sensing, and instrumentation for atmospheric and space research IV (SPIE) 4485, 338–348.

Piersanti, M., Materassi, M., Cicone, A., Spogli, L., Zhou, H., and Ezquer, R. G. (2018). Adaptive local iterative filtering: a promising technique for the analysis of nonstationary signals. *J. Geophys. Res. Space Phys.* 123, 1031–1046. doi:10.1002/2017JA024153

Pilipenko, V., Belakhovsky, V., Engebretson, M. J., Kozlovsky, A., and Yeoman, T. (2015). Are dayside long-period pulsations related to the cusp? *Ann. Geophys.* 33, 395–404. doi:10.5194/angeo-33-395-2015

Pilipenko, V., Belakhovsky, V., Murr, D., Fedorov, E., and Engebretson, M. (2014). Modulation of total electron content by ULF Pc5 waves. *J. Geophys. Res. Space Phys.* 119, 4358–4369. doi:10.1002/2013ja019594

Pilipenko, V. A., Kozyreva, O. V., A.Lorentzen, D., and Baddeley, L. J. (2018). The correspondence between dayside long-period geomagnetic pulsations and the open-closed field line boundary. *J. Atmos. Terr. Phys.* 170, 64–74. doi:10.1016/j.jastp.2018.02.012

Plaschke, F., Angelopoulos, V., and Glassmeier, K.-H. (2013). Magnetopause surface waves: THEMIS observations compared to MHD theory. *J. Geophys. Res. Space Phys.* 118, 1483–1499. doi:10.1002/jgra.50147

Plaschke, F., and Glassmeier, K. H. (2011). Properties of standing Kruskal-Schwarzschild-modes at the magnetopause. *Ann. Geophys.* 29, 1793–1807. doi:10.5194/angeo-29-1793-2011

Plaschke, F., Glassmeier, K.-H., Auster, H. U., Angelopoulos, V., Constantinescu, O. D., Fornaçon, K.-H., et al. (2009). Statistical study of the magnetopause motion: first results from THEMIS. *J. Geophys. Res. Space Phys.* 114, A00C10. doi:10.1029/2008JA013423

Potemra, T. A., Lühr, H., Zanetti, L. J., Takahashi, K., Erlandson, R. E., Marklund, G. T., et al. (1989). Multisatellite and ground-based observations of transient ULF waves. *J. Geophys. Res.* 94, 2543–2554. doi:10.1029/JA094iA03p02543

Redmon, R. J., Denig, W. F., Kilcommons, L. M., and Knipp, D. J. (2017). New DMSP database of precipitating auroral electrons and ions. *J. Geophys. Res. Space Phys.* 122, 9056–9067. doi:10.1002/2016JA023339

Retinò, A., Khotyaintsev, Y., Le Contel, O., Marcucci, M. F., Plaschke, F., Vaivads, A., et al. (2022). Particle energization in space plasmas: towards a multi-point, multi-scale plasma observatory. *Exp. Astron.* 54, 427–471. doi:10.1007/s10686-021-09797-7

Rietveld, M. T., Senior, A., Markkanen, J., and Westman, A. (2019). New capabilities of the upgraded EISCAT high-power HF facility. *Radio Sci.* 51, 1533–1546. doi:10.1002/2016RS006093

Robertson, I. P., and Cravens, T. E. (2003). X-ray emission from the terrestrial magnetosheath. *Geophys. Res. Lett.* 30, 1439. doi:10.1029/2002GL016740

Ruohoniemi, J. M., and Greenwald, R. A. (1996). Statistical patterns of high-latitude convection obtained from Goose Bay HF radar observations. *J. Geophys. Res.* 101, 21743–21763. doi:10.1029/96JA01584

Ruohoniemi, J. M., Greenwald, R. A., Baker, K. B., Villain, J.-P., Hanuise, C., and Kelly, J. (1989). Mapping high-latitude plasma convection with coherent HF radars. *J. Geophys. Res.* 94, 13463–13477. doi:10.1029/JA094iA10p13463

Samson, J. C., Cogger, L. L., and Pao, Q. (1996). Observations of field line resonances, auroral arcs, and auroral vortex structures. *J. Geophys. Res. Space Phys.* 101, 17373–17383. doi:10.1029/96JA01086

Samsonov, A., Branduardi-Raymont, G., Sembay, S., Read, A., Sibeck, D., and Rastaetter, L. (2024). Simulation of the SMILE Soft X-ray Imager response to a southward interplanetary magnetic field turning. *Earth Planet. Phys.* 8, 39–46. doi:10.26464/epp2023058

Samsonov, A., Sembay, S., Read, A., Carter, J. A., Branduardi-Raymont, G., Sibeck, D., et al. (2022). Finding magnetopause standoff distance using a Soft X-ray Imager: 2. methods to analyze 2-D X-ray images. *J. Geophys. Res.:Space Phys.* 127, e2022JA030850. doi:10.1029/2022JA030850

Schultz, A. (2010). Emscope: a continental scale magnetotelluric observatory and data discovery resource. *Data Sci. J.* 8, IGY6–IGY20. doi:10.2481/dsj.ss_igy-009

Shi, X., Hartinger, M. D., Baker, J. B. H., Murphy, B. S., Bedrosian, P. A., Kelbert, A., et al. (2022). Characteristics and sources of intense geoelectric fields in the United States: comparative analysis of multiple geomagnetic storms. *Space weather.* 20, e2021SW002967. doi:10.1029/2021SW002967

Shi, X., Hartinger, M. D., Baker, J. B. H., Ruohoniemi, J. M., Lin, D., Xu, Z., et al. (2020). Multipoint conjugate observations of dayside ULF waves during an extended period of radial IMF. *J. Geophys. Res. Space Phys.* 125, e2020JA028364. doi:10.1029/2020ja028364

Shi, X., Lin, D., Wang, W., Baker, J. B. H., Weygand, J. M., Hartinger, M. D., et al. (2022). Geospace concussion: global reversal of ionospheric vertical plasma drift in response to a sudden commencement. *Geophys. Res. Lett.* 49, e2022GL100014. doi:10.1029/2022GL100014

Shi, X., Schmidt, M., Martin, C. J., Billett, D. D., Bland, E., Tholley, F. H., et al. (2022). pydarn: a python software for visualizing superdarn radar data. *Front. Astronomy Space Sci.* 9, 1022690. doi:10.3389/fspas.2022.1022690

Sibeck, D. G. (1990). A model for the transient magnetospheric response to sudden solar wind dynamic pressure variations. *J. Geophys. Res.* 95, 3755–3771. doi:10.1029/JA095iA04p03755

Sibeck, D. G., Allen, R., Aryan, H., Bodewits, D., Brandt, P., Branduardi-Raymont, G., et al. (2018). Imaging plasma density structures in the soft x-rays generated by solar wind charge exchange with neutrals. *Space Sci. Rev.* 214, 79. doi:10.1007/s11214-018-0504-7

Sibeck, D. G., Baumjohann, W., and Lopez, R. E. (1989). Solar wind dynamic pressure variations and transient magnetospheric signatures. *Geophys. Res. Lett.* 16, 13–16. doi:10.1029/GL016i001p00013

Sibeck, D. G., Borodkova, N., Schwartz, S., Owen, C., Kessel, R., Kokubun, S., et al. (1999). Comprehensive study of the magnetospheric response to a hot flow anomaly. *J. Geophys. Res. Space Phys.* 104, 4577–4593. doi:10.1029/1998JA900021

Silverman, B. W. (1986) "Density estimation for statistics and data analysis," in *Monographs on statistics and applied probability*. London, UK: Chapman & Hall.

Smit, G. R. (1968). Oscillatory motion of the nose region of the magnetopause. *J. Geophys. Res.* 73, 4990–4993. doi:10.1029/JA073i015p04990

Sorathia, K. A., Merkin, V. G., Panov, E. V., Zhang, B., Lyon, J. G., Garretson, J., et al. (2020). Ballooning-interchange instability in the near-earth plasma sheet and auroral beads: global magnetospheric modeling at the limit of the MHD approximation: *Geophys. Res. Lett.*, 47, e2020GL088227. doi:10.1029/2020GL088227

Sorathia, K. A., Michael, A., Merkin, V. G., Ohtani, S., Keesee, A. M., Sciola, A., et al. (2023). Multiscale magnetosphere-ionosphere coupling during stormtime: a case study of the dawnside current wedge. *J. Geophys. Res. Space Phys.* 128, e2023JA031594. doi:10.1029/2023JA031594

Stallone, A., Cicone, A., and Materassi, M. (2020). New insights and best practices for the successful use of empirical mode decomposition, iterative filtering and derived algorithms. *Sci. Rep.* 10, 15161. doi:10.1038/s41598-020-72193-2

Stamm, J., Verinen, J., Urco, J. M., Gustavsson, B., and Chau, J. L. (2021). Radar imaging with EISCAT 3D. *Ann. Geophys.* 39, 119–134doi. doi:10.5194/angeo-39-119-2021

Torr, M. R., Torr, D. G., Zukic, M., Johnson, R. B., Ajello, J., Banks, P., et al. (1995). A far ultraviolet imager for the international solar-terrestrial physics mission. *Space Sci. Rev.* 71, 329–383. doi:10.1007/BF00751335

Tsyganenko, N. A. (1995). Modeling the earth's magnetospheric magnetic field confined within a realistic magnetopause. *J. Geophys. Res.* 100, 5599–5612. doi:10.1029/94JA03193

Tsyganenko, N. A., and Sitnov, M. I. (2007). Magnetospheric configurations from a high-resolution data-based magnetic field model. *J. Geophys. Res. Space Phys.* 112, A06225. doi:10.1029/2007JA012260

Viall, N. M., Kepko, L., and Spence, H. E. (2009). Relative occurrence rates and connection of discrete frequency oscillations in the solar wind density and dayside magnetosphere. *J. Geophys. Res. Space Phys.* 114, A01201. doi:10.1029/2008JA013334

Villante, U., Recchiuti, D., and Di Matteo, S. (2022). The transmission of ULF waves from the solar wind to the magnetosphere: an analysis of some critical aspects. *Front. Astronomy Space Sci.* 9, 835539. doi:10.3389/fspas.2022.835539

Walach, M.-T., and Grocott, A. (2019). SuperDARN observations during geomagnetic storms, geomagnetically active times, and enhanced solar wind driving. *J. Geophys. Res. Space Phys.* 124, 5828–5847. doi:10.1029/2019JA026816

Walach, M.-T., Grocott, A., and Milan, S. E. (2021). Average ionospheric electric field morphologies during geomagnetic storm phases. *J. Geophys. Res. Space Phys.* 126, e2020JA028512. doi:10.1029/2020JA028512

Walsh, B. M., Kuntz, K. D., Busk, S., Cameron, T., Chornay, D., Chuchra, A., et al. (2024). The lunar environment heliophysics x-ray imager (lexi) mission. *Space Sci. Rev.* 220, 37. doi:10.1007/s11214-024-01063-4

Walsh, B. M., Thomas, E. G., Hwang, K.-J., Baker, J. B. H., Ruohoniemi, J. M., and Bonnell, J. W. (2015). Dense plasma and kelvin-helmholtz waves at earth's dayside magnetopause. *J. Geophys. Res. Space Phys.* 120, 5560–5573. doi:10.1002/2015JA021014

Wang, B., Liu, T., Nishimura, Y., Zhang, H., Hartinger, M., Shi, X., et al. (2020a). Global propagation of magnetospheric Pc5 ULF waves driven by foreshock transients. *J. Geophys. Res. Space Phys.* 125, e2020JA028411. doi:10.1029/2020JA028411

Wang, B., Nishimura, Y., Hartinger, M., Sivadas, N., Lyons, L. L., Varney, R. H., et al. (2020b). Ionospheric modulation by storm time Pc5 ULF pulsations and the structure detected by pfisr-themis conjunction. *Geophys. Res. Lett.* 47, e2020GL089060. doi:10.1029/2020GL089060

Wang, C., and Branduardi-Raymont, G. (2022). Progress of solar wind magnetosphere ionosphere link explorer (SMILE) mission. *Chin. J. Space Sci.* 38, 657–661. doi:10.11728/cjss2018.05.657

Wang, C., and Sun, T. R. (2022). Methods to derive the magnetopause from soft X-ray images by the SMILE mission. *Geosci. Lett.* 9, 30. doi:10.1186/s40562-022-00240-z

Waters, C. L., Anderson, B. J., Green, D. L., Korth, H., Barnes, R. J., and Vanhamäki, H. (2019). Science data products for AMPERE. *ISSI Sci. Rep. Ser.*, 141–165. doi:10.1007/978-3-030-26732-2_7

Watson, C., Jayachandran, P., Singer, H. J., Redmon, R. J., and Danskin, D. (2015). Large-amplitude gps tec variations associated with pc5–6 magnetic field variations observed on the ground and at geosynchronous orbit. *J. Geophys. Res. Space Phys.* 120, 7798–7821. doi:10.1002/2015ja021517

Watson, C., Jayachandran, P. T., and MacDougall, J. W. (2016). Characteristics of gps tec variations in the polar cap ionosphere. *J. Geophys. Res. Space Phys.* 121, 4748–4768. doi:10.1002/2015JA022275

Weygand, J. M., Hartinger, M. D., Strangeway, R. J., Welling, D. T., Kim, H., Matzka, J., et al. (2023). Interhemispheric asymmetry due to IMF by within the cusp spherical elementary currents. *J. Geophys. Res. Space Phys.* 128, e2023JA031430. doi:10.1029/2023JA031430

Yau, A. W., and James, H. G. (2015). Cassiope enhanced polar outflow probe (e-POP) mission overview. *Space Sci. Rev.* 189, 3–14. doi:10.1007/s11214-015-0135-1

Yizengaw, E., Zesta, E., Moldwin, M. B., Magoun, M., Tripathi, N. K., Surussavadee, C., et al. (2018). ULF wave-associated density irregularities and scintillation at the equator. *Geophys. Res. Lett.* 45, 5290–5298. doi:10.1029/2018GL078163

Zhang, B., Sorathia, K. A., Lyon, J. G., Merkin, V. G., Garretson, J. S., and Wiltberger, M. (2019). GAMERA: a three-dimensional finite-volume MHD solver for non-orthogonal curvilinear geometries. *Astrophysical J. Suppl. Ser.* 244, 20. doi:10.3847/1538-4365/ab3a4c

frontiers | Frontiers in Astronomy and Space Sciences

TYPE Original Research
PUBLISHED 28 August 2024
DOI 10.3389/fspas.2024.1431238

OPEN ACCESS

EDITED BY
Fabio Lepreti,
University of Calabria, Italy

REVIEWED BY
Jean-Francois Ripoll,
CEA DAM Île-de-France, France
Adriana Settino,
Institute für Weltraumforschung, Austria
Matteo Faganello,
UMR7345 Physique des interactions ioniques et moléculaires (P2IM), France

*CORRESPONDENCE
Harley M. Kelly,
h.kelly21@imperial.ac.uk

RECEIVED 11 May 2024
ACCEPTED 26 July 2024
PUBLISHED 28 August 2024

CITATION
Kelly HM, Archer MO, Ma X, Nykyri K, Eastwood JP and Southwood DJ (2024) Identification of Kelvin-Helmholtz generated vortices in magnetised fluids.
Front. Astron. Space Sci. 11:1431238.
doi: 10.3389/fspas.2024.1431238

Identification of Kelvin-Helmholtz generated vortices in magnetised fluids

Harley M. Kelly[1]*, Martin O. Archer[1], Xuanye Ma[2], Katariina Nykyri[2,3], Jonathan P. Eastwood[1] and David J. Southwood[1]

[1]Department of Physics, Space, Plasma, and Climate Community, Imperial College London, London, United Kingdom, [2]Physical Sciences Department, Embry Riddle Aeronautical University, Daytona Beach, FL, United States, [3]National Aeronautics and Space Administration (NASA), Goddard Space Flight Center, Greenbelt, MD, United States

The Kelvin-Helmholtz Instability (KHI), arising from velocity shear across the magnetopause, plays a significant role in the viscous-like transfer of mass, momentum, and energy from the shocked solar wind into the magnetosphere. While the KHI leads to growth of surface waves and vortices, suitable detection methods for these applicable to magnetohydrodynamics (MHD) are currently lacking. A novel method is derived based on the well-established λ-family of hydrodynamic vortex identification techniques, which define a vortex as a local minimum in an adapted pressure field. The $\mathbf{J}\times\mathbf{B}$ Lorentz force is incorporated into this method by using an effective total pressure in MHD, including both magnetic pressure and a pressure-like part of the magnetic tension derived from a Helmholtz decomposition. The λ_{MHD} method is shown to comprise of four physical effects: vortical momentum, density gradients, fluid compressibility, and the rotational part of the magnetic tension. A local three-dimensional MHD simulation representative of near-flank magnetopause conditions (plasma β's 0.5–5 and convective Mach numbers $M_f \sim 0.4$) under northward interplanetary magnetic field (IMF) is used to validate λ_{MHD}. Analysis shows it correlates well with hydrodynamic vortex definitions, though the level of correlation decreases with vortex evolution. Overall, vortical momentum dominates λ_{MHD} at all times. During the linear growth phase, density gradients act to oppose vortex formation. By the highly nonlinear stage, the formation of small-scale structures leads to a rising importance of the magnetic tension. Compressibility was found to be insignificant throughout. Finally, a demonstration of this method adapted to tetrahedral spacecraft observations is performed.

KEYWORDS

Kelvin-Helmholtz instability, magnetopause, surface wave, vortex identification, simulations, magnetohydrodynamics, KHI, MHD

1 Introduction

The complex interaction between Earth's intrinsic magnetic field and the solar wind results in a cavity called the magnetosphere, bounded by the magnetopause. Various physical processes exist which allow solar wind mass, energy, and momentum to penetrate this magnetic barrier, driving magnetospheric dynamics and also causing significant space weather effects (Buzulukova and Tsurutani, 2022). The three main mechanisms

by which this penetration occurs are magnetic reconnection (Dungey, 1961), a quasi-viscous interaction (Axford and Hines, 1961; Axford, 1964), and diffusive transfer (Tsurutani and Thorne, 1982). The dominant transfer mechanism at Earth is dependent on the local Interplanetary Magnetic Field (IMF) and plasma conditions. Northward IMF conditions are conducive to viscous-like transfer, whereas southward IMF conditions enable magnetic reconnection-driven transfer to dominate. The viscous-like interaction between magnetospheric and solar wind plasma's is predominantly driven by the Kelvin-Helmholtz instability (KHI), a fluid-like instability at interfaces with a velocity shear (Chandrasekhar, 1961), which leads to the generation and evolution of surface waves and vortices on the magnetopause (Hwang et al., 2022).

KH waves and vortices at the magnetopause form from small deformations of the boundary about equilibrium, called seed perturbations (Hasegawa et al., 2009). Because of the continuous magnetosheath flow adjacent to the magnetopause, plasma parcels closer to the boundary must move faster around these seed perturbations than ones further away. From Bernoulli's principle, this establishes a pressure gradient which acts to further deform the magnetopause surface. These larger deformations subsequently drive greater pressure gradients and so on. Thus, in the absence of an additional force to counteract this process and stabilise the boundary, the velocity shear is KH unstable. This process occurs not only in the space plasmas at the magnetopause, it has also been observed or predicted at other planetary magnetopauses (Masters et al., 2012; Paral and Rankin, 2013; Ruhunusiri et al., 2016; Masters, 2018; Dang et al., 2022; Montgomery et al., 2023; Donaldson et al., 2024), the magnetopause of magnetised moon Ganymede (Kaweeyanun et al., 2021), comet tails (Ershkovich, 1980), and along the surface of CMEs (Nykyri and Foullon, 2013).

In the initial linear growth phase of the KHI, the deformations of the magnetopause can be described as magnetopause surface waves (MSWs) from linear MHD wave theory (Pu and Kivelson, 1983). Surface waves are magnetosonic modes which can only propagate tangentially to a boundary or surface, requiring them to have maximum amplitude at the interface and decay along the boundary normal on both sides (Kivelson and Chen, 1995). This means they can be mathematically formulated from evanescent magnetosonic waves on each side of an assumed discontinuity, tied together through boundary conditions. Surface waves are elliptically polarised with opposite polarisation on either side of the boundary, forming flow vortices centred on the interface (Dungey and Southwood, 1970).

MSWs usually originate at the near-equatorial dayside magnetopause flanks and propagate tailward due to advection by the magnetosheath flow (Song et al., 1988). As MSWs travel tailwards, their amplitudes continue to grow due to the KHI. The magnetosheath side of the interface will eventually start to carry the deformed magnetopause along with it. This results in the interface itself rolling-up into a vortex shape, which is typically seen in the instability's nonlinear stage (Fujimoto et al., 2006). This nonlinear growth can subsequently trigger secondary processes such as vortex-induced reconnection (Nykyri and Otto, 2001; Nakamura et al., 2017; 2013), the Rayleigh-Taylor instability (Guglielmi et al., 2010), and kinetic (ion and electron) instabilities (Nykyri et al., 2006; Moore et al., 2016; 2017; Ma et al., 2021a; Nykyri et al., 2021). This makes the KHI a mechanism for cross-scale energy transfer. Understanding how the KHI's MSWs/vortices are generated and transfer energy across the magnetopause is an active field of research that has existed since its discovery (see reviews by e.g., Zhang et al., 2022; Masson and Nykyri, 2018; Faganello and Califano, 2017; Kivelson and Chen, 1995).

By approximating the magnetopause as an unbounded tangential discontinuity between two incompressible plasmas (subscripts 1 and 2), Chandrasekhar (1961) used linear incompressible MHD theory to show that MSWs with normalised wave vector $\hat{\mathbf{k}}$ are unstable to the KHI if Equation 1 is satisfied:

$$\underbrace{\left(\hat{\mathbf{k}}\cdot(\mathbf{v}_1-\mathbf{v}_2)\right)^2}_{\text{Flow Shear Driver}} - \underbrace{\frac{\rho_1+\rho_2}{\rho_1\rho_2}}_{\text{Density Weighting}} \underbrace{\frac{1}{\mu_0}\left[\left(\mathbf{B}_1\cdot\hat{\mathbf{k}}\right)^2+\left(\mathbf{B}_2\cdot\hat{\mathbf{k}}\right)^2\right]}_{\text{Magnetic Tension Stabiliser}} > 0 \text{ then KHI unstable.} \quad (1)$$

Here $\mathbf{v}_{1,2}$ is the fluid velocity, $\rho_{1,2}$ is the density, and $\mathbf{B}_{1,2}$ is the magnetic field vector on either side of the fluid boundary. Unfortunately, this approach requires unrealistic assumptions of unbounded magnetic field lines, incompressibility, homogeneity, and an infinitesimally thin boundary layer, all of which we will show to be important along a realistic magnetopause below. While this condition has often been applied to observational case studies of the KHI to demonstrate whether the boundary is KHI unstable or not, it ought to be remembered that this condition strictly applies only at the source region of the linear stage of the KHI. Hence, when maturer vortices have developed, the data collected by a spacecraft crossing the vortex may not satisfy this condition anymore. Furthermore, it has been shown in MHD simulations that the properties (amplitude and frequency) of the KHI seed spectrum affect the growth and size of the Kelvin-Helmholtz waves–this may help explain the enhanced geo-effectiveness of solar wind structures with certain periodicities (Nykyri et al., 2017).

Equation 1 shows that wave vectors aligned with the flow shear most efficiently support the flow shear driver term of the KHI. However, this does not mean the most unstable $\hat{\mathbf{k}}$ is necessarily aligned with the flow shear because of the second term, the stabilising effect of magnetic tension. For magnetic fields parallel to $\hat{\mathbf{k}}$, the KHI will be suppressed by the magnetic tension if the relative speed does not exceed the root-mean-square Alfvén speed in the two media. This is intuitive–as the surface begins to deform, the frozen-in field lines will also be deformed, which magnetic tension will oppose. In contrast, magnetic fields orthogonal to $\hat{\mathbf{k}}$ result in no curvature of field lines and hence no tension force. Thus the KHI was thought to be uninfluenced by such a magnetic field. If both magnetic fields are perpendicular to the shear flow, the most unstable $\hat{\mathbf{k}}$ is aligned with the flow shear, whereas for magnetic fields not strictly aligned with the flow and under typical magnetopause conditions, $\hat{\mathbf{k}}$ is most unstable perpendicular to the magnetospheric magnetic field (Southwood, 1968; Walker, 1981). Crucially, these conclusions are only true in the unbounded quasi-steady state. In reality, closed magnetospheric magnetic field lines in the vicinity of the magnetopause are necessarily bounded by the ionosphere–sometimes known as "line tying" (Miura and Kan, 1992).

The ionosphere is highly reflecting to magnetosonic modes such as surface waves, almost perfectly reflecting them and thus anchoring closed magnetic field lines in the ionosphere

(Kivelson and Southwood, 1988). Thus unlike the unbounded case where a spectrum of field-aligned wavenumbers are possible, the ionospheric boundary conditions quantise the possible field-aligned wavenumbers. The result is that linear surface waves necessarily should have standing structure along the field (Chen and Hasegawa, 1974; Plaschke and Glassmeier, 2011; Archer et al., 2019; 2021). Unlike in the unbounded state, where the field lines would just move with the plasma, in the bounded state the field will now impose a magnetic tension restoring force even when it is orthogonal to the flow shear. In local simulations, this has shown to stop the vortex development if the z-extent around the equatorial plane is not large enough (Brackbill and Knoll, 2001; Hashimoto and Fujimoto, 2006; Takagi et al., 2006). In addition to this, it allows for the field topology to evolve. Over time, as the KHI progresses into the nonlinear stage, the bounded magnetic field can become twisted into flux ropes (Otto and Fairfield, 2000; Hwang et al., 2020; 2022) meaning that the magnetic tension will become increasingly important even when the magnetic field is orthogonal to the flow shear. This results in current sheets being generated in the mid-latitudes eventually inducing magnetic reconnection (Faganello et al., 2012; 2014). Furthermore, this twisting requires additional energy which reduces the growth rate of the KHI or stabilises the boundary entirely (Miura, 1987). This process is typical of the low-latitude flank magnetopause (e.g., Hwang et al., 2022).

So far only the incompressible regime has been considered, but plasma's are malleable and therefore compressibility cannot be ignored. Indeed the vortices produced by the KHI act as obstacles to the driving flow, which can lead to compressions and even shocks within the plasma (e.g., Palermo et al., 2011). The fast magnetosonic convective Mach number, M_f, is a dimensionless number defined as a ratio of the flow speed in the obstacle frame, u, and the magnetosonic speed, u_f, such that $M_f = u/u_f$. This ratio is used to determine how compressible a flow is (Miura, 1990; Miura and Kan, 1992; Palermo et al., 2011), since the proportional change in density due to flow variations scales as $\sim M_f^2$. Values of $M_f < 0.3$ are typically considered incompressible as they result in $\lesssim$ 10% changes in density. Equation 1 shows that unstable surface waves can be generated on a incompressible infinitesimally thin tangential discontinuity when the velocity shear exceeds some critical threshold. Compressibility lowers this threshold relative to the incompressible situation and thus has a destabilising effect; the extent to which Fejer (1964), Sen (1965), and Southwood (1968) disagreed. Further to this, Sen (1965) also suggested that compressibility has both a destabilising effect on the lower critical shear flow velocity, and stabilising effect on the wave growth rate (i.e., a reduction of the growth rate) if the shear flow speed is sufficiently smaller than the magnetoacoustic speed. Pu and Kivelson (1983) coupled the results of these works by showing that there are two different modes, each with different upper and lower critical shear velocities. The modes are only unstable if the shear velocity is between the upper and lower critical shear velocity values. Pu and Kivelson (1983) show that the lower critical velocity shear of both modes is due to the stabilising effect of magnetic tension, which they show compressibility lowers for both modes. The upper critical velocity is due to a transition of the surface evanescent wave to a leaky oscillatory wave or "body wave" which carries energy away from the boundary and into the magnetosphere and magnetosheath, consequently stabilising the KHI. They show that compressibility increases the growth rate of one of the modes slightly and significantly reduces the growth rate of the other. They conclude that the impact of compressibility depends on the tangential wave vector, but generally compressibility does not significantly alter the threshold shear velocity in comparison to the incompressible limit. Crucially, these works insufficiently describe reality by approximating the magnetopause as a tangential discontinuity, making them only valid for wavelengths much larger than the boundary thickness.

Inconsistencies in growth rates at short wavelengths arise when the magnetopause's finite thickness is ignored (Lerche, 1966), as the effects of a finite thickness stabilises the magnetopause to short wavelengths. In the compressible case KHI growth rates are reduced by the background magnetic field component parallel to the shear flow direction when using a finite thickness for the magnetopause (Ong and Roderick, 1972), agreeing with the tangential discontinuity findings of Sen (1965) and Pu and Kivelson (1983). The compressible KHI growth rates on a finite boundary were first found with linear theory by Miura and Pritchett (1982), which advanced MHD simulations of the KHI are now capable of recovering (Briard et al., 2024). As well as the growth rates, the upper and lower critical velocity conditions introduced by Pu and Kivelson (1983) are also affected when instead considering a finite boundary thickness. The lower critical shear velocity is zero when the magnetic field is orthogonal to both the shear flow and the mode's wave vector (Miura and Kan, 1992). In addition, the upper critical velocity shear limit is removed when including an inner boundary within the magnetosphere due to the interaction of reflected waves with the magnetopause (Fujita et al., 1996). In summary, the role of compressibility is dependent on the thickness of the shear interface (Miura and Pritchett, 1982) as compressibility plays a significant role in the gradual–but not total–stabilisation of the boundary due to the finite magnetopause thickness (Miura, 1992).

Palermo et al. (2011) investigated the influence of plasma homogeneity and compressibility on the formation of KH vortices and found that compressibility, inhomogeneity, and magnetopause thickness all play a role in vortex formation and propagation and state that compressibility effects stabilise the magnetopause.

Other studies have shown that plasma inhomogeneity decreases growth rates as the gradients increase (Amerstorfer et al., 2010). Ma et al. (2024) suggest that the KHI growth rate is insensitive to the density gradient across the shear flow boundary in the compressible regime and go on to show that these variations affect the secondary processes which the KHI trigger. This further reinforces that linear incompressible theory can only approximately describe the KHI along the magnetopause. These studies suggest that magnetopause thickness, magnetic tension, and compressibility stabilise the magnetopause to the KHI, and plasma inhomogeneity destabilises it but beyond this does not affect the growth rate.

Overall, whilst this shows that the role of compressibility and magnetic tension on the KHI is a stabilising one, the significance of magnetic tension, compressibility, and density variations on vortex formation at the magnetopause is still an open question. One reason for this is because identifying MSWs and their coupled vortices using *in-situ* measurements or simulation is not trivial (Plaschke, 2016). Given the major role that the Kelvin-Helmhholtz instability is thought to play in the viscous-like interaction between the solar wind and magnetosphere, the ability

to clearly identify the vortices produced by this process is important. This paper introduces a novel vortex identification method for Ideal MHD, based on existing methods from hydrodynamics. Current techniques, both in hydrodynamics and space plasma physics, are summarised in Section 2. Section 3 derives the new MHD-valid vortex identification method, which we call λ_{MHD}. We then apply the λ_{MHD} method to a simple MHD simulation of the KHI in Section 4, comparing the results to previous methods and assessing the importance of different physical effects on the vortices it identifies. We also discuss potential *in-situ* applications.

2 Vortex identification techniques

2.1 Defining a vortex

Although a vortex is a pervasive and familiar concept which is qualitatively understood as a region of swirling fluid about some arbitrary axis line, perhaps remarkably a universally accepted mathematical vortex definition still does not exist (Jeong and Hussain, 1995; Cai et al., 2018; Yao and Hussain, 2018). To aid the discussion, it is important to understand the origins of a vortex in general. Vortices are formed when shearing momentum is redirected in some way, translating it into rotational momentum. Without an adequate restoring centripetal force, the centrifugal motion of the fluid in a vortex will tear itself apart, diffusing it. In hydrodynamics, the centripetal force that prevents this usually comes from gradients in pressure which originate from velocity gradients, following Bernoulli's principle. This is known as cyclostrophic balance and is only true in a steady inviscid planar flow (Jeong and Hussain, 1995).

The MHD case complicates this by introducing magnetic pressure and magnetic tension forces. In MHD the restoring force will also include magnetic field contributions which are caused when the field is perturbed by the moving plasma (Collado-Vega et al., 2018). As the stress in an MHD fluid is anisotropic, due to magnetic tension introducing bias along the field direction, the consequential pressure contribution from the field will be a complex superposition of the magnetic pressure and some part of the magnetic tension (this is explored further in Section 3.1). This added complexity means that MHD requires some formal vortex definition beyond that of hydrodynamics.

2.2 Existing hydrodynamic approaches

Identifying and/or quantifying a vortex is a problem which still exists and is widely researched in the hydrodynamic community (see review by Zhang et al., 2018, and references therein). Most of these methods typically stem from the velocity gradient tensor, $\nabla\mathbf{v}$ where

$$\mathbf{G} = \nabla\mathbf{v} = \begin{bmatrix} \partial_1 v_1 & \partial_1 v_2 & \partial_1 v_3 \\ \partial_2 v_1 & \partial_2 v_2 & \partial_2 v_3 \\ \partial_3 v_1 & \partial_3 v_2 & \partial_3 v_3 \end{bmatrix}. \tag{2}$$

One example of a popular vortex core line identification technique derived from the velocity gradient tensor is the Q definition (Hunt et al., 1988). This defines a vortex as a connected fluid region with a positive second invariant of $\nabla\mathbf{v}$. Finding the characteristic equation of $\mathbf{G}$ gives

$$\det(\mathbf{G} - \lambda\mathbf{I}) = \lambda^3 - P\lambda^2 + Q\lambda - R = 0 \tag{3}$$

where the first, second, and third invariants of $\mathbf{G}$ are defined respectively as

$$P = \mathrm{Tr}(\mathbf{G}) \quad ; \quad Q = \frac{1}{2}\left[\mathrm{Tr}(\mathbf{G})^2 - \mathrm{Tr}(\mathbf{G}^2)\right] \quad ; \quad R = \det(\mathbf{G}). \tag{4}$$

For an incompressible fluid ($\nabla\cdot\mathbf{v} = \mathrm{Tr}(\mathbf{G}) = 0$), the Q criterion is equivalent to a region where the magnitude of the rotation rate tensor, $\mathbf{\Omega} = \frac{1}{2}\left(\mathbf{G}^T - \mathbf{G}\right)$, is larger than the magnitude of the strain-rate tensor, $\mathbf{S} = \frac{1}{2}\left(\mathbf{G}^T + \mathbf{G}\right)$. This is expressed as $\left(\|\mathbf{\Omega}\|_F^2 - \|\mathbf{S}\|_F^2\right)$ where $\|\cdot\|_F$ is the Frobenius norm given by $\|\underline{\mathbf{X}}\|_F = \sqrt{\sum_{i=1}^{n}\sum_{j=1}^{m} X_{ij}^2}$. Due to its simplicity, this strictly incompressible definition of Q is usually applied, even when dealing with compressible fluids.

Another popular vortex core line identification technique derived from the velocity gradient tensor, and based on locating local pressure minima, is the λ_2 definition (Jeong and Hussain, 1995). The technique starts with the Navier-Stokes momentum equation and derives the pressure Hessian, containing local pressure extrema information. After discarding unsteady irrotational straining and viscous effects, which are unrelated to vortical motion, this becomes

$$\partial_i\partial_j P_{\mathrm{adp}} = S_{ik}S_{kj} + \Omega_{ik}\Omega_{kj}, \tag{5}$$

where P_{adp} is the adapted pressure (pressure with the unsteady irrotational straining and viscous effects removed). An adapted pressure minimum in some plane requires, through a second partial derivative test on P_{adp}, two negative eigenvalues of $\mathbf{S}^2 + \mathbf{\Omega}^2$. Hence a vortex core in this method is defined as a connected region which satisfies this condition. This can be simplified by sorting the eigenvalues in descending order: $\lambda_1 > \lambda_2 > \lambda_3$ and stating a vortex occurs where $\lambda_2 < 0$ (a step-by-step derivation can be found in the appendix of Cucitore et al., 1999). λ_2 can be interpreted as identifying a local pressure minima in some arbitrary intersecting plane. Due to how the value is constructed, the magnitude of the parameters does not have any physical significance except for comparison to other values of itself. Cucitore et al. (1999) show that the λ_2 method is a requirement of some measure of the rotation rate prevailing over some measure of the strain rate, implying that λ_2 and Q are comparable.

Both of these criteria are only valid for homogeneous and incompressible hydrodynamic fluids. In addition, as they both only use the velocity vector field, they are ignorant to the momentum they represent. Extensions to these techniques do exist which provide weighting dependent on momentum. The simplest is weighted-λ_2 (Yao and Hussain, 2018) (denoted as $\overline{\lambda_2}$ herein) which is identical to λ_2 but weights Equation 5 by density. This results in a shifting of power from high velocity vortices to high momentum vortices. A further extension is known as λ_ρ (Yao and Hussain, 2018) which extends λ_2 to be valid for compressible, inhomogeneous hydrodynamic fluids. This is achieved by using the symmetric part to the tensor product of the momentum gradient tensor, $\nabla(\rho\mathbf{v})$, and the velocity gradient tensor, $\nabla\mathbf{v}$, along with the symmetric part of the momentum compressibility gradient tensor, $\nabla\left[(\nabla\cdot\mathbf{v})\rho\mathbf{v}\right]$. λ_ρ can be broken into three parts which represent the vortical momentum, the fluid compressibility, and the density gradients. If the definition is

applied to an incompressible and homogeneous fluid then it reduces to $\overline{\lambda_2}$. A useful feature of the Q and λ-family of techniques is that they are Galilean invariant (Jeong and Hussain, 1995), meaning the methods are consistent across all inertial frames of reference.

2.3 Current approaches to vortex identification at the magnetopause

Typically, MSWs due to the KHI at the magnetopause are identified *in-situ* by using hodograms to show quasi-periodic fluctuations of the magnetopause surface passing over spacecraft (Hasegawa et al., 2004). This method is deficient if only single spacecraft measurements are used as it can be difficult to characterise structure size (Hasegawa et al., 2004). As well as this, the method cannot identify magnetopause vortex structures (Cai et al., 2018). Vortical patterns will be present in the data from both surface roll-up and the boundary adjacent vortices the waves generate in the boundary-adjacent flow. It is important to be able to distinguish between them as surface roll-ups only occur in the nonlinear stages of the KHI but boundary-adjacent vortical flow can occur at any stage (Chandrasekhar, 1961; Hwang et al., 2022). This makes identifying vortices and their coupled surface waves two different problems.

Numerous vortex identification techniques applicable to the magnetopause have been developed but all have deficiencies (see review by Hasegawa, 2012). For example, a sensible starting place for vortex identification would be using the vorticity vector. However, at shear boundary regions vorticity is high even in the absence of any rotating flows, meaning that it is not suitable for KH vortex identification. Takagi et al. (2006) suggested using low-density plasma moving faster than the magnetosheath plasma to detect surface roll-ups. However, Plaschke et al. (2014) showed that this signature is not unique to surface roll-ups due to the plasma depletion layer and vortices from MSWs providing false-positives. Alternatively, based on a hybrid Vlasov simulation of the KHI, Settino et al. (2021) suggest kinetic signatures such as ion non-Maxwellianity, total current density, temperature anisotropy, agyrotropy, and magnetic field gradients might serve as proxies for KH-vortices.

Another popular method used for both simulation and *in-situ* analysis investigates local total pressure minima, where the total pressure is the sum of thermal and magnetic pressures (Nykyri et al., 2017; Rice et al., 2022). Pressure minima are coupled to vortices due to Bernoulli's principle as discussed above. This approach, and using the vorticity vector, typically fails when fluctuations are large or if other physical processes which can interfere with the dynamics of the KHI (e.g., reconnection) are taking place (Settino et al., 2021). Other drawbacks of local pressure minima arise due to the vortex not containing a three-dimensional pressure minima and also pressure minima not always being associated with vortices as other physical process can create them.

The simpler hydrodynamic vortex identification techniques (Q and λ_2) have also been used to study the KHI at Earth's magnetopause, though this is only possible for multi-point analysis due to the necessity of calculating gradients (Settino et al., 2021). Cai et al. (2018) used data from the Cluster Mission (Escoubet et al., 2001) to identify vortical structures at Earth's magnetopause. They applied the method to magnetic field data rather than the velocity data, assuming these vary similarly via the frozen-in flux theorem. They conclude that Q is easy to implement but imprecise and that λ_2 is more precise but does not provide geometric information about the vortex core. These results agree with a different study performed by Collado-Vega et al. (2018) who investigated the effectiveness of Q and λ_2 in identifying vortices in a 3-dimensional BATS-R-US global MHD magnetosphere simulation (Tóth et al., 2005). They state that neither method is immune to false identifications and conclude by stating that incorporating the effects of the magnetic field will likely increase the scientific yield. Since both techniques derive from hydrodynamics, this can only be done by deriving the equivalent to the λ-family of methods from the MHD equations.

3 The λ method for ideal MHD

3.1 MHD effective pressure

The λ-family of definitions all work by using a second partial derivative test on some adapted pressure Hessian to find local pressure minima. Local pressure minima here refers to a minima in pressure in a plane, not a three dimensional minima as some vortices only have minima in a plane perpendicular to a vortex axis rather than a three dimensional minima (e.g., Burgers vortex). In the case of hydrodynamics without any external forces, the only inviscid force acting on the fluid arises from thermal pressure gradients. Thus thermal pressure is the field used, adapted by discarding any contributions which cause pressure minima without being associated with vortical flow, e.g., sink flow (Jeong and Hussain, 1995). However, in MHD the plasma is also subject to magnetic pressure and magnetic tension forces. The total pressure generally used in ideal MHD is the sum of magnetic pressure, $P_{\mathrm{mag}} = B^2/(2\mu_0)$, and thermal pressure, $P_{\mathrm{therm}} = nk_BT$. However this does not necessarily describe all the pressure-like forces on the plasma–those which can be expressed as an irrotational field $-(\nabla P)$. The magnetic tension $\mathbf{B}\cdot\nabla\mathbf{B}/\mu_0$ may also have a pressure-like part to it. One example of this is the magnetic dipole, which is a current- and force-free magnetic field. Since this exhibits magnetic pressure gradients, these must be completely cancelled by magnetic tension forces; thus tension can in part contribute to the total of pressure-like forces in ideal MHD. In an alternative case where current is induced, such as in a field aligned current, the magnetic tension will be a highly rotational field as stress is transmitted along the field. This highlights that in a dynamic environment such as KH vortices, the magnetic tension will be composed of both rotational and irrotational components.

The fundamental theorem of vector calculus states that any vector field, which exists in the domain V and is twice continuously differentiable inside V, can be decomposed into the sum of a curl-free (irrotational, $-\nabla P$), and divergence-free (rotational $\nabla\times\mathbf{U}$), field. This is also known as a Helmholtz decomposition. Applied to the magnetic tension this gives

$$\boldsymbol{\tau} = -\nabla P_{\mathrm{ten}} + \nabla\times\mathbf{U} = \boldsymbol{\tau}_{\mathrm{irr}} + \boldsymbol{\tau}_{\mathrm{rot}}, \tag{6}$$

where P_{ten} is the pressure field associated with the irrotational part of the tension force and $\mathbf{U}$ is the vector potential field describing the

rotational part to the tension. The Helmholtz decomposition allows for an effective total pressure field in MHD to be defined as the sum of thermal pressure, magnetic pressure, and the pressure-like part of the tension:

$$P_{\text{eff}} = nk_B T + \frac{B^2}{2\mu_0} + P_{\text{ten}} = P_{\text{therm}} + P_{\text{mag}} + P_{\text{ten}}. \tag{7}$$

A general solution to Equation 6 can be derived so that P_{ten} can be investigated

$$\boldsymbol{\tau}(\mathbf{r}) = -\nabla \underbrace{\left(\frac{1}{4\pi} \int_V \frac{\nabla' \cdot \boldsymbol{\tau}(\mathbf{r}')}{|\mathbf{r}-\mathbf{r}'|} \mathrm{d}V' - \frac{1}{4\pi} \oint_S \hat{\mathbf{n}}' \cdot \frac{\boldsymbol{\tau}(\mathbf{r}')}{|\mathbf{r}-\mathbf{r}'|} \mathrm{d}S' \right)}_{P_{\text{ten}}(\mathbf{r})} + \nabla \times \underbrace{\left(\frac{1}{4\pi} \int_V \frac{\nabla' \times \boldsymbol{\tau}(\mathbf{r}')}{|\mathbf{r}-\mathbf{r}'|} \mathrm{d}V' - \frac{1}{4\pi} \oint_S \hat{\mathbf{n}}' \times \frac{\boldsymbol{\tau}(\mathbf{r}')}{|\mathbf{r}-\mathbf{r}'|} \mathrm{d}S' \right)}_{\mathbf{U}(\mathbf{r})}. \tag{8a}$$

$$= -\nabla P_{\text{ten}} + \nabla \times \mathbf{U} \tag{8b}$$

where S is the enclosing surface of V.

Axiomatically, P_{ten} and $\mathbf{U}$ are not unique. Any arbitrary constant scalar can be added to P_{ten} to provide the same distinct $\boldsymbol{\tau}_{\text{irr}} = -\nabla P_{\text{ten}}$ solution. Similarly, any arbitrary gradient field can be added to $\mathbf{U}$ to give the same unique solution to $\boldsymbol{\tau}_{\text{rot}} = \nabla \times \mathbf{U}$. As the effective pressure itself is not directly required in λ-family methods, only its Hessian, this gauge freedom is unimportant here.

Computationally, it is more efficient to perform the Helmholtz decomposition in Fourier space

$$\boldsymbol{\tau} = \iiint \hat{\boldsymbol{\tau}}(\mathbf{k}) e^{i\mathbf{k}\cdot\mathbf{r}} dV_k, \tag{9}$$

where $\hat{\boldsymbol{\tau}}$ denotes the Fourier Transform of the magnetic tension. In an unbounded domain this requires that the tension decays faster than $1/r$. By splitting the tension's Fourier transform $\hat{\boldsymbol{\tau}}(\mathbf{k})$ into its components parallel and perpendicular to $\mathbf{k}$

$$\hat{\boldsymbol{\tau}}_{\parallel}(\mathbf{k}) = \frac{\mathbf{k}\cdot\hat{\boldsymbol{\tau}}(\mathbf{k})}{|\mathbf{k}|^2}\mathbf{k}, \tag{10}$$

$$\hat{\boldsymbol{\tau}}_{\perp}(\mathbf{k}) = -\mathbf{k}\times\frac{\mathbf{k}\times\hat{\boldsymbol{\tau}}(\mathbf{k})}{|\mathbf{k}|^2}, \tag{11}$$

it can be seen that

$$\hat{\boldsymbol{\tau}}(\mathbf{k}) = \hat{\boldsymbol{\tau}}_{\parallel}(\mathbf{k}) + \hat{\boldsymbol{\tau}}_{\perp}(\mathbf{k}) \tag{12a}$$

$$= -i\mathbf{k}\frac{i\mathbf{k}\cdot\hat{\boldsymbol{\tau}}(\mathbf{k})}{|\mathbf{k}|^2} + i\mathbf{k}\times\frac{i\mathbf{k}\times\hat{\boldsymbol{\tau}}(\mathbf{k})}{|\mathbf{k}|^2} \tag{12b}$$

$$= -i\mathbf{k}\hat{P}_{\text{ten}}(\mathbf{k}) + i\mathbf{k}\times\hat{\mathbf{U}}(\mathbf{k}) \tag{12c}$$

where the Fourier Transforms of the scalar field P_{ten} and the vector field $\mathbf{U}$ are defined as

$$\hat{P}_{\text{ten}}(\mathbf{k}) = i\frac{\mathbf{k}\cdot\hat{\boldsymbol{\tau}}(\mathbf{k})}{|\mathbf{k}|^2}, \tag{13}$$

$$\hat{\mathbf{U}}(\mathbf{k}) = i\frac{\mathbf{k}\times\hat{\boldsymbol{\tau}}(\mathbf{k})}{|\mathbf{k}|^2}. \tag{14}$$

Substituting into Equation 9 demonstrates this provides the Helmholtz decomposition

$$\boldsymbol{\tau} = \underbrace{\iiint -i\mathbf{k}\hat{P}_{\text{ten}}(\mathbf{k}) e^{i\mathbf{k}\cdot\mathbf{r}} dV_k}_{-\nabla P_{\text{ten}}} + \underbrace{\iiint i\mathbf{k}\times\hat{\mathbf{U}}(\mathbf{k}) e^{i\mathbf{k}\cdot\mathbf{r}} dV_k}_{\nabla\times\mathbf{U}}, \tag{15}$$

since in Fourier space $\nabla \rightarrow i\mathbf{k}$. The Fourier method has been used to perform the decomposition seen in the following section.

3.2 λ_{MHD} derivation

Here we derive a λ-family vortex definition applicable to ideal MHD, which we call λ_{MHD}. The derivation closely follows that of λ_ρ found in Yao and Hussain (2018). The aim is to find the Hessian of the MHD effective pressure defined in Section 3.1 so that a second partial derivative test can be performed on it to identify local pressure minima. Gravitational effects are assumed to be negligible. We neglect viscous effects in the derivation below due to space plasma being collisionless. However, this definition is valid for a viscous ideal MHD fluid as a viscosity term in the pressure Hessian is neglected as viscosity can provide centripetal forces (e.g., Kármán's viscous pump) and remove the pressure minima in the fluid. Neglecting this term allows for the method to be able to successfully identify a vortex even when pressure-minima are not providing the centripetal restoring force (see Jeong and Hussain, 1995; Yao and Hussain, 2018, for further description of the viscous case in hydrodynamics).

The derivation starts with the ideal MHD Cauchy-Momentum equation, where the Helmholtz decomposition of the magnetic tension has been performed

$$\frac{\partial}{\partial t}(\rho\mathbf{v}) + \nabla\cdot(\rho\mathbf{v}\mathbf{v}) = -\nabla P_{\text{eff}} + \boldsymbol{\tau}_{\text{rot}}. \tag{16}$$

Rewriting this in tensor notation (using the Einstein summation convention) for component i and taking the gradient in coordinate j,

$$\partial_t\partial_j(\rho v_i) + \partial_j\partial_k(\rho v_i v_k) = -\partial_j\partial_i P_{\text{eff}} + \partial_j\tau_{i\text{rot}}. \tag{17}$$

Apply the chain rule twice

$$\begin{aligned}&\partial_t\partial_j(\rho v_i) + \partial_j v_k\partial_k(\rho v_i) + v_k\partial_k\partial_j(\rho v_i)\\ &+\partial_j(\rho v_i)\partial_k v_k + (\rho v_i)\partial_k\partial_j v_k = -\partial_j\partial_i P_{\text{eff}} + \partial_j\tau_{i\text{rot}}.\end{aligned} \tag{18}$$

Using the definition of the material derivative $\frac{D}{Dt} = \partial_t + v_k\partial_k$ this can be simplified to

$$\frac{D}{Dt}\left(\partial_j(\rho v_i)\right) + \partial_j v_k\partial_k(\rho v_i) + \partial_j\left((\rho v_i)\partial_k v_k\right) = -\partial_j\partial_i P_{\text{eff}} + \partial_j\tau_{i\text{rot}}. \tag{19}$$

Taking the symmetric part of Equation 19 by applying to each tensor A_{ij} the symmetric operator $1/2\left(A_{ij} + A_{ji}\right)$

$$\begin{aligned}&\frac{D}{Dt}\left(\frac{1}{2}\left(\partial_j(\rho v_i) + \partial_i(\rho v_j)\right)\right) + \frac{1}{2}\left(\partial_j v_k\partial_k(\rho v_i) + \partial_i v_k\partial_k(\rho v_j)\right)\\ &+\frac{1}{2}\left(\partial_j\left((\rho v_i)\partial_k v_k\right) + \partial_i\left((\rho v_j)\partial_k v_k\right)\right) = -\partial_j\partial_i P_{\text{eff}} + \frac{1}{2}\left(\partial_j\tau_{i\text{rot}} + \partial_i\tau_{j\text{rot}}\right).\end{aligned} \tag{20}$$

Substitute in the symmetric, $S_{ij} = 1/2\left(\partial_j v_i + \partial_i v_j\right)$, and anti-symmetric, $\Omega_{ij} = 1/2\left(\partial_j v_i - \partial_i v_j\right)$, parts of the velocity gradient tensor

$$\begin{aligned}&\frac{D}{Dt}\left(\frac{1}{2}\left(\partial_j(\rho v_i) + \partial_i(\rho v_j)\right)\right) + \rho\left(S_{ik}S_{kj} + \Omega_{ik}\Omega_{kj}\right) + \frac{\partial_k\rho}{2}\left(v_i\partial_j v_k + v_j\partial_i v_k\right)\\ &+\frac{1}{2}\left(\partial_j\left((\rho v_i)\partial_k v_k\right) + \partial_i\left((\rho v_j)\partial_k v_k\right)\right) = -\partial_j\partial_i P_{\text{eff}} + \frac{1}{2}\left(\partial_j\tau_{i\text{rot}} + \partial_i\tau_{j\text{rot}}\right).\end{aligned} \tag{21}$$

The effective pressure Hessian (denoted **H**) can now be written as,

$$-H_{ij} = -\partial_j \partial_i P_{\text{eff}} = E_{ij} + M_{ij} + D_{ij} + C_{ij} + T_{ij}. \tag{22a}$$

Where each term represents a different physical property:

$$\text{Unsteady Strain: } E_{ij} = \frac{D}{Dt}\left(\frac{1}{2}\left(\partial_j(\rho v_i) + \partial_i(\rho v_j)\right)\right), \tag{22b}$$

$$\text{Vortical Momentum: } M_{ij} = \rho\left(S_{ik}S_{kj} + \Omega_{ik}\Omega_{kj}\right), \tag{22c}$$

$$\text{Density Gradients: } D_{ij} = \frac{\partial_k \rho}{2}\left(v_i \partial_j v_k + v_j \partial_i v_k\right), \tag{22d}$$

$$\text{Compressibility: } C_{ij} = \frac{1}{2}\left(\partial_j\left((\rho v_i)\,\partial_k v_k\right) + \partial_i\left(\left(\rho v_j\right)\partial_k v_k\right)\right), \tag{22e}$$

$$\text{Rotational Magnetic Tension: } T_{ij} = -\frac{1}{2}\left(\partial_j \tau_{i\text{rot}} + \partial_i \tau_{j\text{rot}}\right). \tag{22f}$$

As discussed by Jeong and Hussain (1995) and Yao and Hussain (2018), there is an inconsistency between the existence of a pressure minimum and a vortex core in Equation (22a). Simply finding a local pressure minimum is not sufficient in identifying a vortex core as unsteady irrotational motion can cause pressure minima in a fluid without vortical flow as a consequence of unsteady strain in the fluid. In the example of a surface wave in an incompressible isothermal hydrodynamic fluid, a vortex would not be identifiable in pressure alone as there would not be a pressure minimum despite vortical flow being present. However, removing the unsteady strain provides the minimum needed in the adapted pressure Hessian to allow for vortex identification in this case. Choosing to neglect the unsteady strain effect in Equation 22a completes the derivation,

$$-\mathbf{H} = \mathbf{M} + \mathbf{D} + \mathbf{C} + \mathbf{T}. \tag{23}$$

Equation 23 outlines that only contributions from $\mathbf{M}+\mathbf{D}+\mathbf{C}+\mathbf{T}$ are required to identify a pressure minimum in a plane, which requires two positive eigenvalues of the pressure Hessian tensor (Jeong and Hussain, 1995; Yao and Hussain, 2018). Consequently, λ_{MHD} defines a vortex as a connected region with two negative eigenvalues of $\mathbf{M}+\mathbf{D}+\mathbf{C}+\mathbf{T}$. Since this tensor is real and symmetric, it has real eigenvalues only. Thus if its eigenvalues $\lambda_1 > \lambda_2 > \lambda_3$, then λ_{MHD} is equivalent to the requirement that $\lambda_2 < 0$ within the vortex core.

In summary, λ_{MHD} adds a correction term to λ_ρ which extends its usage to a magnetised ideal MHD fluid. λ_{MHD} is constructed of four terms which each represent different physical effects believed to affect the formation of the vortices such as in the KHI: vortical momentum (**M**), density gradients (**D**), fluid compressibility (**C**), and rotational magnetic tension (**T**).

4 Application to local MHD simulation

To demonstrate λ_{MHD} and its potential usage in identifying MSWs and vortices at the magnetopause due to KHI, we apply it to data from a local MHD simulation of the KHI. Here local refers to the simulation being a simplified and restricted domain in the vicinity of the magnetopause shear flow. This is in contrast to global simulations, which model the entire magnetosphere–solar wind interaction (e.g., Michael et al., 2021).

4.1 Simulation overview

We use a local MHD simulation representative of near-flank magnetopause conditions (Ma et al., 2020) under northward IMF. This region was chosen as it is the location where KHI is predicted to be most unstable along the magnetopause due to the large velocity shear (Southwood, 1968). Northward IMF is chosen as it is also most unstable orientation predicted by linear theory (Chandrasekhar, 1961) and confirmed by observations (Kavosi and Raeder, 2015). As well as this, northward IMF prevents large-scale reconnection being induced by magnetic shear (Vernisse et al., 2016; Fadanelli et al., 2018; Sisti et al., 2019). The plasma beta has a value of $\beta = 5.0$ in region 1 (the magnetosheath), meaning magnetic field dynamics dominate over plasma dynamics; and $\beta = 0.5$ in region 2 (magnetosphere), meaning that plasma dynamics dominate over the magnetic field here. The fast magnetosonic Mach number in the simulation frame has values of $M_f \sim 0.4$, corresponding to the weakly compressional regime where compressibility should be non-negligible. The Alfvén Mach number has moderate values of $M_A \sim 0.89$ in region 1 and $M_A \sim 0.55$ in region 2, meaning that magnetic tension cannot be neglected. These Mach numbers have been calculated in the simulation frame as the vortex is approximately stationary in the centre of the simulation throughout (cf. Palermo et al., 2011).

The MHD KHI is numerically simulated by solving a full set of normalised resistive MHD equations using a leap-frog scheme in a Cartesian coordinate system (Otto, 1990; Nykyri and Otto, 2001; Ma et al., 2014a; b, 2017). The x-direction points along the normal to the unperturbed sheared flow layer, the y-direction is along the sheared flow direction, and the z-direction is determined by the right-hand rule. All physical quantities are normalised by characteristic values and their initial states are outlined in Table 1. The length scale, L_0, magnetic field scaling factor, B_0, and number density scaling factor, n_0 may be chosen freely, whereas all other scaling quantities are derived from these. To provide physical context, we have assigned values to the dimensionless simulation units which best represent the near-flank magnetopause (Ma et al., 2020). However, these values are arbitrary and do not affect the physics of the simulation or any of the results presented.

The whole simulation domain is given by $[-L_x, L_x] \times [-L_y, L_y] \times [-L_z, L_z]$ along the x-, y-, and z-directions, where $L_x = 25L_0$, $L_y = 10L_0$, and $L_z = 120L_0$. The grid has 203 cells in each direction with a resolution of $0.1L_0$ in the y-direction, $0.6L_0$ in the z-direction and is stretched along the x-direction with a minimum resolution of $0.1L_0$. The boundary conditions along the y-direction are periodic. Along the x-direction, the boundaries are closed, in which $v_x = 0$ and $\partial_x = 0$ for the rest of the quantities. The dimension along x is large enough to ignore the influence from the boundaries such as MHD wave reflections. To maintain the top boundary from the perturbation, an artificial friction term $-\nu(z)(\mathbf{v} - \mathbf{v_0})$ is applied to the right-hand side of the momentum equation in the simulation (Ma et al., 2017). Here, $\mathbf{v_0}$ is the unperturbed bulk velocity, which also represents the solar wind or ionosphere speed. The friction term tends to force the plasma to move at its initial velocity, or equivalently it absorbs perturbations, maintaining the initial boundary layer away from the equatorial plane. The friction coefficient is given by $\nu(z) = 0.5\{2 - \tanh[(z + z_\nu)/L_0 D_\nu] + \tanh[(z - z_\nu)/L_0 D_\nu]\}$, $z_\nu = 30L_0$,

TABLE 1 Table showing the normalisation constants and initial state used in the simulation.

Quantity	Value	Initial state		
		Region 1 ($x > 0$)	Region 2 ($x < 0$)	x-profile
Length Scale, L_0	600 km			
Magnetic Field, B_0	60 nT	$(0, 0, 0.5B_0)^T$	$(0, 0, B_0)^T$	$1/2(B_{z1} + B_{z2}) + 1/2(B_{z1} - B_{z2}) \tanh(x/L_0)\mathbf{e}_z$
Number Density, n_0	11cm^{-3}	$0.8n_0$	$1.2n_0$	$1/2(n_1 + n_2) + 1/2(n_1 - n_2) \tanh(x/L_0)$
Velocity, V_{A0}	$B_0/\sqrt{\mu_0\rho_0} = 394$ km/s	$-0.5V_{A0}$	$0.5V_{A0}$	$0.5 \tanh(x/L_0)\mathbf{e}_y$
Pressure, P_0	$B_0^2/2\mu_0 = 1.4$nPa	$1.25P_0$	$0.5P_0$	$P_1 + (B_{z1}^2 - B_z^2(x))/2\mu_0$
Plasma Beta, β	P_{therm}/P_{mag}	5	0.5	
Alfvén Mach Number, M_A	$\lvert V\rvert/V_A$	0.89	0.55	
Fast Mach Number, M_f	$\lvert V\rvert/u_f$	0.39	0.46	
Time, t_0	$L_0/V_{A0} \sim 1.5$ s			
Atwood Number, A	$(\rho_2 - \rho_1)/(\rho_1 + \rho_2) = 0.2$			

and $D_v = 3$, which has been switched on only near the top and bottom boundaries (Ma et al., 2017; Ma et al., 2021b).

To overcome issues with Fourier analysis and noise from differentiation, we trilinear interpolate all the data to a regular grid of resolution $0.1L_0$ in all directions for our investigations. The simulation boundary conditions are valid for the Fourier approach to the Helmholtz decomposition of the magnetic tension. The y-boundary is periodic, which a Fast Fourier Transform assumes. The x-dimension is suitably large that perturbations decay before reaching the simulation edges (the x-extent of the simulation is twice that shown in Figure 1). The large dimension along the z-direction, along with the frictional term at the boundary, means that the Alfvén wave is fully damped before it reaches the top/bottom simulation edges. We found no evidence of Gibbs effects present from the application of Fourier approach to the Helmholtz decomposition.

The initial steady state is a one-dimensional transition layer with a flow shear, the conditions of which are outlined in Table 1. This transition layer is initially imposed by a hyperbolic tangent function with characteristic thickness of L_0 and maintains the total force balance across the sheared flow layer (i.e., the sum of the thermal pressure and magnetic pressure is constant). The KHI is triggered by a velocity perturbation localised in the vicinity of the equatorial plane (i.e., $z = 0$), which is given by $\mathbf{v} = \nabla\Phi(x, y) \times \mathbf{e}_z f(z)$. Here, the stream function is $\Phi(x, y) = \delta v \cos(k_y y) \cosh^{-2sec}(x/l_x)$, normal scale of the perturbation $l_x = 2L_0$, KH wavenumber $k_y = \pi/L_y$, amplitude of the velocity perturbation $\delta v = V_{A0}/20$, and the localisation function $f(z)$ is given by $f(z) = 0.5\{\tanh[(z + z_d)/L_0 D_z] - \tanh[(z - z_d)/L_0 D_z]\}$, where $z_d = 20L_0$, and $D_z = 3$.

Figure 1 shows 3 snapshots of the simulation in the equatorial plane. $t = 30t_0$ is approximately during the quasi-linear surface wave stage, $t = 80t_0$ is during the nonlinear surface roll-up stage of the KHI, and $t = 130t_0$ is during the turbulent stage beyond the surface roll-up. These three stages are used throughout this work. At time $t = 80t_0$, and $t = 130t_0$ there are secondary KHI forming as highlighted in panels 1b and 1c. The dashed black line is plotted along the $\rho = \rho_0$ line as a visual aid to the reader for identifying the proxy-boundary. As $M_f \sim 0.4$ this proxy-boundary should be little affected by compressible effects. Note also that different methods of magnetopause identification in simulations are known not to always be co-located (García and Hughes, 2007; Gordeev et al., 2013). It does not feature in the turbulent stage as there is no clear boundary between the two sides.

4.2 Results and discussion

4.2.1 Exploring P_{ten}

A key step in the derivation of λ_{MHD} is the realisation that a part of the magnetic tension contributes to the pressure-like forces on the plasma, with this achieved through a Helmholtz decomposition of the magnetic tension into rotational and irrotational vector fields. Figure 2 shows this decomposition. In the quasi-linear stage ($t = 30t_0$), tension is shown to be acting as a stabilising force opposing the deformation of the boundary as expected. The tension is entirely rotational in this initial stage, as expected for a linear incompressible surface wave (Plaschke, 2016). This implies the tension field is not yet perturbed enough to provide a (nonlinear) pressure-like contribution. In the nonlinear surface roll-up stage ($t = 80t_0$), the tension field has become sufficiently twisted for the tension to start exhibiting a pressure-like part, but the tension overall is still predominantly rotational. The force is again pointing in directions to try and restore the boundary to its original shape–with the pressure-like part now also contributing to this. In the turbulent stage ($t = 130t_0$) it becomes unclear on the behaviour of the tension as the KHI-generated structures have evolved turbulently–it is however clear that the forces are still predominantly rotational. The tension generally has a larger magnitude in regions where secondary KHI are present.

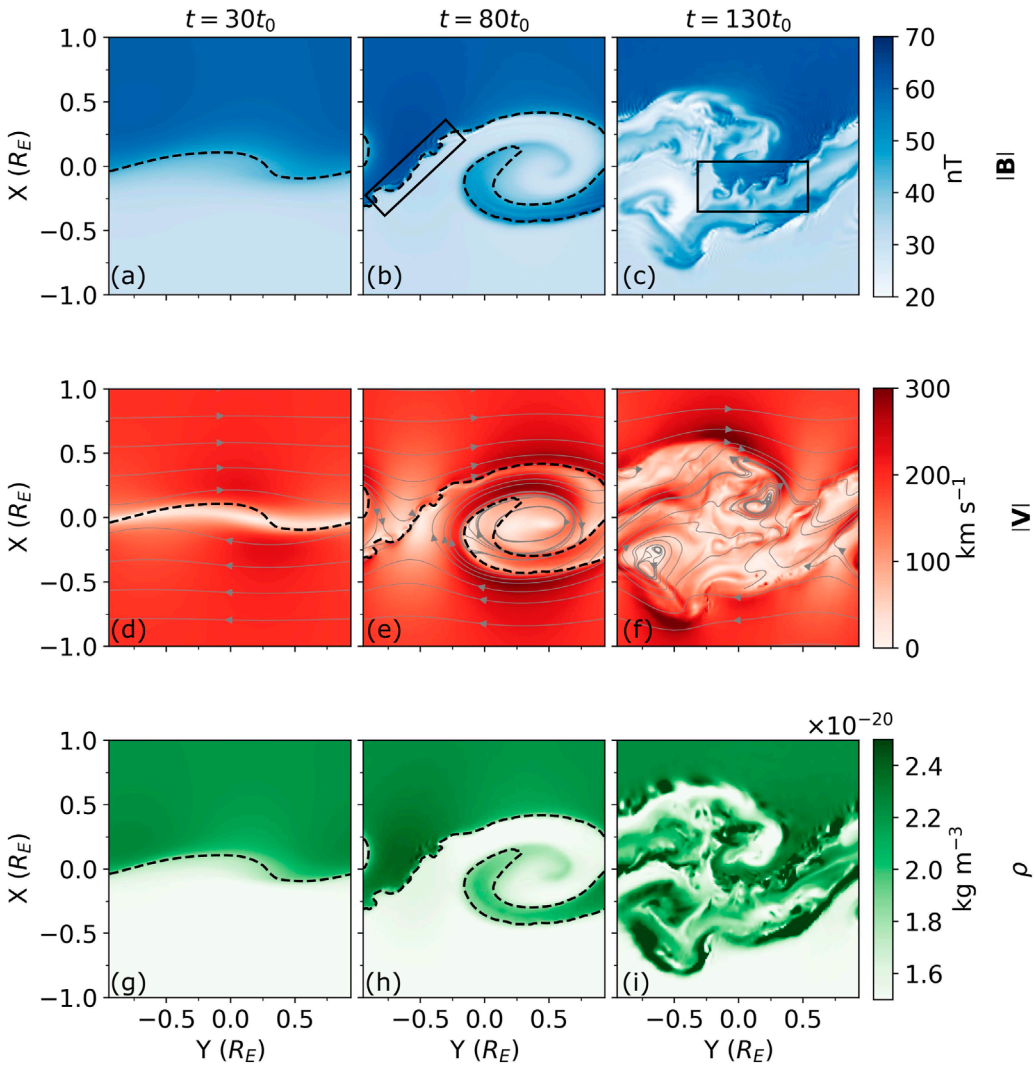

FIGURE 1
An equatorial ($z = 0$) view of the magnitude of the magnetic field, magnitude of the velocity, and density at the quasi-linear ($t = 30t_0$) (panels **A,D,G**), nonlinear surface roll-up ($t = 80t_0$) (panels **B,E,H**) and turbulent ($t = 130t_0$) stages (panels **C,F,I**) of the simulation. The black boxes in panels b and c highlight secondary KHI. The dashed black line is plotted along $\rho = \rho_0$ contour as a proxy for the boundary between the two sides. There are streamlines present in grey on the velocity plots to demonstrate the velocity shear.

Since λ_{MHD} relies upon finding an effective pressure minimum, we show the various forms of pressure in Figure 3. Here the variation of the pressure fields about their respective mean is shown–this eliminates any bias from P_{ten} lacking uniqueness. In the quasi-linear stage, the effective pressure has a single minimum near the centre of the simulation between the points where the boundary is most deformed. In the nonlinear stage, the effective pressure has a minimum near the centre of the surface roll up. There is now also an obvious maximum adjacent to it. Along the boundary in the region of secondary KHI (as highlighted in Figure 1B) several small-scale effective pressure minima are also present. There are also other minima in regions where it is clear turbulence/inhomogeneity is present by looking at the other pressures. It is evident that δP_{Ten} does not play a major role in how the total effective pressure is defined as it is generally an order of magnitude smaller than the other pressure variations. δP_{Ten} becomes larger in regions where the magnetic field lines are contorting, but overall it is smaller than $\delta P_{\mathrm{therm}} + \delta P_{\mathrm{mag}}$. This can also be seen in Figure 3C where the δP_{Ten} minima appear to sit along the upper and lower boundaries of the mixed/turbulent plasma and the homogeneous plasma.

Like the tension force itself, $|\delta P_{\mathrm{Ten}}|$ appears to be largest in regions where secondary smaller-scale KHI structures are present. This is likely down to the following two reasons. Firstly, recall that magnetic tension is related to the curvature of field lines, meaning rolled-up smaller scale structures will have greater tension. Additionally, the growth rate of smaller scale structures is greater than larger scale ones (Nagano, 1979; Sundberg et al., 2010; Rice et al., 2022) meaning they will roll-up and evolve faster, i.e., increasing the field line curvature.

4.2.2 Validating λ_{MHD}

Section 4.2.1 demonstrates that the contributions to the effective pressure from the pressure-like part of the magnetic tension are

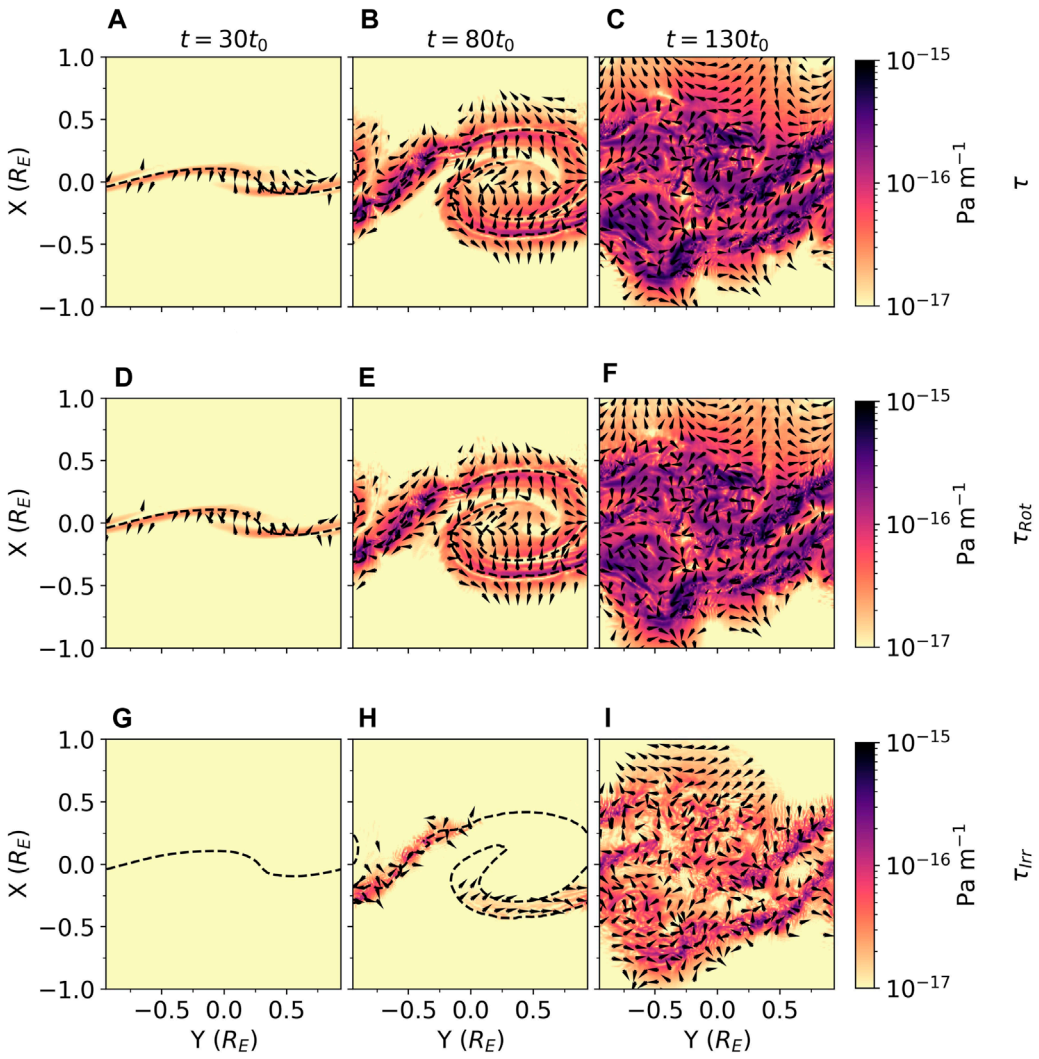

FIGURE 2
An equatorial ($z = 0$) view of the total $\boldsymbol{\tau}$, irrotational part, $\boldsymbol{\tau}_{Irr}$, and rotational part, $\boldsymbol{\tau}_{Rot}$, of the magnetic tension as found through a Helmholtz decomposition. In colour is the magnitude with overlaying unit vectors to indicate the acting direction in the xy-plane. The quasi-linear ($t = 30t_0$) (panels **A,D,G**), nonlinear surface roll-up ($t = 80t_0$) (panels **B,E,H**), and turbulent ($t = 130t_0$) stages (panels **C,F,I**) of the simulation are shown. The dashed black line is plotted along $\rho = \rho_0$ contour as a proxy for the boundary between the two sides.

small for this simulation. Consequently, hydrodynamic techniques might be sufficient in identifying vortices for the simplified magnetopause in this simulation. We therefore compare λ_{MHD} to the other vortex criteria mentioned in Section 2.2.

The different vortex methods are applied to every cell in the simulation, where spatial derivatives are undertaken through second order accurate central differences in the interior points and first order accurate differences at the boundaries. To remove machine noise in the gradients we apply a multidimensional Gaussian filter with a standard deviation of 0.5 grid cells. The smoothed data is then passed through a $3 \times 3 \times 3$-cell multidimensional median filter to ensure that the regions are 'connected' – meaning that more than one adjacent cell in a plane must be identified as vortical for a positive identification. Typically with these types of techniques a threshold is chosen to define a vortex (Dong and Tian, 2020), however we have chosen not to do this to allow for a more complete comparison of the techniques and what they physically represent.

Figure 4 shows the λ_{MHD} vortex definition compared to the 2-dimensional velocity streamlines (v_z is negligible throughout this plane) to qualitatively assess whether the technique is correctly identifying vortices. In the quasi-linear stage of the KHI ($t = 30t_0$), there is a single vortex core identified (region 1) which is centred around the steep edge of the deformed shear flow boundary. After some evolution to the nonlinear roll-up stage ($t = 80t_0$), the previous vortex has now evolved and been stretched and torn into four large structures (regions 2, 4, 5, 6). The strongest signature in the simulation is region 2, a structure at the edge of the simulation that is the leading edge of the rolled up surface (remembering the boundary conditions in y are periodic). The other three structures are in the centre of the simulation, again where the surface roll-up is present. Interestingly, the secondary small-scale KHI vortices

10.3389/fspas.2024.1431238

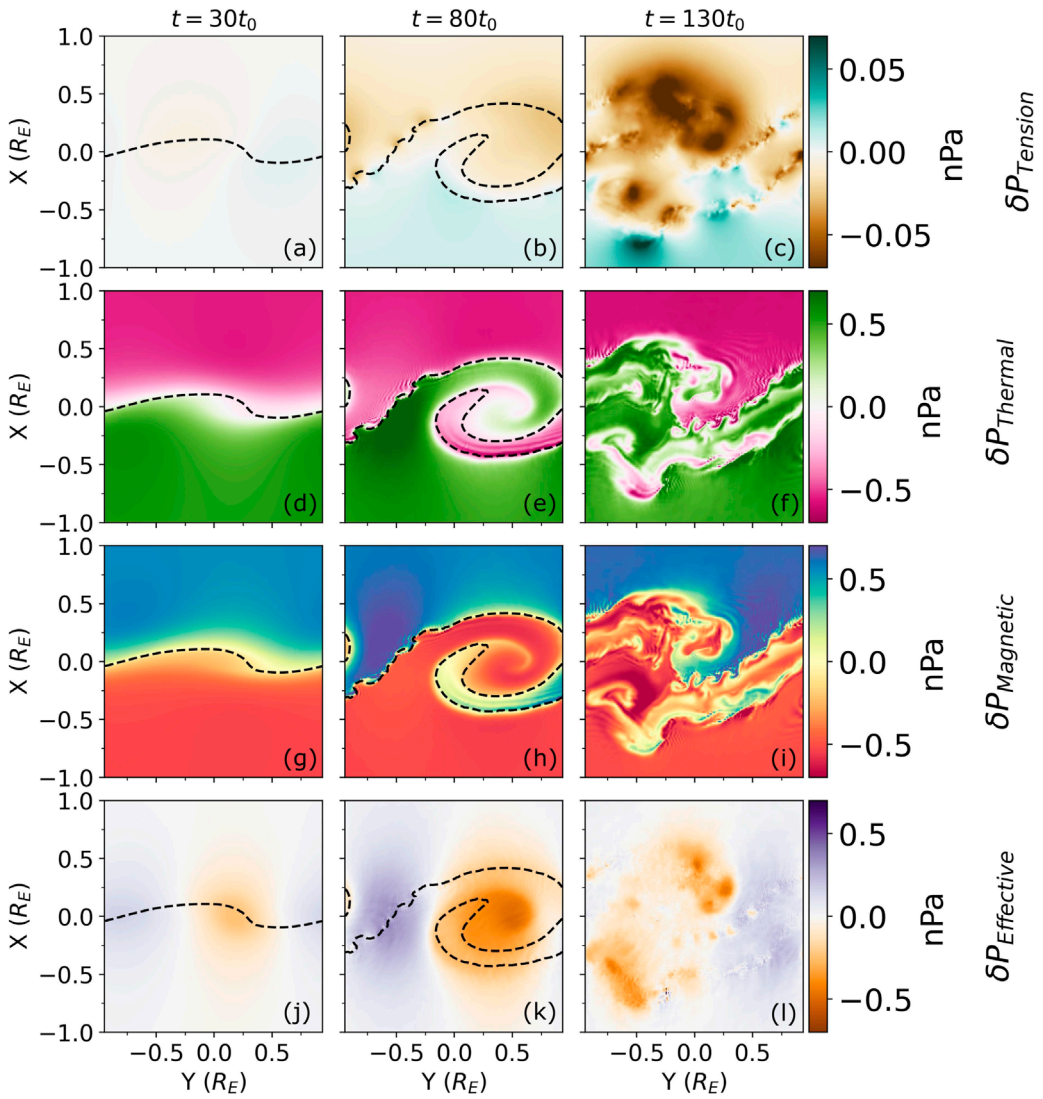

FIGURE 3
An equatorial ($z = 0$) view of the perturbations from the mean pressure due to magnetic tension, thermal pressure, magnetic pressure, and total pressure. The quasi-linear ($t = 30t_0$) (panels **A,D,G,J**), nonlinear surface roll-up ($t = 80t_0$) (panels **B,E,H,K**) and turbulent ($t = 130t_0$) stages (panels **C,F,I,L**) of the simulation. The dashed black line is plotted along $\rho = \rho_0$ contour as a proxy for the boundary between the two sides.

(region 3) have a stronger signature than the three vortex structures within the roll-up (regions 4, 5, 6). It appears the vortices are all situated where the principal curvature of the boundary is greatest, with the strength being proportional in some way to the curvature of the boundary i.e., stronger vortices deform the boundary more.

The original large-scale vortex becomes unidentifiable in the turbulent stage, it is possible that region 4 becomes region 7 and region 5 becomes region 9, but this is ambiguous. Instead strong λ_{MHD} signatures are present in much of the simulation domain due to lots of small-scale vortical structures being present throughout. There are two large vortices present (regions 7 and 9). Some of the strongest signatures are found where secondary KHI is present (region 8). Generally, speaking λ_{MHD} grows with time as the strongest signatures are seen in the turbulent stage and the weakest in the quasi-linear stage.

Figure 5A shows a zoom in of vortex region 4 from the nonlinear roll-up stage. In the simulation frame the vortex is not immediately apparent in the flow, despite λ_{MHD} identifying a distinct vortex in this region. However, exploiting the Galilean invariance of the method, we transform the velocity field into a different frame in panel b. This clearly demonstrates an isolated vortex is present, hence the distinct regions identified by λ_{MHD} within the KHI roll-up are real vortical features in the flow. This again highlights the need for vortex identification techniques, since they can pinpoint vortices which are not clear from visual analysis. We emphasise that the vortices these techniques identify are not simply the large-scale roll-up structure of the boundary overall, but flow vortices present as substructure within this roll-up which are ultimately responsible for the boundary deformations.

Figure 6 shows the MHD effective pressure with overlaying contours of the different vortex identification methods (λ_{MHD} and

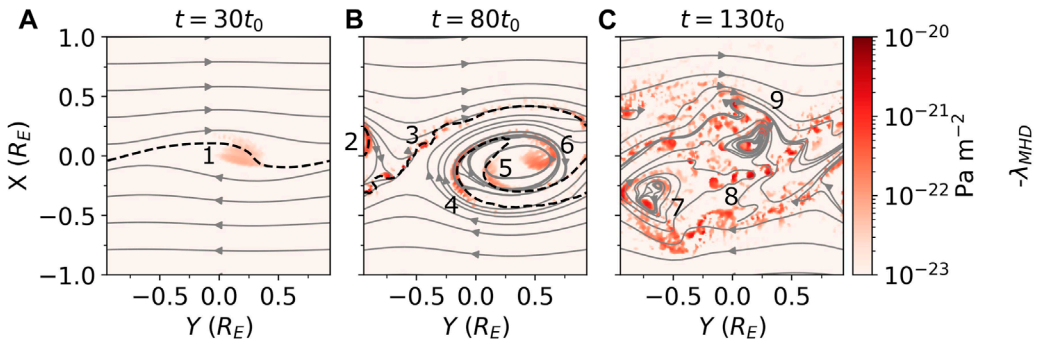

FIGURE 4
An equatorial ($z = 0$) view of vortex identification method $-\lambda_{MHD}$ values on a $\log_{10}$ colour-scale. The quasi-linear ($t = 30t_0$) (panel **A**), nonlinear surface roll-up ($t = 80t_0$) (panel **B**) and turbulent ($t = 130t_0$) stages (panel **C**) of the simulation. In grey are 2D velocity field streamlines. The numbers in the plot indicate regions of interest discussed in the text. The dashed black line is plotted along $\rho = \rho_0$ contour as a proxy for the boundary between the two sides.

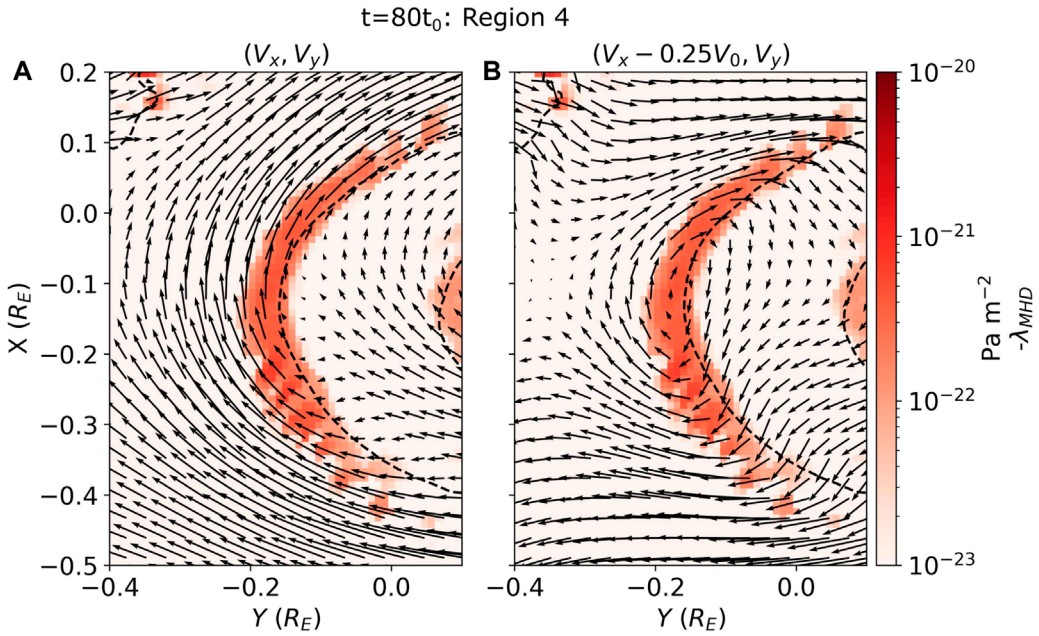

FIGURE 5
An equatorial ($z = 0$) view of vortex identification method $-\lambda_{MHD}$ values on a $\log_{10}$ colour-scale. Region 4 (see Figure 4B) of the nonlinear surface roll-up ($t = 80t_0$) stage is shown. Panel a and b show the same λ_{MHD} colour map calculated in the simulation frame. In black are 2D velocity field quivers, panel **(A)** shows the original velocity field quivers, panel **(B)** shows a Galilean transformed field where the $V'_x = V_x - 0.25V_{A0}$. The dashed black line is plotted along $\rho = \rho_0$ contour as a proxy for the boundary between the two sides.

those mentioned in Section 2.2), which should identify pressure minima. Contour levels have been arbitrarily chosen to display behaviour at extremes of large and small values that constitute a vortex (without any data-driven thresholds imposed; cf. Dong and Tian, 2020) for more comprehensive comparison of the different methods. Visually comparing the hydrodynamic criteria and λ_{MHD}, it appears that all the definitions of a vortex identify similarly compact regions. This further qualitatively validates λ_{MHD} and also suggests the simpler hydrodynamic criteria may be used as proxies for λ_{MHD}. Since each method makes different levels of assumptions about the fluid, comparing the different definitions explores how introducing these different physical effects affects the regions identified as a vortex core, hence their importance in vortex formation and evolution.

Q and λ_2 perform almost identically across the three time steps shown in Figure 6 and identify similar regions to those discussed in Figure 4. The criteria identify regions where the local boundary is most deformed and by comparing to effective pressure in Figure 3, it is clear that they are locating local pressure minima in the quasi-linear stage. In the nonlinear and turbulent stages, this is less clear. The minima located by them differ to the local minima in the effective pressure plots. The effective pressure appears to highlight the general region however the criteria clearly outlines the vortex core regions. This is because the neglected parts of the adapted

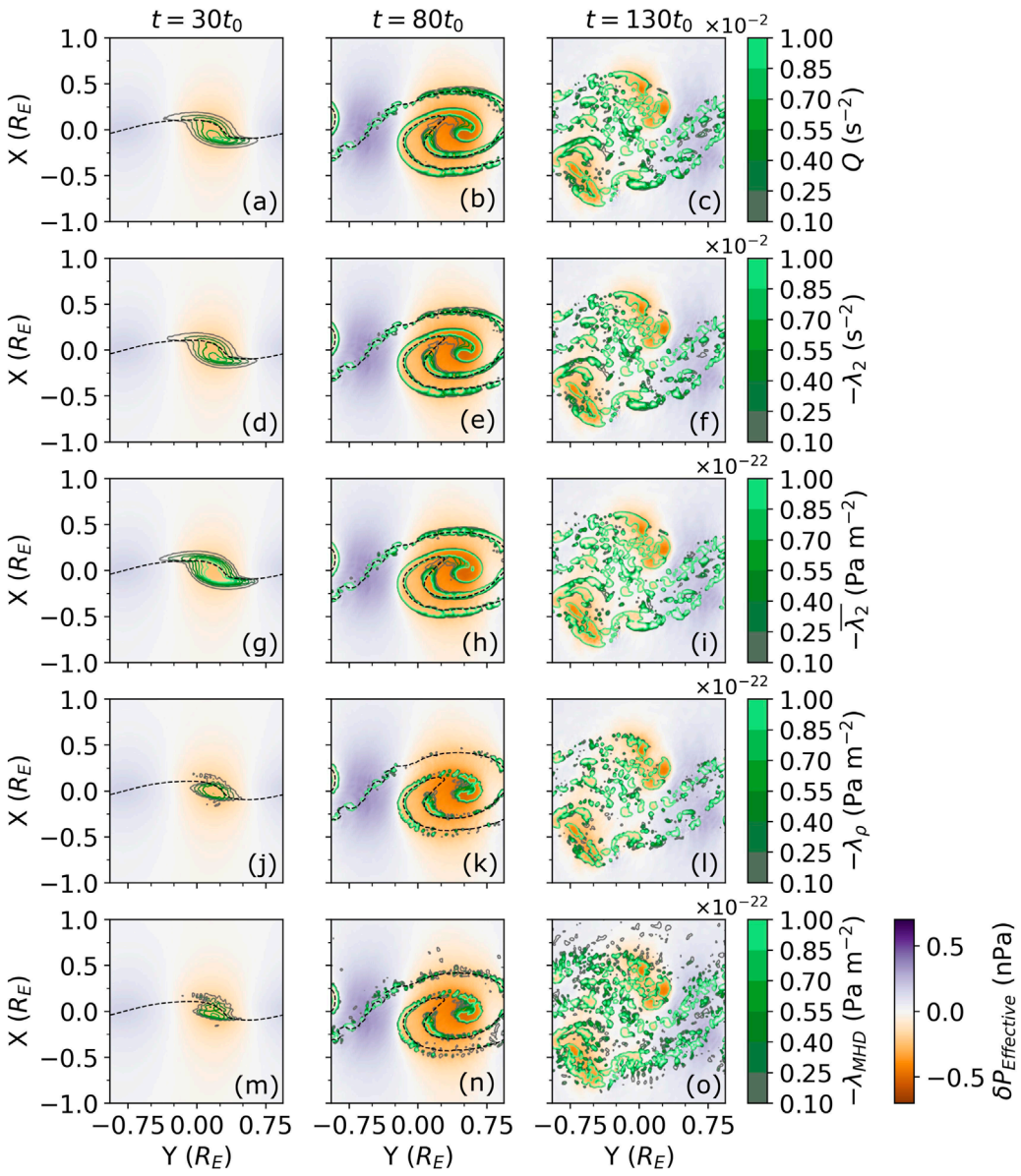

FIGURE 6
An equatorial ($z = 0$) view of contours for different vortex techniques on a linear colour-scale. These are plotted over the effective pressure variations from the mean. The quasi-linear ($t = 30t_0$) (panels **A,D,G,J,M**), nonlinear surface roll-up ($t = 80t_0$) (panels **B,E,H,K,N**), and turbulent ($t = 130t_0$) stages (panels **C,F,I,L,O**) of the simulation. The dashed black line is plotted along $\rho = \rho_0$ contour as a proxy for the boundary between the two sides.

effective pressure Hessian are non-negligible in these stages and neglecting them allows for a clearer identification. This suggests that making these adaptations to the pressure Hessian are vital to the success of the λ-family of techniques. Furthermore, it demonstrates that while local total pressure minima may be reliable in the quasi-linear stage as an approximate identification tool, beyond this the method is not precise enough and advanced vortex identification techniques are necessary.

Comparing Q and λ_2 to $\overline{\lambda_2}$ probes the importance of momentum flow over velocity flow in the identification of a vortex. Crucially, the power and strength of those regions shift to locations where there is larger vortical momentum instead of just vortical velocity. Since $\overline{\lambda_2}$ simply weights λ_2 by local density, the sign remains unchanged and thus it identifies identical regions to λ_2. Unlike Q and λ_2, the units of $\overline{\lambda_2}$ are comparable to those of λ_{MHD} allowing for direct comparisons to be made between the two criteria. In this simulation, the λ_2 and $\overline{\lambda_2}$ results do not appear to differ much–this is likely due to the uniform initial density along the shear direction. Comparing the results of λ_ρ to that of $\overline{\lambda_2}$ allows for an insight into how fluid compressibility and density gradients influence where a vortex core is identified. It is apparent that these two factors do influence vortex identification as there is an obvious reduction in the volume that λ_ρ identifies as vortical compared to the less advanced methods. In particular, the vortex appears less strongly in λ_ρ at the $t = 30t_0$ stage compared to the earlier considered methods. In the later stages of the KHI, there are more detached vortical regions seen in λ_ρ compared

to the less advanced methods. This suggest that λ_ρ is capable of distinguishing between multiple vortices in close proximity. The less advanced methods appear to smear these multiple vortices into one large vortex core structure making them less useful if studying vortex shedding, complex regions, or turbulent stages. Due to this, λ_ρ is better suited for revealing finer details of the complex physics taking place.

λ_{MHD} includes the influence of the magnetic field to the definition of a vortex core. λ_{MHD} appears to identify almost the same structures as λ_ρ, indicating that magnetic tension may not play a dominant role in the large-scale vortices in this simulation. This is somewhat expected since under northward IMF the magnetic tension is least effective at suppressing the KHI, and the scale of variations along the anchored field lines are much larger than those perpendicular to the field (Equation 1). Nonetheless, λ_{MHD} does identify additional finer-scale archipelago-like structures less dominant in the hydrodynamic approaches. These occur at the small-scale secondary KH vortices, likely because the tension term becomes more important in these regions as previously discussed in Section 4.2.1. As many of these values are relatively close to zero, this may suggest that in practical applications a higher threshold value than the lowest contour displayed of 0.01×10^{-22} Pa m^{-2} may be needed for the λ_{MHD} (and maybe λ_ρ) technique(s). This would reduce the number of small scale structures being identified, enabling focus on stronger vortices and their large-scale structure. How best to set such vortex thresholds is an area of ongoing research even in hydrodynamics (Chakraborty et al., 2005; Pierce et al., 2013; Liu et al., 2019; Dong and Tian, 2020).

Figure 7 shows 2-dimensional histograms over the entire simulation domain quantitatively comparing each hydrodynamic vortex criterion (vertical axes) with λ_{MHD} (horizontal axes). In all the histograms there is a main data population confined to a $y \propto x$ line (except for Q where the criteria for a vortex is positive not negative making it $y \propto -x$ instead) meaning all the techniques have a good correlation with λ_{MHD} – especially λ_ρ during the linear and nonlinear stages. This is reflected in the strong Pearson's correlation coefficients, R. There are two secondary populations in the histograms. The first is along the $y = 0$ region–largely with negative λ_{MHD} values. These correspond to regions where λ_{MHD} has identified a vortex where the hydrodynamic definition has not. Assuming λ_{MHD} is successfully identifying vortices and given the only difference between it and the λ_ρ definition is the introduction of the rotational tension term, this feature must be due to magnetic field effects that λ_{MHD} is able to extract which the hydrodynamic definitions cannot. The second is around the $x = 0$ region, this is due to the hydrodynamic definitions identifying larger regions as vortical compared to λ_{MHD}. This supports the previous finding that the simpler hydrodynamic definitions have a poorer precision than λ_ρ or λ_{MHD}. As the simulation becomes turbulent, there is a larger variance about the linear relationship between the hydrodynamic and MHD methods, though the correlation is still reasonable. The increased variance is expected as, e.g., the magnetic tension term becomes more important in the small-scale structures which form. An analysis of each technique's performance against λ_{MHD} can provide a better understanding of how different regimes can affect vortex formation and identification.

The Q, λ_2, and $\overline{\lambda_2}$ comparisons all demonstrate good correlations with the λ_{MHD} technique which strongly suggests that compressibility and plasma inhomogeneity do not play a significant role in the identification of the vortex, as these techniques are ignorant of these effects. The secondary populations break this pattern and are not as present in λ_ρ which reinforces that the regions identified by the simplest hydrodynamic criteria are not as precise as the more advanced methods. Previous research has found that the simpler hydrodynamic techniques struggle to distinguish between two vortices situated close together in space and tend to blur the volumes into one large structure (Cai et al., 2018; Collado-Vega et al., 2018) – our results agree with these findings.

The square of Pearson's correlation coefficient between λ_ρ and λ_{MHD} indicates the amount of variance in λ_{MHD} explainable by hydrodynamic effects alone. λ_ρ has a very good Pearson's correlation coefficient with λ_{MHD} of 0.97 in the quasi-linear stage, hence vortex identification is virtually entirely described by hydrodynamics and magnetic effects are negligible during this early stage of the KHI within this simulation (again likely due to the northward IMF conditions used along with long field lines). As it evolves into the nonlinear surface roll-up stage, hydrodynamics only explains 71% of the variations present. Magnetic tension term therefore plays a non-negligible role, likely due to magnetic tension's effects becoming more important as secondary KHI begin to form. In the turbulent stage of the KHI, less than half (47%) of the variations in λ_{MHD} are due to hydrodynamic effects alone, meaning that magnetic tension becomes an essential component likely due to the increased number of smaller-scale magnetic structures present.

The analysis has shown that (for this simulation at least) Q, λ_2, and $\overline{\lambda_2}$ are good approximations of a vortex in the MHD regime. However, they are prone to false-identifications as they struggle to distinguish between multiple vortices in close proximity. Including density gradient and compressibility effects allows λ_ρ to more successfully distinguish between these close proximity vortices, allowing it to provide more precise vortex identifications. Effects from magnetic tension, only incorporated into λ_{MHD}, become more important over time due to structural evolution and field line twisting, wrapping, and distortion. While the different vortex criteria include and/or exclude different physical effects related to vortex formation, quantitatively comparing these eigenvalues does not self-consistently enable a thorough investigation of the interplay these physical effects since each criterion has a different eigenvector. A different quantitative method needs to be used to fully explore how each different term, and therefore effect, influences vortex identification.

4.2.3 Contributions to λ_{MHD}

As derived in Section 3.2, there are four physical effects which contribute to λ_{MHD}: vortical momentum (**M**), fluid compressibility (**C**), density gradients (**D**), and the rotational tension (**T**). Here we investigate to what extent each contributes to λ_{MHD} within the simulation.

The effective pressure Hessian tensor, **H**, is real and symmetric (hence also Hermitian). It therefore has real eigenvalues whose eigenvectors can be chosen to be real and orthonormal. From the spectral theorem the Hessian's eigenvalue can be rewritten as a linear combination of eigenvector projections, known as a spectral eigendecomposition. Let $\widehat{\mathbf{V}}_{H,2}$ be the normalised eigenvector of **H** corresponding to the second eigenvalue, λ_{MHD}.

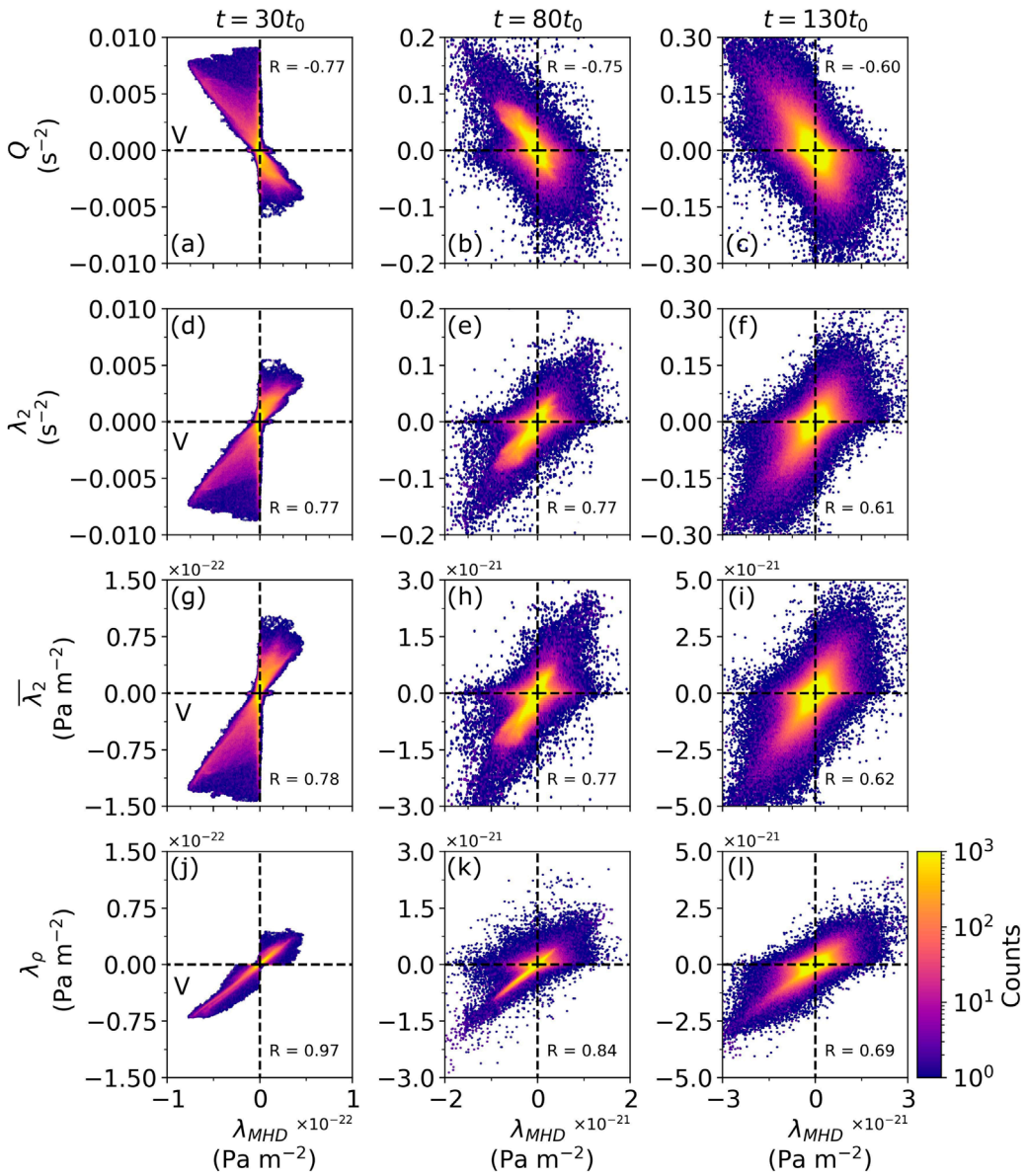

FIGURE 7
2D histograms across the entire simulation domain comparing λ_{MHD} with the hydrodynamic vortex criteria. Counts are plotted using a $\log_{10}$ colour scale. The quadrant which represents a vortex in both λ_{MHD} and the comparison definition is labelled with 'V'. The R value denotes Pearson's correlation coefficient. Analysis of the quasi-linear ($t = 30t_0$) (panels **A,D,G,J**), nonlinear surface roll-up ($t = 80t_0$) (panels **B,E,H,K**), and turbulent ($t = 130t_0$) stages (panels **C,F,I,L**) are shown.

Right multiply Equation (23) by $\widehat{\mathbf{V}}_{H,2}$ and left multiply by the transpose to get,

$$\lambda_{\mathrm{MHD}} = -\widehat{\mathbf{V}}_{H,2}^{T}\mathbf{H}\widehat{\mathbf{V}}_{H,2} \tag{24a}$$

$$= \widehat{\mathbf{V}}_{H,2}^{T}\mathbf{M}\widehat{\mathbf{V}}_{H,2} + \widehat{\mathbf{V}}_{H,2}^{T}\mathbf{D}\widehat{\mathbf{V}}_{H,2} + \widehat{\mathbf{V}}_{H,2}^{T}\mathbf{C}\widehat{\mathbf{V}}_{H,2} + \widehat{\mathbf{V}}_{H,2}^{T}\mathbf{T}\widehat{\mathbf{V}}_{H,2} \tag{24b}$$

$$= \lambda_M + \lambda_D + \lambda_C + \lambda_T. \tag{24c}$$

For clarity $\lambda_{M,D,C,T}$ are not eigenvalues of their respective matrices, but are the contributions to the λ_{MHD} eigenvalue of $\mathbf{H}$. This demonstrates how each term directly contributes to λ_{MHD} which allows for quantitative analysis and comparison of the different contributions each physical effect has on λ_{MHD}. It is widely accepted that magnetic tension is a stabilising force for the KHI so it is sensible the derivation has it subtracted instead of added. Regions where tension acts to stabilise, i.e., regions where a vortex exists, thus become identified as vortical.

Figure 8 shows a spatial map of the contribution each term has to λ_{MHD} at each of the three stages considered. The values shown are processed like before. In overview, it is clear that the vortical momentum term (panels a–c) generally dominates the λ_{MHD} definition, supporting the conclusion that Q, λ_2, and $\overline{\lambda_2}$ are reasonable approximations of λ_{MHD}. The other terms appear to act as corrections to the vortical momentum term. Density gradients (panels d–f) generally oppose the vortical momentum. The fluid

10.3389/fspas.2024.1431238

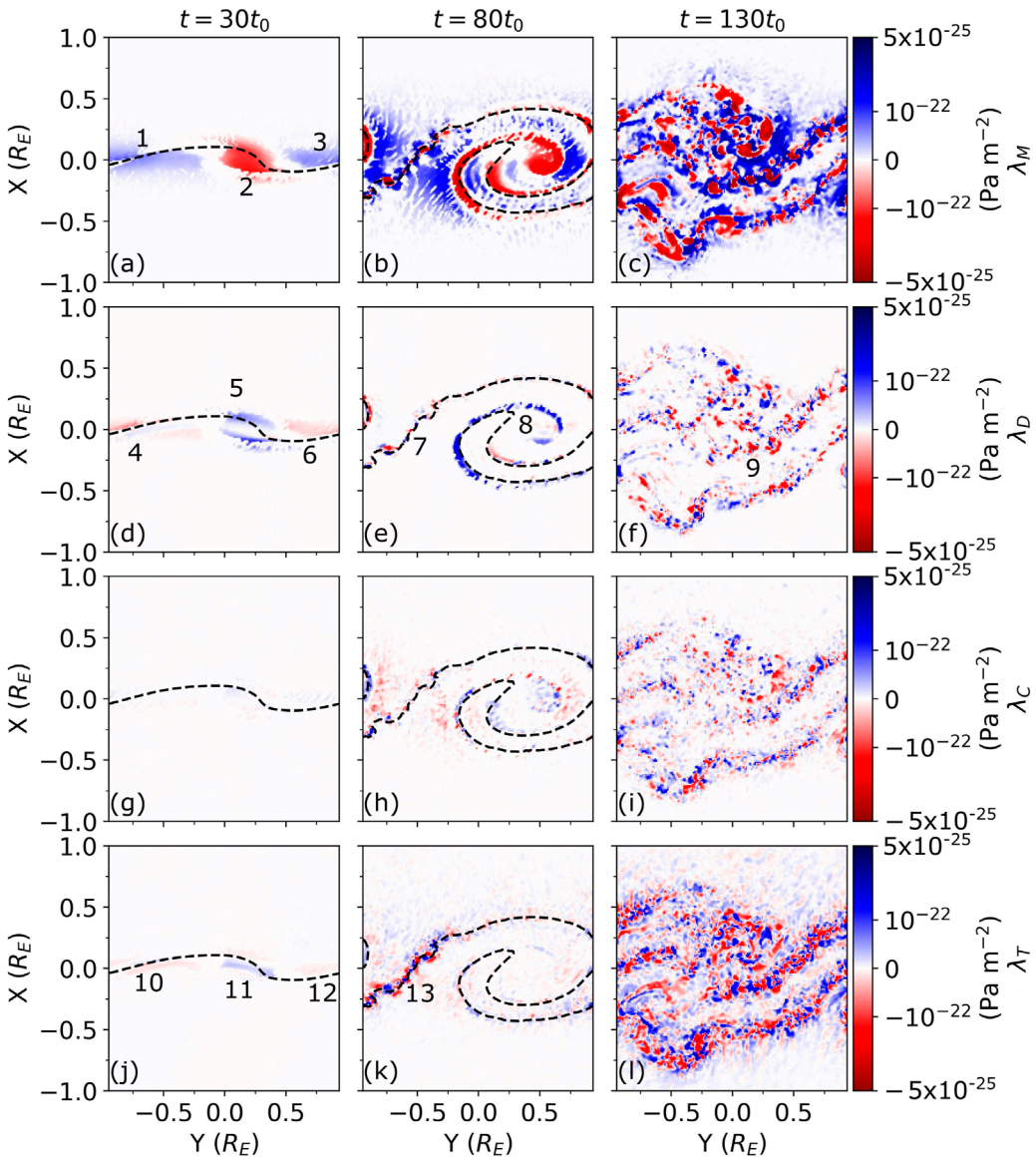

FIGURE 8
An equatorial ($z = 0$) view of each contributing term to λ_{MHD}. The values on a symlog$_{10}$ colour-scale where the linear scale is between $\pm 10^{-22}$ Pa m^{-2}. Negative regions (red) support λ_{MHD}, positive values (blue) are regions in opposition with λ_{MHD}. The quasi-linear ($t = 30t_0$) (panels **A,D,G,J**), nonlinear surface roll-up ($t = 80t_0$) (panels **B,E,H,K**) and turbulent ($t = 130t_0$) stages (panels **C,F,I,L**) are shown. The dashed black line is plotted along $\rho = \rho_0$ contour as a proxy for the boundary between the two sides.

compressibility term (panels g–i) is generally small at all three stages shown. Over the course of the three stages, the rotational component of the magnetic tension (panels j–l) tends to grow in regions where smaller-scale vortices form, reinforcing its importance over these scales. However, all the terms appear to have a complex relationship with λ_{MHD} overall, supporting in some locations but opposing in others.

In the quasi-linear stage, vortical momentum is the dominant term. There are two different populations in this term, the first (region 2) is in support of a vortex and lies between where the interface is most deformed. The other population (regions 1 and 3) oppose a vortex. Density gradients (panel d) oppose the formation of a vortex at the centre of simulation (region 5). Interestingly, this opposition is strongest at the edges along the normal of the vortical momentum region (2) rather than at the centre. This serves to reduce the volume being identified as vortical and is the reason the λ_{MHD} method is more precise, allowing for better vortex core identification. This suggests that the density gradient term is crucial for the reliable identification of multiple vortices in close proximity. Furthermore, the density gradient term contributes to the existence of vortices at the outer edges of the simulation near the boundary (regions 4 and 6) where vortical momentum is not present (regions 1 and 3) – this may alternatively be a reduction in the non-vortex signature provided by the momentum term. Further investigation is needed into the physical interpretation of this, which we leave to future work since overall these regions are not identified as vortices. Compressibility appears negligible at this stage. The rotational

10.3389/fspas.2024.1431238

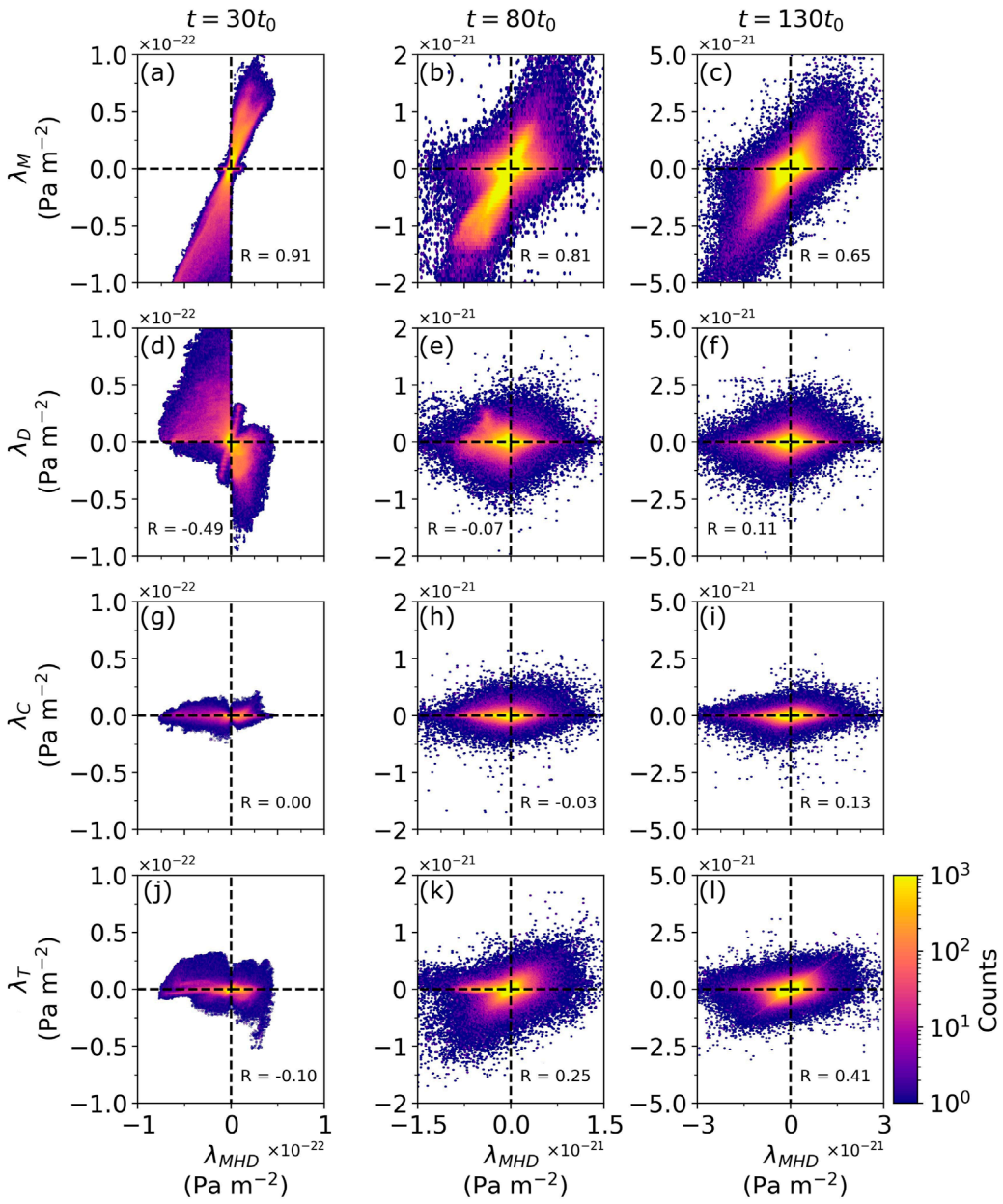

FIGURE 9
A 2D histogram across the simulation domain comparing λ_{MHD} with the terms contributing to it. Counts are plotted using a $\log_{10}$ colour scale. The R value shown is the Pearson's correlation coefficient. Analysis of the quasi-linear ($t = 30t_0$) (panels **A,D,G,J**), nonlinear surface roll-up ($t = 80t_0$) (panels **B,E,H,K**), and turbulent ($t = 130t_0$) stages (panels **C,F,I,L**) are shown.

tension term is complex in regions 10, 11, 12 – there is weak opposition along the boundary (the dashed line) in regions 10, 11, and 12 implying tension is acting to stabilise the boundary as expected. However, the term appears to weakly support off the boundary in these regions too. Reasoning for this is unclear. It is worth noting that regions 4 and regions 10 look very similar, as do regions 6 and 12 however this may just be a consequence of the structure shape.

In the nonlinear surface roll-up stage, the density gradient term strongly opposes the larger scale vortex (region 8) but has little power on the small-scale secondary KHI (region 7) implying the term may have a scale–or KHI-stage–bias. The density gradient term appears to have the same relationship with the small-scale secondary KH vortices (region 7) as it has with the single vortex in the quasi-linear stage–it opposes the formation of a vortex at the centre of simulation on edges of the region of vortical momentum, but not at the centre where it supports it. The compressibility term does not appear to show any obvious trend and is generally small at this stage. The rotational magnetic tension term has become large in region 13 where the small-scale secondary KH vortices are present, opposing their formation. It appears to have little impact on the large scale vortex.

In the turbulent stage, the density gradient term appears to have the same relationship with the small-scale secondary KH

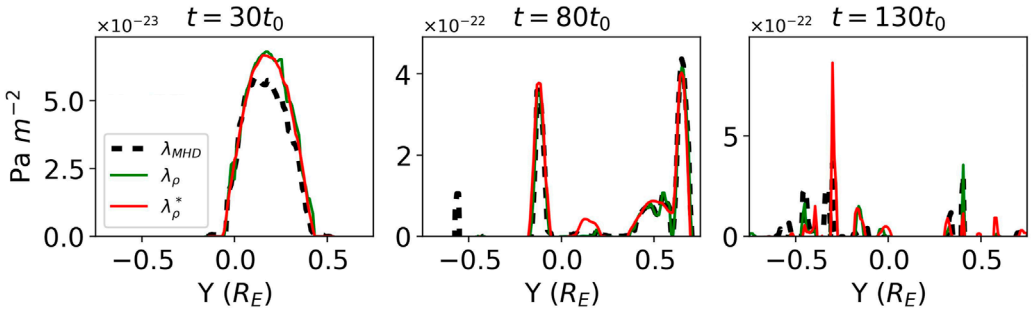

FIGURE 10
A spatial slice through the $x = z = 0$ line of the simulation showing $-\lambda_{\mathrm{MHD}}$, $-\lambda_\rho$, and $-\lambda_\rho^*$ values. Only the vortex identifying values are shown.

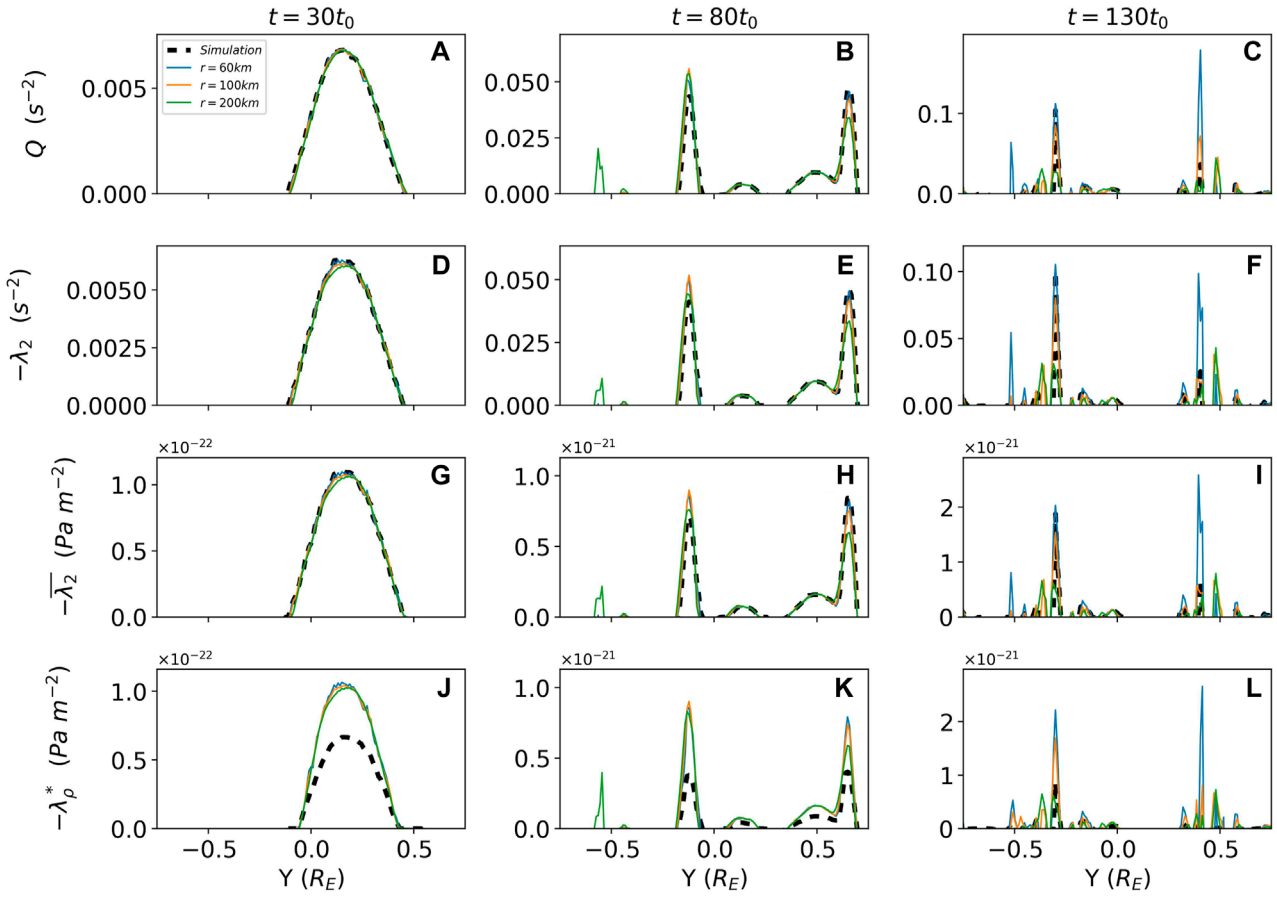

FIGURE 11
Vortex criteria values are shown using multi-spacecraft techniques with a mesocentre along the spatial slice through $x = z = 0$ of the simulation with varying radial distances between spacecraft. Only the vortex identifying values are shown. Analysis of the quasi-linear (t = 30t_0) (panels **A,D,G,J**), nonlinear surface roll-up (t = 80t_0) (panels **B,E,H,K**), and turbulent (t = 130t_0) stages (panels **C,F,I,L**) are shown.

vortices (region 9) as it has with the single vortex in the quasi-linear stage. This was also seen in region 7 meaning that the relationships between the physical effects for the secondary KHI at these stages can be considered as analogous to those for the large-scale vortex during its quasi-linear stage. The compressibility term again remains small with no clear relationship to the vortices. Rotational magnetic tension has further grown, now opposing the secondary KH vortices.

These trends have only been qualitatively explored in the equatorial plane. Further quantitative analysis can be made to better understand the general contributions over the entire simulation domain.

Figure 9 shows 2-dimensional histograms of the entire simulation domain comparing each term in Equation 24c with λ_{MHD}. Across all three time steps the fluid compressibility term is small and poorly correlated to λ_{MHD} implying that fluid

compressibility is not a dominant component in the existence of a KH vortex in this simulation. This might be attributed to the low convective fast magnetosonic Mach number used in this simulation, meaning the plasma is weakly compressible (representative of the near-flank magnetopause environment; Ma et al., 2020).

Figure 9D shows that the density gradient term strongly opposes the formation of a vortex in the quasi-linear stage of its growth but becomes less significant in the later stages. This suggests that the density difference across the shearing fluid is important in the initial stages of KH wave formation. Physically this makes sense, as the flow with a lower density will have insufficient momentum to change the direction of the high momentum flow with heavier mass making the initial wave harder to generate. Beyond the quasi-linear stage, the flow is sufficiently deformed that this density variation becomes less significant in comparison to the driving shear flow. There is a smaller secondary population in this term which supports the vortex and can also be seen in Figure 8D.

Figures 9J–L also indicates that the rotational component of the magnetic tension term becomes larger as the KHI advances. The plot suggests that during the turbulent stage, where vortices are expected to have a small spatial volume and thus larger tension effects, this term becomes a significant contributor to λ_{MHD}. This is also reflected in the Pearson's correlation value. Finally, the rotational component of the magnetic tension term has multiple populations within itself. In the nonlinear stage, there is a population which sits along a $y \propto x$ line which will be the population where the term supports the identification of a vortex–this likely corresponds to the small scale secondary KH vortices. The second population sits along the $y = 0$ line where the tension term does not contribute to λ_{MHD} – this likely corresponds to the single large scale vortex. This pattern is also present in the turbulent stage. There is a strong population along a $y \propto x$ line indicating that this term is important in the turbulent stage. However, there is a larger spread in the $y = 0$ population which may be because the histograms include the entire simulation domain and so will contain variations out-of-plane which are not seen in Figure 9.

4.2.4 Potential in situ applications

So far λ_{MHD} has been applied to gridded simulation data. However, it would be helpful to also explore its potential application to multi-point *in situ* measurements, though somewhat challenging. While the momentum and density gradient terms involve only first-order spatial derivatives, thus can be calculated with four suitably instrumented spacecraft in a tetrahedron, e.g., Magnetospheric Multiscale (MMS) (Burch et al., 2016), the compressibility term involves second-order derivatives which require 10 spacecraft that do not lie on any quadric surface (Zhou and Shen, 2024). Finally, the rotational tension term is challenging since it involves a Helmholtz decomposition, which is inherently non-local requiring information throughout space. It may be possible through Equation 8b and suitable interpolation methods to estimate the decomposition for a multi-spacecraft mission such as HelioSwarm (Klein et al., 2023). Determining how to do this, however, is beyond the scope of this study.

Given these limitations, we simply consider a tetrahedral spacecraft configuration and only use the momentum and density gradient terms to construct the adapted pressure Hessian–essentially an incompressible version of λ_ρ denoted as λ_ρ^* herein. Section 4.2.2 demonstrated λ_ρ accurately approximates λ_{MHD} in this simulation during the linear and nonlinear roll-up stages, with Section 4.2.3 showing compressibility and magnetic tensions make negligible contributions. We show an example application in Figure 10, which uses a spatial slice of the simulation data along the y-axis to emulate a spacecraft encounter with the magnetopause. The figure compares λ_{MHD} with λ_ρ and λ_ρ^*, demonstrating that λ_ρ and λ_ρ^* are near identical techniques which both approximate λ_{MHD} well in the linear, and nonlinear stages here. Unsurprisingly, the techniques appear to be less useful in the turbulent stage, however, they do still replicate the λ_{MHD} results overall. Thus λ_ρ^* may be a sensible proxy which could be realised by tetrahedral *in-situ* data. The qualitative visual differences between the three stages suggests they may also be used to distinguish between different evolutionary phases; a prospect we leave for quantitative exploration in future work.

Regular tetrahedra of spacecraft are considered, with mesocentres along the x-axis. Simulation data are trilinearly interpolated to spacecraft locations. Since spacecraft separation affects the quality and scales over which gradients can be estimated (De Keyser, 2008), we vary the tetrahedra's radial distances r as 60 km, 100 km, and 200 km (the simulation grid spacing is 60 km). These cover the range of MMS separations over the course of the mission, excluding its smallest tetrahedron sizes. Gradients are calculated using techniques outlined in Paschmann and Daly (1998) and are used to calculate $Q, \lambda_2, \overline{\lambda_2}$, and λ_ρ^*. Figure 11 shows how each technique performs with different tetrahedra sizes, compared also with the true values from the simulation grid.

Figure 11 shows that all the techniques considered might be applied to virtual spacecraft observations with varying success. Generally speaking, the smaller the tetrahedron, the closer the virtual spacecraft value is to the simulation value. All the techniques reliably approximate the simulation values during the linear and nonlinear stages of the KHI regardless of virtual spacecraft separation. Interestingly, the smaller tetrahedron separation more precisely mimics the simulation results of all the techniques but contains larger amounts of noise, likely due to the interpolation–this is best seen in the quasi-linear stage. Notably, the widths of the peaks in the λ_ρ^* technique are narrower than those in the less advanced techniques implying that a more specific region is being located by this technique–the core of the vortex. This is easiest seen when comparing Figures 11A,J.

5 Conclusion

The Kelvin-Helmholtz instability is a dominant driver of the viscous-like transfer of mass, momentum, and energy across the magnetopause through surface waves and their coupled vortices. A vortex detection method suitable for MHD, called λ_{MHD}, has been derived by self-consistently incorporating the $\mathbf{J} \times \mathbf{B}$ Lorentz force into the λ-family of hydrodynamic vortex identification techniques. These methods define a vortex as a local minimum within some 2D plane of an adapted pressure field. Within ideal MHD, the effective pressure field is defined as the sum of the thermal pressure, magnetic pressure, and the pressure-like part of the magnetic tension which is extracted using a Helmholtz decomposition. This is then adapted

by removing the effects of unsteady straining, which can result in pressure minima unrelated to vortices, which is key to the λ-family methods' success. λ_{MHD} has been validated against the velocity field and other hydrodynamic techniques using a local three-dimensional MHD simulation representative of near-flank magnetopause conditions under northward IMF.

λ_{MHD} is composed of four components: vortical momentum, density gradients, fluid compressibility, and the rotational part of the magnetic tension. These effects have separately been shown to influence KHI formation (e.g., Chandrasekhar, 1961; Miura and Pritchett, 1982; Pu and Kivelson, 1983; Amerstorfer et al., 2010; Ma et al., 2024). In this work it was found that the vortical momentum dominates λ_{MHD} in the simulation at all times, meaning that hydrodynamic techniques which capture this effect only, may be good proxies for λ_{MHD}. During the linear growth phase, density gradients generally act to oppose vortex formation but become less important in the later stages of vortex evolution. This is in agreement with previous work where plasma inhomogeneity was found to not affect growth rate (Ma et al., 2024). The rotational part of the magnetic tension has been shown to become important in small-scale structures suggesting that the hydrodynamic definitions would be insufficient at identifying these. Fluid compressibility was found to be insignificant at all stages.

Some of these results will be due to the choice of plasma parameters used, which are representative of the near-flank magnetopause. Dimensionless scaling arguments might infer the implications of this work under different plasma regimes though. The simulation is only weakly compressible ($M_f \sim 0.4$), but compressibility effects are expected to vary as $\sim M_f^2$ (Palermo et al., 2011). Here we shall assume this scaling for the compressibility term, λ_C, and that the vortical momentum term, λ_M, might be unaffected by the convective Mach number. Over the three stages of the simulation presented, the ratio of these terms' standard deviations, $\sigma(\lambda_C)/\sigma(\lambda_M)$, constitute 6%, 14%, and 21% respectively. For the compressibility term to be as significant as the momentum term during the quasi-linear regime, scaling arguments suggest a supermagnetosonic Mach number $\left(M_f \gtrsim 1.6\right)$ would be needed. In contrast, for the nonlinear and turbulent stage, trans-magnetosonic Mach numbers $\left(0.8 \lesssim M_f \lesssim 1.2\right)$ might suffice. These Mach numbers are likely underestimates as we have not taken into account the poor correlation of compressibility with λ_{MHD}. These estimates are in agreement with previous works which suggest compressibility affects the later stages of the KHI (growth rate) more than the initial stages (lower critical velocity). Similar arguments can be made for the magnetic tension term, λ_T, by considering the Alfvén Mach number which is $M_A \sim 0.9$ and $M_A \sim 0.6$ in regions 1 and 2 respectively. The relative importance of magnetic tension should scale as $\sim M_A^{-2}$ (Equation 1). Performing similar analysis to compressibility, we find the ratio of the standard deviations, $\sigma(\lambda_T)/\sigma(\lambda_M)$, to be 10%, 27%, and 47% respectively. For the tension to be of similar importance to the momentum suggests weaker Alfvén Mach numbers $0.3 \lesssim M_A \lesssim 0.6$ may be required on both sides (likely overestimates due to weak correlation). We would expect from linear theory that the field being modelled perfectly transverse to the shear flow will result in the magnetic tension playing a sub-dominant role especially during the linear growth (Chandrasekhar, 1961). Note this scaling argument does not take into account how tension's importance in λ_{MHD} may vary by introducing magnetic shear. This is known to not only increase the tension's stabilising effect on the KHI, but also breaks the north-south symmetry, complicating the KHI's evolution with secondary processes such as vortex-induced reconnection being triggered earlier in the instabilities lifetime than otherwise expected (Vernisse et al., 2016; Fadanelli et al., 2018; Sisti et al., 2019). Our discussion overall highlights how the different physical effects known to affect the KHI depend on both plasma conditions and evolutionary stage.

Due to the higher-order gradients and non-local Helmholtz decomposition required for the calculation of λ_{MHD}, it cannot simply be applied to current tetrahedral spacecraft missions (e.g., MMS) – however this might change with future missions with more spacecraft such as HelioSwarm (Klein et al., 2023; Zhou and Shen, 2024). For tetrahedral missions, an incompressible version of the hydrodynamic definition λ_ρ is the most advanced definition which can be applied. Virtual satellite data from the simulation suggest that this is a good approximation to λ_{MHD}, better than other simpler techniques. Despite this, there are drawbacks of using these for spacecraft data which are not explored here, such as cold magnetospheric ions making it difficult to measure densities and velocities (Archer et al., 2019). It would be advantageous to make use of only measurements unaffected by such instrumental effects, such as the magnetic field. Cai et al. (2018) did this assuming that magnetic field perturbations were correlated to those in velocity. However, this is not necessarily the case as the frozen-in flux theorem applies to magnetic field lines rather than vectors. In linear MHD wave theory the vector perturbations in magnetic field depend on plasma displacement variations along field-lines (Singer et al., 1981). Recent investigations have also shown that in realistic magnetic geometries, magnetic perturbations can even be oppositely polarised to those of the velocity (Archer et al., 2022). Therefore, care is needed in using other quantities as proxies in these vortex identification methods and ideally a full derivation is required for each.

On the whole, all the different techniques explored are useful for identifying vortices in magnetised fluids, and which technique to use is dependent on the desired purpose. Section 4.2.2 shows that hydrodynamic techniques are valid to use in MHD fluids with varying success. We found that the Q, λ_2, and $\overline{\lambda_2}$ techniques reliably locate broad vortical regions, which provide general information of the shape and location of the large-scale vortex. Alternatively, the λ_ρ, and λ_{MHD} techniques, through incorporating further physical effects, allow them to better hone in on the vortex core specifically instead of the wider vortical region. This result is also echoed when exploring tetrahedral spacecraft applications. There are, however, disadvantages to these techniques. The most obvious is that the rotational axis and orientation of the vortex is not captured by any of the scalar criteria considered, meaning complimentary analysis is needed for this (Liu et al., 2019). Another issue is the sensitivity of the different methods, particularly λ_ρ, and λ_{MHD}, to any vortex threshold chosen–a subject of ongoing studies within hydrodynamics also (e.g., Chakraborty et al., 2005; Pierce et al., 2013; Liu et al., 2019). It is important to note that there is no single proper vortex threshold–especially if strong and weak vortices co-exist. Higher thresholds neglect weaker and smaller-scale vortices, while potentially splitting up larger-scale vortices due to their substructure. On the other hand, lower thresholds smear

out weaker vortices by over saturating the stronger ones and may introduce fine-scale structure, which could be related to turbulence or merely instrument/numerical noise. Consequently, it is suggested that any practical applications of a vortex identification method uses some data-driven threshold, bearing in mind the focus of the study at hand and how the threshold level will affect this.

Extensions to the work presented will further our understanding of the factors important for the formation and detection of KH vortices at the magnetopause. Some of the complex relationships found statistically in this paper, such as the two populations surrounding density gradients, require full 3-dimensional analysis to provide physical insight. Applications to several local MHD runs with different plasma conditions (e.g., Otto, 1990; Nykyri and Otto, 2001; Ma et al., 2014a; b, 2017) may help determine how the relationships presented vary with plasma parameters. Moreover, an application to a global magnetosphere model (e.g., Eggington et al., 2022; Tóth et al., 2005; von Alfthan et al., 2014) would capture more realistic magnetic geometries allowing for a more representative study of the dependencies found here. Finally, applications to real multi-point spacecraft data should be demonstrated. Overall, the vortex identification techniques discussed in this paper have the potential to become useful tools both in simulations and observations, enabling robust detection of events and investigation of the physical effects behind vortex formation, which could certainly complement other current topics of research related to the KHI such as vortex-induced reconnection and cross-scale coupling.

Data availability statement

The datasets presented in this study can be found in online repositories. The names of the repository/repositories and accession number(s) can be found below: https://figshare.com/articles/journal_contribution/Identification_of_Kelvin-Helmholtz_Generated_Vortices_in_Magnetised_Fluids/25640418 Repository name: Figshare.

Author contributions

HK: Conceptualization, Formal Analysis, Investigation, Methodology, Visualization, Writing–original draft, Writing–review and editing. MA: Conceptualization, Investigation, Methodology, Supervision, Writing–review and editing. XM: Conceptualization, Methodology, Writing–review and editing. KN: Conceptualization, Methodology, Writing–review and editing. JE: Writing–review and editing. DS: Writing–review and editing.

Funding

The author(s) declare that financial support was received for the research, authorship, and/or publication of this article. HK was supported by the United Kingdom Research and Innovation (UKRI) Science and Technology Facilities Council (STFC) under studentship ST/W507519/1. MA was supported by UKRI (STFC/EPSRC) Stephen Hawking Fellowship EP/T01735X/1 and UKRI Future Leaders Fellowship MR/X034704/1. JE was supported by UKRI (STFC) grant ST/W001071/1. MA and KN were additionally supported by the International Space Science Institute (ISSI) in Bern, through ISSI International Team project #546 "Magnetohydrodynamic Surface Waves at Earth's Magnetosphere (and Beyond)". XM and NK are supported by NASA 80NSSC23K0899, XM is also supported by NASA 80NSSC20K1279, and DOE DE-SC0022952.

Acknowledgments

Conflict of interest

The authors declare that the research was conducted in the absence of any commercial or financial relationships that could be construed as a potential conflict of interest.

The author(s) declared that they were an editorial board member of Frontiers, at the time of submission. This had no impact on the peer review process and the final decision.

Publisher's note

References

Amerstorfer, U. V., Erkaev, N. V., Taubenschuss, U., and Biernat, H. K. (2010). Influence of a density increase on the evolution of the Kelvin–Helmholtz instability and vortices. *Phys. Plasmas* 17, 072901. doi:10.1063/1.3453705

Archer, M. O., Hartinger, M. D., Plaschke, F., Southwood, D. J., and Rastaetter, L. (2021). Magnetopause ripples going against the flow form azimuthally stationary surface waves. *Nat. Commun.* 12, 5697. doi:10.1038/s41467-021-25923-7

Archer, M. O., Hietala, H., Hartinger, M. D., Plaschke, F., and Angelopoulos, V. (2019). Direct observations of a surface eigenmode of the dayside magnetopause. *Nat. Publ. Group* 10, 615. doi:10.1038/s41467-018-08134-5

Archer, M. O., Southwood, D. J., Hartinger, M. D., Rastaetter, L., and Wright, A. N. (2022). How a realistic magnetosphere alters the polarizations of surface, fast magnetosonic, and Alfvén waves. *J. Geophys. Res. Space Phys.* 127, e2021JA030032. doi:10.1029/2021JA030032

Axford, W. I. (1964). Viscous interaction between the solar wind and the earth's magnetosphere. *Planet. Space Sci.* 12, 45–53. doi:10.1016/0032-0633(64)90067-4

Axford, W. I., and Hines, C. O. (1961). A unifying theory of high-latitude geophysical phenomena and geomagnetic storms. *Can. J. Phys.* 39, 1433–1464. doi:10.1139/p61-172

Brackbill, J. U., and Knoll, D. A. (2001). Transient magnetic reconnection and unstable shear layers. *Phys. Rev. Lett.* 86, 2329–2332. doi:10.1103/PhysRevLett.86.2329

Briard, A., Ripoll, J.-F., Michael, A., Gréa, B.-J., Peyrichon, G., Cosmides, M., et al. (2024). The inviscid incompressible limit of Kelvin–Helmholtz instability for plasmas. *Front. Phys.* 12. doi:10.3389/fphy.2024.1383514

Burch, J. L., Moore, T. E., Torbert, R. B., and Giles, B. L. (2016). Magnetospheric multiscale overview and science objectives. *Space Sci. Rev.* 199, 5–21. doi:10.1007/s11214-015-0164-9

Buzulukova, N., and Tsurutani, B. (2022). Space Weather: from solar origins to risks and hazards evolving in time. *Front. Astronomy Space Sci.* 9. doi:10.3389/fspas.2022.1017103

Cai, D., Lembège, B., Hasegawa, H., and Nishikawa, K.-I. (2018). Identifying 3-D vortex structures at/around the magnetopause using a tetrahedral satellite configuration. *J. Geophys. Res. Space Phys.* 123 (10), 158–10,176. doi:10.1029/2018JA025547

Chakraborty, P., Balachandar, S., and Adrian, R. J. (2005). On the relationships between local vortex identification schemes. *J. Fluid Mech.* 535, 189–214. doi:10.1017/S0022112005004726

Chandrasekhar, S. (1961). "Hydrodynamic and hydromagnetic stability," in *Publication title: international series of monographs on physics ADS bibcode: 1961hhs* (Oxford University Press: bookC).

Chen, L., and Hasegawa, A. (1974). A theory of long-period magnetic pulsations: 2. Impulse excitation of surface eigenmode. *J. Geophys. Res. (1896-1977)* 79, 1033–1037. doi:10.1029/JA079i007p01033

Collado-Vega, Y. M., Kalb, V. L., Sibeck, D. G., Hwang, K.-J., and Rastätter, L. (2018). Data mining for vortices on the Earth's magnetosphere – algorithm application for detection and analysis. *Ann. Geophys.* 36, 1117–1129. Publisher: Copernicus GmbH. doi:10.5194/angeo-36-1117-2018

Cucitore, R., Quadrio, M., and Baron, A. (1999). On the effectiveness and limitations of local criteria for the identification of a vortex. *Eur. J. Mech. - B/Fluids* 18, 261–282. doi:10.1016/S0997-7546(99)80026-0

Dang, T., Lei, J., Zhang, B., Zhang, T., Yao, Z., Lyon, J., et al. (2022). Oxygen ion escape at venus associated with three-dimensional kelvin-helmholtz instability. *Geophys. Res. Lett.* 49, e2021GL096961. doi:10.1029/2021GL096961

De Keyser, J. (2008). Least-squares multi-spacecraft gradient calculation with automatic error estimation. *Ann. Geophys.* 26, 3295–3316. Publisher: Copernicus GmbH. doi:10.5194/angeo-26-3295-2008

Donaldson, K., Olsen, A. J., Paty, C. S., and Caggiano, J. (2024). Characterizing the solar wind-magnetosphere viscous interaction at Uranus and Neptune. *J. Geophys. Res.: Space Phys.* 129, e2024JA032518. doi:10.1029/2024JA032518

Dong, Y., and Tian, W. (2020). On the thresholds of vortex visualisation methods. *Int. J. Comput. Fluid Dyn.* 34, 267–277. doi:10.1080/10618562.2020.1745781

Dungey, J. W. (1961). Interplanetary magnetic field and the auroral zones. *Phys. Rev. Lett.* 6, 47–48. doi:10.1103/PhysRevLett.6.47

Dungey, J. W., and Southwood, D. J. (1970). Ultra low frequency waves in the magnetosphere. *Space Sci. Rev.* 10, 672–688. doi:10.1007/BF00171551

Eggington, J. W. B., Desai, R. T., Mejnertsen, L., Chittenden, J. P., and Eastwood, J. P. (2022). Time-varying magnetopause reconnection during sudden commencement: global MHD simulations. *J. Geophys. Res. Space Phys.* 127, e2021JA030006. doi:10.1029/2021JA030006

Ershkovich, A. I. (1980). Kelvin-Helmholtz instability in type-1 comet tails and associated phenomena. *Space Sci. Rev.* 25, 3–34. doi:10.1007/BF00200796

Escoubet, C. P., Fehringer, M., and Goldstein, M. (2001). English*Introduction*
 the Cluster mission. *Ann. Geophys.* 19, 1197–1200. Publisher: Copernicus GmbH. doi:10.5194/angeo-19-1197-2001

Fadanelli, S., Faganello, M., Califano, F., Cerri, S. S., Pegoraro, F., and Lavraud, B. (2018). North-south asymmetric kelvin-helmholtz instability and induced reconnection at the earth's magnetospheric flanks. *J. Geophys. Res. Space Phys.* 123, 9340–9356. doi:10.1029/2018JA025626

Faganello, M., and Califano, F. (2017). Magnetized Kelvin–Helmholtz instability: theory and simulations in the Earth's magnetosphere context. *J. Plasma Phys.* 83, 535830601. doi:10.1017/S0022377817000770

Faganello, M., Califano, F., Pegoraro, F., and Andreussi, T. (2012). Double mid-latitude dynamical reconnection at the magnetopause: an efficient mechanism allowing solar wind to enter the Earth's magnetosphere. *Europhys. Lett.* 100, 69001. doi:10.1209/0295-5075/100/69001

Faganello, M., Califano, F., Pegoraro, F., and Retinò, A. (2014). Kelvin-Helmholtz vortices and double mid-latitude reconnection at the Earth's magnetopause: comparison between observations and simulations. *Europhys. Lett.* 107, 19001. doi:10.1209/0295-5075/107/19001

Fejer, J. A. (1964). Hydromagnetic stability at a fluid velocity discontinuity between compressible fluids. *Phys. Fluids* 7, 499–503. doi:10.1063/1.1711229

Fujimoto, M., Nakamura, T. K. M., and Hasegawa, H. (2006). Cross-scale coupling within rolled-up MHD-scale vortices and its effect on large scale plasma mixing across the magnetospheric boundary. *Space Sci. Rev.* 122, 3–18. doi:10.1007/s11214-006-7768-z

Fujita, S., Glassmeier, K.-H., and Kamide, K. (1996). MHD waves generated by the Kelvin-Helmholtz instability in a nonuniform magnetosphere. *J. Geophys. Res. Space Phys.* 101, 27317–27325. doi:10.1029/96JA02676

García, K. S., and Hughes, W. J. (2007). Finding the Lyon-Fedder-Mobarry magnetopause: a statistical perspective. *J. Geophys. Res. Space Phys.* 112. doi:10.1029/2006JA012039

Gordeev, E., Facskó, G., Sergeev, V., Honkonen, I., Palmroth, M., Janhunen, P., et al. (2013). Verification of the GUMICS-4 global MHD code using empirical relationships. *J. Geophys. Res. Space Phys.* 118, 3138–3146. doi:10.1002/jgra.50359

Guglielmi, A. V., Potapov, A. S., and Klain, B. I. (2010). Rayleigh-Taylor-Kelvin-Helmholtz combined instability at the magnetopause. *Geomagnetism Aeronomy* 50, 958–962. doi:10.1134/S0016793210080050

Hasegawa, H. (2012). Structure and dynamics of the magnetopause and its boundary layers. *Monogr. Environ. Earth Planets* 1, 71–119. doi:10.5047/meep.2012.00102.0071

Hasegawa, H., Fujimoto, M., Phan, T.-D., Rème, H., Balogh, A., Dunlop, M. W., et al. (2004). Transport of solar wind into Earth's magnetosphere through rolled-up Kelvin–Helmholtz vortices. *Nature* 430, 755–758. doi:10.1038/nature02799

Hasegawa, H., Retinò, A., Vaivads, A., Khotyaintsev, Y., André, M., Nakamura, T. K. M., et al. (2009). Kelvin-Helmholtz waves at the Earth's magnetopause: multiscale development and associated reconnection. *J. Geophys. Res. Space Phys.* 114. doi:10.1029/2009JA014042

Hashimoto, C., and Fujimoto, M. (2006). Kelvin–Helmholtz instability in an unstable layer of finite-thickness. *Adv. Space Res.* 37, 527–531. doi:10.1016/j.asr.2005.06.020

Hunt, J. C. R., Wray, A. A., and Moin, P. (1988). Eddies, streams, and convergence zones in turbulent flows. *NTRS Author Affil. Camb. Univ. Engl. NASA Ames Res. Cent. Stanf. Univ. NTRS Document ID 19890015184 NTRS Res. Cent. Leg. CDMS (CDMS).*

Hwang, K.-J., Dokgo, K., Choi, E., Burch, J. L., Sibeck, D. G., Giles, B. L., et al. (2020). Magnetic reconnection inside a flux rope induced by kelvin-helmholtz vortices. *J. Geophys. Res. Space Phys.* 125, e2019JA027665. doi:10.1029/2019JA027665

Hwang, K.-J., Weygand, J. M., Sibeck, D. G., Burch, J. L., Goldstein, M. L., Escoubet, C. P., et al. (2022). Kelvin-Helmholtz vortices as an interplay of magnetosphere-ionosphere coupling. *Front. Astronomy Space Sci.* 9. doi:10.3389/fspas.2022.895514

Jeong, J., and Hussain, F. (1995). On the identification of a vortex. *J. Fluid Mech.* 285, 69–94. doi:10.1017/S0022112095000462

Kavosi, S., and Raeder, J. (2015). Ubiquity of kelvin–helmholtz waves at earth's magnetopause. *Nat. Commun.* 6, 7019. doi:10.1038/ncomms8019

Kaweeyanun, N., Masters, A., and Jia, X. (2021). Analytical assessment of kelvin-helmholtz instability growth at ganymede's upstream magnetopause. *J. Geophys. Res. Space Phys.* 126, e2021JA029338. doi:10.1029/2021JA029338

Kivelson, M. G., and Chen, S.-H. (1995). "enThe magnetopause: surface waves and instabilities and their possible dynamical consequences," in *Physics of the magnetopause* (American Geophysical Union AGU), 257–268. doi:10.1029/GM090p0257

Kivelson, M. G., and Southwood, D. J. (1988). Hydromagnetic waves and the ionosphere. *Geophys. Res. Lett.* 15, 1271–1274. doi:10.1029/GL015i011p01271

Klein, K. G., Spence, H., Alexandrova, O., Argall, M., Arzamasskiy, L., Bookbinder, J., et al. (2023). Helioswarm: a multipoint, multiscale mission to characterize turbulence. *Space Sci. Rev.* 219, 74. doi:10.1007/s11214-023-01019-0

Lerche, I. (1966). Validity of the hydromagnetic approach in discussing instability of the magnetospheric boundary. *J. Geophys. Res. (1896-1977)* 71, 2365–2371. doi:10.1029/JZ071i009p02365

Liu, C., Gao, Y.-s., Dong, X.-r., Wang, Y.-q., Liu, J.-m., Zhang, Y.-n., et al. (2019). Third generation of vortex identification methods: omega and Liutex/Rortex based systems. *J. Hydrodynamics* 31, 205–223. doi:10.1007/s42241-019-0022-4

Ma, X., Delamere, P., Nykyri, K., Burkholder, B., Eriksson, S., and Liou, Y.-L. (2021). Ion dynamics in the meso-scale 3-d kelvin–helmholtz instability: perspectives from test particle simulations. *Front. Astronomy Space Sci.* 8. doi:10.3389/fspas.2021.758442

Ma, X., Delamere, P., Nykyri, K., Otto, A., Eriksson, S., Chai, L., et al. (2024). Density and magnetic field asymmetric kelvin-helmholtz instability. *J. Geophys. Res. Space Phys.* 129, e2023JA032234. doi:10.1029/2023JA032234

Ma, X., Delamere, P., Otto, A., and Burkholder, B. (2017). Plasma transport driven by the three-dimensional Kelvin-Helmholtz instability. *J. Geophys. Res. Space Phys.* 122 (10), 382–10,395. doi:10.1002/2017JA024394

Ma, X., Nykyri, K., Dimmock, A., and Chu, C. (2020). Statistical study of solar wind, magnetosheath, and magnetotail plasma and field properties: 12+ years of THEMIS observations and MHD simulations. *J. Geophys. Res. Space Phys.* 125, e2020JA028209. doi:10.1029/2020JA028209

Ma, X., Otto, A., and Delamere, P. A. (2014a). Interaction of magnetic reconnection and Kelvin-Helmholtz modes for large magnetic shear: 1. Kelvin-Helmholtz trigger. *J. Geophys. Res. Space Phys.* 119, 781–797. doi:10.1002/2013ja019224

Ma, X., Otto, A., and Delamere, P. A. (2014b). Interaction of magnetic reconnection and kelvin-helmholtz modes for large magnetic shear: 2. Reconnection trigger. *J. Geophys. Res. Space Phys.* 119, 808–820. doi:10.1002/2013ja019225

Masson, A., and Nykyri, K. (2018). Kelvin–Helmholtz instability: lessons learned and ways forward. *Space Sci. Rev.* 214, 71. doi:10.1007/s11214-018-0505-6

Masters, A. (2018). A more viscous-like solar wind interaction with all the giant planets. *Geophys. Res. Lett.* 45, 7320–7329. doi:10.1029/2018GL078416

Masters, A., Achilleos, N., Cutler, J. C., Coates, A. J., Dougherty, M. K., and Jones, G. H. (2012). Surface waves on Saturn's magnetopause. *Planet. Space Sci.* 65, 109–121. doi:10.1016/j.pss.2012.02.007

Michael, A. T., Sorathia, K. A., Merkin, V. G., Nykyri, K., Burkholder, B., Ma, X., et al. (2021). Modeling kelvin-helmholtz instability at the high-latitude boundary layer in a global magnetosphere simulation. *Geophys. Res. Lett.* 48, e2021GL094002. doi:10.1029/2021GL094002

Miura, A. (1987). Simulation of Kelvin-Helmholtz instability at the magnetospheric boundary. *J. Geophys. Res. Space Phys.* 92, 3195–3206. doi:10.1029/JA092iA04p03195

Miura, A. (1990). Kelvin-Helmholtz instability for supersonic shear flow at the magnetospheric boundary. *Geophys. Res. Lett.* 17, 749–752. doi:10.1029/GL017i006p00749

Miura, A. (1992). Kelvin-Helmholtz instability at the magnetospheric boundary: dependence on the magnetosheath sonic Mach number. *J. Geophys. Res. Space Phys.* 97, 10655–10675. doi:10.1029/92JA00791

Miura, A., and Kan, J. R. (1992). Line-tying effects on the Kelvin-Helmholttz instability. *Geophys. Res. Lett.* 19, 1611–1614. doi:10.1029/92GL01448

Miura, A., and Pritchett, P. L. (1982). Nonlocal stability analysis of the MHD Kelvin-Helmholtz instability in a compressible plasma. *J. Geophys. Res. Space Phys.* 87, 7431–7444. doi:10.1029/JA087iA09p07431

Montgomery, J., Ebert, R. W., Allegrini, F., Bagenal, F., Bolton, S. J., DiBraccio, G. A., et al. (2023). Investigating the occurrence of kelvin-helmholtz instabilities at Jupiter's dawn magnetopause. *Geophys. Res. Lett.* 50, e2023GL102921. doi:10.1029/2023GL102921

Moore, T. W., Nykyri, K., and Dimmock, A. P. (2016). Cross-scale energy transport in space plasmas. *Nat. Phys.* 12, 1164–1169. doi:10.1038/nphys3869

Moore, T. W., Nykyri, K., and Dimmock, A. P. (2017). Ion-scale wave properties and enhanced ion heating across the low-latitude boundary layer during kelvin-helmholtz instability. *J. Geophys. Res. Space Phys.* 122 (11), 128–11,153. doi:10.1002/2017JA024591

Nagano, H. (1979). Effect of finite ion larmor radius on the Kelvin-Helmholtz instability of the magnetopause. *Planet. Space Sci.* 27, 881–884. doi:10.1016/0032-0633(79)90013-8

Nakamura, T. K. M., Daughton, W., Karimabadi, H., and Eriksson, S. (2013). Three-dimensional dynamics of vortex-induced reconnection and comparison with THEMIS observations. *J. Geophys. Res. Space Phys.* 118, 5742–5757. doi:10.1002/jgra.50547

Nakamura, T. K. M., Eriksson, S., Hasegawa, H., Zenitani, S., Li, W. Y., Genestreti, K. J., et al. (2017). Mass and energy transfer across the earth's magnetopause caused by vortex-induced reconnection. *J. Geophys. Res. Space Phys.* 122 (11), 505–11,522. doi:10.1002/2017JA024346

Nykyri, K., and Foullon, C. (2013). First magnetic seismology of the CME reconnection outflow layer in the low corona with 2.5-D MHD simulations of the Kelvin-Helmholtz instability. *Geophys. Res. Lett.* 40, 4154–4159. doi:10.1002/grl.50807

Nykyri, K., Ma, X., Dimmock, A., Foullon, C., Otto, A., and Osmane, A. (2017). Influence of velocity fluctuations on the Kelvin-Helmholtz instability and its associated mass transport. *J. Geophys. Res. Space Phys.* 122, 9489–9512. doi:10.1002/2017JA024374

Nykyri, K., Ma, X., and Johnson, J. (2021). *Magnetospheres in the solar system*. Editors R. Maggiolo, N. André, H. Hasegawa, and D. T. Welling, 2, 109–121. doi:10.1002/9781119815624.ch7

Nykyri, K., and Otto, A. (2001). Plasma transport at the magnetospheric boundary due to reconnection in kelvin-helmholtz vortices. *Geophys. Res. Lett.* 28, 3565–3568. doi:10.1029/2001GL013239

Nykyri, K., Otto, A., Lavraud, B., Mouikis, C., Kistler, L. M., Balogh, A., et al. (2006). Cluster observations of reconnection due to the kelvin-helmholtz instability at the dawnside magnetospheric flank. *Ann. Geophys.* 24, 2619–2643. doi:10.5194/angeo-24-2619-2006

Ong, R. S. B., and Roderick, N. (1972). On the kelvin-Helmholtz instability of the Earth's magnetopause. *Planet. Space Sci.* 20, 1–10. doi:10.1016/0032-0633(72)90135-3

Otto, A. (1990). 3D resistive MHD computations of magnetospheric physics. *Comput. Phys. Commun.* 59, 185–195. doi:10.1016/0010-4655(90)90168-Z

Otto, A., and Fairfield, D. H. (2000). Kelvin-Helmholtz instability at the magnetotail boundary: MHD simulation and comparison with Geotail observations. *J. Geophys. Res. Space Phys.* 105, 21175–21190. doi:10.1029/1999JA000312

Palermo, F., Faganello, M., Califano, F., Pegoraro, F., and Le Contel, O. (2011). Compressible kelvin-helmholtz instability in supermagnetosonic regimes: compressible k-h instability in supermagnetosonic regimes. *J. Geophys. Res. Space Phys.* 116. doi:10.1029/2010JA016400

Paral, J., and Rankin, R. (2013). Dawn–dusk asymmetry in the kelvin–helmholtz instability at mercury. *Nat. Commun.* 4, 1645. doi:10.1038/ncomms2676

Paschmann, G., and Daly, P. W. (1998). Analysis Methods for Multi-Spacecraft Data. ISSI Scientific Reports Series SR-001 1.

Pierce, B., Moin, P., and Sayadi, T. (2013). Application of vortex identification schemes to direct numerical simulation data of a transitional boundary layer. *Phys. Fluids* 25, 015102. doi:10.1063/1.4774340

Plaschke, F. (2016). "enULF waves at the magnetopause," in *Low-frequency waves in space plasmas* (American Geophysical Union AGU), 193–212. doi:10.1002/9781119055006.ch12

Plaschke, F., and Glassmeier, K.-H. (2011). Properties of standing Kruskal-Schwarzschild-modes at the magnetopause. *Ann. Geophys.* 29, 1793–1807. Publisher: Copernicus GmbH. doi:10.5194/angeo-29-1793-2011

Plaschke, F., Taylor, M. G. G. T., and Nakamura, R. (2014). Alternative interpretation of results from Kelvin-Helmholtz vortex identification criteria. *Geophys. Res. Lett.* 41, 244–250. doi:10.1002/2013GL058948

Pu, Z.-Y., and Kivelson, M. G. (1983). Kelvin:Helmholtz instability at the magnetopause: solution for compressible plasmas. *J. Geophys. Res. Space Phys.* 88, 841–852. doi:10.1029/JA088iA02p00841

Rice, R. C., Nykyri, K., Ma, X., and Burkholder, B. L. (2022). Characteristics of kelvin–helmholtz waves as observed by the MMS from september 2015 to march 2020. *J. Geophys. Res. Space Phys.* 127, e2021JA029685. doi:10.1029/2021JA029685

Ruhunusiri, S., Halekas, J. S., McFadden, J. P., Connerney, J. E. P., Espley, J. R., Harada, Y., et al. (2016). MAVEN observations of partially developed Kelvin-Helmholtz vortices at Mars. *Geophys. Res. Lett.* 43, 4763–4773. doi:10.1002/2016GL068926

Sen, A. K. (1965). Stability of the magnetospheric boundary. *Planet. Space Sci.* 13, 131–141. doi:10.1016/0032-0633(65)90182-0

Settino, A., Perrone, D., Khotyaintsev, Y. V., Graham, D. B., and Valentini, F. (2021). Kinetic features for the identification of kelvin–helmholtz vortices in *in situ* observations. *Astrophysical J.* 912, 154. Publisher: The American Astronomical Society. doi:10.3847/1538-4357/abf1f5

Singer, H. J., Southwood, D. J., Walker, R. J., and Kivelson, M. G. (1981). Alfven wave resonances in a realistic magnetospheric magnetic field geometry. *J. Geophys. Res. Space Phys.* 86, 4589–4596. doi:10.1029/JA086iA06p04589

Sisti, M., Faganello, M., Califano, F., and Lavraud, B. (2019). Satellite data-based 3-D simulation of kelvin-helmholtz instability and induced magnetic reconnection at the earth's magnetopause. *Geophys. Res. Lett.* 46, 11597–11605. doi:10.1029/2019GL083282

Song, P., Elphic, R. C., and Russell, C. T. (1988). ISEE 1 and 2 observations of the oscillating magnetopause. *Geophys. Res. Lett.* 15, 744–747. doi:10.1029/GL015i008p00744

Southwood, D. J. (1968). The hydromagnetic stability of the magnetospheric boundary. *Planet. Space Sci.* 16, 587–605. doi:10.1016/0032-0633(68)90100-1

Sundberg, T., Boardsen, S. A., Slavin, J. A., Blomberg, L. G., and Korth, H. (2010). The kelvin–helmholtz instability at mercury: an assessment. *Planet. Space Sci.* 58, 1434–1441. doi:10.1016/j.pss.2010.06.008

Takagi, K., Hashimoto, C., Hasegawa, H., Fujimoto, M., and TanDokoro, R. (2006). Kelvin-Helmholtz instability in a magnetotail flank-like geometry: three-dimensional MHD simulations. *J. Geophys. Res. Space Phys.* 111. doi:10.1029/2006JA011631

Tóth, G., Sokolov, I. V., Gombosi, T. I., Chesney, D. R., Clauer, C. R., De Zeeuw, D. L., et al. (2005). Space Weather Modeling Framework: a new tool for the space science community. *J. Geophys. Res. Space Phys.* 110. doi:10.1029/2005JA011126

Tsurutani, B. T., and Thorne, R. M. (1982). Diffusion processes in the magnetopause boundary layer. *Geophys. Res. Lett.* 9, 1247–1250. doi:10.1029/GL009i011p01247

Vernisse, Y., Lavraud, B., Eriksson, S., Gershman, D. J., Dorelli, J., Pollock, C., et al. (2016). Signatures of complex magnetic topologies from multiple reconnection sites induced by Kelvin-Helmholtz instability. *J. Geophys. Res. Space Phys.* 121, 9926–9939. doi:10.1002/2016JA023051

von Alfthan, S., Pokhotelov, D., Kempf, Y., Hoilijoki, S., Honkonen, I., Sandroos, A., et al. (2014). Vlasiator: first global hybrid-Vlasov simulations of Earth's foreshock and magnetosheath. *J. Atmos. Solar-Terrestrial Phys.* 120, 24–35. doi:10.1016/j.jastp.2014.08.012

Walker, A. D. M. (1981). The Kelvin-Helmholtz instability in the low-latitude boundary layer. *Planet. Space Sci.* 29, 1119–1133. doi:10.1016/0032-0633(81)90011-8

Yao, J., and Hussain, F. (2018). Toward vortex identification based on local pressure-minimum criterion in compressible and variable density flows. *J. Fluid Mech.* 850, 5–17. doi:10.1017/jfm.2018.465

Zhang, H., Zong, Q., Connor, H., Delamere, P., Facskó, G., Han, D., et al. (2022). Dayside transient phenomena and their impact on the magnetosphere and ionosphere. *Space Sci. Rev.* 218, 40. doi:10.1007/s11214-021-00865-0

Zhang, Y., Liu, K., Xian, H., and Du, X. (2018). A review of methods for vortex identification in hydroturbines. *Renew. Sustain. Energy Rev.* 81, 1269–1285. doi:10.1016/j.rser.2017.05.058

Zhou, Y., and Shen, C. (2024). Estimating gradients of physical fields in space. *Ann. Geophys.* 42, 17–28. Publisher: Copernicus GmbH. doi:10.5194/angeo-42-17-2024

frontiers | Frontiers in Astronomy and Space Sciences

TYPE Review
PUBLISHED 24 December 2024
DOI 10.3389/fspas.2024.1422341

OPEN ACCESS

EDITED BY
David Knudsen,
University of Calgary, Canada

REVIEWED BY
Vladimir Krasnoselskikh,
UMR7328 Laboratoire de Physique et Chimie de l'Environnement et de l'Espace (LPC2E), France
R. S. Pandey,
Amity University, India

*CORRESPONDENCE
M. W. Dunlop,
malcolm.dunlop@stfc.ac.uk

RECEIVED 23 April 2024
ACCEPTED 05 December 2024
PUBLISHED 24 December 2024

CITATION
Dunlop MW, Fu H-S, Shen C, Tan X, Dong X-C, Yang Y-Y, Robert P and Escoubet CP (2024) Curlometer and gradient techniques: past and future applications.
Front. Astron. Space Sci. 11:1422341.
doi: 10.3389/fspas.2024.1422341

Curlometer and gradient techniques: past and future applications

M. W. Dunlop[1,2]*, H.-S. Fu[1], C. Shen[3], X. Tan[1], X.-C. Dong[4], Y.-Y. Yang[5], P. Robert[6] and C. P. Escoubet[7]

[1]School of Space and Earth Sciences, Beihang University, Beijing, China, [2]Rutherford Appleton Laboratory Space, Science and Technology Facilities Council, Didcot, United Kingdom, [3]School of Science, Harbin Institute of Technology, Shenzhen, China, [4]Department of Geophysics, Yunnan University, Kumning, China, [5]National Institute of Natural Hazards, Ministry of Emergency Management of China, Beijing, China, [6]Laboratoire de Physique des Plasmas, Ecole Polytechnique, Palaiseau, France, [7]European Space Agency/European Space Research and Technology Centre, Noordwijk, Netherlands

We review the range of applications and use of multi spacecraft techniques, applicable to close formation arrays of spacecraft, focusing on spatial gradient based methods, and the curlometer in particular. The curlometer was originally applied to Cluster multi-spacecraft magnetic field data, but later was updated for different environments and measurement constraints such as the NASA MMS mission, small-scale formation of 4 spacecraft; the 3 spacecraft configurations of the NASA THEMIS mision, and derived 2-4 point measurements from the ESA Swarm mission. In general, spatial gradient based methods are adaptable to a range of multi-point and multi-scale arrays. We also review the range of other techniques based on the computation of magnetic field gradients and magnetic field topology in general, including: magnetic rotation analysis and various least squares approaches. We review Taylor expansion methodology (FOTE), in particular, which has also been applied to both Cluster and MMS constellations, as well as interpretation of simulations. Four-point estimates of magnetic gradients are limited by uncertainties in spacecraft separations and the magnetic field, as well as the presence of non-linear gradients and temporal evolution. Nevertheless, the techniques can be reliable in many magnetospheric regions where time stationarity is largely applicable, or when properties of the morphology can be assumed (for example, the expected orientation of underlying large-scale structure). Many magnetospheric regions have been investigated directly (illustrated here by the magnetopause, ring current and field-aligned currents at high and low altitudes), and options for variable numbers of spacecraft have been considered. The comparative use of plasma measurements and possible new methodology for arrays of spacecraft greater than four are also considered briefly.

KEYWORDS

curlometer analysis, multi-spacecraft, analysis methods, magnetosphere, magnetic gradients and reconstruction

1 Introduction

The four Cluster II spacecraft (Escoubet et al., 2001) allowed 3-D structure and temporal evolution to be probed through the development of multi-spacecraft techniques for the first

time. These techniques specifically allow spatial gradients of key quantities to be analyzed, typically through first order approximations, or Taylor expansion around measurement points (e.g., Fu et al., 2015). Such analysis was first described in a book on collected multi-spacecraft analysis techniques in 1998 (Paschmann and Daly, 1998). The application of these multi-spacecraft methods was updated in (Paschmann and Daly, 2008), where here we focus on magnetic gradients and specifically magnetic currents (e.g., Dunlop and Eastwood, 2008; Shen and Dunlop, 2008; Vogt et al., 2008). The operation of Cluster provided a spacecraft configuration which maintained a quasi-tetrahedral formation for much of its life and Cluster is still the only space physics mission to provide fully four-point coverage over a large spatial range of scales; over a time epoch of two solar cycles (see Dunlop et al., 2021b; Escoubet et al., 2021).

The methodology, covering a wide range of analysis techniques, has been continuously developed to determine key quantities and investigate a large number of phenomena and has been applied to other missions in the 22 years since then (such as MMS, THEMIS and Swarm). The Magnetospheric Multi-Scale (MMS) mission maintained a close four spacecraft configuration on smaller separation scales (a few *km*) than Cluster for much of its orbit (Burch et al., 2016), while during extended operations (Angelopoulos, 2008), some of the NASA THEMIS spacecraft flew in a 3-spacecraft configuration in the magnetosphere and the ESA Swarm low orbit (LEO) polar mission provided both 2 and 3 spacecraft measurements in close formations (Friis-Christensen et al., 2008) on meso-scales (~100 *km*).

The future interest in multi-spacecraft methods remains strong; particularly in their development to make best use of planned larger arrays of spacecraft capable of probing multiscale phenomena, e.g., Plasma Observatory (Retinò et al., 2022), AME (Dai et al., 2020) and Helioswarm (Klein et al., 2023).

2 The curlometer and basic concepts

2.1 Integral method

The application of the curlometer to Cluster data was reviewed by Dunlop and Eastwood (2008). More recently, its adaption to the context of the high altitude ionosphere, focusing on the determination of field-aligned currents (FAC) was covered by Dunlop et al. (2020) and Trenchi et al. (2020) [see other papers in the ISSI book on ionospheric multi-spacecraft data analysis tools (Dunlop and Lühr, 2020)]. The method has also been reviewed by (Dunlop et al., 2018; Dunlop et al., 2021a; Dunlop et al., 2021b), and was surveyed by Robert and Dunlop (2022), and its application to the Earth's ring current region has also been recently analysed in the context of MMS data (Tan et al., 2023), who also addressed its accuracy in different regimes. The Cluster Science archive (http://www.cosmos.esa.int/web/csa/software) contains method implementations also in the technical note by Middleton and Masson (2016).

The calculation uses the integral form of Ampère's law, i.e., $\mu_0 \boldsymbol{J} = \mathbf{curl}(\boldsymbol{B})$ neglecting the displacement current ($\mu_0 \varepsilon_0 \partial \boldsymbol{E}/\partial t$) for high electrical conductivity (Russell et al., 2016), where $\boldsymbol{B}$ and $\boldsymbol{E}$ are the magnetic and electric fields and $\boldsymbol{J}$ is the current density. The technique (Dunlop et al., 1988; Robert et al., 1998a) combines four, non-planar spatial positions to make a linear estimate of the electric current density, i.e., $\mu_0 <\boldsymbol{J}> .\left(\Delta \boldsymbol{R}_i \Delta \boldsymbol{R}_j\right) = \Delta \boldsymbol{B}_i . \Delta \boldsymbol{R}_j - \Delta \boldsymbol{B}_j . \Delta \boldsymbol{R}_i$, where $\Delta \boldsymbol{B}_i$, $\Delta \boldsymbol{R}_i$ are the differences in the measured magnetic field at positions (i, j) to a reference spacecraft, giving a rugged and simple formalism (see also Section 2.2). The current density normal to each face of the spacecraft tetrahedral configuration is represented by the terms on the left-hand side of the equation. One of the four normal components is redundant and can be used to check stability of the estimate (Dunlop et al., 2018; Dunlop et al., 2020), by choosing different faces in the estimate of $\boldsymbol{J}$. For irregular spacecraft configurations, this also allows some flexibility to choose which face gives the best estimate of a component, where the relative alignment of the spacecraft configuration to the local field geometry is significant and often only one face determines a stable $\boldsymbol{J}$ component (see also the methodology in Vogt et al., 2009; Shen et al., 2012b).

A partial estimate of one component can still provide useful information if the large-scale current orientation is assumed, such as for FACs and in the case of the *in situ* ring current, where the azimuth component is significant (Zhang et al., 2011). For example, the three magnetospheric THEMIS spacecraft (Yang et al., 2016) can be used as shown in the left panel of Figure 1 in the ring current, but these assumptions can severely limit the stability of the estimates (Tan et al., 2023), and indeed the need to project the normal component into the ring plane means assumptions on the form of the large-scale currents are critical. The right-hand panel in Figure 1, illustrates that Swarm close configurations can also be used for partial and full current estimates with assumptions on the stationarity of the currents (over a few seconds) and that the field-aligned component is dominant or force-free (Shen et al., 2012a; Ritter et al., 2013; Vogt et al., 2013; Dunlop et al., 2015b, references in Dunlop and Lühr, 2020).

The right-hand side of Figure 1 illustrates the adaption in Dunlop et al. (2015b), where adjacent positions are used to form at least four points in space. As with the standard form of the curlometer, the convection time across the array is the relevant temporal scale for the estimates. In the case of Swarm this is typically 5–10 s for separation scales of around 100–150 km for the Swarm A,C pair of spacecraft, which fly side by side in near circular, polar orbits (~500 km altitude). Swarm B flies at a slightly higher altitude in an orbit but is only in alignment at specific times during the mission. In the special close configuration shown in Figure 1, a series of values can be made from different combinations of the five points (A,B,C,A',C'), providing information on any temporal changes as well as comparative estimates. For resolving the FAC component ACA'C' provides a vertical component of J (Ritter et al., 2013). The configuration ABC provides simultaneous measurements, but suffers from the fact that the plane is not well aligned to the FACs.

Although generally robust, the relative structure scales applying affect the validity range of the estimates. For Cluster separations (>100 km), the dominant error arises from nonlinear gradients, while at MMS separations (~5–10 km) measurement uncertainties can be important [typically these affect the estimate below a threshold |J| (Dunlop et al., 2018), i.e., for the small MMS tetrahedron scales (a few km), measurement uncertainty (~0.1 nT in B; ~100 m for R and millisecond timing) drives the error unless the current density is greater than several nAm^{-2}]. Both Runov et al. (2005) and Forsyth et al. (2011), for example, have examined the effect of the characteristic scale of current structures

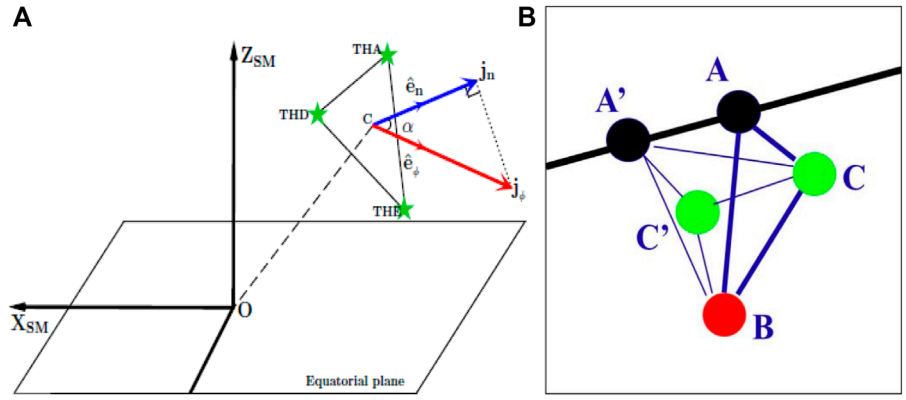

FIGURE 1
A configuration of the three THEMIS spacecraft in the ring current [from Yang et al. (2016), **(A)**], where the current density normal to the THEMIS plane can be projected into Jϕ direction as shown, and a configuration of the three Swarm spacecraft (A,B,C) with adjacent positions (A',C') taken from a few seconds earlier **(B)**.

on the use of quality estimates and indeed Tan et al. (2023) have compared MMS to Cluster results, which sample on distinct large and small spatial scales in the ring current. The linear estimator Q = |divB|/|curl(B)| has been used extensively as an indirect quality parameter (Robert et al., 1998a; Haaland et al., 2004b), along with the constellation shape (elongation and planarity) as discussed in more detail in Section 2.2. The linear estimate of the average value of divB over the volume of the tetrahedron is an integral part of the method and is given by $<div(\boldsymbol{B})>\left|\Delta \boldsymbol{R}_i.\Delta \boldsymbol{R}_{\hat{j}}\Delta \boldsymbol{R}_k\right| = \left|\sum_{cyclic}\Delta \boldsymbol{B}_i.\Delta \boldsymbol{R}_{\hat{j}}\Delta \boldsymbol{R}_k\right|$,

$$\text{e.g. } <div(\boldsymbol{B})>_{1234}\left(\Delta \boldsymbol{R}_{12}\cdot\Delta \boldsymbol{R}_{13}\wedge\Delta \boldsymbol{R}_{14}\right) = \Delta \boldsymbol{B}_{12}\cdot\Delta \boldsymbol{R}_{13}\wedge\Delta \boldsymbol{R}_{14} + \Delta \boldsymbol{B}_{13}\cdot \Delta \boldsymbol{R}_{14}\wedge\Delta \boldsymbol{R}_{12} + \Delta \boldsymbol{B}_{14}\cdot\Delta \boldsymbol{R}_{12}\wedge\Delta \boldsymbol{R}_{13}.$$

This full combination of the four positions are needed for Q to be used which is found unreliable if the spacecraft configuration is highly irregular and not well aligned to the background magnetic field structure. The estimate of Q has also been used in qualification of the FOTE (First-Order Taylor Expansion) method (see Section 2.3).

In the magnetosphere, the effect of dipole non-linear gradients, not associated with current density [first noted in Dunlop et al. (2002), while Grimald et al. (2012) considered this in the context of the ring current], can be minimised by subtracting the dipole (or IGRF) field from the measured magnetic field to give magnetic residuals, e.g., for studies of the *in situ* ring current (Yang et al., 2016), where dipole gradients are significant and at low altitude orbits (LEO) where the formation of magnetic residuals is normal practice, particularly for Swarm (Ritter et al., 2013; Dunlop et al., 2020).

2.2 The influence of elongation, planarity and Q: the limiting case

At the mesoscales of Cluster separations, the accuracy of the curlometer estimate primarily depends on how the neglected non-linear gradients contribute in the context of the spacecraft constellation, i.e., its scale, shape (irregularity) and relative orientation to the measured current structure. This is also true at smaller separation scales (e.g., for MMS) but then measurement errors (in the magnetic field, position and timing) also become significant. For Cluster, therefore, the spatial sampling through the constellation shape was considered. To characterize the shape using the three eigenvalues of the volumetric tensor **R** are $\mathbf{W}_1$, $\mathbf{W}_2$, $\mathbf{W}_3$ (in order of magnitude, i.e., $\mathbf{W}_1 > \mathbf{W}_2 > \mathbf{W}_3$) the square roots a, b, and c are used to define: elongation $E = 1-(b/a)$ and planarity $P = 1-(c/b)$. These parameters can be used to check the degree of irregularity of the tetrahedral shape, so that they complement the value of Q, since this because a poor indicator for irregular tretrahedral shape.

In terms of the curlometer approximation, whether the method is used on three magnetospheric spacecraft from the THEMIS mission, or the tetrahedral constellations of MMS and Cluster, current density components are calculated starting from a single plane formed by 3 spacecraft. We therefore need to calculate, to first order, the closed integral (Equation 1) of the magnetic field and divide it by the area of the triangle formed by 3 spacecraft (see also discussion of the integral forms in Section 2.3).

$$\mu_0 J_{av} = \frac{\oint \vec{B}\bullet d\vec{s}}{S} \tag{1}$$

Under the condition of limited observation data, we calculate the integral of the magnetic field, and the area of the triangle formed by three positions, from the following Equations 2, 3 (as written above in condensed notation).

$$\oint_{123}\vec{B}\bullet d\vec{s} \approx \left(\frac{\vec{B_1}+\vec{B_2}}{2}\right)\bullet(\vec{r_2}-\vec{r_1}) + \left(\frac{\vec{B_2}+\vec{B_3}}{2}\right)\bullet(\vec{r_3}-\vec{r_2}) + \left(\frac{\vec{B_3}+\vec{B_1}}{2}\right)\bullet(\vec{r_1}-\vec{r_3}) \tag{2}$$

$$S_{123} = \left|\frac{(\vec{r_2}-\vec{r_1})\times(\vec{r_3}-\vec{r_1})}{2}\right| = \left|\frac{(\vec{r_3}-\vec{r_{21}})\times(\vec{r_1}-\vec{r_2})}{2}\right| = \left|\frac{(\vec{r_1}-\vec{r_3})\times(\vec{r_2}-\vec{r_3})}{2}\right| \tag{3}$$

In the limiting case, the three spacecraft are collinear. Suppose that spacecraft 3 is between 1 and 2, with a distance t from 1 and a distance 1-t from 2.

$$\vec{\boldsymbol{B}_3} = (1-t)\vec{\boldsymbol{B}_1} + t\vec{\boldsymbol{B}_2} + \vec{\Delta \boldsymbol{B}} \tag{4}$$

$$\left(\vec{\boldsymbol{r}_1} - \vec{\boldsymbol{r}_3}\right) = t\left(\vec{\boldsymbol{r}_1} - \vec{\boldsymbol{r}_2}\right) \tag{5}$$

$$\left(\vec{\boldsymbol{r}_3} - \vec{\boldsymbol{r}_2}\right) = (1-t)\left(\vec{\boldsymbol{r}_1} - \vec{\boldsymbol{r}_2}\right) \tag{6}$$

$\vec{\Delta \boldsymbol{B}}$ in Equation 4 is the non-linearity term, but it could have contributions from the nonlinearity of the magnetic field, measurement errors of magnetometer, differences between the measurement at each spacecraft and time-varying error introduced by time interpolation. Putting Equations 4–6 to Equation 2, we get Equation 7

$$\oint_{123} \vec{\boldsymbol{B}} \bullet d\vec{s} \approx \left(\vec{\Delta \boldsymbol{B}}/2\right) \bullet \left(\vec{\boldsymbol{r}_1} - \vec{\boldsymbol{r}_2}\right) \tag{7}$$

If $\vec{\Delta \boldsymbol{B}}$ is not zero, which is almost certain, then in this limiting case the integral of the magnetic field is not zero, while the area of the triangle formed by the three spacecraft is exactly zero; producing an infinite current error. Thus, when the 3 spacecraft are collinear, the actual current density cannot be obtained. Even if the three are not collinear, the calculated current density will increase dramatically as they approach the collinear position. Because of the nonlinear term, the area approaches zero faster than the curve integral approaches zero. Estimating accurate error is limited by the difficulty of obtaining the exact nonlinear term, however, future work will attempt to quantify this. It should also be noted that the parameter Q cannot be well used in this limit, because *curB* becomes infinite but not *divB*. Thus, Q will remain a very low value and lose its expected function. In past analysis, therefore, the Elongation for a triangle has been used to gain an empirical reliability and exclude bad results. In other words, only those calculation results meeting a certain Elongation condition (e.g., less than 0.8) can be trusted.

For the case of the full four spacecraft tetrahedral configurations (as for MMS and Cluster), a further step is needed as three current density components are obtained from three of the four planes in a tetrahedron. The current density vector is then obtained by solving equations (as indicated above). Using subscripts 1, 2, and 3 to represent the average current density J and the normal direction N of the three planes, respectively.

$$\begin{cases} N_{1x}J_x + N_{1y}J_y + N_{1z}J_z = J_1 \\ N_{2x}J_x + N_{2y}J_y + N_{2z}J_z = J_2 \\ N_{3x}J_x + N_{3y}J_y + N_{3z}J_z = J_3 \end{cases} \tag{8}$$

By denoting $N = \begin{bmatrix} N_{1x} & N_{1y} & N_{1z} \\ N_{2x} & N_{2y} & N_{2z} \\ N_{3x} & N_{3y} & N_{3z} \end{bmatrix}, J_{xyz} = \begin{bmatrix} J_x \\ J_y \\ J_z \end{bmatrix}, J_{123} = \begin{bmatrix} J_1 \\ J_2 \\ J_3 \end{bmatrix}$, then Equation 8 is reduced to Equation 9. And Jxyz is obtained (Equation 10).

$$NJ_{xyz} = J_{123} \tag{9}$$

$$J_{xyz} = N^{-1}J_{123} \tag{10}$$

The calculation process is actually naturally stable because of the closure of the equations for a sampled volume through Ampères law, and in addition the fourth face of the tetrahedron provides a check on the estimates. Nevertheless, if matrix N is not well-conditioned (i.e., ill-conditioned or near singular), we cannot get the true current (as will occur if the constellation is near planar). As mentioned earlier, the matrix N is made up of normal vectors on three planes, and the most likely (or perhaps the only) factor for poor quality is that some normal vectors are closely to be parallel. The effect on Q in this case is not well understood, but further work is expected to clarify this through specific analysis in the future. Currently, we can conservatively choose to trust the results obtained by the tetrahedral configuration with better non-coplanar conditions. This condition has been evaluated in the past through the added use of the Planarity, i.e., typically limiting this also below 0.8 (In practice, both parameters are combined into a quality index as the square route of the sum of the squares of E and P with this value <0.8, typically).

When using the curlometer method, careful attention to the configuration parameters of the constellation must be paid, therefore, due to the existence of these factors (arising from the neglected nonlinearity of the physical quantities). Tailored analysis of specific events can reduce the risk of calculation anomalies and in the case of large amounts of data can be statistically processed. Clearly, sampling by more spacecraft (and more than four spacecraft in particular) can help stabilize the estimate through alternative choice of the planes and by selection of particular tetrahedra within the constellation, but then the tracking of the more complex constellations requires more management. This and the use of the quality indicators, have been considered, for example, for new, proposed constellation mission operations, such as Plasma Observatory (Retinò et al., 2022) and Helioswarm (Klein et al., 2023).

2.3 Advanced integral theorems: geometrical approach

The curlometer method rests on the ability to estimate linear gradients in the measured quantities (specifically the magnetic field) between spacecraft positions. Apart from the linear interpolation method (Chanteur and Harvey, 1998) and the least-squares method (Harvey, 1998), the geometrical method (integral theorems), introduced above is the third way to obtain general estimators of the linear gradients of physical quantities. Recently, Shen and Dunlop (2023) have made full use of a geometrical method (summarized below in Equations 11–26) to derive the gradient, divergence, and curl of physical quantities with the integral theorems. Furthermore, this geometrical method has the special advantage to easily derive the field gradients for observations made by a planar constellation. The errors in the estimators of the linear gradients from the geometrical method were found to enter at second-order and it was illustrated that the method based on integral theorems are equivalent to the spatial interpolation method (Chanteur, 1998; Chanteur and Harvey, 1998; Vogt et al., 2009) and the least-squares method (Harvey, 1998; De Keyser, 2008; Hamrin et al., 2008) for deriving linear gradients.

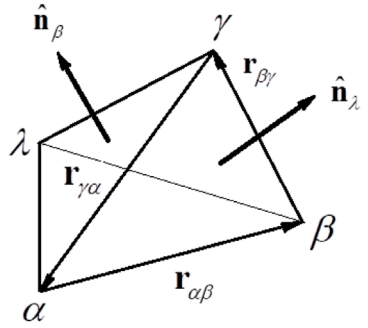

FIGURE 2
Demonstration of the constellation tetrahedron (Shen and Dunlop, 2023).

In Figure 2 the position vectors of the four spacecraft in a tetrahedral configuration are $\mathrm{r}_\alpha(\alpha = 1,2,3,4)$. The barycenter coordinates are chosen as $\mathbf{r}_c \equiv \frac{1}{N}\sum_{\alpha=1}^{N}\mathbf{r}_\alpha = 0$. The spacecraft α, β, and γ constitute a face triangle as discussed earlier $\Delta_{\alpha\beta\gamma}$, where the vertex opposite to this is λ, as shown in Figure 2. The three vertices α, β, and γ of the face $\Delta_{\alpha\beta\gamma}$ are defined to rotate anticlockwise around its normal $\hat{\mathbf{n}}_\lambda$. In this notation, the vector area of the face $\Delta_{\alpha\beta\gamma}$ of the tetrahedron is

$$\mathbf{S}_\lambda = \mathbf{S}_{\alpha\beta\gamma} = \frac{1}{2}\mathbf{r}_{\alpha\beta}\times\mathbf{r}_{\beta\gamma} = \frac{1}{2}\left|\mathbf{r}_{\alpha\beta}\times\mathbf{r}_{\beta\gamma}\right|\hat{\mathbf{n}}_\lambda \tag{11}$$

The volume of the tetrahedron is

$$V = -\frac{1}{6}r_{\beta\alpha}\cdot\left(r_{\beta\lambda}\times r_{\beta\gamma}\right) \tag{12}$$

For a certain arbitrary scalar field f, vector field $\mathbf{u}$ and tensor field $\mathbf{T}$, the αth satellite of the constellation yields the scalar field f_α, vector field $\mathbf{u}_\alpha$ and tensor field $\mathbf{T}_\alpha$. The scalar field f, vector field $\mathbf{u}$ and tensor field $\mathbf{T}$ obey the following integral theorems (Bittencourt, 2004):

$$\int_V \nabla f \mathrm{d}V = \oint_s f\mathrm{d}\mathbf{S} \tag{13}$$

$$\int_V \nabla\mathbf{u}\mathrm{d}V = \oint_S \mathrm{d}\mathbf{S}\,\mathbf{u} \tag{14}$$

$$\int_V \nabla\cdot\mathbf{u}dV = \oint_S \mathbf{u}\cdot d\mathbf{S} \tag{15}$$

$$\int_V \nabla\times\mathbf{u}dV = \oint_S d\mathbf{S}\times\mathbf{u} \tag{16}$$

$$\int_V \nabla\cdot\mathbf{T}\mathrm{d}V = \oint_S \mathrm{d}\mathbf{S}\cdot\mathbf{T} \tag{17}$$

Starting from these integral theorems, Shen and Dunlop (2023) have obtained the estimators of the gradients of a scalar field f, vector field $\mathbf{u}$ and tensor field $\mathbf{T}$, as well as the curl and divergence of the vector field $\mathbf{u}$, respectively, as below:

$$\langle\nabla f\rangle = -\frac{1}{3V}\sum_{\lambda=1}^{4} f_\lambda\mathbf{S}_\lambda \tag{18}$$

$$\langle\nabla\mathbf{u}\rangle = -\frac{1}{3V}\sum_{\lambda=1}^{4}\mathbf{S}_\lambda\mathbf{u}_\lambda \tag{19}$$

$$\langle\nabla\cdot\mathbf{T}\rangle = -\frac{1}{3V}\sum_{\lambda=1}^{4}\mathbf{S}_\lambda\cdot\mathbf{T}_\lambda \tag{20}$$

$$\langle\nabla\times\mathbf{u}\rangle = -\frac{1}{3V}\sum_{\lambda=1}^{4}\mathbf{S}_\lambda\times\mathbf{u}_\lambda \tag{21}$$

$$\langle\nabla\cdot\mathbf{u}\rangle = -\frac{1}{3V}\sum_{\lambda=1}^{4}\mathbf{S}_\lambda\cdot\mathbf{u}_\lambda \tag{22}$$

Considering the reciprocal vector $\mathbf{k}_\alpha$ as defined by Chanteur (1998)

$$\mathbf{k}_\alpha = \frac{\mathbf{r}_{\beta\lambda}\times\mathbf{r}_{\beta\gamma}}{\mathbf{r}_{\beta\alpha}\cdot\left(\mathbf{r}_{\beta\lambda}\times\mathbf{r}_{\beta\gamma}\right)} = -\frac{1}{3V}\mathbf{S}_\alpha \tag{23}$$

then the above estimators are identical to those from the interpolation method (Chanteur, 1998).

The integral theorems method, however, has one special advantage, it can easily derive the field gradients for measurements from a planar constellation [e.g., as for the three-spacecraft THEMIS (Friis-Christensen et al., 2006) or Swarm (Angelopoulos, 2009) configurations].

By using the following integral theorem applied to the triangle $\Delta_{\alpha\beta\gamma}$:

$$\oint_C \phi d\mathbf{l} = \int_S d\mathbf{S}\times\nabla\phi \tag{24}$$

the averaged gradient of the scalar field in the plane of the constellation is readily derived as the following formula (Shen and Dunlop, 2023)

$$\langle\nabla\phi\rangle_\perp = -\frac{1}{2S_{\alpha\beta\gamma}}\phi_{\{\alpha}\mathbf{r}_{\beta\gamma\}}\times\hat{\mathbf{n}} \tag{25}$$

Similarly, for a vector field $\mathbf{u}$, its averaged gradient of the scalar field in the plane of the constellation is

$$\langle\nabla\mathbf{u}\rangle_\perp = -\frac{1}{2S_{\alpha\beta\gamma}}\mathbf{u}_{\{\alpha}\mathbf{r}_{\beta\gamma\}}\times\hat{\mathbf{n}} \tag{26}$$

A rigid error analysis has been made for this geometric approach based on Taylor expansion (Shen and Dunlop, 2023). It is verified that the truncation error of the method is at the order of $(L/D)^2$, where L is the characteristic size of the constellation tetrahedron (Robert et al., 1998b) and D is the length scale of the field structure measured. It is found that the truncation error for deriving the linear gradient with the four point measurements by Cluster and MMS is actually very small and Cluster (Escoubet et al., 1997; Escoubet et al., 2001), THEMIS (Angelopoulos, 2009) and MMS (Burch et al., 2016) are generally able to yield stable estimates of current density, charge density, curvature of magnetic field lines, and other related parameters (Shen et al., 2003; Haaland et al., 2021; Pitout and Bogdanova, 2021; Shen et al., 2021b; Robert and Dunlop, 2022).

3 Magnetic gradients and topology

The gradient and curvature terms in the dyadic of the magnetic field, B, can be linearly estimated (Chanteur, 1998; Harvey, 1998; Shen and Dunlop, 2008; Vogt et al., 2008; Shen et al., 2012a; Shen et al., 2012b), from which the current density can be obtained.

Key methodology includes magnetic curvature and rotation analysis (Shen et al., 2007; Shen et al., 2012a); least squares analysis of planar reciprocal vectors (De Keyser et al., 2007; Hamrin et al., 2008; Vogt et al., 2009; Vogt et al., 2013), and a range of techniques related to Taylor expansion around the measurement points (FOTE method, see Section 3.3). Estimates based on these gradient methods basically depend on both the integrity of the spacecraft array and stationary properties (temporal dependence) of the magnetic structures, although additional constraints or assumptions can be incorporated. More recently, the polynomial reconstruction of the magnetic field topology has been explored using MMS data by Denton et al. (2020), Denton et al. (2022).

3.1 Magnetic rotation analysis applications

In addition to estimating direct gradients, Magnetic Curvature Analysis (MCA) (Shen et al., 2003) and Magnetic Rotation Analysis (MRA) (Shen et al., 2007) give the 3-D topology of the magnetic field (curvature radius, normal direction and binormal direction of the magnetic field-lines). Particular results have been obtained in the magnetotail current sheet (Shen et al., 2008a; Shen et al., 2008b; Rong et al., 2011); the Earth's ring current (Shen et al., 2014); flux ropes and plasmoids (Zhang et al., 2013; Yang et al., 2014); reconnection regions (Lavraud et al., 2016; Zhang et al., 2016), and in the cusp and at the magnetopause (Shen et al., 2011; Xiao et al., 2018).

The curvature of field-lines (from MCA) from Cluster located within the ring current are shown on the left-hand side of Figure 3, which indicates current strength in a complimentary manner to the magnetic gradient based J calculation. The plot shows a decrease in relative curvature, which implies a growth of the implied current density which is related to increasing geomagnetic activity (e.g., SYM-H). There is also a dawn-dusk asymmetry, which is most apparent at lower activity levels. The right-hand side of Figure 3 shows that the method can resolve the form of the tail current sheet in terms of different current sheet geometry. As discussed by Rong et al. (2011) these can be classified as: normal, flattened and tilted. These distinct geometries result from the combined MCA/MRA methodology, where the key properties of curvature radius, normal direction and binormal direction are extracted to inform the sheet characteristics controlling current sheet dynamics.

3.2 Least-squares methods for multi-point gradient computation

Typically, instruments record multiple data points in the convection time needed to cover a comparable distance to the separation scales, which in principle carry information relevant for calculation of the gradient, as was already noted by Harvey (1998). This is particularly true if a certain degree of time invariance in the structures of interest can be assumed. The Gradient Analysis by Least-Squares (GALS) technique (Hamrin et al., 2008) and the Least-Squares Gradient Calculation (LSGC) technique (De Keyser et al., 2007; De Keyser, 2008) apply these ideas. The latter is based on least squares gradient calculation by approximating the measured quantity (scalar or vector) through Taylor series expansion around the measurement reference point (typically the barycenter). This expansion describes the magnetic field, for example, its spatial and temporal gradients and non-linear terms at higher-order. An assumption that the gradients are constant on certain spatial scales, allows higher-order terms to be estimated. It follows that, in practice, an iterative, weighted least-squares, procedure can be devised.

The method can provide error estimates on the results. As in the case of the curlometer, these reflect errors in both the measurement and non-linear behaviour, (to simplify, uncorrelated measurement errors as well as homogeneity parameters can be assumed for all three components). The property that divB = 0, that the parallel magnetic field gradient is zero, or static structures can be added as constraints. An important application of a higher number of spacecraft is in error control. Although other numbers of measurement points can be used, quality of the results depends on the measurement errors.

It is worth also noting here that the conventional ways to calculate the gradient involve the calculating of the inverse of volume tensor (e.g., Chanteur, 1998; Harvey, 1998; Shen et al., 2003; Shen et al., 2007). The volume tensor would become an ill-conditioned matrix, however, when Cluster tetrahedron becomes an irregular shape, e.g., plane-like or line-like, so that the direct calculation of the inverse of volume tensor would yield significant error and gradient cannot be correctly calculated in this case.

Shen et al. (2012b) avoided the problem of irregular shaped configurations of spacecraft, by introducing a procedure where transforming coordinates into the eigenvector space of volume tensor allows the gradient to be universally calculated. The gradient calculation can involve the inverse of volume tensor (e.g., Chanteur, 1998; Harvey, 1998; Shen et al., 2003; Shen et al., 2007), which is problematic for very irregular shapes. A bonus of the approach of Shen et al. (2012b) is that it can be applied to three-point magnetic field observations (e.g., as in the case of THEMIS), to give current density and the vorticity of plasma flow, and to three-point plasma measurement for the vorticity of K-H waves (as for Cluster).

3.3 FOTE methods and applications: local Taylor expansion

The FOTE method is based on the Jacobian matrix δB, which is a 3 × 3 real matrix $\delta B_{ij} = \partial B_i/\partial r_j$. With four-point measurements of magnetic fields, ∂B_i and ∂r_j can be easily obtained. Theoretically, such matrix has three eigenvectors, e_1, e_2, e_3, and correspondingly three eigenvalues, λ_1, λ_2, λ_3. The sum of these three eigenvalues is zero ($\lambda 1+\lambda 2+\lambda 3 \equiv \nabla \cdot B = 0$), because the magnetic field is "non-divergent." This implies that either all the eigenvalues are real or one is real while the two others are conjugate complex (Fu et al., 2015; Fu et al., 2020).

The immediate application of the FOTE method is to find magnetic nulls (particularly in regions containing magnetic reconnection X-lines); complementing the analysis based on the use of the Poincare index (Xiao et al., 2006; Xiao et al., 2007) and field line reconstruction methods (He et al., 2008a; He et al.,

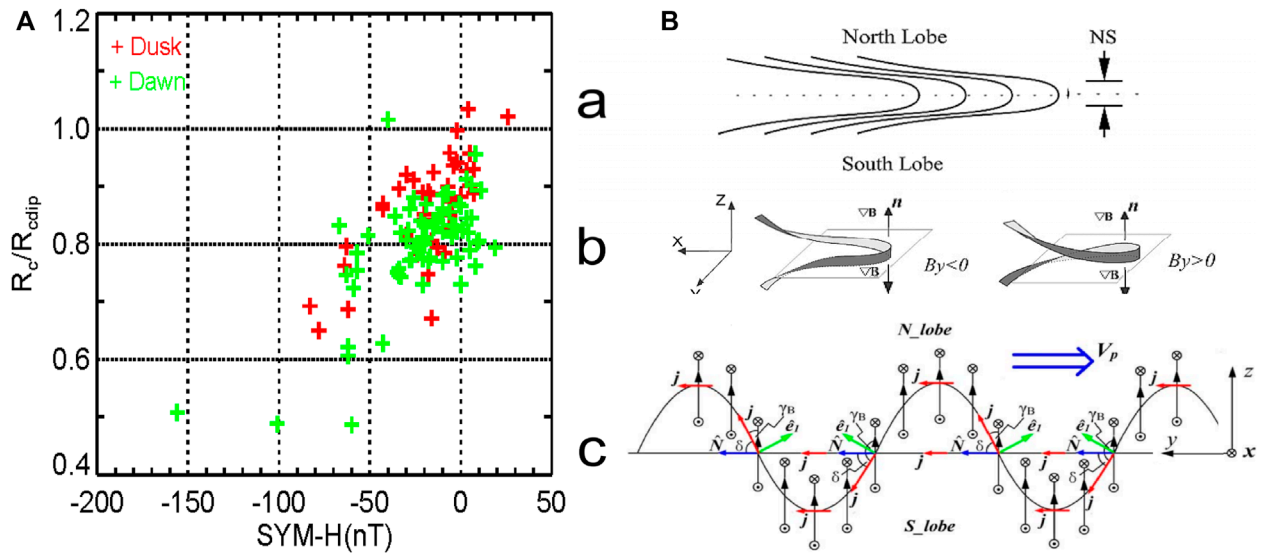

FIGURE 3
(A) Field-line curvature relative to that of the model dipole field for a set of ring current crossings sampled by Cluster (Shen et al., 2014), where dusk and dawn locations have different colours. **(B)** Cartoon of the types of field topology (Rong et al., 2011) found in the cross tail current sheet: (a) normal current sheet, (b) flattened current sheet (c) tilted current sheet (after Dunlop et al., 2021a).

2008b; Dunlop et al., 2009). Assuming that the magnetic field changes linearly around the spacecraft tetrahedron, the position of a magnetic null can be resolved if we perform the first-order Taylor expansion of magnetic fields around this null, $\mathbf{B}(\mathbf{r}) = \delta\mathbf{B}\cdot(\mathbf{r}-\mathbf{r}_0)$, where r_0 is the spacecraft position, r is the distance from spacecraft to the null, and B(r) is the magnetic field measured by each spacecraft. Applying the four-spacecraft measurements to this equation, r is easily resolved, and therefore, the null position is known (Fu et al., 2015). Notice that the null-spacecraft distance is a three-dimensional vector. Such distance, however, may involve uncertainties if the null is a quasi-2D structure (e.g., X-null). In other words, if the null is 2-D, the derived null-spacecraft distance in the "out-of-plane" direction is unreliable (Fu et al., 2019). In such situation, we only consider the 2-D null-spacecraft distance, i.e., the null-spacecraft distance in the reconnection plane.

Magnetic null types can also be identified. Since the sum of the three eigenvalues is zero ($\lambda_1+\lambda_2+\lambda_3 \equiv \nabla\cdot\mathbf{B}=0$), either all the eigenvalues are real or at least one is real and the other two are conjugate and complex. The different conditions affect the type of null: it is radial when the eigenvalues are real for both A- and B-type. A combination of one positive and two negative eigenvalues gives an A-type null, while two positive and one negative eigenvalue gives a B-type. In the other case, where only one eigenvalue is real, the null is an As- and Bs-type spiral (the As null corresponds to a positive real eigenvalue and the Bs null to a negative real eigenvalue). Sometimes large instrument uncertainties or magnetic field non-linearity mean the type cannot be identified, so is labelled "unknown". A, B, As, and Bs are all the null types in 3D regime. They are labeled by using the symbols △, ▷, ▲, ►, respectively (Fu et al., 2015; Fu et al., 2020).

The FOTE method can also determine the dimensionality of a magnetic null. Among the three eigenvalues of the Jacobian matrix, if one eigenvalue is significantly smaller than the two others, the three-dimensional A- and B-null will degenerate into two-dimensional X-null, or in other words, the magnetic topology will have a 2-D appearance; if the real part is significantly smaller than the imaginary part, the three-dimensional As- and Bs-null will degenerate into two-dimensional O-null, which certainly has the 2-D appearance (Fu et al., 2015; Wang et al., 2020). Typically, in spacecraft measurements, we simplify A and B nulls to X null if the three eigenvalues satisfy $\min(|\lambda|) < \frac{1}{4}\cdot\max(|\lambda|)$ and simplify As and Bs nulls to O null if the real and imaginary parts of the three eigenvalues satisfy $\max(|\mathrm{Real}(\lambda)|) < \frac{1}{4}\cdot\min(|\mathrm{Imag}(\lambda)|)$. The A, B, As, and Bs nulls are 3-D structures, while the X and O nulls are 2-D structures. Such 2-D structures are characterized by negligible magnetic fields in the "out-of-plane" direction. In space plasmas, the O null (or O line) is referred to plasmoid or flux rope. Figure 4 shows an example for the application of the FOTE method to find magnetic nulls during 12 magnetic-reconnection events detected by the MMS mission at the Earth's magnetopause, with the null-spacecraft distance (see the left-side vertical axis), null types (see the symbols), null dimensionality (see the labeling system at the bottom of the figure), and the analysis error (see the gray shade and the right-side vertical axis) exhibited (adapted from Fu et al., 2019).

During periods of magnetic reconnection, the open angle of separatrix-lines can be resolved by the method. The Jacobian matrix δB has three eigenvectors, e_1, e_2, e_3, and correspondingly three eigenvalues, $\lambda_1, \lambda_2, \lambda_3$. The open angle of two separatrix-lines is determined by the two eigenvectors related to the two large eigenvalues. The angle between these two eigenvectors is the open angle of the two separatrix-lines (Chen et al., 2018). For example, if $\lambda_1 > \lambda_2 > \lambda_3$, the open angle is the angle between e_1 and e_2. Such an open angle directly determines the reconnection rate of a reconnection process (Chen et al., 2019; Wang et al., 2020). Figure 5 is an example, showing the

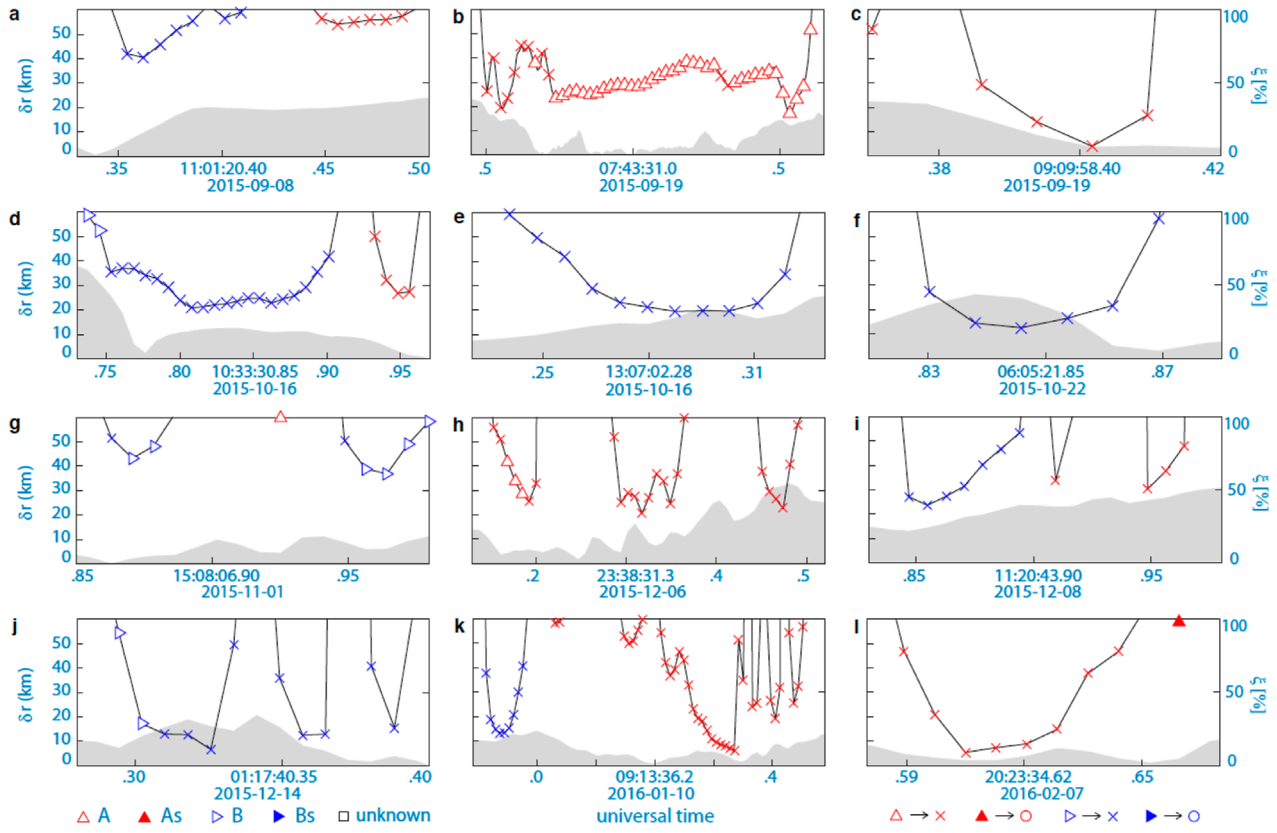

FIGURE 4
An example illustrating the application of the FOTE method to find magnetic nulls during 12 reconnection events **(A–L)** at the Earth's magnetopause (after Fu et al., 2019).

application of the FOTE method to resolve the open angle of separatrix-lines and deduce the reconnection rate during an unsteady reconnection at the Earth's magnetopause (adapted from Wang et al., 2020).

The FOTE method can be used in the reconstruction of magnetic topology around magnetic nulls. In eigenvector coordinates $e_1e_2e_3$, we trace and inverse-trace a few points around the null to obtain the magnetic field topology. The step length of trace/inverse-trace is typically set to be the local magnetic strength (Fu et al., 2016). Figure 6 illustrate the application of the FOTE method to reconstruct the topology of a radial-type magnetic null and a spiral-type magnetic null, which is also referred to the magnetic flux rope in spacecraft observations (modified from Fu et al., 2017; Wang Z. et al., 2019).

Finally, in terms of the errors during applications of the method to real data, we require the null-spacecraft distance to be less than the local ion inertial length, in order to guarantee that the null positions are accurately resolved. In addition, to guarantee that the null properties are accurately identified, we define two parameters ($\eta \equiv |\nabla \cdot \mathbf{B}|/|\nabla \times \mathbf{B}|$ and $\xi \equiv |(\lambda_1+\lambda_2+\lambda_3)|/|\lambda|_{max}$) and require them to be smaller than 0.4. These criteria are derived from the comprehensive test of three-dimensional simulation data (Fu et al., 2015; Fu et al., 2016).

4 Application of the curlometer to currents in the magnetosphere

Due to its robust and flexible nature, the curlometer calculation is perhaps the most widely used in the magnetosphere (notably applied in: the magnetopause boundary layer (Dunlop et al., 2002; Haaland et al., 2004a, e.g., Dunlop and Balogh, 2005; Panov et al., 2006; Panov et al., 2008; Shi et al., 2019); the magnetotail (Runov et al., 2006, e.g., Nakamura et al., 2008; Narita et al., 2013); the ring current (Vallat et al., 2005; Zhang et al., 2011, e.g., Shen et al., 2014; Yang et al., 2016); field-aligned currents (e.g., Forsyth et al., 2008; Marchaudon et al., 2009; Shi et al., 2010; Shi et al., 2012; Dunlop and Lühr, 2020) and other transient signatures and in the solar wind (e.g., Eastwood et al., 2002; Xiao et al., 2004; Shen et al., 2008a; Roux et al., 2015). Some of these applications are briefly reviewed here.

4.1 Basic use of the curlometer and time stationarity

The magnetopause boundary layer (MPBL) matched well the scale size of the early Cluster mission phases (100–2,000 km spacecraft separation). Figure 7 shows examples from Haaland et al.

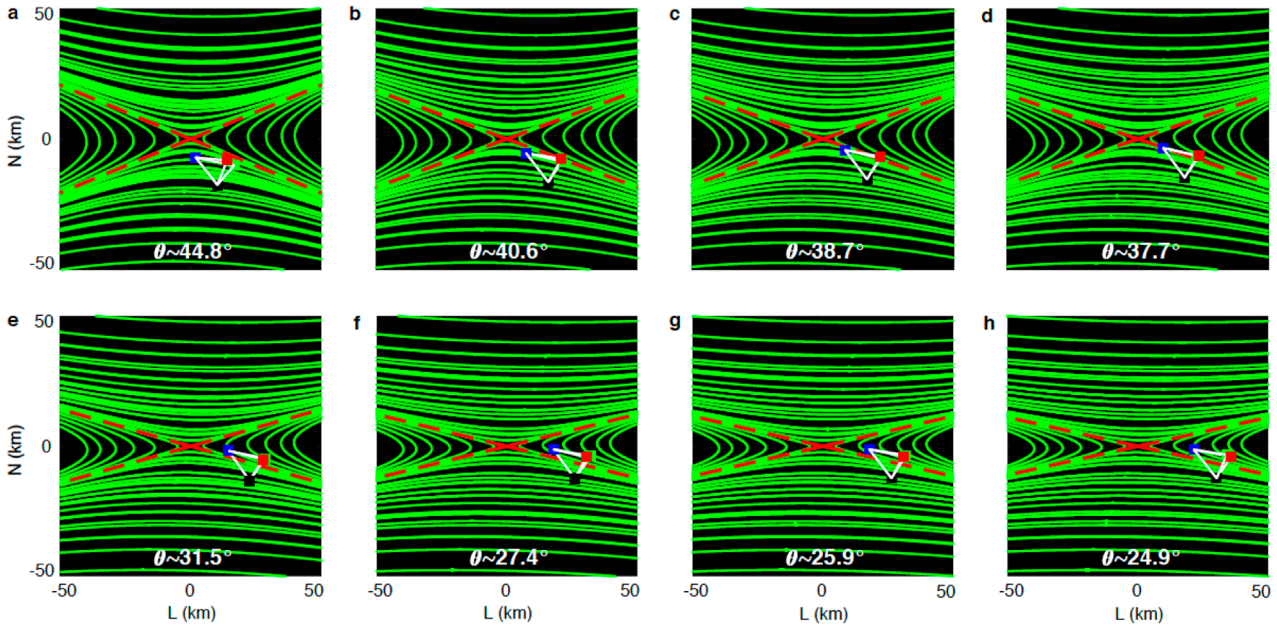

FIGURE 5
An example showing the application of the FOTE method to resolve the open angle of separatrix-lines during an unsteady reconnection. The angles between the two separatrix lines are **(A)** θ = 44°.8, **(B)** θ = 40°.6, **(C)** θ = 38°.7, **(D)** θ = 37°.7, **(E)** θ = 31°.5, **(F)** θ = 27°.4, **(G)** θ = 25°.9, **(H)** θ = 24°.9 (after Wang et al., 2020).

(2004a), Dunlop and Balogh (2005). The left panel shows that J orientations are predominantly in the MP plane during a number of in/out crossings resulting from magnetopause motion (average speed ~25 km/s; with average thicknesses ~1,200 km), while the right panel shows a thin MPBL with high current density. Typically, the Earth's magnetopause thickness varies from 100s of km (a few ion gyro radii) to 1,000s of km (Berchem and Russell, 1982; Paschmann et al., 2005; Panov et al., 2008), while corresponding current densities vary from 10 to 200 nA/m^2. In Figure 7A, the signatures outside the main MP crossing period are magnetosheath FTEs, where the current is along the mean reconnected flux tube direction (also studied by Pu et al., 2005).

Table 1 gives a summary of typical current density values in the Earth's environment, based on estimates of large-scale morphology and transient structure.

Figure 7 also illustrates that the combination of the curlometer and discontinuity analysis (which can obtain boundary orientation and motion (see Dunlop and Woodward, 1998; Dunlop et al., 2002; Haaland et al., 2004a) can confirm the thickness of the current layer and the alignment of J in the local MP plane. Broad scaling of |J| (10–50 nAm^{-2}) depending on a range of thicknesses, ΔD, can be shown to be consistent with the effective planar current $(\Delta B/\Delta D)/\mu_0$. The Cluster results tend to underestimate current for higher J and thicker boundary layers (compared to the separation). Indeed, the existence of small-scale sub-layers within the MPBL, having high intensity currents, were not often resolved by Cluster, but were seen by MMS (Dunlop et al., 2021a). The MVAJ method, referred to in the right panel of Figure 7 [see also Xiao et al. (2004), who apply the method to FTE orientations] better ties the orientation of the current sheet to J (minimum variance of J obtains the orientation of a near 1D current sheet, since div J = 0, when μ0J = curl B). The velocity of the current sheet can also be obtained (Haaland et al., 2004b), where different estimates of orientation all agree to within a few %.

A second key region demonstrating the capabilities of the curlometer became accessible after the launch of the multi-point measurements from Swarm at low-Earth orbit (LEO) altitudes. Although Swarm is a three-spacecraft mission and is not always in a close constellation, the method can be generalised by using nearby positions in time as indicated in Figure 1. This provides estimates even for only 2 or 3 closely separated spacecraft when either the dominant currents are field-aligned (FAC) or characteristic currents are locally static, [typical in this region of the high altitude ionosphere and thermosphere, e.g., Ritter and Lühr, 2006; Ritter et al., 2013; Dunlop et al., 2015a; Dunlop et al., 2015b; Dong et al., 2023, and references in Dunlop and Lühr (2020)]. Subtraction of the main, background field components prior to application of the method is essential At these low LEO altitudes (400–600 km), the main, background field must be subtracted to avoid the effect of zero current non-linear gradients [typically the IGRF or Chaos model (e.g., Olsen et al., 2014) are subtracted].

Typical convection times of ~10–15s apply in the case of the Swarm spacecraft separations of ~100–150 km at mid to high latitudes. Thus, the multi-spacecraft estimate depends on the FACs not being highly time dependent (e.g., ULF or Alfvén waves); but usually this is only relevant for small-scale currents, which can be easily identified by differences in field measured at the individual spacecraft. Thus, in addition to identifying smaller scale and time dependent structures, the extended methodology maps

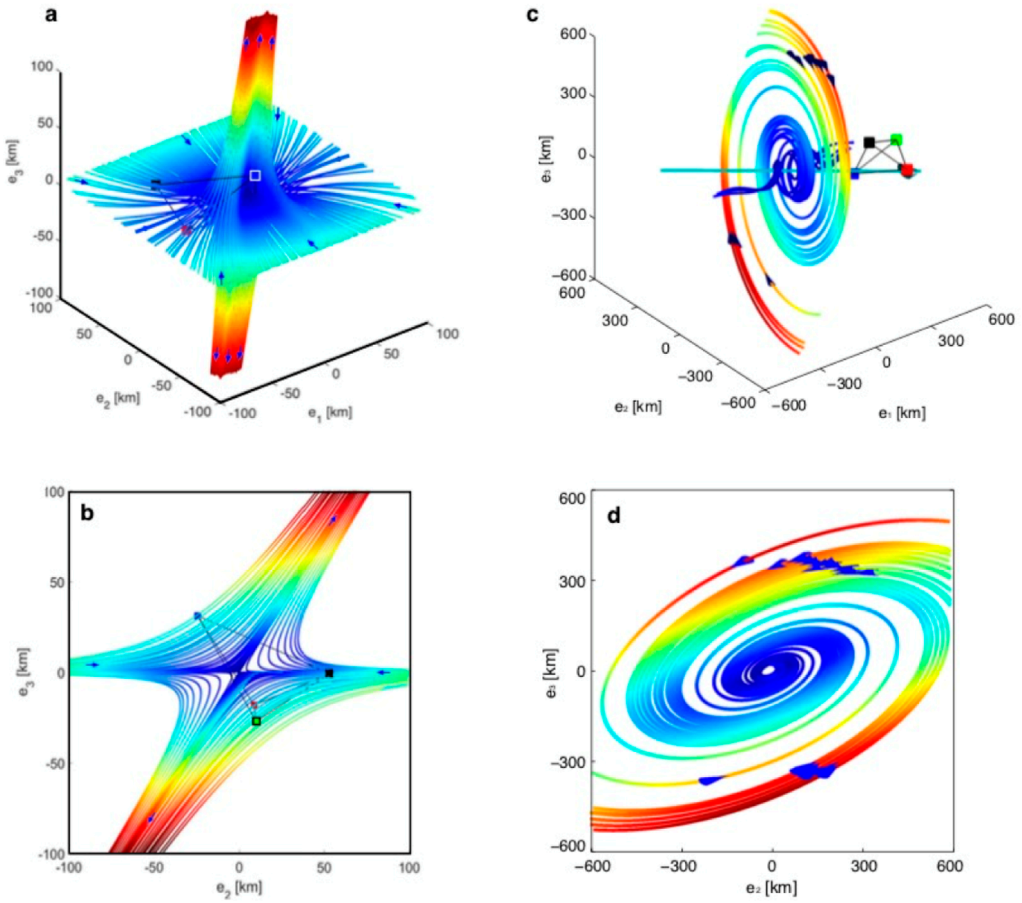

FIGURE 6
An example illustrating the application of the FOTE method to reconstruct the topology of a radial-type null and a spiral-type null (modified from Fu et al., 2017; Wang Z. et al., 2019). **(A)** Three-dimensional view of the radial-type null. **(B)** Two-dimensional view of the radial-type null. **(C)** Three-dimensional view of the spiral-type null. **(D)** Two-dimensional view of the spiral-type null.

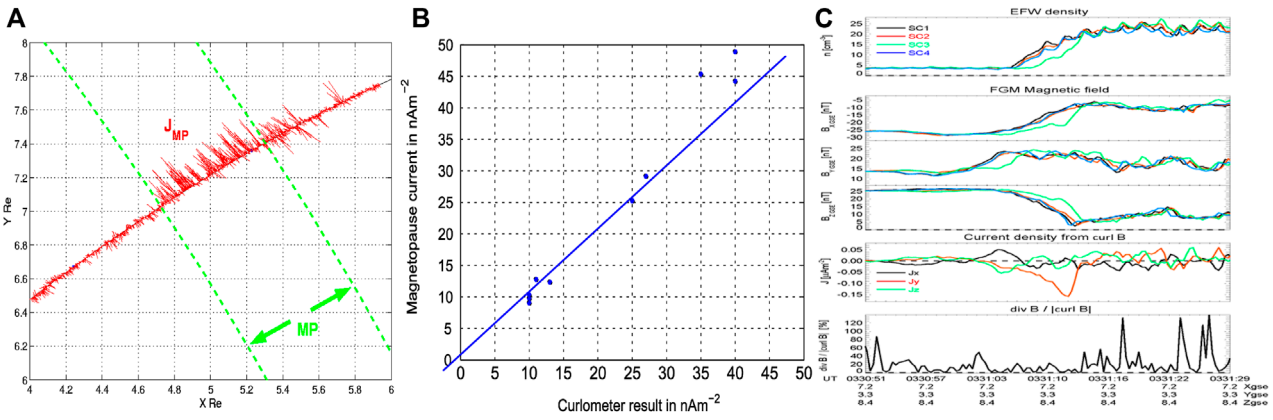

FIGURE 7
After Dunlop et al. (2021a): **(A)** Current density vectors for a period of MP oscillations on the 26 January 2001, showing alignment to the MP boundary **(B)** Comparison of the current density estimated from an equivalent Chapman-Ferraro sheet to the curlometer at the MP (from Dunlop and Balogh, 2005) **(C)** Plot of plasma density, magnetic field and current density (values of Q bottom panel), showing a thin magnetopause (on 2 March 2002), where the separations were ~100 km and estimated current densities reach 160 nAm^{-2}, extending over 200 km (Haaland et al., 2004b).

TABLE 1 Typical current density values (from Dunlop et al., 2021a).

Feature/Region	Typical values for J
Magnetopause currents	~10 nA m^{-2} (Dunlop and Eastwood, 2008), to 100 s nA m^{-2} (see, e.g., Panov et al., 2008)
Currents in flux transfer events	~1 nA m^{-2} (Dunlop and Eastwood, 2008) up to 10 nA m^{-2} (Pu et al., 2005)
Current at the cusp boundaries	~20 nA m^{-2} (Dunlop et al., 2002)
Field aligned currents (FAC)	~2 μA m^{-2} at 500 km altitude and ~20 nA m^{-2} at 2.5 RE altitude (Dunlop et al., 2005)
Magnetotail current sheet	up to ~30 nA m^{-2} (Runov et al., 2006)
Plasma sheet boundary layer	~10 nA m^{-2}, (Nakamura et al., 2004)
Ring current	9–27 nA m^{-2} at 4–4.5 RE, (Zhang et al., 2011)
Solar wind current sheet	~10 nA m^{-2} (Eastwood et al., 2002)

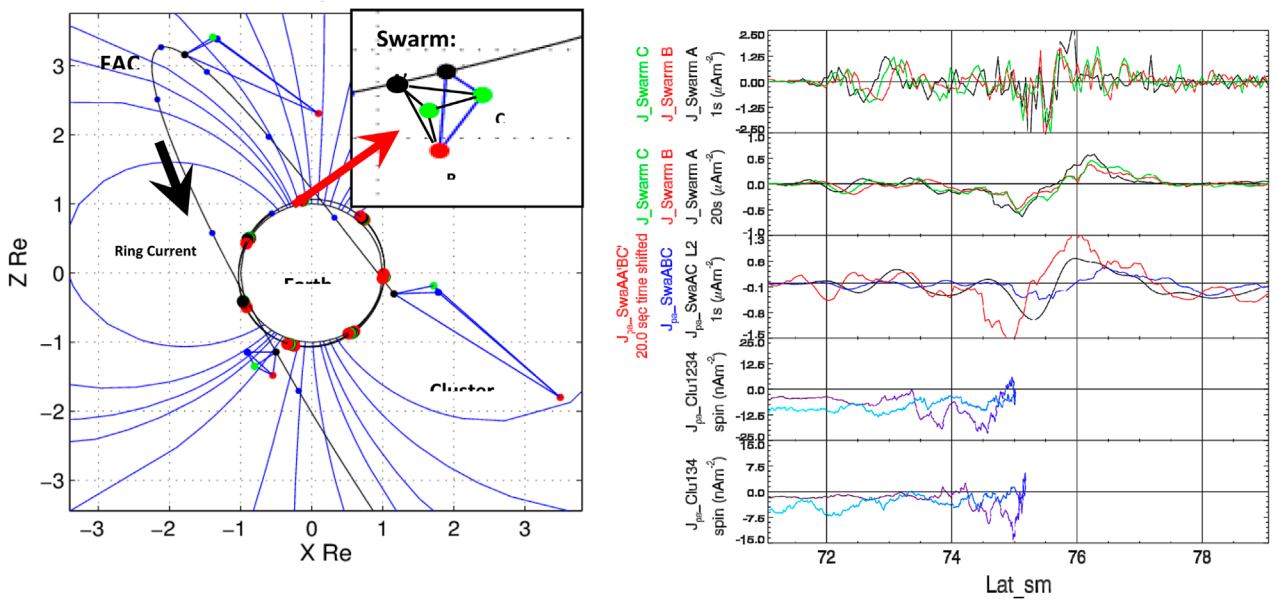

FIGURE 8
A Cluster and Swarm conjunction, taken from Dunlop et al. (2015a), projected into Z,X_{GSM} (left panel). Configurations of Cluster are enlarged by a factor of 3. Cluster moves from dusk (front) to dawn, moving from lower- to high-latitudes (marked FAC) near the R2 auroral boundary and back. The Swarm orbit lies close to Z,X_{GSM}, passing under the Cluster orbit and across the polar cap during the high-latitude Cluster positions. Thus, the magnetic footprints of Cluster cut across those of Swarm within minutes of the Swarm pass. The right-hand plots show Swarm and Cluster FAC estimates as a function of MLAT. The top two panels are unfiltered and 20s filtered, single spacecraft FACs (for Swarm A, B, C), while the middle panel shows different Swarm multi-spacecraft estimates (red line is the 4-point method; the blue line is the ABC planar configuration, and the smooth black line is the level 2 dual spacecraft estimate). Cluster FACs, estimated for the face perpendicular to the magnetic field, and the full curlometer are in the lower panels (where the dark blue trace is the initial crossing and the light blue trace corresponds to the times after the conjunction when Cluster moves back to lower latitudes at different local times (after Dunlop et al., 2021a).

out the morphology and dynamics of larger scale current systems, e.g., region 1, region 2 and NBZ FAC systems (see review in Mcpherron et al., 1973; Shiokawa et al., 1998; Cao et al., 2010).

Figure 1B shows the Swarm configuration, as considered in Dunlop et al. (2015a) for a close conjunction of Cluster and Swarm (as shown in Figure 8). A series of 2, 3 and 4 spacecraft estimates for the FACs can be made (in the context of the time shifted positions), while 4-spacecraft positions also give very low Q estimates (a few %). Changing the choice of the selected spacecraft positions can indicate how stable the estimates are (note that the effective barycentres of each set are slightly different). These comparative estimates are shown on the right-hand side of Figure 8, which also shows (top two panels) the filtered single spacecraft FAC estimates from *dB/dt* (Lühr et al., 2015). The 4-point estimates of the FAC profiles match those estimated from Cluster measurements most closely (with suitable scaling). Cluster moves to higher MLAT values

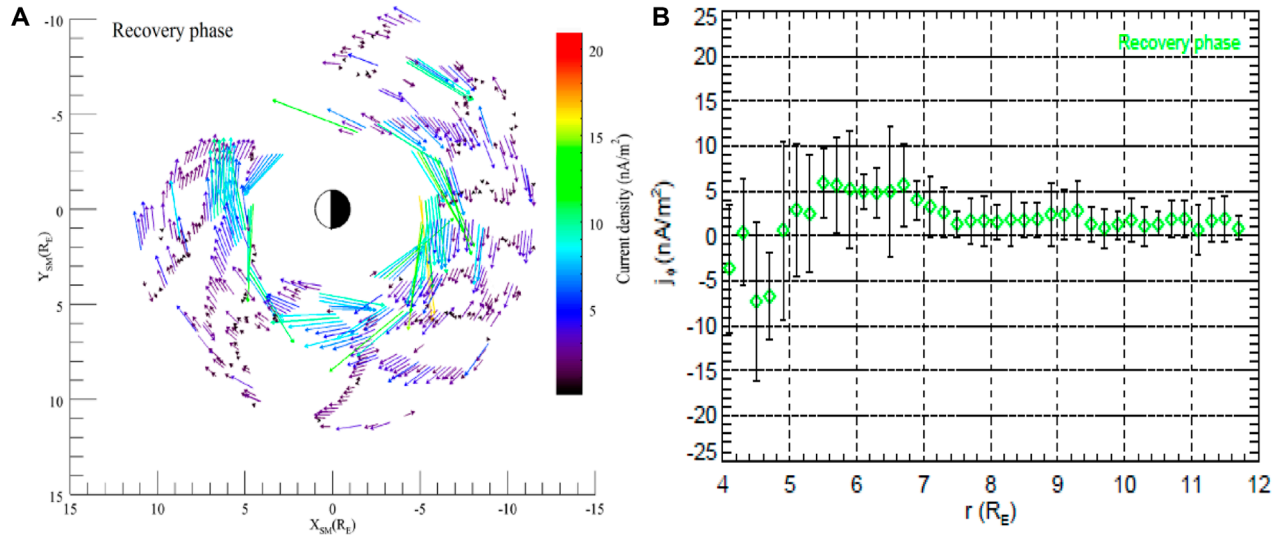

FIGURE 9
(A) Current densities projected into the ring plane are shown in a similar way (from THEMIS) for all storm activities during the recovery phase, showing the wider range of radial coverage achieved (for about 4–12 R_E) and an enhanced current near midnight LT for storm events. **(B)** Radial profile of the current density from THEMIS measurements (after Dunlop et al., 2021a).

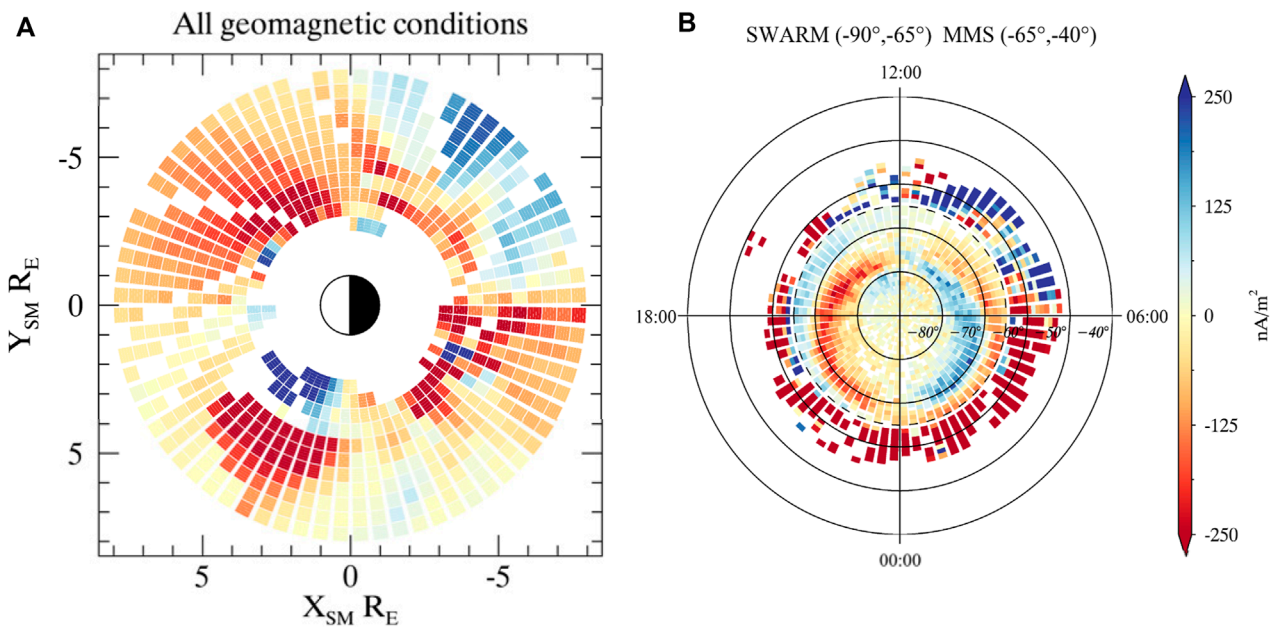

FIGURE 10
Plots of the morphology of current density in the ring current [**(A)**; from J_ϕ] and comparison of FACs from $J_{||}$, measured both adjacent to the RC and by Swarm in the ionosphere **(B)**, after Carter et al. (2024). Note that the $J_{||}$ current densities from MMS have been scaled in strength to the expected density at swarm altitudes. This is expected to be an overestimate, particularly for the sub-auroral regions.

and then back to lower MLAT in its traversal of the region but cross the local time of the Swarm orbit within minutes of the Swarm pass. The results imply that ~ 1–200 *km* Swarm currents (at LEO altitudes) can coherently map to Cluster.

The 4-point calculation can also identify any perpendicular components and estimates for this event appear to show possible, associated hall signatures consistent with wire model FACs (see Gjerloev and Hoffman, 2002; Ritter et al., 2004; Wang et al., 2006; Liang and Liu, 2007; Shore et al., 2013). Related methods dealing with FAC estimates have been cross-compared to assess key events by Trenchi et al. (2020) and a similar time-shifted Swarm configuration, tailored to the low latitude regions, has attempted to extract low latitude currents (Fillion et al., 2021).

A third key region, suitable for adaption of the curlometer is the Earth's ring current (RC). This was studied early with Cluster (Dandouras et al., 2018; Dunlop et al., 2018), and then using the

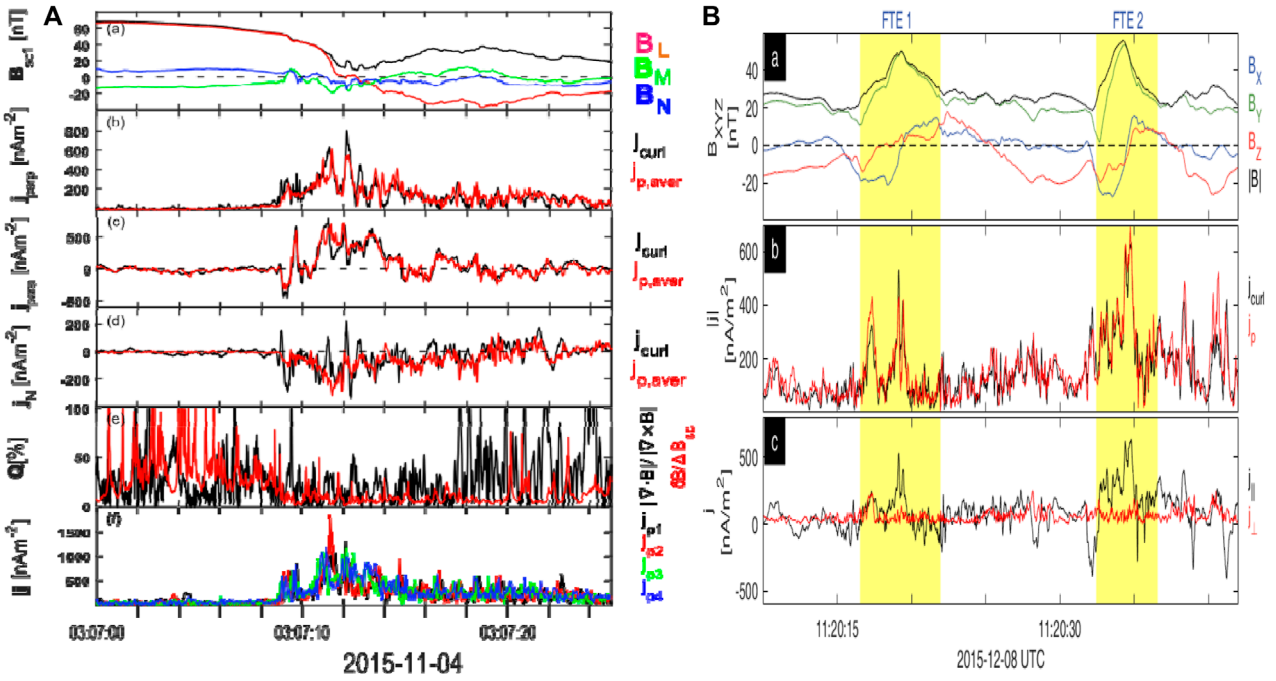

FIGURE 11
After Dunlop et al. (2021a): **(A)** A typical MP crossing for a thickness of ~350 km seen by MMS (after Dunlop et al., 2018), showing: (a) L, M, N coordinates of the magnetic field, (b) to (d) the perpendicular (Chapman-Ferraro), parallel (field-aligned) and normal components of both ***J*** from the curlometer estimate and the mean value of the 4-spacecraft ion moments, (e) the quality parameter Q compared to a crude (upper) estimate of the measurement errors from δB/ΔB, (f) the individual |***J***| from the plasma moments at each spacecraft. **(B)** Detailed current structures of two ion-scale FTEs: (a) magnetic field with bipolar signatures in the normal component (B_x) during each FTE interval; (b) A consistent current result from the curlometer and plasma moments, respectively, and (c) Parallel and perpendicular currents (after Dong et al., 2017).

3-spacecraft magnetospheric THEMIS spacecraft, as mentioned in Section 2.1. More recently MMS measurements have been used to estimate the ring current densities. There are contrasts between each: Cluster only accessed the mesoscale separations; the 3 THEMIS spacecraft limit the estimate to the normal current component, and MMS only has survey magnetic field data (with no thermal plasma) in the RC region. As first reported by Vallat et al. (2005), the Cluster polar orbit cuts north to south through the ring plane, allowing all local times to be scanned over the mission (Zhang et al., 2011) for a narrow range of radial distance (~4–4.5 R_E). Typically, the azimuthal component, J_ϕ, can be made, where the IGRF model is subtracted to reduce the effect of non-linear dipole gradients (mentioned in Section 2.1). Full azimuthal scans can highlight local time asymmetry in the RC and a possible relation to asymmetries at the MP has been suggested by Haaland and Gjerloev (2013).

As shown on the left-hand side of Figure 1, the three magnetospheric THEMIS spacecraft I near equatorial orbits also provide a wide MLT coverage (Yang et al., 2016), but for a range of radial distances, as shown in the left panel of Figure 9, so that L-shell profile can be revealed together with the Westward-Eastward current boundary on the inner edge of the RC, as shown in the right panel of Figure 9.

MMS also samples the ring current in a near equatorial orbit, providing a comparative RC estimate covering the same region as THEMIS on small separation scales. Thus, MMS can better resolve the trends seen in both the radial and azimuthal morphology, and also can identify small scale intense currents, which are not resolved by Cluster or THEMIS. The recent studies using MMS data (Tan et al., 2023), mentioned in Section 2.1 show both large and small-scale structures can be present, extending the earlier studies with Cluster and THEMIS. The morphology of the RC (left hand side of Figure 10) is broadly consistent with previous *in situ* studies with strong dawn/dusk and noon midnight asymmetry, but shows more detailed structure, with Tan et al. (2023) reporting a layered structure in latitude. A partial RC (or banana current), with an inner eastward current (blue) is most clear in the noon to dusk quadrant. There is no evidence of enhancement on the dusk-side during geomagnetically active periods.

Comparison of the Swarm low-altitude, dual-satellite FAC data with mapped MMS FAC signatures measured adjacent to the RC shows that RC behaviour and R2 FACs can be investigated directly (see right hand side of Figure 10) and show consistent patterns. The statistical coverage has some overlap in the location of Swarm FACs and the mapped locations of parallel currents measured adjacent to the RC (between 60 and 70 deg). In the auroral zone (particularly inside 65 deg, shown as a dashed circle), there is a qualitative R1/R2 pattern.

4.2 Recent application to MMS configuration scales

The current density can be obtained from velocity and density moments of the 3D plasma distributions for all ion species and

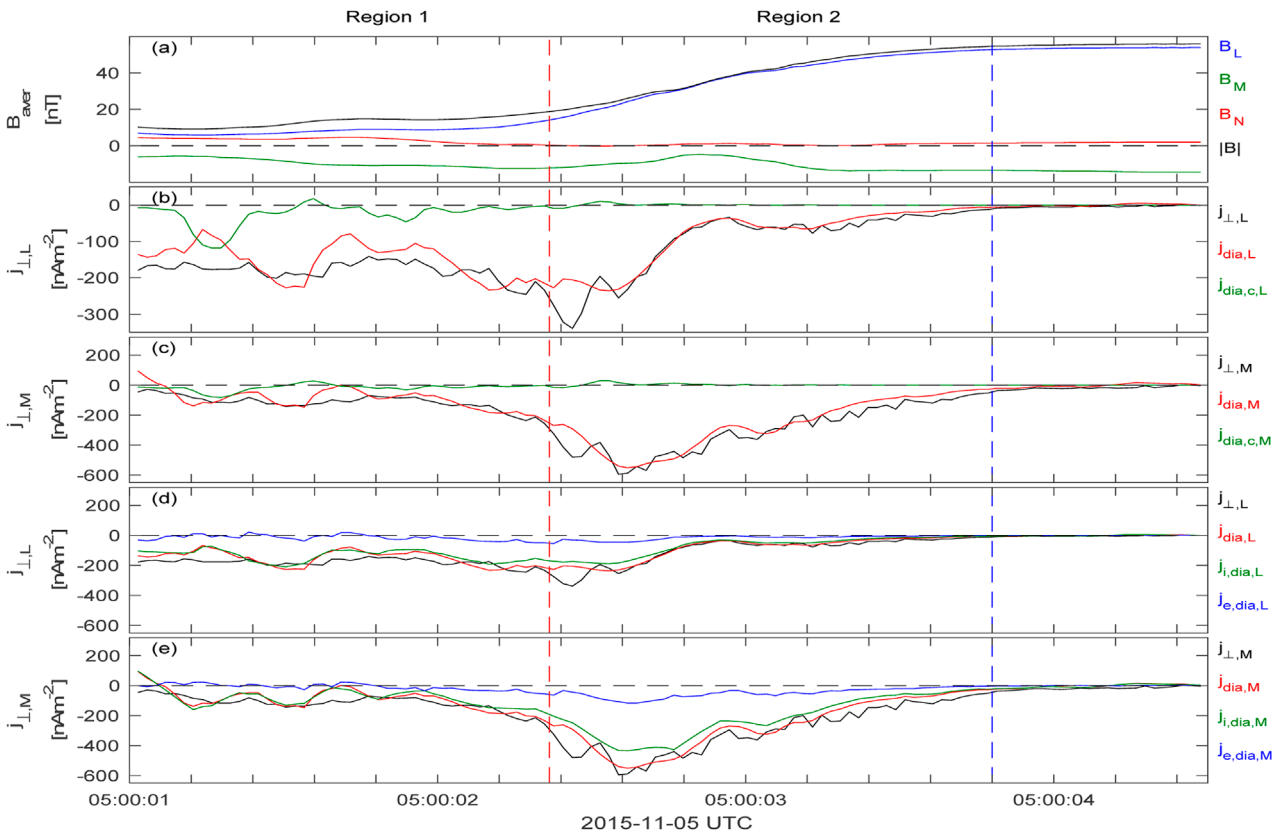

FIGURE 12
Sources of a thin magnetopause current sheet calculated by MMS data. **(A)** Four spacecraft average magnetic field; **(B, C)** perpendicular current from four spacecraft plasma moments $j_{\perp}$ (black), diamagnetic drift current j_{dia} (red), and curvature drift current j_{dia}, c (green); **(D, E)** perpendicular current $j_{\perp}$ (black), diamagnetic drift current jdia (red), and ion/electron diamagnetic drift current $j_{i,\,dia}$ (green)/$j_{e,\,dia}$ (blue). The Figure is adapted from Dong et al. (2018).

electrons. Cluster, for example, was limited to low cadence (since the full distribution is taken over a spacecraft spin period) and typically particle distributions are measured over a limited energy range [the use of particle moments previously can be found in Henderson et al. (2008), Petrukovich et al. (2015), and indeed (Yao et al., 2014), who also used pressure gradients to estimate the perpendicular current density]. The MMS mission can measure plasma distributions at high-time resolution (primarily in the outer magnetosphere). The MMS constellation is generally much smaller size than the prevailing ion structure, while the Cluster configuration was usually of order or greater than the MPBL, for example. In many regions of the magnetosphere there are intense small-scale currents which are missed on the separation scales of Cluster (100 s *km*) so typically the curlometer tends to underestimate the current density. On MMS separation scales, however, the ion-scale structures can be well resolved. A number of studies have used MMS plasma moments to estimate the currents (e.g., Lavraud et al., 2016; Phan et al., 2016) and comparing these estimates to the curlometer can reveal details of sub-structure; smaller scale current layers, and details of the current carriers. Moreover, Cluster and MMS conjunctions (for example, at different locations on the MP) provide the opportunity to compare across multiple spatial scales. Below we briefly show two aspects of this analysis [a more complete treatment d given in Dunlop et al. (2021a)].

4.2.1 Sub-structure in the MP and FTEs

The left-hand side of Figure 11 shows a typical MMS magnetopause crossing where the curlometer current densities are plotted with the current density estimated from the plasma moments $[(\boldsymbol{J} = \sum \boldsymbol{q n_s V_s} \sim \boldsymbol{q n}(\boldsymbol{V_i} - \boldsymbol{V_e})]$, which can be estimated at each spacecraft position. The plasma currents closely follow the curlometer when averaged over the four spacecraft positions. The normal component (panel d) shows the most significant differences between the plasma currents and the curlometer. Panel (e) shows that for currents below ~50 nAm^{-2} both the measurement errors and Q are significant. Despite the close curlometer agreement with the spatially averaged plasma current (i.e., the mean current over the tetrahedron), the estimates at each spacecraft (bottom panel) vary significantly between each position. This might suggest small scale (filamentary) structure within the magnetopause layer, where the dominant current carriers are measured by the plasma moments (this would be consistent with the intense, narrow bursts of current seen in the curlometer profiles), and appears to be typical of the magnetopause layer (Dong et al., 2017). This substructure was not well resolved by Cluster (except for the smallest separation scales) and the Cluster array tends to miss these filamentary currents.

Many recent MMS studies have also focused on the ion-scale structure of FTEs (e.g., Eastwood et al., 2016; Zhao et al., 2016;

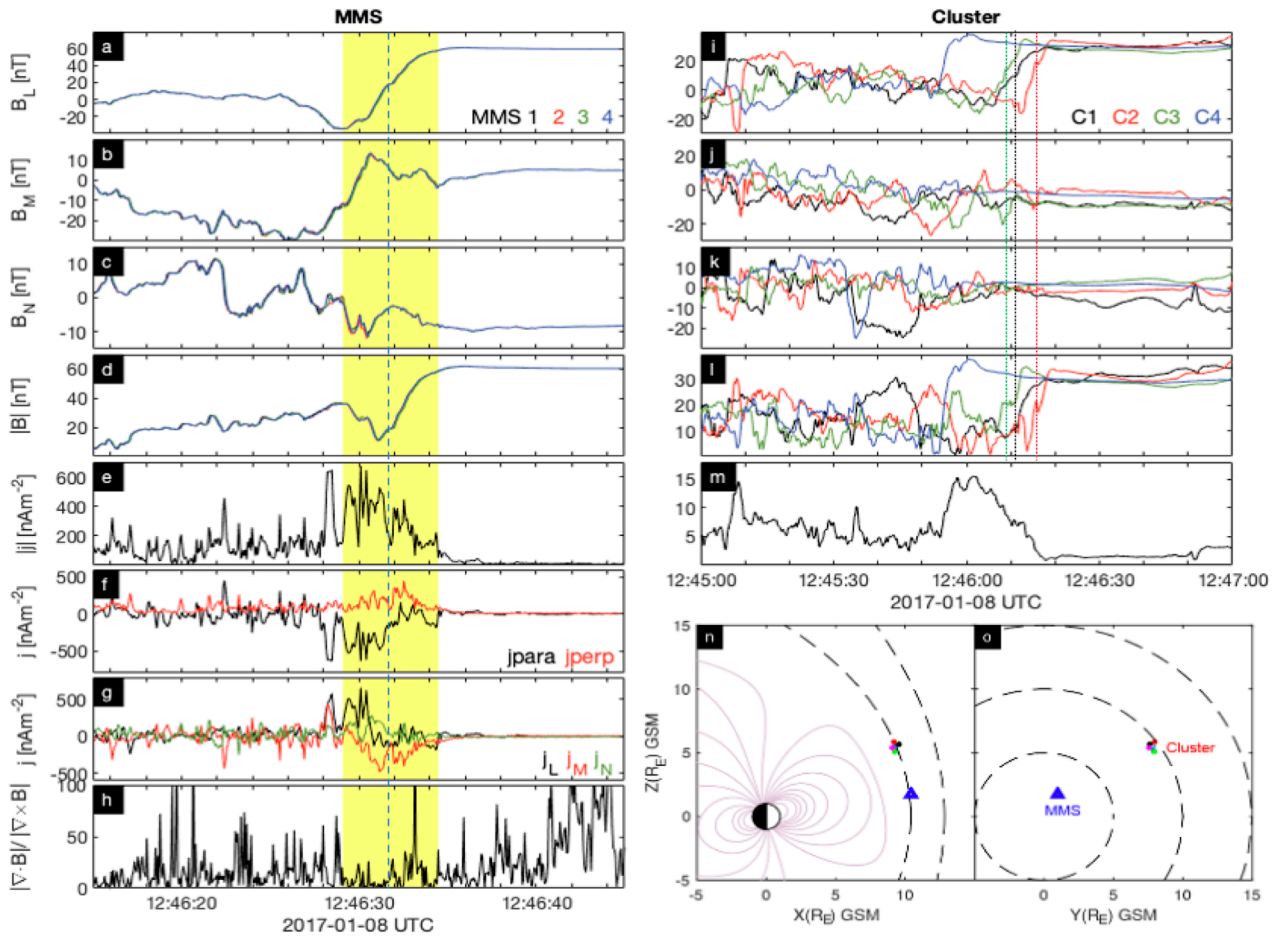

FIGURE 13
Magnetic field and current observed by a simultaneous MMS (left) and Cluster (right) magnetopause crossing (after Dunlop et al., 2021a). **(A–D, I–L)** Vector magnetic field in GSM coordinates. **(E, M)** Electric current from curlometer method. **(F)** MMS current in parallel and perpendicular direction, respectively. **(G)** MMS current in local boundary normal coordinate. **(N-O)** Magnetopause crossings locations of MMS ([10.4, 1.0, 1.8] R_E) and Cluster ([9.6, 7.6, 5.7] R_E) at XZ and YZ plane, respectively (safter Dunlop et al., 2021a).

Dong et al., 2017; Teh et al., 2017; Alm et al., 2018; Hwang et al., 2018; Dong et al., 2020). As first reported by Eastwood et al. (2016), agreement between the curlometer and plasma moments can be shown for current density in ion-scale FTEs, where filamentary currents were found and the main current carriers were electrons. The right-hand side of Figure 11 shows two ion-scale FTEs and their detailed current structures (Dong et al., 2017). The currents are highly inhomogeneous and mainly located in either the centre of the flux rope or on the leading edge [this was also true in the Roux et al. (2015) study of a large-scale FTE]. Central bifurcated features in the flux ropes were also present, while as a result of force-free structures, the parallel currents dominate.

4.2.2 Carriers and sources of magnetopause current

Figure 12 shows a thin MP current layer (~100 km) event encountered by MMS, which was studied by Dong et al. (2018). There is a comparable perpendicular current from the contributions of the ions and electrons in the boundary layer, but the parallel current appears to be dominated by the electron carriers. For the perpendicular currents, the diamagnetic current term ($\boldsymbol{J_{dia}} = \frac{B\times\nabla p_\perp}{B^2}$) and the directly measured $J_\perp$ shows good agreement (red line in Figures 12B, C) while the curvature current $\boldsymbol{J_{dia,c}} = -\frac{p_\parallel - p_\perp}{B^2 R_c}\boldsymbol{B}\times\boldsymbol{n}$ can be neglected (green line in Figures 12B, C). When the diamagnetic current is separated into ion and electron components, the perpendicular current is dominated by the ion diamagnetic current ($J_{i,dia}$: 85%, $J_{e,dia}$: 15%, Figures 12D, E). The ions and electrons ultimately carry comparable current through the redistribution of the electric field. The electron current deviates at a narrow front layer in region 2 which suggests non-MHD behaviour (beyond Chapman-Ferraro).

Note that the matched plasma and magnetic field measurements from MMS mean that the flow vorticity can be obtained from the curlometer estimates (Dunlop et al., 2002), providing linear estimates for velocity, in addition. Electron vorticities related with electron currents have been studied in the turbulent magnetosheath (Phan et al., 2016; Chasapis et al., 2018), and coherent Alfvén vortices in the same region (Wang T. et al., 2019) can be inferred from alignment of parallel current density and ion vorticity.

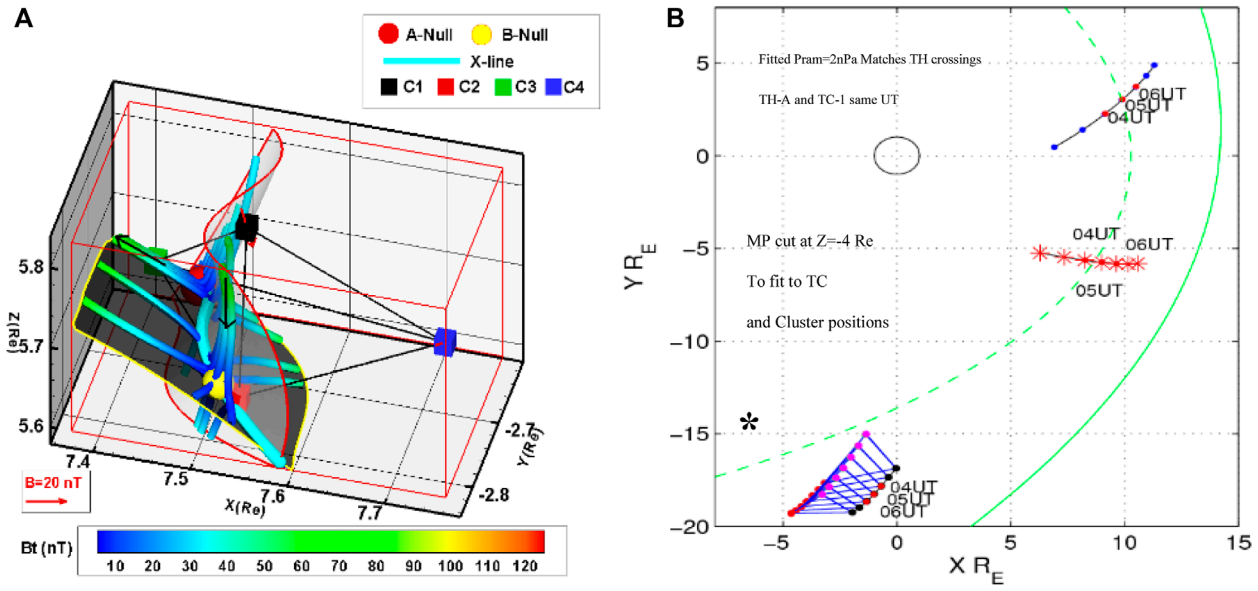

FIGURE 14
(A) Shows the reconstruction of an X-line geometry, where Cluster, located at high latitudes, repeatedly sampled magnetic nulls within the ion diffusion region, while Doublestar also sampled active reconnection signatures (FTEs) at low latitudes (after Dunlop et al., 2009). **(B)** A conjunction of the 5-THEMIS, 4-Cluster and 1-DSP spacecraft, covering a wide range of local time across the MP (after Dunlop et al., 2011) during periods of multiple, active reconnection sites, where all spacecraft are located at different positions along an extended, tilted (S-shaped) merging line.

4.2.3 Simultaneous MMS and cluster magnetopause crossings

A simultaneous MMS and Cluster crossing of the magnetopause (MPBL) at two different locations is shown in Figure 13, where MMS is located near the subsolar region and Cluster is located on the high latitude post-noon region (Figures 13N, O) and MMS crosses into the magnetosphere ~20 s later than Cluster. The MMS spacecraft are ~8 km apart, which is much smaller than the estimated current layer of ~440 km, while the Cluster spacecraft are ~3,500 km apart, which is large compared to the current layer at their location of ~1,400 km. Thus, the small-scale current structure can be resolved by MMS, while the overall MP current is underestimated by Cluster. In fact, the average MMS current (shaded region, Figure 13E) is ~220 nA/m^{-2}; one order of magnitude larger than estimated at Cluster (Figure 13M), although the simple 1-D (Chapman-Ferraro) current sheet estimated from the change in B and the thickness only differs by a factor of 2-3.

The parallel current measured by MMS (j_{para}) is dominant in the magnetosheath boundary layer, where magnetic field component B_L contra-rotates to a negative value (Figures 13A, F). This B_L feature is also observed by Cluster (Figure 13I), suggesting a similar current structure at both MMS and Cluster locations. The main MMS current sheet has a bifurcated structure, divided by a small current region, noted by the vertical dashed line. This small region corresponds to a flat B_L structure (Figure 13A), which is similar to that seen at Cluster 1, 2 and 3 (vertical dashed line, Figure 13I). This suggests the bifurcated current structure extends to the region of Cluster, but is not observed by Cluster 4 ~15 s beforehand, implying it is also highly dynamic.

Sampling the MPBL at two locations during specific IMF conditions has shown similar overall form for the magnetic field, suggesting that the MP can have similar current structure across a wide region. In another simultaneous event, however, studied by Escoubet et al. (2020) during a high-speed jet in the magnetosheath, the magnetopause current structures at Cluster and MMS are totally different. Similar current structures across a wide region may therefore only remain during relatively stable solar wind conditions.

5 Conclusion

The multi-spacecraft estimates of current density and spatial gradients from Cluster, and the later adaptions to the circumstances of the Swarm and MMS missions, have provided key information on large and small magnetospheric current systems and related transient structures, resolving 3-D currents for a range of conditions in widely different geospace regions. The curlometer in particular, has proved to be reliable and robust. The applicability of the method is limited by certain constraints, particularly those for relatively small structures compared to the spacecraft separation distances. These constraints depend on the form of the spacecraft configuration and the presence of magnetic contributions from other (non-current) sources. Particle moments, give direct, complementary current density estimates, which can be also used to add constraints in generalised methods computing magnetic gradients beyond linear order (Shen et al., 2021a; Shen et al., 2021c).

New constellation missions can make use of further adaptations of this multi-spacecraft methodology within the framework of extended arrays of more than four satellites, particularly when distributed across distinct spatial scales, where the comparative

results with MMS, Cluster and THEMIS, as illustrated here, can be re-visited. Figure 14 illustrates two early examples, where close conjunctions of Cluster, Doublestar and THEMIS were interpreted in the context of both local magnetopause structure and the larger scale surrounding phenomena, which provided evidence of the operation of multiple X-lines (see also the discussion in Section 4.2). The adaption of the various quality indicators have been considered, for example, to the new, proposed constellation missions, such as Plasma Observatory (Retinò et al., 2022) and Helioswarm (Klein et al., 2023). As discussed here, there is a balance between the use of either the Q divergence condition or the configuration shape (E and P), depending on the overall comparative spatial scale of the differential measurements. Where fast plasma measurements are available to produce high time resolution moments (n, V, T), then this information can help better resolve the spatial gradients on multiple spatial scales. Finally, we note here that the low frequency spectral response in the measurements (reflecting the time stationarity over the spacecraft arrays) will be an important consideration for applications to configurations of spacecraft which sample distinct spatial scales.

Plain text

This article is an account of analysis methods relating to spatial gradients obtained from the differential measurements taken by formations of multiple spacecraft. It focusses on the so named curlometer method, which uses four positions in space to estimate electric current density from the magnetic field. Originally, these measurements were from the set of four ESA Cluster II spacecraft. The curlometer produced many results throughout the magnetosphere, while more recently it has been applied to data from other missions of multiple spacecraft (the NASA MMS and THEMIS missions and the ESA Swarm Earth explorer mission). Although there are certain caviats on its application, the technique has proved to be rugged and stable. Other techniques, such as those estimating magnetic field geometry and gradients, have incorporated the curlometer and the application if these is also covered.

- Robust multi-spacecraft analysis method relating to spatial gradients.
- Estimates of the vector, *in situ*, electric current density directly.
- Wide application throughout the magnetosphere from magnetic field measurements.

Author contributions

MD: Conceptualization, Data curation, Funding acquisition, Methodology, Writing–original draft, Writing–review and editing. H-SF: Conceptualization, Investigation, Methodology, Writing–original draft. CS: Investigation, Methodology, Writing–original draft. XT: Data curation, Investigation, Methodology, Software, Writing–review and editing. X-CD: Conceptualization, Investigation, Methodology, Writing–review and editing. Y-YY: Conceptualization, Methodology, Writing–review and editing. PR: Conceptualization, Methodology, Writing–review and editing. PE: Data curation, Validation, Writing–review and editing.

Funding

The author(s) declare that financial support was received for the research, authorship, and/or publication of this article. This work is supported by the NSFC grants 42350710793, 41821003, 42174208; by NERC grants NE/P016863/1 and NE/W003309/1 and by STFC in-house research grant ST/M001083/1.

Acknowledgments

The Swarm satellite data used in this study are available from ESA at http://swarm-diss.eo.esa.int/. For MMS data visit https://lasp.colorado.edu/mms/sdc/public/. Cluster data can be found at http://www.cosmos.esa.int/web/csa/.

Conflict of interest

The authors declare that the research was conducted in the absence of any commercial or financial relationships that could be construed as a potential conflict of interest.

Publisher's note

References

Alm, L., Farrugia, C. J., Paulson, K. W., Argall, M. R., Torbert, R. B., Burch, J. L., et al. (2018). Differing properties of two ion-scale magnetopause flux ropes. *J. Geophys. Res. Space Phys.* 123, 114–131. doi:10.1002/2017JA024525

Angelopoulos, V. (2008). The THEMIS mission. *Space Sci. Rev.* 141, 5–34. doi:10.1007/s11214-008-9336-1

Angelopoulos, V. (2009). "The THEMIS mission," in *The THEMIS mission*. Editors J. L. Burch, and V. Angelopoulos (New York, NY: Springer), 5–34. doi:10.1007/978-0-387-89820-9_2

Berchem, J., and Russell, C. T. (1982). The thickness of the magnetopause current layer: ISEE 1 and 2 observations. *J. Geophys. Res. Space Phys.* 87, 2108–2114. doi:10.1029/JA087iA04p02108

Bittencourt, J. A. (2004). *Fundamentals of plasma physics*. New York, NY: Springer. doi:10.1007/978-1-4757-4030-1

Burch, J. L., Moore, T. E., Torbert, R. B., and Giles, B. L. (2016). Magnetospheric multiscale overview and science objectives. *Space Sci. Rev.* 199, 5–21. doi:10.1007/s11214-015-0164-9

Cao, J.-B., Yan, C., Dunlop, M., Reme, H., Dandouras, I., Zhang, T., et al. (2010). Geomagnetic signatures of current wedge produced by fast flows in a plasma sheet. *J. Geophys. Res. Space Phys.* 115. doi:10.1029/2009JA014891

Carter, J. A., Dunlop, M., Forsyth, C., Oksavik, K., Donovon, E., Kavanagh, A., et al. (2024). Ground-based and additional science support for SMILE. *Earth Planet. Phys.* 8, 275–298. doi:10.26464/epp2023055

Chanteur, G. (1998). "Spatial interpolation for four spacecraft: theory," in *Analysis methods for multi-spacecraft data*. Editors G. Paschmann, and P. W. Daly (Noordwijk, Netherlands: ESA Publications Division), 349–370.

Chanteur, G., and Harvey, C. C. (1998). "Spatial interpolation for four spacecraft: application to magnetic gradients," in *Analysis methods for multi-spacecraft data*. Editors G. Paschmann, and P. W. Daly (Noordwijk, Netherlands: ESA Publications Division), 371–394.

Chasapis, A., Yang, Y., Matthaeus, W. H., Parashar, T. N., Haggerty, C. C., Burch, J. L., et al. (2018). Energy conversion and collisionless plasma dissipation channels in the turbulent magnetosheath observed by the magnetospheric multiscale mission. *Astrophysical J.* 862, 32. doi:10.3847/1538-4357/aac775

Chen, X. H., Fu, H. S., Liu, C. M., Cao, D., Wang, Z., Dunlop, M. W., et al. (2018). Magnetic nulls in the reconnection driven by turbulence. *Astrophysical J.* 852, 17. doi:10.3847/1538-4357/aa9991

Chen, Z. Z., Fu, H. S., Wang, Z., Liu, C. M., and Xu, Y. (2019). Evidence of magnetic nulls in the reconnection at bow shock. *Geophys. Res. Lett.* 46, 10209–10218. doi:10.1029/2019GL084360

Dai, L., Wang, C., Cai, Z., Gonzalez, W., Hesse, M., Escoubet, P., et al. (2020). AME: a cross-scale constellation of CubeSats to explore magnetic reconnection in the solar-terrestrial relation. *Front. Phys.* 8, 89. doi:10.3389/fphy.2020.00089

Dandouras, I., Rochel-Grimald, S., Vallat, C., and Dunlop, M. W. (2018). "Terrestrial ring current: a review of cluster results based on the curlometer technique," in *Electric currents in geospace and beyond. American geophysical union*. Editors A. Keiling, O. Marghitu, and M. Wheatland (John Wiley and Sons), 115–126. doi:10.1002/9781119324522.ch7

De Keyser, J. (2008). Least-squares multi-spacecraft gradient calculation with automatic error estimation. *Ann. Geophys.* 26, 3295–3316. doi:10.5194/angeo-26-3295-2008

De Keyser, J., Darrouzet, F., Dunlop, M. W., and Décréau, P. M. E. (2007). Least-squares gradient calculation from multi-point observations of scalar and vector fields: methodology and applications with Cluster in the plasmasphere. *Ann. Geophys.* 25, 971–987. doi:10.5194/angeo-25-971-2007

Denton, R. E., Liu, Y.-H., Hasegawa, H., Torbert, R. B., Li, W., Fuselier, S., et al. (2022). Polynomial reconstruction of the magnetic field observed by multiple spacecraft with integrated velocity determination. *J. Geophys. Res.* 127. doi:10.1029/2022JA030512

Denton, R. E., Torbert, R. B., Hasegawa, H., Dors, I., Genestreti, K. J., Argall, M. R., et al. (2020). Polynomial reconstruction of the reconnection magnetic field observed by multiple spacecraft. *J. Gephys. Res.* 125. doi:10.1029/2019JA027481

Dong, X. C., Dunlop, M. W., Trattner, K. J., Phan, T. D., Fu, H. S., Cao, J. B., et al. (2017). Structure and evolution of flux transfer events near dayside magnetic reconnection dissipation region: MMS observations. *Geophys. Res. Lett.* 44, 5951–5959. doi:10.1002/2017gl073411

Dong, X. C., Dunlop, M. W., Wang, T. Y., Cao, J. B., Trattner, K. J., Bamford, R., et al. (2018). Carriers and sources of magnetopause current: MMS case study. *J. Geophys. Res. Space Phys.* 123, 5464–5475. doi:10.1029/2018ja025292

Dong, X. C., Dunlop, M. W., Wang, T. Y., Trattner, K. J., Russell, C. T., and Giles, B. (2020). MMS observation of secondary magnetic reconnection beside ion-scale flux rope at the magnetopause. *Geophys. Res. Lett.* 47. doi:10.1029/2020gl089075

Dong, X. C., Dunlop, M. W., Xiao, C., Wei, D., Wang, T. Y., and Zhao, J. S. (2023). Simultaneous mesoscale polar cusp field-aligned currents measured on mid- and low-altitude satellites. *Geophys. Res. Lett.* 50, e2022GL102460. doi:10.1029/2022GL102460

Dunlop, M. W., and Balogh, A. (2005). Magnetopause current as seen by Cluster. *Ann. Geophys.* 23, 901–907. doi:10.5194/angeo-23-901-2005

Dunlop, M. W., Balogh, A., Glassmeier, K. H., and Robert, P. (2002). Four-point Cluster application of magnetic field analysis tools: the Curlometer. *J. Geophys. Res. Space Phys.* 107. doi:10.1029/2001ja005088

Dunlop, M. W., Dong, X. C., Wang, T. Y., Eastwood, J. P., Robert, P., Haaland, S., et al. (2021a). Curlometer technique and applications. *J. Geophys. Res. Space Phys.* 126. doi:10.1029/2021ja029538

Dunlop, M. W., and Eastwood, J. P. (2008). "The curlometer and other gradient based methods," in *Multi-spacecraft analysis methods revisited*. Editors G. Paschmann, and P. W. Daly (Noordwijk, Netherlands: ESA Communications Keplerlaan), 17–26.

Dunlop, M. W., Haaland, S., Dong, X. C., Middleton, H. R., Escoubet, C. P., Yang, Y. Y., et al. (2018). "Multipoint analysis of electric currents in geospace using the curlometer technique," in *Electric currents in geospace and beyond. American geophysical union*. Editors A. Keiling, O. Marghitu, and M. Wheatland (John Wiley and Sons), 67–80. doi:10.1002/9781119324522.ch4

Dunlop, M. W., and Lühr, H. (2020). *Ionospheric multi-spacecraft analysis tools*. Springer. doi:10.1007/978-3-030-26732-2

Dunlop, M. W., Southwood, D. J., Glassmeier, K. H., and Neubauer, F. M. (1988). Analysis of multipoint magnetometer data. *Adv. Space Res.* 8, 273–277. doi:10.1016/0273-1177(88)90141-X

Dunlop, M. W., Taylor, M. G. G. T., Davies, J. A., Owen, C. J., Pu, Z., Laakso, H., et al. (2005). Coordinated cluster/double star observations of dayside reconnection signatures. *Ann. Geophys.* 23 (8), 2867–2875.

Dunlop, M. W., Wang, T., Dong, X., Haarland, S., Shi, Q., Fu, H., et al. (2021b). "Multispacecraft measurements in the magnetosphere," in *Magnetospheres in the solar system. American geophysical union*. Editors R. Maggiolo, N. André, H. Hasegawa, and D. T. Welling (John Wiley and Sons), 637–656. doi:10.1002/9781119815624.ch40

Dunlop, M. W., and Woodward, T. I. (1998). "Multi-spacecraft discontinuity analysis: orientation and motion," in *Analysis methods for multi-spacecraft data*. Editors G. Paschmann, and P. W. Daly (Noordwijk, Netherlands: ESA Publications Division), 271–306.

Dunlop, M. W., Yang, J. Y., Yang, Y. Y., Lühr, H., and Cao, J. B. (2020). "Multi-spacecraft current estimates at swarm," in *Ionospheric multi-spacecraft analysis tools*. Editors M. W. Dunlop, and H. Lühr (Springer), 83. doi:10.1007/978-3-030-26732-2_5

Dunlop, M. W., Yang, J. Y., Yang, Y. Y., Xiong, C., Lühr, H., Bogdanova, Y. V., et al. (2015a). Simultaneous field-aligned currents at Swarm and Cluster satellites. *Geophys. Res. Lett.* 42, 3683–3691. doi:10.1002/2015gl063738

Dunlop, M. W., Yang, Y. Y., Yang, J. Y., Lühr, H., Shen, C., Olsen, N., et al. (2015b). Multispacecraft current estimates at swarm. *J. Geophys. Res. Space Phys.* 120, 8307–8316. doi:10.1002/2015ja021707

Dunlop, M. W., Zhang, Q.-H., Bogdanova, Y. V., Lockwood, M., Pu, Z., Hasegawa, H., et al. (2011). Extended magnetic reconnection across the dayside magnetopause. *Phys. Rev. Lett.* 107, 025004. doi:10.1103/PhysRevLett.107.025004

Dunlop, M. W., Zhang, Q. H., Xiao, C. J., He, J. S., Pu, Z., Fear, R. C., et al. (2009). Reconnection at high latitudes: antiparallel merging. *Phys. Rev. Lett.* 102, 075005. doi:10.1103/PhysRevLett.102.075005

Eastwood, J. P., Balogh, A., Dunlop, M. W., and Smith, C. W. (2002). Cluster observations of the heliospheric current sheet and an associated magnetic flux rope and comparisons with ACE. *J. Geophys. Res. Space Phys.* 107 (SSH 9-1), 9. doi:10.1029/2001JA009158

Eastwood, J. P., Phan, T. D., Cassak, P. A., Gershman, D. J., Haggerty, C., Malakit, K., et al. (2016). Ion-scale secondary flux ropes generated by magnetopause reconnection as resolved by MMS. *Geophys. Res. Lett.* 43, 4716–4724. doi:10.1002/2016GL068747

Escoubet, C. P., Fehringer, M., and Goldstein, M. (2001). *Introduction*The cluster mission. *Ann. Geophys.* 19, 1197–1200. doi:10.5194/angeo-19-1197-2001

Escoubet, C. P., Hwang, K. J., Toledo-Redondo, S., Turc, L., Haaland, S. E., Aunai, N., et al. (2020). Cluster and MMS simultaneous observations of magnetosheath high speed jets and their impact on the magnetopause. *Front. Astronomy Space Sci.* 6, 78. doi:10.3389/fspas.2019.00078

Escoubet, C. P., Masson, A., Laakso, H., Goldstein, M. L., Dimbylow, T., Bogdanova, Y. V., et al. (2021). Cluster after 20 years of operations: science highlights and technical challenges. *J. Geophys. Res. Space Phys.* 126, e29474. doi:10.1029/2021JA029474

Escoubet, C. P., Schmidt, R., and Goldstein, M. L. (1997). Cluster - science and mission overview. *Space Sci. Rev.* 79, 11–32. doi:10.1023/A:1004923124586

Fillion, M., Hulot, G., Alken, P., Chulliat, A., and Vigneron, P. (2021). Multispacecraft current density estimates in the low- and mid-latitude F-region ionosphere using the swarm constellation. *J. Geophys. Res. Space Phys.* 126, e28872. doi:10.1029/2020JA028872

Forsyth, C., Lester, M., Cowley, S. W. H., Dandouras, I., Fazakerley, A. N., Fear, R. C., et al. (2008). Observed tail current systems associated with bursty bulk flows and auroral streamers during a period of multiple substorms. *Ann. Geophys.* 26, 167–184. doi:10.5194/angeo-26-167-2008

Forsyth, C., Lester, M., Fazakerley, A. N., Owen, C. J., and Walsh, A. P. (2011). On the effect of line current width and relative position on the multi-spacecraft curlometer technique. *Planet. Space Sci.* 59, 598–605. doi:10.1016/j.pss.2009.12.007

Friis-Christensen, E., Lühr, H., and Hulot, G. (2006). Swarm: a constellation to study the Earth's magnetic field. *Earth, Planets Space* 58, 351–358. doi:10.1186/BF03351933

Friis-Christensen, E., Lühr, H., Knudsen, D., and Haagmans, R. (2008). Swarm – an Earth observation mission investigating geospace. *Adv. Space Res.* 41, 210–216. doi:10.1016/j.asr.2006.10.008

Fu, H. S., Cao, J. B., Cao, D., Wang, Z., Vaivads, A., Khotyaintsev, Y. V., et al. (2019). Evidence of magnetic nulls in electron diffusion region. *Geophys. Res. Lett.* 46, 48–54. doi:10.1029/2018GL080449

Fu, H. S., Cao, J. B., Vaivads, A., Khotyaintsev, Y. V., Andre, M., Dunlop, M., et al. (2016). Identifying magnetic reconnection events using the FOTE method. *J. Geophys. Res. Space Phys.* 121, 1263–1272. doi:10.1002/2015JA021701

Fu, H. S., Vaivads, A., Khotyaintsev, Y. V., André, M., Cao, J. B., Olshevsky, V., et al. (2017). Intermittent energy dissipation by turbulent reconnection. *Geophys. Res. Lett.* 44, 37–43. doi:10.1002/2016GL071787

Fu, H. S., Vaivads, A., Khotyaintsev, Y. V., Olshevsky, V., André, M., Cao, J. B., et al. (2015). How to find magnetic nulls and reconstruct field topology with MMS data? *J. Geophys. Res. Space Phys.* 120, 3758–3782. doi:10.1002/2015ja021082

Fu, H. S., Wang, Z., Zong, Q., Chen, X. H., He, J. S., Vaivads, A., et al. (2020). "Methods for finding magnetic nulls and reconstructing field topology," in *Dayside magnetosphere interactions*. *American geophysical union*. Editors Q. Zong, P. Escoubet, D. Sibeck, G. Le, and H. Zhang (John Wiley and Sons), 153–172. doi:10.1002/9781119509592.ch9

Gjerloev, J. W., and Hoffman, R. A. (2002). Currents in auroral substorms. *J. Geophys. Res. Space Phys.* 107 (SMP 5-1), 5–13. doi:10.1029/2001JA000194

Grimald, S., Dandouras, I., Robert, P., and Lucek, E. (2012). Study of the applicability of the curlometer technique with the four Cluster spacecraft in regions close to Earth. *Ann. Geophys.* 30, 597–611. doi:10.5194/angeo-30-597-2012

Haaland, S., and Gjerloev, J. (2013). On the relation between asymmetries in the ring current and magnetopause current. *J. Geophys. Res. Space Phys.* 118, 7593–7604. doi:10.1002/2013ja019345

Haaland, S., Hasegawa, H., Paschmann, G., Sonnerup, B., and Dunlop, M. (2021). 20 Years of cluster observations: the magnetopause. *J. Geophys. Res. Space Phys.* 126, e2021JA029362. doi:10.1029/2021JA029362

Haaland, S., Sonnerup, B., Dunlop, M., Balogh, A., Georgescu, E., Hasegawa, H., et al. (2004a). Four-spacecraft determination of magnetopause orientation, motion and thickness: comparison with results from single-spacecraft methods. *Ann. Geophys.* 22, 1347–1365. doi:10.5194/angeo-22-1347-2004

Haaland, S., Sonnerup, B. U. Ö., Dunlop, M. W., Georgescu, E., Paschmann, G., Klecker, B., et al. (2004b). Orientation and motion of a discontinuity from Cluster curlometer capability: minimum variance of current density. *Geophys. Res. Lett.* 31. doi:10.1029/2004GL020001

Hamrin, M., Rönnmark, K., Börlin, N., Vedin, J., and Vaivads, A. (2008). GALS – gradient analysis by least squares. *Ann. Geophys.* 26, 3491–3499. doi:10.5194/angeo-26-3491-2008

Harvey, C. C. (1998). "Spatial gradients and the volumetric tensor," in *Analysis methods for multi-spacecraft data*. Editors G. Paschmann, and P. W. Daly (Noordwijk, Netherlands: ESA Publications Division), 307–322.

He, J. S., Tu, C. Y., Tian, H., Xiao, C. J., Wang, X. G., Pu, Z. Y., et al. (2008a). A magnetic null geometry reconstructed from Cluster spacecraft observations. *J. Geophys. Res. Space Phys.* 113. doi:10.1029/2007JA012609

He, J. S., Zong, Q. G., Deng, X. H., Tu, C. Y., Xiao, C. J., Wang, X. G., et al. (2008b). Electron trapping around a magnetic null. *Geophys. Res. Lett.* 35, L14104. doi:10.1029/2008GL034085

Henderson, P. D., Owen, C. J., Lahiff, A. D., Alexeev, I. V., Fazakerley, A. N., Yin, L., et al. (2008). The relationship between $\mathbf{j} \times \mathbf{B}$ and $\nabla \cdot \mathbf{P}_e$ in the magnetotail plasma sheet: cluster observations. *J. Geophys. Res. Space Phys.* 113. doi:10.1029/2007ja012697

Hwang, K. J., Sibeck, D. G., Burch, J. L., Choi, E., Fear, R. C., Lavraud, B., et al. (2018). Small-scale flux transfer events formed in the reconnection exhaust region between two X lines. *J. Geophys. Res. Space Phys.* 123, 8473–8488. doi:10.1029/2018JA025611

Klein, K. G., Spence, H., Alexandrova, O., Argall, M., Arzamasskiy, L., Bookbinder, J., et al. (2023). HelioSwarm: a multipoint, multiscale mission to characterize turbulence. *Space Sci. Rev.* 219, 74. doi:10.1007/s11214-023-01019-0

Lavraud, B., Zhang, Y. C., Vernisse, Y., Gershman, D. J., Dorelli, J., Cassak, P. A., et al. (2016). Currents and associated electron scattering and bouncing near the diffusion region at Earth's magnetopause. *Geophys. Res. Lett.* 43, 3042–3050. doi:10.1002/2016GL068359

Liang, J., and Liu, W. W. (2007). A MHD mechanism for the generation of the meridional current system during substorm expansion phase. *J. Geophys. Res. Space Phys.* 112. doi:10.1029/2007JA012303

Lühr, H., Park, J., Gjerloev, J. W., Rauberg, J., Michaelis, I., Merayo, J. M. G., et al. (2015). Field-aligned currents' scale analysis performed with the Swarm constellation. *Geophys. Res. Lett.* 42, 1–8. doi:10.1002/2014gl062453

Marchaudon, A., Cerisier, J. C., Dunlop, M. W., Pitout, F., Bosqued, J. M., and Fazakerley, A. N. (2009). Shape, size, velocity and field-aligned currents of dayside plasma injections: a multi-altitude study. *Ann. Geophys.* 27, 1251–1266. doi:10.5194/angeo-27-1251-2009

McPherron, R. L., Russell, C. T., and Aubry, M. P. (1973). Satellite studies of magnetospheric substorms on August 15, 1968: 9. Phenomenological model for substorms. *J. Geophys. Res.* 78, 3131–3149. doi:10.1029/JA078i016p03131

Middleton, H. R., and Masson, A. (2016). The Curlometer Technique: a beginner's guide. Available at: http://www.cosmos.esa.int/web/csa/multi-spacecraft (Accessed April 11, 2024).

Nakamura, R., Baumjohann, W., Fujimoto, M., Asano, Y., Runov, A., Owen, C. J., et al. (2008). Cluster observations of an ion-scale current sheet in the magnetotail under the presence of a guide field. *J. Geophys. Res. Space Phys.* 113. doi:10.1029/2007JA012760

Narita, Y., Nakamura, R., and Baumjohann, W. (2013). Cluster as current sheet surveyor in the magnetotail. *Ann. Geophys.* 31, 1605–1610. doi:10.5194/angeo-31-1605-2013

Olsen, N., Lühr, H., Finlay, C., Sabaka, T., Michaelis, I., Rauberg, J., et al. (2014). The CHAOS-4 geomagnetic field model. *Geophys. J. Int.* 197, 815–827. doi:10.1093/gji/ggu033

Panov, E. V., Büchner, J., Fränz, M., Korth, A., Savin, S. P., Fornaçon, K. H., et al. (2006). CLUSTER observation of collisionless transport at the magnetopause. *Geophys. Res. Lett.* 33. doi:10.1029/2006GL026556

Panov, E. V., Büchner, J., Fränz, M., Korth, A., Savin, S. P., Rème, H., et al. (2008). High-latitude Earth's magnetopause outside the cusp: cluster observations. *J. Geophys. Res. Space Phys.* 113. doi:10.1029/2006ja012123

Paschmann, G., and Daly, P. W. (1998). *Analysis methods for multi-spacecraft data*. Noordwijk, Netherlands: ESA Publications Division.

Paschmann, G., and Daly, P. W. (2008). *Multi-spacecraft analysis methods revisited*. Noordwijk, Netherlands: ESA Communications Keplerlaan.

Paschmann, G., Schwartz, S. J., Escoubet, C. P., and Haaland, S. (2005). *Outer magnetospheric boundaries: cluster results*. Springer/ISSI. doi:10.1007/1-4020-4582-4

Petrukovich, A., Artemyev, A., Vasko, I., Nakamura, R., and Zelenyi, L. (2015). Current sheets in the Earth magnetotail: plasma and magnetic field structure with cluster project observations. *Space Sci. Rev.* 188, 311–337. doi:10.1007/s11214-014-0126-7

Phan, T. D., Eastwood, J. P., Cassak, P. A., Øieroset, M., Gosling, J. T., Gershman, D. J., et al. (2016). MMS observations of electron-scale filamentary currents in the reconnection exhaust and near the X line. *Geophys. Res. Lett.* 43, 6060–6069. doi:10.1002/2016GL069212

Pitout, F., and Bogdanova, Y. V. (2021). The polar cusp seen by cluster. *J. Geophys. Res. Space Phys.* 126, e2021JA029582. doi:10.1029/2021JA029582

Pu, Z. Y., Zong, Q. G., Fritz, T. A., Xiao, C. J., Huang, Z. Y., Fu, S. Y., et al. (2005). Multiple flux rope events at the high-latitude magnetopause: cluster/rapid observation on 26 january, 2001. *Surv. Geophys.* 26, 193–214. doi:10.1007/s10712-005-1878-0

Retinò, A., Khotyaintsev, Y., Le Contel, O., Marcucci, M. F., Plaschke, F., Vaivads, A., et al. (2022). Particle energization in space plasmas: towards a multi-point, multi-scale plasma observatory. *Exp. Astron.* 54, 427–471. doi:10.1007/s10686-021-09797-7

Ritter, P., and Lühr, H. (2006). Curl-B technique applied to Swarm constellation for determining field-aligned currents. *Earth, Planets Space* 58, 463–476. doi:10.1186/BF03351942

Ritter, P., Lühr, H., and Rauberg, J. (2013). Determining field-aligned currents with the Swarm constellation mission. *Earth, Planets Space* 65, 1285–1294. doi:10.5047/eps.2013.09.006

Ritter, P., Lühr, H., Viljanen, A., Amm, O., Pulkkinen, A., and Sillanpää, I. (2004). Ionospheric currents estimated simultaneously from CHAMP satelliteand IMAGE ground-based magnetic field measurements: a statisticalstudy at auroral latitudes. *Ann. Geophys.* 22, 417–430. doi:10.5194/angeo-22-417-2004

Robert, P., and Dunlop, M. W. (2022). Use of twenty years CLUSTER/FGM data to observe the mean behavior of the magnetic field and current density of Earth's magnetosphere. *J. Geophys. Res. Space Phys.* 127. doi:10.1029/2021ja029837

Robert, P., Dunlop, M. W., Roux, A., and Chanteur, G. (1998a). "Accuracy of current density determination," in *Analysis methods for multi-spacecraft data*. Editors G. Paschmann, and P. W. Daly (Noordwijk, Netherlands: ESA Publications Division), 395–418.

Robert, P., Roux, A., Harvey, C. C., Dunlop, M. W., Daly, P. W., and Glassmeier, K.-H. (1998b). "Tetrahedron geometric factors," in *Analysis methods for multi-spacecraft data*. Editors G. Paschmann, and P. W. Daly (Noordwijk, Netherlands: ESA Publications Division), 323–348.

Rong, Z. J., Wan, W. X., Shen, C., Li, X., Dunlop, M. W., Petrukovich, A. A., et al. (2011). Statistical survey on the magnetic structure in magnetotail current sheets. *J. Geophys. Res. Space Phys.* 116. doi:10.1029/2011JA016489

Roux, A., Robert, P., Fontaine, D., Contel, O. L., Canu, P., and Louarn, P. (2015). What is the nature of magnetosheath FTEs? *J. Geophys. Res. Space Phys.* 120, 4576–4595. doi:10.1002/2015JA020983

Runov, A., Sergeev, V. A., Baumjohann, W., Nakamura, R., Apatenkov, S., Asano, Y., et al. (2005). Electric current and magnetic field geometry in flapping magnetotail current sheets. *Ann. Geophys.* 23, 1391–1403. doi:10.5194/angeo-23-1391-2005

Runov, A., Sergeev, V. A., Nakamura, R., Baumjohann, W., Apatenkov, S., Asano, Y., et al. (2006). Local structure of the magnetotail current sheet: 2001 Cluster observations. *Ann. Geophys.* 24, 247–262. doi:10.5194/angeo-24-247-2006

Russell, C. T., Luhmann, J. G., and Strangeway, R. J. (2016). *Space physics: an introduction*. Cambridge: Cambridge University Press. doi:10.1017/9781316162590

Shen, C., and Dunlop, M. (2023). Field gradient analysis based on a geometrical approach. *J. Geophys. Res. Space Phys.* 128, e2023JA031313. doi:10.1029/2023JA031313

Shen, C., Dunlop, M., Ma, Y. H., Chen, Z. Q., Yan, G. Q., Liu, Z. X., et al. (2011). The magnetic configuration of the high-latitude cusp and dayside magnetopause under strong magnetic shears. *J. Geophys. Res. Space Phys.* 116, n/a-n/a. doi:10.1029/2011ja016501

Shen, C., and Dunlop, M. W. (2008). "Geometrical structure analysis of the magnetic field," in *Multi-spacecraft analysis methods revisited*. Editors G. Paschmann, and P. W. Daly (Noordwijk, Netherlands: ESA Communications Keplerlaan), 27–32.

Shen, C., Li, X., Dunlop, M., Liu, Z. X., Balogh, A., Baker, D. N., et al. (2003). Analyses on the geometrical structure of magnetic field in the current sheet based on cluster measurements. *J. Geophys. Res. Space Phys.* 108. doi:10.1029/2002ja009612

Shen, C., Li, X., Dunlop, M., Shi, Q. Q., Liu, Z. X., Lucek, E., et al. (2007). Magnetic field rotation analysis and the applications. *J. Geophys. Res. Space Phys.* 112. doi:10.1029/2005ja011584

Shen, C., Liu, Z. X., Li, X., Dunlop, M., Lucek, E., Rong, Z. J., et al. (2008a). Flattened current sheet and its evolution in substorms. *J. Geophys. Res. (Space Physics)* 113, A07S21. doi:10.1029/2007JA012812

Shen, C., Rong, Z. J., and Dunlop, M. (2012a). Determining the full magnetic field gradient from two spacecraft measurements under special constraints. *J. Geophys. Res. Space Phys.* 117. doi:10.1029/2012JA018063

Shen, C., Rong, Z. J., Dunlop, M. W., Ma, Y. H., Li, X., Zeng, G., et al. (2012b). Spatial gradients from irregular, multiple-point spacecraft configurations. *J. Geophys. Res. Space Phys.* 117. doi:10.1029/2012ja018075

Shen, C., Rong, Z. J., Li, X., Dunlop, M., Liu, Z. X., Malova, H. V., et al. (2008b). Magnetic configurations of the tilted current sheets in magnetotail. *Ann. Geophys.* 26, 3525–3543. doi:10.5194/angeo-26-3525-2008

Shen, C., Yang, Y. Y., Rong, Z. J., Li, X., Dunlop, M., Carr, C. M., et al. (2014). Direct calculation of the ring current distribution and magnetic structure seen by Cluster during geomagnetic storms. *J. Geophys. Res. Space Phys.* 119, 2458–2465. doi:10.1002/2013ja019460

Shen, C., Zhang, C., Rong, Z., Pu, Z., Dunlop, M. W., Escoubet, C. P., et al. (2021a). Nonlinear magnetic gradients and complete magnetic geometry from multispacecraft measurements. *J. Geophys. Res. Space Phys.* 126, e2020JA028846. doi:10.1029/2020JA028846

Shen, C., Zhou, Y., Gao, L., Wang, X., Pu, Z., Escoubet, C. P., et al. (2021b). Measurements of the net charge density of space plasmas. *J. Geophys. Res. Space Phys.* 126, e2021JA029511. doi:10.1029/2021JA029511

Shen, C., Zhou, Y., Ma, Y., Wang, X., Pu, Z., and Dunlop, M. (2021c). A general algorithm for the linear and quadratic gradients of physical quantities based on 10 or more point measurements. *J. Geophys. Res. Space Phys.* 126, e2021JA029121. doi:10.1029/2021JA029121

Shi, J., Guo, J., Dunlop, M., Zhang, T., Liu, Z., Lucek, E., et al. (2012). Inter-hemispheric asymmetry of dependence of the cusp location on dipole tilt during northward IMF conditions. *Ann. Geophys.* 30, 21–26. doi:10.5194/angeo-30-21-2012

Shi, J. K., Cheng, Z. W., Zhang, T. L., Dunlop, M., Liu, Z. X., Torkar, K., et al. (2010). South-north asymmetry of field-aligned currents in the magnetotail observed by Cluster. *J. Geophys. Res. Space Phys.* 115. doi:10.1029/2009JA014446

Shi, Q. Q., Tian, A. M., Bai, S. C., Hasegawa, H., Degeling, A. W., Pu, Z. Y., et al. (2019). Dimensionality, coordinate system and reference frame for analysis of in-situ space plasma and field data. *Space Sci. Rev.* 215, 35. doi:10.1007/s11214-019-0601-2

Shiokawa, K., Baumjohann, W., Haerendel, G., Paschmann, G., Fennell, J. F., Friis-Christensen, E., et al. (1998). High-speed ion flow, substorm current wedge, and multiple Pi 2 pulsations. *J. Geophys. Res. Space Phys.* 103, 4491–4507. doi:10.1029/97JA01680

Shore, R. M., Whaler, K. A., Macmillan, S., Beggan, C., Olsen, N., Spain, T., et al. (2013). Ionospheric midlatitude electric current density inferred from multiple magnetic satellites. *J. Geophys. Res. Space Phys.* 118, 5813–5829. doi:10.1002/jgra.50491

Tan, X., Dunlop, M. W., Dong, X. C., Yang, Y. Y., Du, Y. S., Shen, C., et al. (2023). Ring current morphology from MMS observations. *J. Geophys. Res. Space Phys.* 128. doi:10.1029/2023ja031372

Teh, W. L., Nakamura, T. K. M., Nakamura, R., Baumjohann, W., Russell, C. T., Pollock, C., et al. (2017). Evolution of a typical ion-scale magnetic flux rope caused by thermal pressure enhancement. *J. Geophys. Res. Space Phys.* 122, 2040–2050. doi:10.1002/2016JA023777

Trenchi, L., Kauristie, K., Käki, S., Vanhamäki, H., Juusola, L., Blagau, A., et al. (2020). "ESA field-aligned currents—methodology inter-comparison exercise," in *Ionospheric multi-spacecraft analysis tools*. Editors M. W. Dunlop, and H. Lühr (Springer), 167. doi:10.1007/978-3-030-26732-2_8

Vallat, C., Dandouras, I., Dunlop, M., Balogh, A., Lucek, E., Parks, G. K., et al. (2005). First current density measurements in the ring current region using simultaneous multi-spacecraft CLUSTER-FGM data. *Ann. Geophys.* 23, 1849–1865. doi:10.5194/angeo-23-1849-2005

Vogt, J., Albert, A., and Marghitu, O. (2009). Analysis of three-spacecraft data using planar reciprocal vectors: methodological framework and spatial gradient estimation. *Ann. Geophys.* 27, 3249–3273. doi:10.5194/angeo-27-3249-2009

Vogt, J., Paschmann, G., and Chanteur, G. (2008). "Reciprocal vectors," in *Multi-spacecraft analysis methods revisited*. Editors G. Paschmann, and P. W. Daly (Noordwijk, Netherlands: ESA Communications Keplerlaan), 33–46.

Vogt, J., Sorbalo, E., He, M., and Blagau, A. (2013). Gradient estimation using configurations of two or three spacecraft. *Ann. Geophys.* 31, 1913–1927. doi:10.5194/angeo-31-1913-2013

Wang, H., Ma, S. Y., Lühr, H., Liu, Z. X., Pu, Z. Y., Escoubet, C. P., et al. (2006). Global manifestations of a substorm onset observed by a multi-satellite and ground station network. *Ann. Geophys.* 24, 3491–3496. doi:10.5194/angeo-24-3491-2006

Wang, T., Alexandrova, O., Perrone, D., Dunlop, M., Dong, X., Bingham, R., et al. (2019). Magnetospheric multiscale observation of kinetic signatures in the Alfvén vortex. *Astrophysical J.* 871, L22. doi:10.3847/2041-8213/aafe0d

Wang, Z., Fu, H. S., Liu, C. M., Liu, Y. Y., Cozzani, G., Giles, B. L., et al. (2019). Electron distribution functions around a reconnection X-line resolved by the FOTE method. *Geophys. Res. Lett.* 46, 1195–1204. doi:10.1029/2018GL081708

Wang, Z., Fu, H. S., Vaivads, A., Burch, J. L., Yu, Y., and Cao, J. B. (2020). Monitoring the spatio-temporal evolution of a reconnection X-line in space. *Astrophysical J.* 899, L34. doi:10.3847/2041-8213/abad2c

Xiao, C., Liu, W., Shen, C., Zhang, H., and Rong, Z. (2018). Study on the curvature and gradient of the magnetic field in Earth's cusp region based on the magnetic curvature analysis method. *J. Geophys. Res. (Space Physics)* 123, 3794–3805. doi:10.1029/2017JA025028

Xiao, C. J., Pu, Z. Y., Ma, Z. W., Fu, S. Y., Huang, Z. Y., and Zong, Q. G. (2004). Inferring of flux rope orientation with the minimum variance analysis technique. *J. Geophys. Res. Space Phys.* 109. doi:10.1029/2004JA010594

Xiao, C. J., Wang, X. G., Pu, Z. Y., Ma, Z. W., Zhao, H., Zhou, G. P., et al. (2007). Satellite observations of separator-line geometry of three-dimensional magnetic reconnection. *Nat. Phys.* 3, 609–613. doi:10.1038/nphys650

Xiao, C. J., Wang, X. G., Pu, Z. Y., Zhao, H., Wang, J. X., Ma, Z. W., et al. (2006). *In situ* evidence for the structure of the magnetic null in a 3D reconnection event in the Earth's magnetotail. *Nat. Phys.* 2, 478–483. doi:10.1038/nphys342

Yang, Y. Y., Shen, C., Dunlop, M., Rong, Z. J., Li, X., Angelopoulos, V., et al. (2016). Storm time current distribution in the inner equatorial magnetosphere: THEMIS observations. *J. Geophys. Res. Space Phys.* 121, 5250–5259. doi:10.1002/2015ja022145

Yang, Y. Y., Shen, C., Zhang, Y. C., Rong, Z. J., Li, X., Dunlop, M., et al. (2014). The force-free configuration of flux ropes in geomagnetotail: cluster observations. *J. Geophys. Res. Space Phys.* 119, 6327–6341. doi:10.1002/2013ja019642

Yao, Z. H., Pu, Z. Y., Owen, C. J., Fu, S. Y., Chu, X. N., Liu, J., et al. (2014). Current reduction in a pseudo-breakup event: THEMIS observations. *J. Geophys. Res. Space Phys.* 119, 8178–8187. doi:10.1002/2014ja020186

Zhang, Q. H., Dunlop, M. W., Lockwood, M., Holme, R., Kamide, Y., Baumjohann, W., et al. (2011). The distribution of the ring current: cluster observations. *Ann. Geophys.* 29, 1655–1662. doi:10.5194/angeo-29-1655-2011

Zhang, Y. C., Shen, C., Liu, Z. X., Rong, Z. J., Zhang, T. L., Marchaudon, A., et al. (2013). Two different types of plasmoids in the plasma sheet: cluster multisatellite analysis application. *J. Geophys. Res. Space Phys.* 118, 5437–5444. doi:10.1002/jgra.50542

Zhang, Y. C., Shen, C., Marchaudon, A., Rong, Z. J., Lavraud, B., Fazakerley, A., et al. (2016). First *in situ* evidence of electron pitch angle scattering due to magnetic field line curvature in the Ion diffusion region. *J. Geophys. Res. Space Phys.* 121, 4103–4110. doi:10.1002/2016JA022409

Zhao, C., Russell, C. T., Strangeway, R. J., Petrinec, S. M., Paterson, W. R., Zhou, M., et al. (2016). Force balance at the magnetopause determined with MMS: application to flux transfer events. *Geophys. Res. Lett.* 43, 11941–11947. doi:10.1002/2016GL071568

Frontiers in
Astronomy and Space Sciences

Explores planetary science and extragalactic astronomy in all wavelengths

Advances the understanding of our universe - from planetary science to extragalactic astronomy, to high-energy and astroparticle physics.

Discover the latest Research Topics

See more →

Frontiers

Avenue du Tribunal-Fédéral 34
1005 Lausanne, Switzerland
frontiersin.org

Contact us

+41 (0)21 510 17 00
frontiersin.org/about/contact